XXVIII. Symposium Electromagnetic Phenomena in Nonlinear Circuits

Conference Proceedings

University of Maribor Press

University of Maribor

Faculty of Electrical Engineering
and Computer Science

XXVIII Symposium Electromagnetic Phenomena in Nonlinear Circuits (EPNC 2024)

Conference Proceedings

Editors
Martin Petrun
Andrzej Demenko
Wojciech Pietrowski

May 2025

Title **XXVIII. Symposium Electromagnetic Phenomena in Nonlinear Circuits (EPNC 2024)**

Subtitle **Conference Proceedings**

Editors Martin Petrun
(University of Maribor, Faculty of Electrical Engineering and Computer Science)

Andrzej Demenko
(Poznan University of Technology)

Wojciech Pietrowski
(Poznan University of Technology)

Technical editor Jan Perša
(University of Maribor, University Press)

Cover designer Jan Perša
(University of Maribor, University Press)

Graphic material Sources are own unless otherwise noted.
Authors of proceedings & Petrun, Demenko, Pierowski (editors), 2024

Conference XXVIII Symposium Electromagnetic Phenomena in Nonlinear Circuits (EPNC 2024)

Date and location June 18th to June 21st 2024, Portorož, Slovenia

International steering committee Anouar Belahcen
(Aalto University, Finland)

Grzegorz Cieślar
(Medical University of Silesia, Poland)

Andrzej Demenko
(Chairman, Poznan University of Technology, Poland)

Herbert De Gersem
(Technische Universität Darmstadt, Germany)

Sven Exnowski
(South Westphalia University of Applied Sciences, Germany)

Michal Frivaldsky
(University of Žilina, Slovakia)

Jacek Gieras
(UTC Aerospace Systems, Rockford, Illinois, United States of America)

Kay Hameyer
(RWTH Aachen University, Germany)

Mykhaylo Zagirnyak
(Kremenchuk M. Ostrohradskyi National Univ., Ukraine)

Krzysztof Zawirski
(Poznan University of Technology, Poland)

Wojciech Pietrowski
(Secretary, Poznan University of Technology, Poland)

Head of International Organising Commitee Martin Petrun (University of Maribor, Slovenia)

Published by **University of Maribor**
University Press
Slomškov trg 15, 2000 Maribor, Slovenija
https://press.um.si, zalozba@um.si

Issued by **University of Maribor**
Faculty of Electrical Engineering and Computer Science
Koroška cesta 46, 2000 Maribor, Slovenija
https://www.feri.um.si/, feri@um.si

Publication type E-book

Edition 1st

Available at http://press.um.si/index.php/ump/catalog/book/963

Published at Maribor, Slovenia, May 2025

Co-organizer

All proceedings were subjected to double-blind peer review.

CIP - Kataložni zapis o publikaciji
Univerzitetna knjižnica Maribor

621.3:004(082)(0.034.1)

SYMPOSIUM on Electromagnetic Phenomena in Nonlinear Circuits (23 ; 2025 ; Portorož)
XXVIII Symposium on Electromagnetic Phenomena in Nonlinear Circuits [Elektronski vir] : conference proceedings : [June 18th to June 21th, Portorož / editors Martin Petrun, Andrzej Demenko, Wojciech Pietrowski. - 1st ed. - E-zbornik. - Maribor : Univerza v Mariboru, Univerzitetna založba, 2025

Način dostopa (URL): https://press.um.si/index.php/ump/catalog/book/963
ISBN 978-961-286-986-1
doi: 10.18690/um.feri.4.2025
COBISS.SI-ID 234961411

ISBN 978-961-286-986-1 (pdf)

DOI https://doi.org/10.18690/um.feri.4.2025

Price Free copy

For publisher Prof. Dr. Zdravko Kačič,
Rector of University of Maribor

Attribution Petrun, M., Demenko, A., Pietrowski, W. (eds.). (2025). *XXVIII Symposium Electromagnetic Phenomena in Nonlinear Circuits (EPNC 2024): Conference Proceedings*. University of Maribor, University Press. doi: 10.18690/um.feri.4.2025

Table of Contents

Preface EPNC conference proceedings

Martin Petrun

Dear colleagues, authors, and readers,

The 28th EPNC was a remarkable success, and we were delighted to host you in our beautiful Portorož. The conference took place at the Grand Hotel Bernardin and left us with wonderful memories and impressions. We shared and discussed new ideas and breakthroughs, forged new connections, and enjoyed some quality time together.

The conference was divided into four thematic blocks:

- Nonlinear Coupled Electromagnetic Phenomena
- Nonlinear Devices and Systems
- Electromagnetics for Energy
- Bioelectromagnetics

We would like to extend our heartfelt gratitude to our sponsors and partners, whose generous support made this event possible. Special thanks to our Golden Sponsor, Hilti, and our Silver Sponsors, Imperix and Kolektor, as well as all other sponsors listed at the back of this proceeding.

In these conference proceedings, you will find the contributions that were presented at the conference. We trust that you will find these articles both informative and inspiring, fostering new research ideas and further scientific collaboration.

We are looking forward to meet you at the next EPNC conference, where we can continue our journey of scientific discovery together.

DOI
https://doi.org/
10.18690/um.feri.4.2025.1

ISBN
978-961-286-986-1

DATA-DRIVEN SIMULATION OF TRACTION ELECTRICAL MACHINES: A MODELLING STRATEGY FOR MULTI-PHYSICS DATASET GENERATION

COSTANZA ANERDI,[1] SIMONE FERRARI,[1] FABIO FRESCHI,[1]
LUCA GIACCONE,[1] GIANMARCO LORENTI,[1]
GIANMARIO PELLEGRINO, MAURIZIO REPETTO,[1]
LUIGI SOLIMENE,[1] PIERGIORGIO ALOTTO,[2]
FRANCESCO LUCCHINI,[2] RICCARDO TORCHIO[2]

[1] Politecnico di Torino, Department of Energy "Galileo Ferraris", Torino, Italy
costanza.anerdi@polito.it, simone.ferrari@polimi.it, fabio.freschi@polito.it,
luca.giaccone@polito.it, gianmarco.lorenti@polito.it, gianmario.pellegrino@polito.it,
maurizio.repetto@polito.it, luigi.solimene@polito.it
[2] University of Padova, Department of Industrial Engineering, Padova, Italy
piergiorgio.alotto@unipd.it, francesco.lucchini@unipd.it, riccardo.torchio@unipd.it

The design of traction electrical motors faces increasing challenges in satisfying requests for higher efficiency, speed, torque and cost reduction. Furthermore, the design of new machines must deal with the interaction of multiple physical domains, including electromagnetic, thermal, and structural aspects, leading to high computational costs. The adoption of surrogate data-driven models can significantly accelerate the optimized design of traction electrical machines. To this end, we propose a modelling strategy for the multi-physics dataset generation to build a benchmark for data-driven simulations.

Keywords:
electrical machines,
data-driven methods,
multi-objective optimization,
multi-physics analysis,
V-shaped motor

University of Maribor Press

I Introduction

The design of traction electrical motors must face new and difficult tasks, as the demands for performance in terms of efficiency, maximum speed, torque, and cost are always higher. An effective design procedure requires a multi-physical approach to address the interaction between different physical domains, such as electromagnetic, thermal, structural, and acoustic. In addition, the design problem goals often contrast each other:

- Maximizing the torque value requires higher current values, leading to higher power losses and, consequently, higher operating temperatures.
- Maximizing the rotating speed value increases the mechanical stresses on the rotor.

These examples highlight the multi-physical and multi-criteria nature of the traction electrical motor design. The multi-physical analysis can be addressed with the interaction of different analysis codes by transferring forcing terms and material operating points from one to another. These multi-physical analysis tasks are often performed in an optimization algorithm, resulting in considerable computational costs for the design procedure. However, the capabilities shown by the adoption of computational intelligence in engineering design problems help improve computational efficiency for the electrical motor design process [1-3].

Adopting a data-driven approach for the design of traction electrical motors requires defining a dataset of multi-physical solution outputs obtained by finite elements analysis codes. The obtained dataset is adopted to train the data-driven model, which can be used to surrogate the output of the traditional multi-physical analysis approach in a multi-objective optimization process framework. Our goal is to produce suitable data based on multi-physical simulations, providing a benchmark for comparing and testing the accuracy and computational efficiency of different data-driven approaches.

II Case Study

Among different possible motor configurations, a V-shaped Internal Permanent Magnet (IPM) configuration is chosen as a reference. Its geometry is described uniquely by well-defined rules, as are its material characteristics in all the physical domains involved. The encumbrance of the motor (stator outer radius and axial length) is fixed. Supply conditions and circuit data are provided.

The structure will be modelled mainly in its two-dimensional cross-section. The geometric cross-section is defined by the main aspects that can influence performance. In addition, the two-dimensional mesh is created with a suitable number of elements and a distribution that is able to return a sufficient degree of accuracy in all physical domains involved. In the following, the main hypotheses considered for each physical domain:

- Electromagnetic domain: the nonlinear magnetostatic analysis is based on the two-dimensional mesh with material nonlinearities considered at a given reference temperature. Even under magnetostatic formulation, several relative positions between rotor and stator ("snapshots") will be considered, enabling the evaluation of quantities like torque ripple, the magnetic induction waveform within iron, etc. In addition, other machine parameters, like no-load voltage, operating inductance value, etc., could also be added to the results dataset.
- Structural domain: the analysis starts from the two-dimensional mesh of the rotor, considering the maximum rotational speed at a given reference temperature. In particular, the following simplifying hypotheses will be considered:
    - the permanent magnet is constrained on the external contact with the slot, and no relative movement is allowed (no sliding between slot and magnet). The permanent magnet is not constrained on its internal side, giving rise to a worst-case scenario;
    - stresses related to the interference between the rotor core and the shaft are neglected.
- Thermal domain: in this case, the two-dimensional representation is not sufficient as axial thermal flow is crucial. Starting from the cross-section mesh, a three-dimensional domain will be created, and suitable boundary conditions, compatible with a water jacket cooling and potted end winding regions, will be applied to terminate the domain in the axial direction. In addition, the following considerations will be included:
    - In the first version of the dataset (iron and magnet losses neglected), the thermal case will be evaluated in the overload (peak performance)

condition by a thermal transient limited to the test time period of 10 s. It must be remarked that, in these conditions, the contribution of the copper losses is largely dominant over the iron ones, so they could be, in a first attempt, neglected;
- a wire winding is considered so that a homogenized material (copper + slot liner) will be adopted, while a layer of insulation between winding and slot is set;
- heat transfer at the air gap will be considered at the base rotational speed (corner speed).

III Workflow of the dataset-generating procedure

The workflow of the procedure that will build the results dataset is presented in Fig.1 and is made by the following steps:

- Definition of the parametric construction of the motor. All parameters are real-valued, and their number is p. The following physical conditions are valid for all analyses: rotational speed n_0, reference temperature for magnetic material characteristics, supply current phase angle;
- generation of N points belonging to the $\mathcal{R}^p$ space by means of an unstructured and hierarchical quasi-random sampling of the parameters hypercube, $k = 1, \dots, N$ [4];
- generation of the motor geometry on the basis of $\mathbf{x_k}$ by means of SyR-e package [5];
- creation of the corresponding two-dimensional FEMM mesh through LUA scripting [6];
- starting by the two-dimensional triangular mesh, the analyses are performed by dedicated Matlab functions sharing the same triangular mesh and data about materials:
  - electromagnetic: calling the two-dimensional nonlinear solver FEMM, iterating on the relative position of stator and rotor to get the torque ripple. Results: T torque, TR torque ripple, PF power factor, efficiency;
  - structural: applying the elasto-static formulation, present in Matlab PDEsolver [7], on the rotor mesh with centrifugal loads at maximum

rotation speed. Result: maximum value of the von Mises or equivalent tensile stress;
 – thermal: applying a procedure based on the extrusion of two-dimensional mesh with the application of suitable boundary conditions on axial ends. Losses, both in copper slots and in iron, are evaluated by the electromagnetic model and are here used as forcing terms. Results: maximum value of temperature in steady state;
- collection of all results in a dataset containing: for each k^{th} configuration the values of the parameters $\mathbf{x_k}$ and of results $\mathbf{R_k}$.

The complete dataset will be made available to other research groups to compare their results. Details about the diffusion of the dataset and of collection of results will be given at the Symposium.

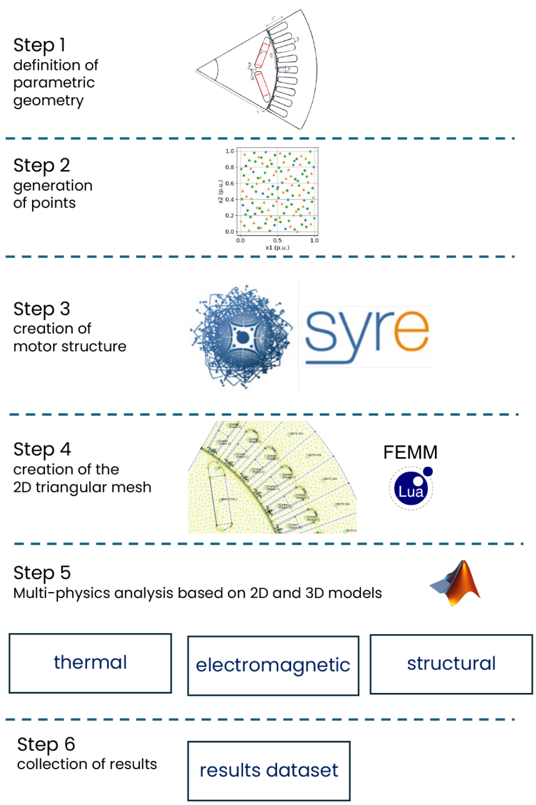

Figure 1: Workflow generating the results dataset.

References

[1] M. H. Mohammadi, V. Ghorbanian, and D. Lowther, "A data-driven approach for design knowledge extraction of synchronous reluctance machines using multi-physical analysis," IEEE Transactions on Industry Applications, vol. 55, no. 4, pp. 3707–3715, 2019.

[2] M. Repetto, "Computational intelligence in electromagnetic analysis," International Compumag Newsletter, 2023.

[3] F. Moraglio, P. Ragazzo, G. Dilevrano, S. Ferrari, G. Pellegrino, and M. Repetto, "A data-driven approach to the design of traction electric motors," in COMPUMAG 2023, the 24th International Conference on the Computation of Electromagnetic Fields, Kyoto, Japan, May 22-26, 2023, 2023.

[4] I. Sobol', "On the distribution of points in a cube and the approximate evaluation of integrals," USSR Computational Mathematics and Mathematical Physics, vol. 7, no. 4, pp. 86–112, 1967.

[5] "SyR-e Synchronous Reluctance – evolution design," https://github.com/SyR-e/syre public, 2024, [Online; accessed 17-Jan-2024].

[6] "Finite Element Method Magnetics - Version 4.2," https://www.femm.info/wiki/Documentation/, 2024, [Online; accessed 30-Jan-2024].

[7] "PDE solver: Solving Partial Differential Equations", https://it.mathworks.com/help/matlab/math/partial-differential-equations.html [Online; accessed 15-Mar-2024].

METHODOLOGY TO DETERMINE THE MAXIMUM ROTATIONAL SPEED FOR THE ARRANGEMENT OF BURIED PERMANENT MAGNETS IN HIGH-SPEED ROTORS OF ELECTRICAL MACHINES

MAXIMILIAN LAUERBURG, KAY HAMEYER
RWTH Aachen University, Institute of Electrical Machines, Aachen, Germany
maximilian.lauerburg@iem.rwth-aachen.de, kay.hameyer@iem.rwth-aachen.de

A methodology to determine the maximum technically feasible rotational speed of rotors constructed with buried permanent magnets is presented. The maximum achievable rotational speed is reached as soon as the permissible space within the rotor is no longer sufficient for the arrangement of the permanent magnets. The methodology couples mechanical and electromagnetic constraints. The results are evaluated based on a V-arrangement of a buried rotor permanent magnet system.

DOI
https://doi.org/
10.18690/um.feri.4.2025.2

ISBN
978-961-286-986-1

Keywords:
high-speed operation, pmsm (permanent magnet synchronous machine), V-arrangement, coupled analytical calculation method, maximum rotational speed for V-arrangement

University of Maribor Press

I Motivation

High-speed operation of electrical machines is essential for mobile applications due to potential increases in the achievable power density [1], [2]. The synchronous machine with buried permanent magnets (IPMSM) is predominantly used in traction drives for electric vehicles when compared to other machine topologies [2].

The feasible electromagnetic design is mainly limited by mechanical constraints at high-speed operation, so that the yield strengths of rotor materials are not exceeded, and mechanical integrity is guaranteed during operation [3], [4].

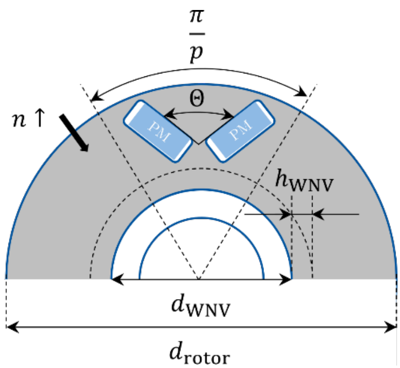

Figure 1: Allowable construction space for a V-arrangement of buried permanent magnets (VPMSM) within a rotor.

An analytical methodology to calculate the maximum mechanical stress in high-speed rotors with regard to the impact of centrifugal force and press fits between rotor components is published in [4] and [5]. The analytical approach enables a representation of the achievable circumferential speed v for different rotor topologies based on material and geometric parameters (1).

The circumferential speed is directly dependent on the ratio R_{p}/ρ between the yield strength and the density of the material used in the outer holding band of the rotor. The notch effect of magnet pockets is considered with the stress concentration factor K_{t}. The press fit between the lamination sheet and the shaft reduces the achievable circumferential speed. The impact primarily depends on the interference δ and the relative distance between the joint diameter d_{WNV} of the shaft-hub connection and the position d_σ with the maximum centrifugal load [4]. E is the homogenised *Young*'s modulus of both construction elements.

$$v \sim \sqrt{\frac{R_\mathrm{P} - \left(\frac{d_\mathrm{WNV}}{d_\sigma}\right)^2 \cdot E \cdot \frac{2\delta}{d_\mathrm{WNV}}}{K_\mathrm{t} \cdot \rho - \left(\frac{d_\mathrm{WNV}}{d_\sigma}\right)^2 \cdot \frac{1}{v_\mathrm{lift}^2} \cdot E \cdot \frac{2\delta}{d_\mathrm{WNV}}}} \tag{1}$$

As the achievable circumferential speed of a rotor cross-section is limited, the rotor diameter d_rotor decreases with increasing rotational speed n as shown in Figure 1. In addition, the shaft-hub connection limits the radial space within the rotor, in which the permanent magnets can be arranged. A minimum thickness h_WNV of the rotor lamination sheet at the bore diameter d_WNV is required to apply the necessary joint pressure to the interference fit. The number of pole pairs p determines the rotor symmetry at the circumference.

An analytical model for calculating the flux density in the air gap during the no-load operation of an IPMSM as a function of the dimensions of the buried permanent magnets and the bridge thicknesses is published in [5]. This electromagnetic model is coupled to the mechanical models in [4] and [5] to obtain a maximum achievable rotational speed n_max, above which the space within the rotor is no longer sufficient for the arrangement of permanent magnets.

Table 1: Material properties

Component	Material	Physical Properties
FL	NO27-14	R_P=416 MPa, ρ=7600 kg/m³
PM	NdFeB	B_r=1.25 T, H_c=-992 kA/m, ρ=7650 kg/m³

II Methodology

Figure 2 shows the process for determining the maximum technically feasible rotational speed. At the beginning of the design process, the power P, the efficiency η to be achieved and the permissible installation space V_zul must be defined. The suitable materials for the ferromagnetic lamination (FL) and the permanent magnets (PM) with their mechanical and electromagnetic properties are selected. Based on the selection for the electrical steel sheet, this is accompanied by a limitation of the maximum fundamental electrical frequency $f_{\mathrm{el,max}}$ so that the iron losses are not becoming too large.

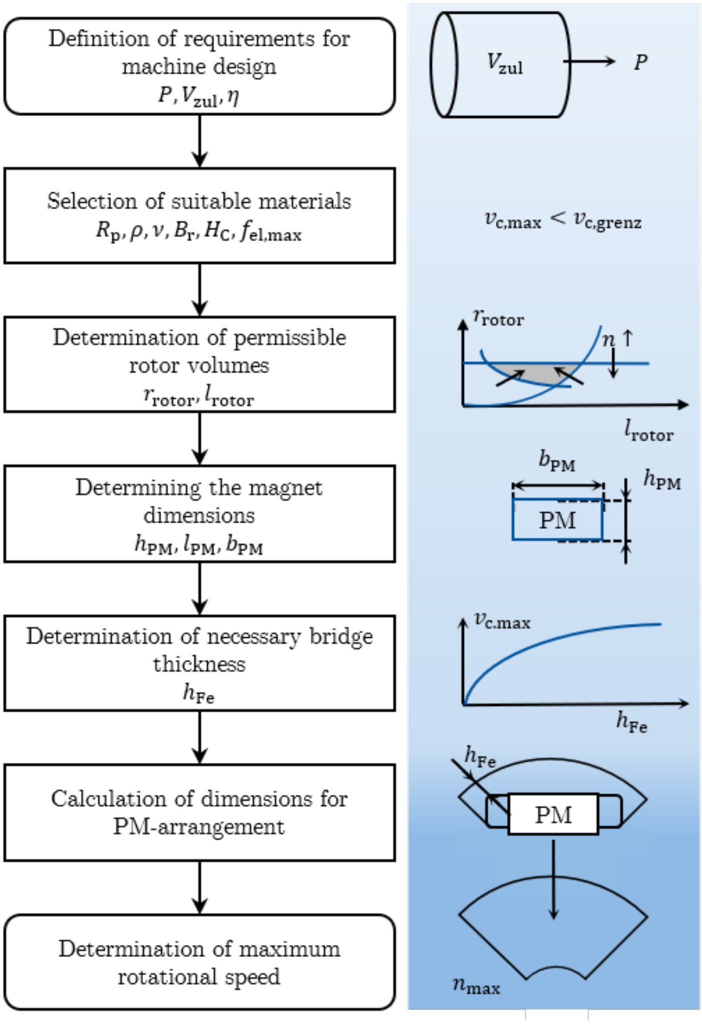

Figure 2: Methodology for determining the maximum technically feasible rotational speed.

The permissible rotor dimensions are calculated based on relationships for structural mechanics and structural dynamics in [5] and [6]. The electromagnetic model in [5] enables the determination of the dimensions of the buried permanent magnets. The required bridge thickness to ensure the rotor integrity is then calculated using the mechanical model.

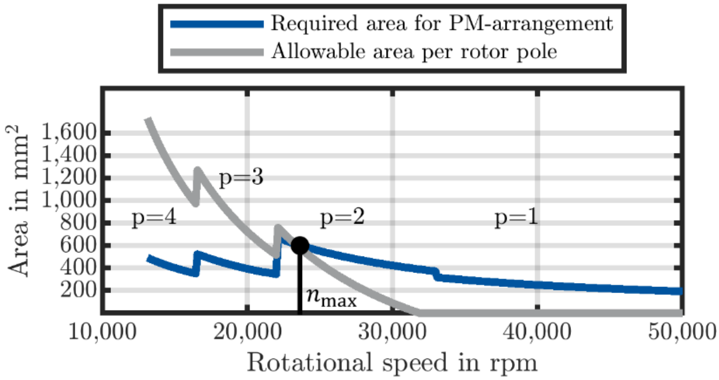

Figure 3: Comparison of space requirement for PM arrangement and allowable space.

Now that the dimensions of a magnet arrangement have been determined, it can be assessed whether the permanent magnets can be arranged inside the rotor. The rotational speed n_{max} above which the arrangement is no longer possible, is the maximum technically feasible rotational speed.

The required area of a PM-arrangement is compared in Figure 3 to the allowable area per rotor pole based on the material parameters given in Table I. At low rotational speed, there is no space restriction for the arrangement of the permanent magnets. The number of pole pairs is abruptly reduced when the defined frequency $f_{\mathrm{el,max}}$ is reached. This results in an instantaneous increase of the allowable and required area. The required area increases so that adequate pole coverage is achieved with the permanent magnets. Overall, the permissible area decreases faster than the required area with increasing rotational speed, so both curves intersect. The intersection point determines the maximum rotational speed n_{max}.

As shown in Figure 4, this intersection point dependent on the required power and the achievable circumferential speed. The smaller the angle Θ of the V-arrangement, the smaller the maximum rotational speed becomes.

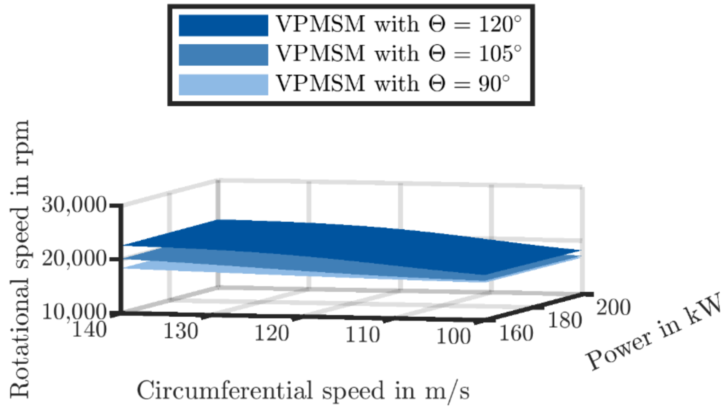

Figure 4: Influence of the angle Θ of the V-arrangement on the achievable maximum rotational speed.

III Conclusion and Outlook

The presented methodology enables the determination of a maximum technically feasible rotational speed with regard to the arrangement of buried permanent magnets. The solution space of possible circumferential and rotational speeds for a PM-arrangement is morphologically limited. This method can be used in the following to compare different PM arrangements such as tangential- and / or spoke-arrangement with regard to the limits of high-speed operation.

References

[1] D. Gerada, A. Mebarki, N. L. Brown, C. Gerada, A. Cavagnino, A. Boglietti, "High-Speed Electrical Machines: Technologies, Trends and Developments", *IEEE Transactions on Industrial Electronics,* vol. 61, No. 6, pp. 2946-2959, 2013.

[2] A. Krings, C. Monissen, "Review and Trends in Electric Traction Motors for Battery Electric and Hybrid Vehicles", *International Conference on Electrical Machines,* Gothenburg, 2020.

[3] M. E. Gerlach, M. Zajonc, B. Ponick, "Mechanical stress and deformation in the rotors of a high-speed PMSM and IM", *e & I Elektrotechnik und Informationstechnik,* vol. 138, pp. 96-109, 2021.

[4] M. Lauerburg, P. Toraktrakul, K. Hameyer, "Design Morphology for High-Speed Rotors in Electrical Machines Based on Analytical Models", *IEEE Workshop on Electrical Machines Design, Control and Diagnosis*, Newcastle, 2023.

[5] M. Lauerburg, P. Toraktrakul, K. Hameyer, "Multi-domain analytical rotor model with buried permanent magnets in V-arrangement for high-speed applications", *Archives of Electrical Engineering,* vol. 72, No. 3, pp. 629-641, 2023.

[6] J. Pyrhönen, T. Jokinen, V. Hrabovacava, "Design of rotating electrical machines", *John Wiley and Sons,* 2nd edition, 2013.

DIMENSIONING FIELD-GRADING MATERIALS IN CABLE JOINTS BY ADJOINT TRANSIENT FINITE-ELEMENT SENSITIVITY ANALYSIS

DOI
https://doi.org/10.18690/um.feri.4.2025.3

ISBN
978-961-286-986-1

MAREN GRETA RUPPERT,[1] HERBERT DE GERSEM,[1]
YVONNE SPÄCK-LEIGSNERING,[1] MYRIAM KOCH[2]

[1] Technical University of Darmstadt, Institute for Accelerator Science and Electromagnetic Fields (TEMF), Darmstadt, Germany
ruppert@temf.tu-darmstadt.de, degersem@temf.tu-darmstadt.de, spaeck@temf.tu-darmstadt.de
[2] Technical University of Darmstadt, High-Voltage Laboratories (HBA), Darmstadt, Germany
myriam.koch@tu-darmstadt.de

An adjoint sensitivity analysis of a nonlinear transient finite-element model allows to determine the sensitivities of the key performance indicators of a cable joint with respect to the parameters of an embedded field-grading material. The example considers a high-voltage DC cable joint submitted to an overvoltage event.

Keywords:
sensitivity analysis,
adjoint method,
finite element method,
electrothermal simulation,
HVDC cable joint

University of Maribor Press

I Introduction

In high-voltage equipment, field grading materials (FGMs) are applied to mitigate spots with high electric field strengths. The field and temperature dependencies of FGMs can be represented by the expression

$$\sigma_{\mathrm{FGM}}(E,\vartheta) = p_1 \frac{1+p_4^{(E-p_2)/p_2}}{1+p_4^{(E-p_3)/p_2}} e^{-p_5\left(\frac{1}{\vartheta}-\frac{1}{\vartheta_0}\right)} , \tag{1}$$

for the FGM's conductivity σ_{FGM}, with E the magnitude of the electric field strength $\boldsymbol{E}(\boldsymbol{r},t)$, $\vartheta(\boldsymbol{r},t)$ the temperature, ϑ_0 a reference temperature and $\{p_1,\dots,p_5\}$ a set of design parameters shaping the material characteristic [1]. Since recently, FGMs can be tailored to the specific design requirements of the HV device [2]. This, however, requires (a) calculating the behaviour of the HV device under transient stresses and (b) calculating the sensitivities of the quantities of interest (QoIs) with respect to a larger number of design parameters characterising the FGM.

II Transient Electrothermal Simulation

The transient excitation and the field and temperature dependence of FGMs necessitates a transient nonlinear multiphysically-coupled finite-element (FE) simulation for determining the nominal electrothermal fields. Adapting the electroquasistatic approximation of the Maxwell equations, the electric field strength is represented by $\boldsymbol{E} = -\nabla\Phi$ with $\Phi(\boldsymbol{r},t)$ the electric scalar potential. The formulation reads

$$-\nabla\cdot(\sigma\nabla\Phi) - \nabla\cdot\frac{\partial}{\partial t}(\varepsilon\nabla\Phi) = 0\,; \tag{2a}$$

$$-\nabla\cdot(\lambda\nabla\vartheta) + \frac{\partial}{\partial t}(c_{\mathrm{V}}\vartheta) = \dot{q}_{\mathrm{Joule}}\,, \tag{2b}$$

with $\varepsilon(\boldsymbol{r},\boldsymbol{E},\vartheta)$ the permittivity, $\lambda(\boldsymbol{r},\vartheta)$ the thermal conductivity, $c_{\mathrm{V}}(\boldsymbol{r},\vartheta)$ the volumetric heat capacity and $\dot{q}_{\mathrm{Joule}} = \sigma E^2$ the Joule loss density. Eq. (2) is discretised in space by lowest-order nodal FE shape functions and in time by the backward Euler method. To cope with the substantially different time scales of both subproblems, a weakly coupled multirate timestepping scheme is employed [3] (Fig. 1).

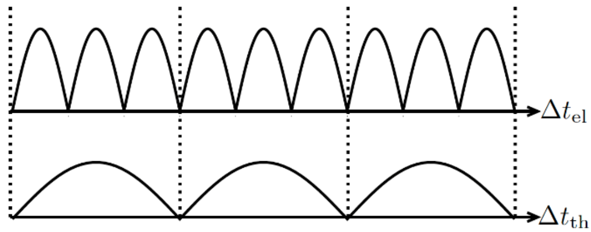

Figure 1: Multirate weakly coupled time-integration scheme: the electroquasistatic subproblem is time-stepped by small time steps Δt_{el}, whereas the thermal subproblem is time-stepped by larger time steps Δt_{th}.

The outcome of the nominal simulation is a set of N_{qoi} QoIs q_i, which are post-processed from (Φ, ϑ) on the computational domain Ω and for the time span $[t_0, t_{\mathrm{f}}]$ by

$$q_i = \int_\Omega \int_{t_0}^{t_{\mathrm{f}}} g_i\,(r, t, \Phi, \vartheta)\mathrm{d}\Omega\mathrm{d}t. \tag{3}$$

Here, the kernels $g_i(r, t, \Phi, \vartheta)$ allow to represent space- or time-integrated QoIs as well as localised or instantaneous QoIs. As examples, the time variation of E at position $\boldsymbol{r}_1$ is extracted by $g_1 = |-\nabla\Phi|\delta(\boldsymbol{r} - \boldsymbol{r}_1)$, whereas the *z*-component of the electric field strength on a line (r_2, φ_2, z), $z \in [z_a, z_b]$ at time instant t_2 is extracted by $g_2 = -\nabla\Phi \cdot \boldsymbol{e}_z\delta(r - r_2)\delta(\varphi - \varphi_2)H(z - z_a)H(z_b - z)\delta(t - t_2)$, with $\delta(s)$ the Dirac-delta function and $H(s)$ the Heaviside step function.

III Adjoint Sensitivity Analysis

In addition to the nominal QoIs q_i, engineers need to know the sensitivities $\frac{\mathrm{d}q_i}{\mathrm{d}p_j}$ of the QoIs with respect to N_{par} design parameters p_j. In a direct sensitivity method, such sensitivities would be post-processed from the derived solutions $\left(\frac{\mathrm{d}\Phi}{\mathrm{d}p_j}, \frac{\mathrm{d}\vartheta}{\mathrm{d}p_j}\right)$, which on their turn are computed from FE solutions of (2) differentiated with respect to each of the design parameters p_j. This becomes prohibitely expensive for large N_{par}, which is the case here, with already 5 parameters for each FGM in addition to the device's geometric parameters.

For a moderate N_{qoi}, the adjoint sensitivity method is preferred [4], [5]. For each kernel g_i, an adjoint solution (η_i, ξ_i) is solved from the adjoint transient linear multiphysically-coupled FE problem

$$-\nabla\cdot(\bar{\bar{\sigma}}_{\mathrm{d}}\nabla\eta_i)+\nabla\cdot\left(\bar{\bar{\varepsilon}}_{\mathrm{d}}\frac{\partial}{\partial t}\nabla\eta_i\right)+\nabla\cdot\left((\bar{\bar{\sigma}}_{\mathrm{d}}\boldsymbol{E}+\boldsymbol{J})\xi_i\right)=\frac{\partial g_i}{\partial\Phi}\ ; \tag{4}$$

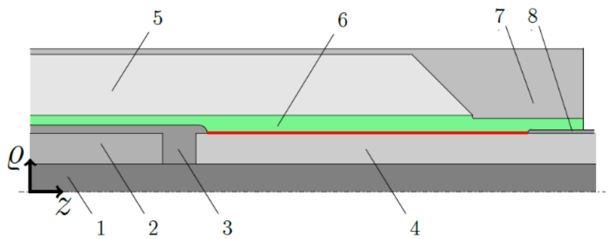

Figure 2: Cross section of a HVDC cable joint with copper conductor (1), aluminum connector (2), conductive silicone rubber (3), cross-linked polyethylene (4), insulating silicone rubber (5), nonlinear field-grading material (6), outer aluminum body (7) and outer cable semiconductor (8).

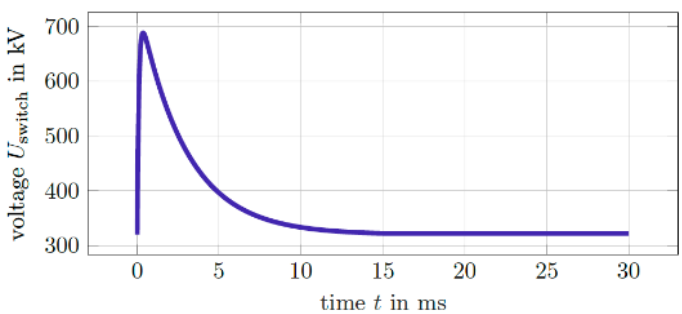

Figure 3: Switching impulse applied to the HVDC cable joint.

$$\begin{aligned}-\nabla\cdot(\lambda\nabla\xi_i)-\left(c_{\mathrm{V}}+\frac{\partial c_{\mathrm{V}}}{\partial\vartheta}\vartheta\right)\frac{\partial\xi_i}{\partial t}+\frac{\partial\lambda}{\partial\vartheta}\nabla\vartheta\cdot\nabla\xi_i\\ -\frac{\partial\sigma}{\partial\vartheta}E^2\xi_i-\frac{\partial\sigma}{\partial\vartheta}\boldsymbol{E}\cdot\nabla\eta_i+\frac{\partial\varepsilon}{\partial\vartheta}\boldsymbol{E}\cdot\frac{\partial}{\partial t}\nabla\eta_i=\frac{\partial g_i}{\partial\vartheta}\,,\end{aligned} \tag{5}$$

where $\bar{\bar{\sigma}}_{\mathrm{d}}$ and $\bar{\bar{\varepsilon}}_{\mathrm{d}}$ the differential conductivity and permittivity [6], evaluated for the nominal solution (Φ_0, ϑ_0) [7]. The adjoint formulation steps backward in time and considers the nonlinear operation points that were already determined by the nominal solver.

IV Example: HVDC Cable Joint

The nominal and adjoint transient electrothermal analysis tools are applied to a HVDC cable joint (Fig. 2) submitted to a transient overvoltage event (Fig. 3). The nominal solution illustrates the field-grading effect (Fig. 4), i.e., the magnitude of the field stays within an acceptable range, despite the heating of the FGM during the overvoltage event. The adjoint solutions allow to determine the sensitivities of the Joule heat $\dot{q}_{\mathrm{Joule}}$ ($g_{\mathrm{Joule}} = \boldsymbol{J} \cdot \boldsymbol{E}$) generated during the overvoltage event with respect to the design parameters of the FGM (Fig. 5, dashed lines). For validation, $\dot{q}_{\mathrm{Joule}}(p_1, p_2)$ has also been calculated by a standard parameter study (Fig. 5, solid lines). The multirate scheme allows to choose a coarse thermal time step (Fig. 6).

V Conclusions

Tuning the properties of a field-grading material, employed within the insulation system of a high-voltage devices, is possible with adjoint sensitivity analysis exerted on the nonlinear transient electrothermal FE model of the device.

Acknowledgement

The authors thank Rashid Hussain for providing the simulation model and material characteristics published in [1]. This work is supported by the DFG project 510839159, the joint DFG/FWF Collaborative Research Centre CREATOR (CRC–TRR361/F90) and the Graduate School Computational Engineering at TU Darmstadt. Yvonne Späck-Leigsnering holds an Athene Young Investigator Fellowship of the TU Darmstadt.

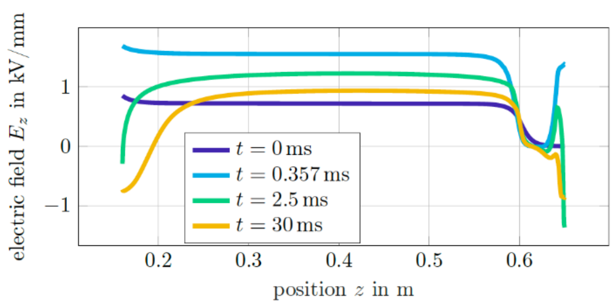

Figure 4: Electric field strength in the FGM, tangentially to the interface between FGM and XLPE (along the red line in Fig. 2).

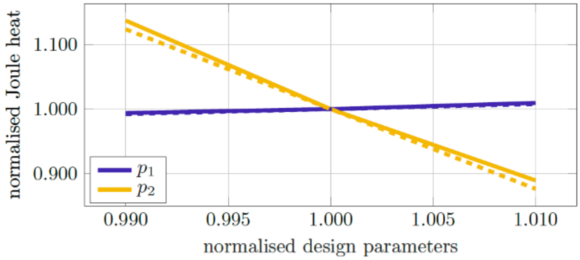

Figure 5: Sensitivities $\frac{\partial \dot{q}_{\mathrm{Joule}}}{\partial p_1}$ and $\frac{\partial \dot{q}_{\mathrm{Joule}}}{\partial p_2}$ calculated by the adjoint sensitivity method, shown as dashed lines at the nominal point $(p_{\mathrm{nom},1}, p_{\mathrm{nom},2})$, which is normalised to (1,1); Dependencies $\dot{q}_{\mathrm{Joule}}(p_1, p_{\mathrm{nom},2})$, and $\dot{q}_{\mathrm{Joule}}(p_{\mathrm{nom},1}, p_2)$ calculated by parameter variations, shown as solid lines, used for validation.

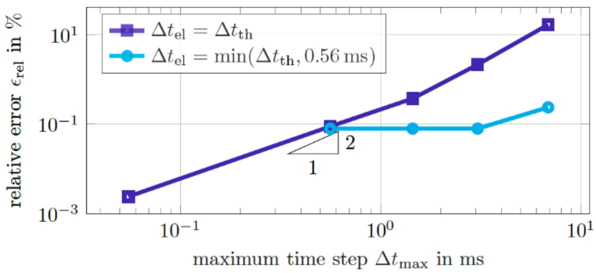

Figure 6: Convergence of the solution with respect to the time-step size: identical time step for both subproblems (dark blue line); time step for the electroquasistatic subproblem limited to 0.56 ms (light blue line).

References

[1] R. Hussain and V. Hinrichsen, "Simulation of thermal behavior of a 320 kV HVDC cable joint with nonlinear resistive field grading under impulse voltage stress," in CIGR´E Winnipeg 2017 Colloquium, 2017.

[2] M. Secklehner, R. Hussain, and V. Hinrichsen, "Tailoring of new field grading materials for HVDC systems," in 13th International Electrical Insulation Conference (INSUCON 2017), 05 2017.

[3] Y. Späck-Leigsnering, E. Gjonaj, H. De Gersem, T. Weiland, M. Gießel, and V. Hinrichsen, "Electroquasistatic-thermal modeling and simulation of station class surge arresters," IEEE Trans. Magn., vol. 52, no. 3, p. 9100104, 03 2016.

[4] S. Li and L. R. Petzold, "Adjoint sensitivity analysis for time-dependent partial differential equations with adaptive mesh refinement," J. Comput. Phys., vol. 198, pp. 310–325, 2004.

[5] J. Sarpe, A. Klaedtke, and H. De Gersem, "A parallel-in-time adjoint sensitivity analysis for a B6 bridge-motor suppy circuit," IEEE Trans. Magn., vol. 0, no. 0, pp. 0–0, 11 2023.

[6] H. De Gersem, I. Munteanu, and T. Weiland, "Construction of differential material matrices for the orthogonal finite-integration technique with nonlinear materials," IEEE Trans. Magn., vol. 44, no. 6, pp. 710–713, 06 2008.

[7] M. G. Ruppert, Y. Späck-Leigsnering, J. Buschbaum, and H. De Gersem, "Adjoint variable method for transient nonlinear electroquasistatic problems," Electr. Eng., vol. 105, no. 4, pp. 2319–2325, 08 2023.

Design and Analysis of the Low Cost Induction Gear for Vertical Axis Wind Turbines

DOI
https://doi.org/10.18690/um.feri.4.2025.4

ISBN
978-961-286-986-1

Michał Mysiński,[1] Cezary Jędryczka,[1]
Łukasz Macyszyn[2]

[1] Poznan University of Technology, Institute of Industrial Electrical Engineering, Poznan, Poland
michal.mysinski@put.poznan.pl, cezary.jedryczka@put.poznan.pl
[2] Poznan University of Technology, Faculty of Mechanical Engineering, Poznan, Poland
lukasz.macyszyn@put.poznan.pl

This paper investigates the concept of induction gear based on eddy current phenomena. In the research, impact of the selected dimensions of the magnetic circuit on the electromagnetic torque and gear estimated efficiency has been examined. Numerical models that employ the finite element method have been developed to determine the electromagnetic performance of variants studied. On this basis, the best design solutions were identified for future studies.

Keywords:
induction gear,
eddy currents,
electromagnetic torque,
finite element method (FEM),
vertical axis wind turbines

University of Maribor Press

I Introduction

Due to lack of mechanical contact leading to practically lack of wear, the magnetic gears have gained increased attention over the world in the past years [1, 2]. Magnetic gears can change speed and transmit torque without any mechanical contact. Therefore, they provide low vibration, low noise, and do not require maintenance. Despite the advantages discussed as a result of the use of permanent magnets and the high mechanical complexity, the magnetic gears are relatively expensive [3]. In this paper, we propose and study the concept of a low-cost and mechanically simple induction gearbox dedicated to work as a multiplier gear for small wind turbines with a vertical axis of rotation (VAWT [4]). The gear ratio (k_m) in the presented concept results from the mechanical difference between the diameter of the drive rotor (with permanent magnets) and the eddy current ring. The models in study assume an analysis of the variation of the eddy current ring width and also a variation of the ring material ratio in Al-Fe and Cu-Fe combinations. In addition, systems with the number of pole pairs p equal to 1 and 2 were considered.

II Concept of Induction Gear

As is well known from Maxwell's fundamental equations according to Faraday's Law, an alternating magnetic field B induces an electric field E in a conductor causing currents I to flow. These currents are known as eddy currents. The current thus induced produces a magnetic field B' counteracting the external field B. This phenomenon is widely used in various fields of engineering, among others, for induction heating or induction braking. Figure 1 shows the operational principle of the prototype.

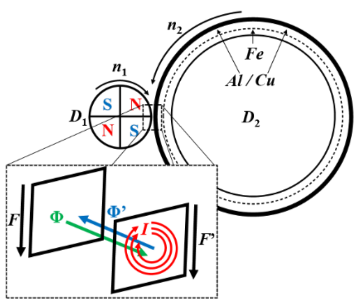

Figure 1: Operational principle of the induction gear

As illustrated in Figure 1 when the rotor D_1 rotates at speed *n1,* it produces from the perspective of a conducting ring an alternating magnetic field Φ excited by the arrangement of neodymium magnets of *p* pairs of poles. Under the influence of the field Φ, eddy currents *I* are induced in the ring made of aluminium and copper/iron, which in turn produce a magnetic flux Φ coupling the two rotating systems (rotor and ring) together. This causes the ring D_2 to rotate at constant load with a speed n_2. The mechanical ratio of diameters can be determined for the system:

$$k_m = \frac{D_2}{D_1} \tag{1}$$

where: D_1 - diameter of the rotor, D_2 - diameter of the ring.

Assuming a rigid transmission as in the mechanical gear, the gear ratio would be equal to k_m. Of course it should be highlight here that due to asynchronous operation resulted from the fundamentals of electrodynamic forces caused by eddy currents the real gear ratio k_{mr} will depend on the load torque of the gear. Another important aspect regarding the proposed concept is that the driving torque can be applied to the ring and, in effect, the rotor with magnets will be driven.

III Numerical Models

To study the performance of the proposed induction gear concept, numerical models exploiting the finite element method (FEM) have been developed in the commercially available Ansys Maxwell FEM package. The six variants of the gear have been studied: a) with the aluminium ring (*Al*), b) with the steel ring covered by the aluminium layer (Al-Fe), and c) with the steel ring covered by the copper layer (*Cu-Fe*). For all three models the rotors of *p*=1 and *p*=2 have been studied, giving in total six variants of the design. All models have been developed incorporating parameterization of the selected design variables, among others, the rotor and ring diameter ratio k_m, the speed ratio ($k_e = n_1 / n_2$) as well as the ring materials described by the parameters w_{Al} and w_{Cu}. In the analysis the planar symmetry of the magnetic field has been assumed and thus the field problem hasbeen reduced to 2D. The diameter D_2 and ring thickness *g* were also parameterized. Figure 2 illustrates the selected parameters incorporated into the models.

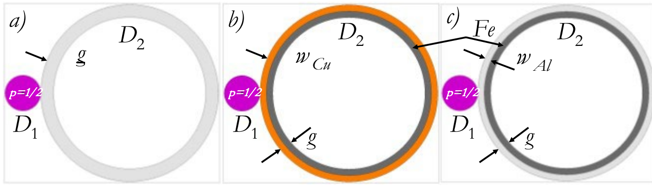

Figure 2: Induction gear models: a) thickness of the ring *g*, b) filling of *Cu-Fe* ring w_{Cu}, c) filling of *Al-Fe* ring w_{Al}

IV Results

Analyses of the performance of the proposed gear have been carried out for the following parameters: Variant a) the (*Al*) ring thickness w_{Al} in the range of 10 to 100 mm and diameter ratio *km* = 5 to 15; Variants b) and c) (*Al-Fe*) and (*Cu-Fe*) the thickness of the aluminium and copper layer w_{Cu} and w_{Al}in the range of 2 to 48 mm (keeping the total thickness of the ring *g* = 50 mm). The diameter D_2 was equal to 350 mm and the k_e was in the range of 5 to 15.

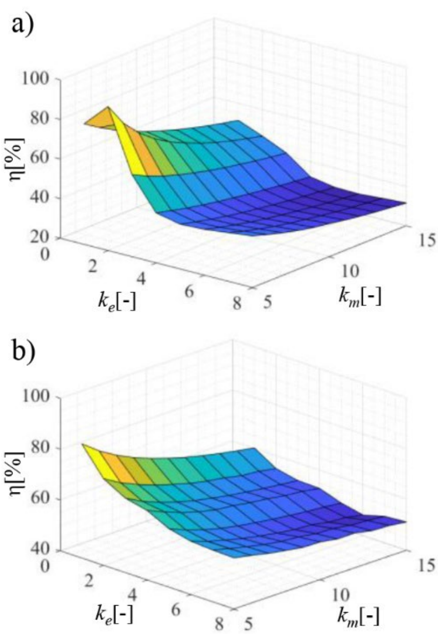

Figure 3: Efficiency of the gearbox as a function of the k_m ratio and the relative speed k_e: a) p=1, b) p=2

In a first step, the efficiency of the gear with aluminium ring has been evaluated in different gear and speed ratios. Efficiency has been evaluated as the ratio of torques (which act on the ring and rotor, respectively) related to the mechanical ratio k_m of the PM rotor and the diameters of the rings. Figure 3 shows the evaluated efficiency of the gearbox as a function of the ratio k_m and the relative speed k_e.

Of course, the efficiency of the system increases with higher the speeds and the lower gear ratios. For further studies, the parameters k_m and k_e have been assumed to be 10 and 1, respectively.

In the next step, the impact of the filling ratios of copper and aluminium for the steel ring has been investigated. The *Al-Fe* and *Cu-Fe* models shown in Figures 2(b) and 2(c) have been examined. Figure 4 shows the efficiencies as a function of the change in ring fill for p=1 and p=2, respectively.

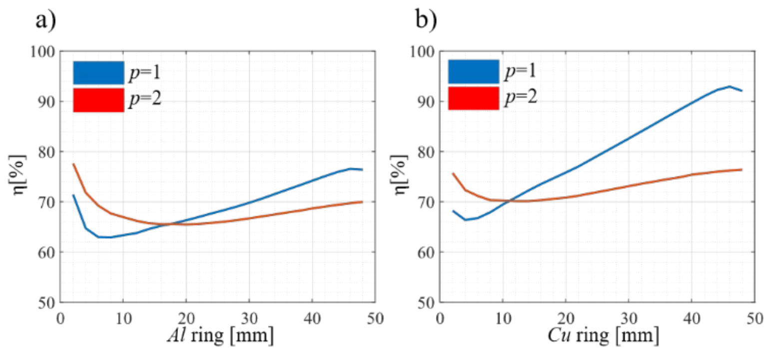

Figure 4: Efficiency of the gearbox as a function of: a) thickness of *Al* ring, b) thickness of *Cu* ring

As a result of its higher conductivity of copper, the *Cu-Fe* design shows higher efficiency values compared to design with aluminium layer over the steel ring. Furthermore, above thickens of 20 mm of conductive material, the gear with single pair of poles in PM rotor performs better than design of 2 pairs of poles. This is due to the grater area of influence of the magnetic flux on the rim for single pair of poles PM rotor.

In the next step, the torques acting on the rotor and on the gear rim were examined. The results of the calculations are summarised in Figure 5, taking into account the number of rotor poles and the material of the ring.

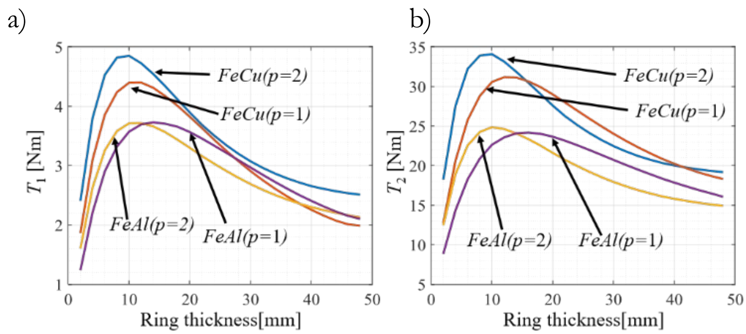

Figure 5: The torque obtained for a) rotor and b) ring

V Conclusions

In the paper the concept of a low-cost induction gear dedicated to work as a multiplier gear for small wind turbines with a vertical axis of rotation has been proposed. The numerical analysis exploiting 2D FEM have been carried out to examine proposed gear performance. The results of the analyses show that the proposed gear can successfully support the operation of the VAWT.

The efficiency, ratio, and price of the gear can be listed as most crucial parameters taken into account during the selection process. It has been demonstrated that incorporating layer of the copper on the steel ring, due to its higher than aluminium conductivity, allows one to achieve higher efficiency of the gear for the same ratio. However, the price and weight of the gear will also increase. Aluminium, on the other hand, is a cheaper and lighter solution despite its lower conductivity.

Further work on the concept of the induction gear for VAWT is related to integrating the PM rotor of the gear as a

rotary part of the electric energy generator. The detailed results of the conducted research will be discussed during the conference and included in the extended version of the paper.

References

[1] Rasmussen P. O., Andersen T. O., Jorgensen F. T. and Nielsen O., "Development of a high-performance magnetic gear," in IEEE Transactions on Industry Applications, vol. 41, no. 3, pp. 764-770, May-June 2005, DOI: 10.1109/TIA.2005.847319.

[2] Kowol M., Kołodziej J., Jagieła M. and Łukaniszyn M., "Impact of Modulator Designs and Materials on Efficiency and Losses in Radial Passive Magnetic Gear," in IEEE Transactions on Energy Conversion, vol. 34, no. 1, pp. 147-154, March 2019, DOI: 10.1109/TEC.2018.2862462.

[3] Macyszyn, L.; Jedryczka, C.; Mysinski, M. Analysis of a Two-Stage Magnetic Precession Gear Dynamics. Energies 2023, 16, 4484. https://doi.org/10.3390/en16114484

[4] Shahariar G. M. H., and Hasan M. R., "Design & construction of a Vertical Axis Wind Turbine," 2014 9th International Forum on Strategic Technology (IFOST), Cox's Bazar, Bangladesh, 2014, pp. 326-329, DOI: 10.1109/IFOST.2014.6991132.

BIAS-CORRECTED EDDY-CURRENT SIMULATION USING A RECURRENT-NEURAL-NET / FINITE-ELEMENT HYBRID MODEL

DOI
https://doi.org/
10.18690/um.feri.4.2025.5

ISBN
978-961-286-986-1

MORITZ VON TRESCKOW, HERBERT DE GERSEM,
DIMITRIOS LOUKREZIS

Technical University of Darmstadt, Institute for Accelerator Science and Electromagnetic Fields (TEMF), Darmstadt, Germany
moritz.von_tresckow@tu-darmstadt.de, degersem@temf.tu-darmstadt.de,
loukrezis@temf.tu-darmstadt.de

This work combines recurrent neural networks (RNNs) with the finite element (FE) method into a hybrid model to correct time-dependent discrepancies in low-fidelity engineering simulations. The hybrid model is trained on sparse data from high- and low-fidelity simulations, employing techniques to prevent overfitting and balance accuracy with neural network generalization. It is successfully applied to an eddy-current simulation of a quadrupole magnet, demonstrating its accuracy in adjusting low-fidelity models. The results confirm the potential of this hybrid modeling approach for model-based predictions in dynamic multi-fidelity modeling contexts.

Keywords:
multi-fidelity modeling,
bias correction,
recurrent neural netwokrs,
finite element method,
magnet

University of Maribor Press

I Introduction

In the context of multi-fidelity modeling, low-fidelity models inevitably exhibit discrepancies with respect to high-fidelity models, due to systematic errors that arise from modeling assumptions, low mesh resolution, or imperfect physical knowledge. Quantifying these discrepancies is important to assess whether a low-fidelity model is sufficiently accurate, especially, when simulating dynamical systems.

The relationship between a high- and low-fidelity system state at time $t \in [0, T]$, $\boldsymbol{a}_t^{\text{hifi}}$ and $\boldsymbol{a}_t^{\text{lofi}}$, respectively, is given as

$$\boldsymbol{a}_t^{\text{hifi}} = \boldsymbol{a}_t^{\text{lofi}} + \delta_t, \tag{1}$$

where $\delta_t : \mathbb{R}^d \to \mathbb{R}^d$ is a discrepancy function capturing systematic errors [1]. In practical scenarios however, the trajectory data $\boldsymbol{A}_{\text{hifi}} := \{\boldsymbol{a}_{t_k}^{\text{hifi}}\}_{t_k \in T_{\text{hifi}}}$ is only known at specific, finite, time instances $T_{\text{hifi}} := \{t_0, \dots, t_{N_T}\}$, where $N_T \in \mathbb{N}$ denotes the number of time instances. Thus, to account for missing time steps, a parametric model, δ_θ, is necessary to approximate the discrepancy function for systemic error approximation [2].

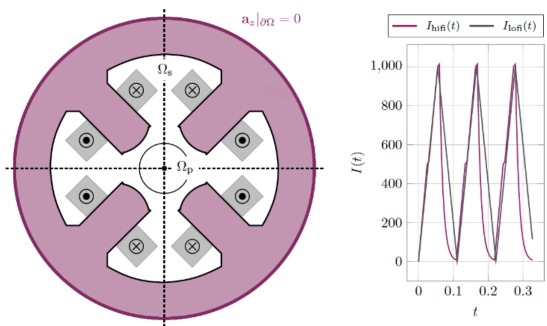

Fig. 1. Left: Schematic of the quadrupole magnet, where $\boldsymbol{\Omega}_{\text{Fe}}$ denotes the domain of the iron yoke, $\boldsymbol{\Omega}_{\text{s}}$ the domain of current excitation and $\boldsymbol{\Omega}_{\text{p}}$ the aperture domain. Right: Current excitation $\mathbf{I}_{\text{hifi}}$ for the high-fidelity model and $\mathbf{I}_{\text{lofi}}$ for the low-fidelity model.

In this work, we propose a framework based on recurrent neural networks (RNNs) and finite element (FE) basis functions, to approximate the model discrepancy $\delta_{\theta*} \approx \delta_t$ in a multi-fidelity, transient, eddy-current simulation of a quadrupole magnet [3].

We employ an upsampling scheme to account for the sparsity of $\boldsymbol{A}_{\mathrm{hifi}}$ and train the model using an upsampled data set. Finally, we use the trained model to derive a correction operator (bias correction), $\boldsymbol{a}^{\mathrm{corr}}$, and improve the performance of the low-fidelity model i.e.

$$\boldsymbol{a}^{\mathrm{corr}} = \boldsymbol{a}_t^{\mathrm{lofi}} + \delta_{\theta^*}, \tag{2}$$

where θ^* is the RNN's trained parameter set.

II FE Model

Choosing the vector potential ansatz $\boldsymbol{b} = \nabla \times \boldsymbol{a}$, with $\boldsymbol{a}$ the magnetic vector potential and $\boldsymbol{b}$ the magnetic flux density, the eddy-current problem can be given as the time-dependent boundary value problem (BVP)

$$\nabla \times (\nu \nabla \times \boldsymbol{a}) + \sigma \frac{\partial \boldsymbol{a}}{\partial t} = \boldsymbol{j}_{\mathrm{s}}\,, \tag{3a}$$
$$\boldsymbol{a}|_{\partial\Omega} = 0\,, \tag{3b}$$

where ν is the reluctivity, σ the conductivity and $\boldsymbol{j}_{\mathrm{s}}$ the source current density.

The geometry of the quadrupole (Fig. 1) is defined on a circular domain Ω, consisting of an iron yoke Ω_{Fe}, coils Ω_{s}, and an aperture Ω_{p}. The domain boundary $\partial\Omega$ consists of the outer boundary of the iron domain $\partial\Omega_{\mathrm{Fe}}$. Due to geometrical considerations, it is sufficient to consider the axial component of the magnetic vector potential, i.e. $\boldsymbol{w}_i = w_i \boldsymbol{e}_z$, with $w_i \in H_0(grad;\Omega)$. The magnetic vector potential is approximated via the ansatz function $\boldsymbol{a} = \sum_{j=1}^{N_{\mathrm{dof}}^{\mathrm{lofi}}} \hat{a}_j \boldsymbol{w}_j$, where the degrees of freedom (dof) $\{\hat{a}_j\}_{j \le N_{\mathrm{dof}}^{\mathrm{lofi}}}$ lie on the mesh nodes. In matrix-vector notation, the FE formulation reads

$$(\Delta t\, \boldsymbol{A} + \boldsymbol{M})\hat{\boldsymbol{a}}_{t_{k+1}} = \Delta t\, \boldsymbol{b}(t_{k+1}) + \boldsymbol{M}\hat{\boldsymbol{a}}_{t_k}, \tag{4}$$

where $\boldsymbol{A}$ *and* $\boldsymbol{M}$ are the stiffness and mass matrix, respectively, and $\boldsymbol{b}$ is the load vector. For the simulation, we apply the conductivity $\sigma_{Fe} = 1.04 \cdot 10^7\ S/m$ and the reluctivity $\nu_{Fe} = 2 \cdot 10^{-3}\, \nu_0$ in the iron yoke Ω_{Fe}, as well as the conductivity $\sigma = 1\ \mathrm{S/m}$ and the reluctivity $\nu_{\mathrm{Fe}} = \nu_0$ in the aperture Ω_{p} and the current-excitation domain Ω_{s}.

Furthermore, we select a constant time step of $\Delta t = 1 \cdot 10^{-2}$ s and apply $N_T = 327$ time steps. The low-fidelity model $\hat{\boldsymbol{a}}^{\mathrm{lofi}}_{t_{k+1}}$ is parametrized with the current I_{lofi} and mesh resolution $N^{\mathrm{lofi}}_{\mathrm{dof}} = 895$, while the high-fidelity model $\hat{\boldsymbol{a}}^{\mathrm{hifi}}_{t_{k+1}}$ with current I_{hifi} and $N^{\mathrm{lofi}}_{\mathrm{dof}} = 277\,594$.

III Hybrid Model Architecture

To approximate the discrepancy function on a low-fidelity mesh, we assume the functional form

$$\delta_{t_k}(\boldsymbol{r}) = \sum_{i=1}^{N^{\mathrm{lofi}}_{\mathrm{dof}}} \hat{\delta}_{i,t_k} \phi_i(\boldsymbol{r}), \tag{5}$$

where $\hat{\delta}_{i,t_k}$ is the coefficient corresponding to the i-th dof in the low-fidelity mesh and $\phi_i(\boldsymbol{r})$ the associated shape function. We employ an RNN to learn the coefficients of (5) using discrepancy data calculated by

$$D_{\mathrm{d}} := \left\{T\left(\boldsymbol{a}^{\mathrm{hifi}}_{t_k}\right) - \boldsymbol{a}^{\mathrm{lofi}}_{t_k}\right\}_{t_k \in T_{\mathrm{hifi}}}, \tag{6}$$

where T is a linear projection operator, $t_k \in T_{\mathrm{hifi}}$ and the FE shape functions resolve the approximation spatially.

By separating the time-dependent aspects from the spatial elements of the discrepancy function, the RNN focuses solely on temporal coefficient variations, while the FE method handles the spatial discretization of the model domain. This separation allows each method to operate within its area of strength, improving the efficiency of the training process.

IV Localized Data Upsampling

To account for sparsity in the training data, we employ upsampling using localized linear interpolation, i.e.,

$$\bar{\delta}_{j_{t+l}} = \delta_{j_k} + l\left(\frac{\delta_{j_{k+1}} - \delta_{j_k}}{j_{k+1} - j_k}\right), \tag{7}$$

for $l = 1, \ldots, j_{k+1} - j_k - 1$, where j_k denotes the time steps for which the high-fidelity data is known. The intermediate artificial system states are coupled with a Gaussian prior to mitigate overfitting in the neural network. This approach, favored for its simplicity and versatility, not only guides NN behavior in sparse data conditions but also uses the Gaussian prior's variance to produce new, artificially bounded states during each training epoch, thus enhancing the model's numerical stability.

V Results

The low-fidelity model uses a much coarse mesh than the high-fidelity model and considers a simplified triangular function for current excitation instead of the true decaying exponential one. The potential distributions obtained with the low-fidelity and bias-corrected models are depicted in Fig. 2a. The integrated discrepancy function over time is shown in Fig. 2b. Relative to the high-fidelity model, the error of the low-fidelity model is $\Delta_{L^2}\boldsymbol{a}^{\mathrm{lofi}} = 39.847\%$, whilst the relative error of the bias-corrected model is $\Delta_{L^2}\boldsymbol{a}^{\mathrm{corr}} = 0.613\%$, which constitutes a major improvement to the low-fidelity model.

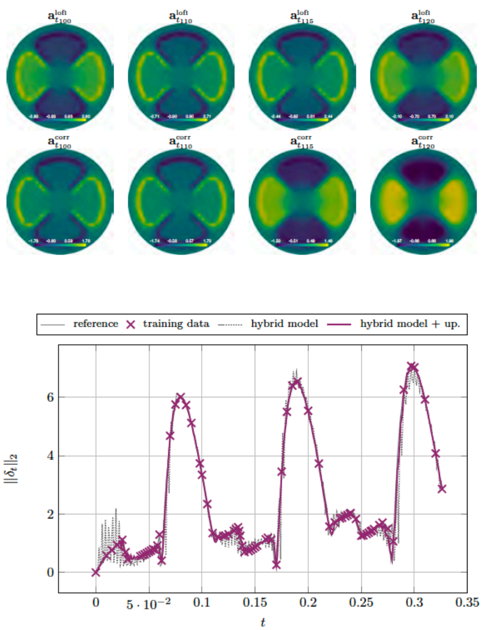

Figure 2: Top: Potential distribution of the low-fidelity and bias-corrected model. Bottom: Integrated discrepancy function over time.

VI Conclusion & Outlook

The hybrid modeling approach yields highly accurate bias-corrected dynamic FE simulations, maintaining error rates below 2% even with irregular behavior and limited data. Future enhancements could come from advanced RNNs, localized Gaussian processes, and tailored, problem-specific loss functions.

Acknowledgment

Moritz von Tresckow acknowledges the support of the German Federal Ministry for Education and Research (BMBF) via the research contract 05K19RDB. Dimitrios Loukrezis and Herbert De Gersem acknowledge the support of the Deutsche Forschungsgemeinschaft (DFG, German Research Foundation), Project-ID 492661287 – TRR 361. The authors acknowledge the financial support of Deutsches Elektronen-Synchrotron DESY.

References

[1] P. D. Arendt, D. W. Apley, and W. Chen, “Quantification of Model Uncertainty: Calibration, Model Discrepancy, and Identifiability,” Journal of Mechanical Design, vol. 134, no. 10, 09 2012, 100908. [Online]. Available: https://doi.org/10.1115/1.4007390.

[2] M. Levine and A. Stuart, “A framework for machine learning of model error in dynamical systems,” Communications of the American Mathematical Society, vol. 2, no. 07, pp. 283–344, 2022.

[3] M. von Tresckow, H. De Gersem, and D. Loukrezis, “Error approximation and bias correction in dynamic problems using a recurrent neural network/finite element hybrid model,” Applied Mathematical Modelling, 2024.

DOI
https://doi.org/10.18690/um.feri.4.2025.6

ISBN
978-961-286-986-1

MODEL-FREE CONTROL OF A DC-DC BOOST CONVERTER BASED ON THE INDUCTOR CURRENT AVERAGING

ANGEL MAUREIRA,[1] SEBASTIÁN RIFFO,[1]
CATALINA GONZÁLEZ- CASTAÑO,[2]
MARCO RIVERA,[1, 3] CARLOS RESTREPO[1]

[1] Universidad de Talca, Faculty of Engineering, Curico, Chile
amaureira15@alumnos.utalca.cl, sebastian.riffo@utalca.cl, marcoriv@utalca.cl, crestrepo@utalca.cl
[2] Universidad Andres Bello, Facultad de Ingeniería, Centro de Transformacion Energética, Santiago, Chile
catalina.gonzalez@unab.cl
[3] University of Nottingham, Faculty of Engineering, Power Electronics and Machine Centre, Nottingham, United Kingdom of Great Britain and Northern Ireland
Marco.Rivera@nottingham.ac.uk

In this work, a new model-free predictive control (MF-PC) technique is presented for controlling dc-dc converters based on calculating the slope of each switching instant. This technique has the simplicity required for converters operating at high frequencies. The simulation results show that the proposed method is robust against parameters and model changes compared to classical predictive controls.

Keywords:
power electronics,
predictive control,
digital control,
boost converter,
current control

University of Maribor Press

I Introduction

Model-free predictive control (MF-PC) theory has emerged as an alternative to conventional MPC (model predictive control) to address problems that can arise from poor model estimation or the loss of model accuracy, mainly caused by variations in the system's environmental conditions or operating point [1, 2, 3]. Besides the fact that it is not possible to know with certainty the model of the system to be controlled, either due to its high mathematical complexity or because, on some occasions, it has yet to be known a priori what will be connected to the system [1]. In any case, the MPC control will degrade, which will cause sub-optimal operation.

Although model predictive control (MPC) is widely used in power electronics, most of the applications reported in the literature have been focused on ac-dc and dc-ac converters [4, 5]. This is also the case with MF-PC applications, with a low number of works focused on dc-dc applications. However, the increase in the implementation of microgeneration systems, supported by the growth of dc-based renewable energies, such as PV systems and other dc-powered loads, promotes dc-based energy distribution on a residential scale. Being also supported by several studies that highlight the potential of dc microgrids and their involved dc-dc converters minimizing energy losses during its distribution [6, 7, 8]. Therefore, it is expected that having more efficient dc-dc converters, with lower costs, higher reliability, and low ripple in the output current, could drive the increased deployment of residential dc microgrids.

Additionally, dc-dc power converters have an important role in various energy applications, such as aircraft, electric vehicles, ship, dc homes, data center and microgrids [9]. This evidences the need to evaluate and study new approaches to the elements involved in this type of converter, as is the case of promising control strategies such as MF-PC.

Considering the above-mentioned, this paper proposes an MF-PC of the dc-dc boost converter shown in Fig. 1 to estimate the inductor's positive and negative current slopes with high accuracy and low computational cost.

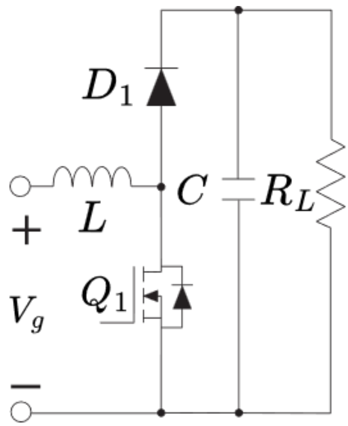

Figure 1: Boost converter.

II Control Description

The inductor current in classical second-order DC-DC power converters have a triangular waveform due to the semiconductors switching. Depending on the switching state, the slope of this current will be positive or negative. If the switching state is 1, meaning the switch is closed, the slope will always be positive, and vice versa. These two slopes can be calculated as follows in a discrete system with the proposed control topology:

$$m_k^1 = \begin{cases} 1000, & if\ k = 0 \\ m_{k-1}^1, & if\ Q_1 = 0\ or\ \frac{i_{Lk} - i_{Lk-1}}{Ts} <= 0 \\ \frac{i_{Lk} - i_{Lk-1}}{Ts}, & if\ Q_1 = 1\ and\ \frac{i_{Lk} - i_{Lk-1}}{Ts} > 0 \end{cases} \tag{1}$$

$$m_k^2 = \begin{cases} -1000, & if\ k = 0 \\ m_{k-1}^2, & if\ Q_1 = 0\ or\ \frac{i_{Lk} - i_{Lk-1}}{Ts} >= 0 \\ \frac{i_{Lk} - i_{Lk-1}}{Ts}, & if\ Q_1 = 1\ and\ \frac{i_{Lk} - i_{Lk-1}}{Ts} < 0 \end{cases} \tag{2}$$

whereas (1) is the positive slope calculation when the switching state is 1 and (2) is the negative slope calculation when the switching state is 0.

With this slope's values, we can estimate the inductor current for both switching states as follows:

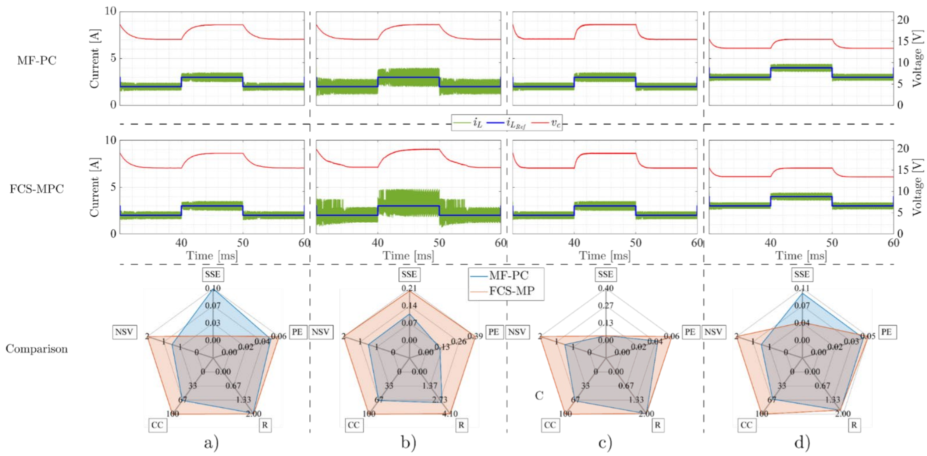

Figure 2: Simulation results for the boost converter: a) Converter operating at its nominal values ($v_i = 12\ V$, $R_L = 10\ \Omega$, $L = 94\ \mu H$ and $C = 250\ \mu F$) while the current reference changes between 2 A and 3 A, b) converter operating with a inductor of $L = 47\ \mu H$ (theoretical nominal value of $L = 94\ \mu H$), c) converter operating with a capacitor of $C = 100\ \mu F$ (theoretical nominal value of $C = 250\ \mu F$), d) converter operating with a resistor of $R_L = 5\ \Omega$ (theoretical nominal value of $R_L = 10\ \Omega$) while the current reference changes between 3 A and 4 A.

$$i_{L_{k+1}} = \begin{cases} i_{L_k} + m_K^1 T_s, & \text{if } Q_1 = 1 \\ i_{L_k} + m_K^2 T_s, & \text{if } Q_1 = 0 \end{cases} \tag{3}$$

where Ts is the sample time of the measured current. With this prediction, we can use an appropriate cost function and then choose the state that minimizes it the most. In this case, the cost function must be calculated for both current predictions, one with the positive slope and the other with the negative slope. We can also calculate the average of the slopes, which helps us to reduce prediction error in systems with more noise. The calculation can be seen in (4).

$$m_{mean}^1 = \sum_{n=1}^{N} m_n^1 \tag{4}$$

III Simulation results

Simulation results are summarized in Fig. 2. The proposed controller is compared with the classical FCS-MPC (finite control set-model predictive control) by means of a spider chart focusing on the following performance measures: steady-state error (SSE), prediction error (PE), ripple (R), computational cost (CC) in percentage (where the FCS-MPC is 100%), and number of sensed variables (NSV). In all the tests, the parameters R_L, L, and C are physically changed on the power converter, while the nominal values in the controller's code are maintained.

IV Conclusions

A model-free predictive control approach based on the inductor current averaging for the dc-dc boost converter has been presented. A comparison with the FCS-MPC approach was performed, evaluating the steady-state error, prediction error, current ripple, computational cost, and the number of sensed variables required by each control technique. The proposed MF-PC controller exhibits a superior dynamic characteristics to the FCS-MPC in all the cases.

References

[1] M. a. V.-Z. S. a. R. J. a. H. R. Khalilzadeh, "Model-free predictive control of motor drives and power converters: A review," Ieee Access, 2021.

[2] A. Stenman, "Model-free predictive control," in Proceedings of the 38th IEEE Conference on Decision and Control (Cat. No.99CH36304), vol. Proceedings of the 38th IEEE Conference on Decision and Control (Cat. No.99CH36304), 1999, pp. 3712-3717 vol.4.

[3] M. a. S. W. a. H. A. Nauman, "Model-Free Predictive Control and Its Applications," Energies, vol. 15, no. 14, p. 5131, 2022.

[4] I. a. M. C. A. J. Jlassi, "Open-circuit fault-tolerant operation of permanent magnet synchronous generator drives for wind turbine systems using a computationally efficient model predictive current control," IET Electric Power Applications, vol. 15, no. 7, pp. 837-846, 2021.

[5] B. a. A. V. G. a. J. M. Hredzak, "A Model Predictive Control System for a Hybrid Battery-Ultracapacitor Power Source," IEEE Transactions on Power Electronics, vol. 29, no. 3, pp. 1469-1479, 2014.

[6] H. a. N. M. a. I. T. Kakigano, "Loss evaluation of DC distribution for residential houses compared with AC system," in The 2010 International Power Electronics Conference - ECCE ASIA, 2010.

[7] H. E. a. D. F. a. N. M. a. K. S. a. G. J. M. Gelani, "AC vs. DC Distribution Efficiency: Are We on the Right Path?," Energies, vol. 14, no. 13, 2021.

[8] H. E. a. D. F. a. S. K. a. N. M. a. N. K. A. K. a. Y. Y. Gelani, "Efficiency Comparison of AC and DC Distribution Networks for Modern Residential Localities," Applied Sciences, vol. 9, no. 582, 2019.

[9] B. S. a. P. M. Revathi, "Solar PV Fed DC Microgrid: Applications, Converter Selection, Design and Testing," IEEE Access, vol. 10, pp. 87227-87240, 2022.

ADRC LOAD SIDE SPEED CONTROLLER PARAMETERS ADJUSTMENT BASED ON A NEURAL MODEL APPLIED FOR A NONLINEAR TWO-MASS DRIVE SYSTEM

DOI
https://doi.org/
10.18690/um.feri.4.2025.7

ISBN
978-961-286-986-1

GRZEGORZ KACZMARCZYK,[1] RADOSLAW STANISLAWSKI,[1]
MARCIN KAMINSKI,[1] LUKASZ KNYPINSKI,[2]
DANTON DIEGO FERREIRA[3]

[1] University of Science and Technology, Faculty of Electrical Engineering, Department of Electrical Machines, Drives and Measurements, Wroclaw, Poland
grzegorz.kaczmarczyk@pwr.edu.pl, radoslaw.stanislawski@pwr.edu.pl, marcin.kaminski@pwr.edu.pl
[2] Poznan University of Technology, Institute of Electrical Engineering and Electronics, Poznan, Poland
lukasz.knypinski@put.poznan.pl
[3] Federal University of Lavras (UFLA), Department of Automatics, Lavras, Brazil
danton@ufla.br

The paper is focused on improvements to the conventional speed controller based on Active Disturbance Rejection Control (ADRC) applied for a two-mass electric drive system. The described ADRC structure is based on load-side speed measurement. The paper compares the base structure dynamics with the overall system behavior when plant parameters are changed. The proposed ADRC algorithm extension performs soft controller parameters adjustment to improve the dynamics and plant response. The presented approach accomplishes adaptation capabilities with the use of a Radial Function Neural Network (RBFNN). The article compares the dynamic response of the plant controlled by the conventional ADRC algorithm and the designed neural adaptation extension through the conducted experimental tests.

Keywords:
active disturbance rejection control,
nonlinear drive system,
radial basis eunction neural network,
speed controller,
two-mass drive system

University of Maribor Press

I Introduction

Modern electric drive systems are demanded to provide an excellent dynamic response of the plant combined with robustness to some phenomena which can occur unexpectedly. A control system can be considered robust if a change in plant parameters does not alter its response (completely or within the accepted range). However, in case of complex mechanical constructions, change of inertia may cause non-negligible difference in plant behavior. Even though the response may be generally eligible, inconsistencies, oscillations, and ruggedness should still be mitigated. Finally, the mentioned inconveniences may affect the controlled object with failures or, in extreme conditions, sudden stability loss. Thus, it is crucial to mitigate speed lurches in sensitive plants. The proposed approach presents an online controller parameters adjustment algorithm accomplished by the RBFNN inclusion.

II Plant Model

The object analyzed in the article consists of two electric machines and a long, elastic shaft (connecting the motor with the load). Comprehensive analysis of the considered drive is presented in [1]. The mechanical part can be described as follows:

$$\begin{cases} J_1\dot{\omega}_1 = T_e - \big(T_T + D(\omega_1 - \omega_2)\big) - T_{f1} \\ J_2\dot{\omega}_2 = \big(T_T + D(\omega_1 - \omega_2)\big) - T_L - T_{f2} \end{cases} \tag{1-2}$$

and:

$$\dot{T}_T = K_c(\omega_1 - \omega_2), \tag{3}$$

where: T_e is the electromagnetic torque, T_T is the torsional torque, T_L is the load torque, K_c is the stiffness coefficient, D is the damping coefficient, T_{f1} and T_{f2} are the friction torques.

III Control System

One of the most common control method is known as Active Disturbance Rejection Control. It focuses on simplifying the plant model and implementing it in the form of a multi-integrator block. It minimizes the influence of external disturbances by storing an additional state variable and providing it to the control system. ADRC has been described in detail in [2]. Due to the fact, that ADRC approach is strongly dependent on the plant parameters, a risk of sudden, significant plant change is a huge concern. The algorithm proposed in the paper is based on the idea of load side speed measurement only. That being said, referring to the plant model, the demanded motor speed change is achieved by calculating the third derivative of load machine speed which, after transformation, can be described with the following equation:

$$\dddot{\omega}_2 = \frac{D}{J_2}\ddot{\omega}_2 - \frac{K_c}{J_2}\dot{\omega}_2 + bu + A, \tag{4}$$

where: u is the control signal (electromagnetic torque), $b = \frac{K_c}{J_1 J_2}$, A is the additional disturbance. The described ADRC load side speed controller algorithm, applied for nonlinear two-mass system, has been thoroughly analyzed in [3].

The main assumption of the proposed approach is to extend the standard ADRC controller with an additional, floating coefficient, which can align the values of the tuned parameters in a limited range on the fly. Taking the current state of the plant into account, the controller follows the reference speed trajectory more accurately. To achieve this, an RBFNN was employed. Thus, the proposed ADRC speed controller equation can be presented with the following formula:

$$u_0 = \left(k_p\left(\omega_{ref} - \omega_2\right) - k_d z_2 - k_{dd} z_3\right) y_{RBF}, \tag{5}$$

where y_{RBF} is the RBFNN output, and can be described as follows:

$$y_{RBF} = \sum w_i exp\left(-\frac{\|\boldsymbol{x} - \boldsymbol{C}_i\|^2}{2\sigma^2}\right), \tag{6}$$

where: $\boldsymbol{C}_i$ is the neuron center vector, $\boldsymbol{x}$ is the input, σ is the scaling factor, w_i is the weight coefficient. The final structure of proposed algorithm is shown in Figure 1.

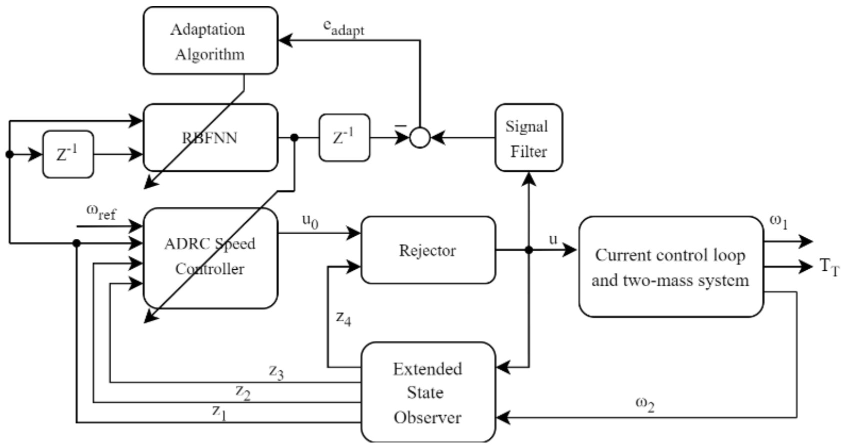

Figure 1: The proposed ADRC structure with neural parameters adjustment.

IV Experiment

The conducted tests were carried out using laboratory electric drive system with an elastic coupling [1]. Numerical calculations were executed with the use of *dSpace 1103* rapid-development programmable device. The overall scheme of the test bench is shown in Figure 2.

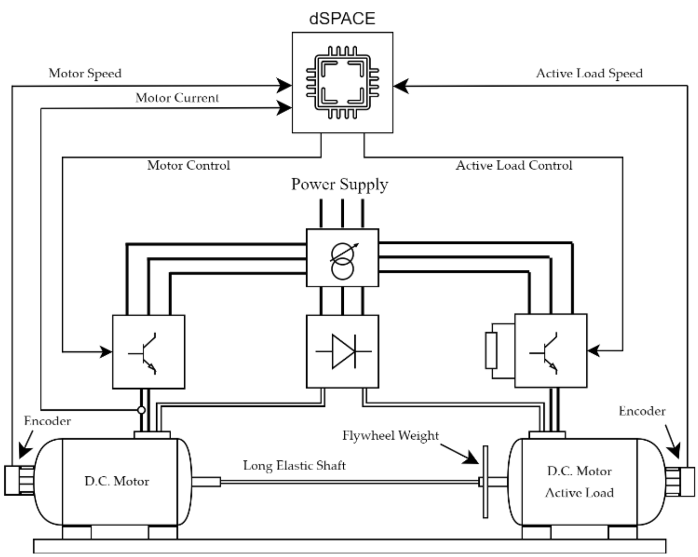

Figure 2: Schematic diagram of experimental setup with a two-mass system.

In the beginning of the test series it was crucial to investigate if the conventional ADRC structure behavior satisfies the dynamic demanding in case load machine time constant is increased ($T_2 = 3T_{2n}$). The obtained results (including the zoom-in showing the steady state transition) are presented in Figure 3. The presented speed transients show a small inconvenience. The conventional ADRC structure does not make the actual speed value follow its reference trajectory precisely. The lurch, visible at $t = 21$s, may be harmful to the mechanical structure. In order to eliminate the visible nuisance, the second attempt assumed that all tuned controller parameters were increased with a specific, constant value. The obtained results were significantly better in the steady state transition. However, after additional load torque appeared, the system was unable to damp the occurred oscillations. Thus, the response of the proposed ADRC-RBFNN was compared to the conventional structure with increased controller parameters. The obtained results of both approaches are shown in Figure 4.

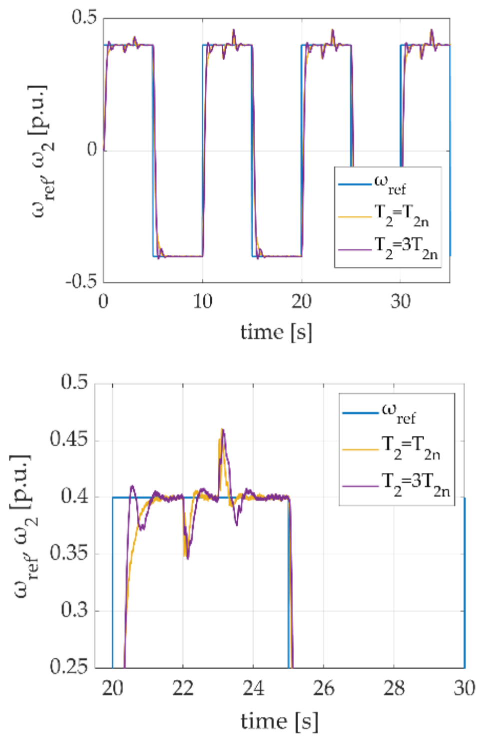

Figure 3: Results (speed transients) of ADRC algorithm (applied for a drive with elastic connection) achieved under different values of the load machine time constant.

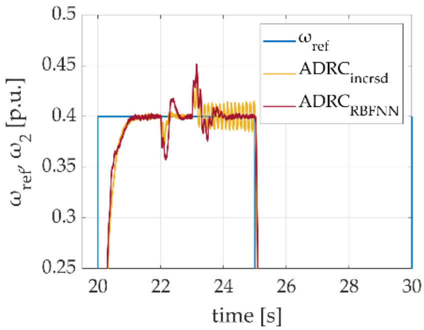

Figure 4: The load speed transients for changed time constant value including modified control structures (zoom).

V Conclusions

The presented approach demonstrates an extended ADRC load side speed controller. The introduced improvement adjusts the selected controller parameters in a small, limited range, basing on the system feedback. By doing so, robustness of the control algorithm has been increased. Applying an RBFNN allows compensating the occurred disturbances and lurches caused by significant time constant change of the plant. The conducted experiments prove that the proposed algorithm deals with the described problem and constitutes a promising base for future works and upcoming research.

References

[1] Kaczmarczyk, G.; Stanislawski, R.; Szrek, J.; Kaminski, M. Adaptive Sliding Mode Control Based on a Radial Neural Model Applied for an Electric Drive with an Elastic Shaft. *Energies* 2024, *17*, 833. https://doi.org/10.3390/en17040833

[2] J. Han, "From PID to Active Disturbance Rejection Control," in *IEEE Transactions on Industrial Electronics*, vol. 56, no. 3, pp. 900-906, March 2009, doi: 10.1109/TIE.2008.2011621.

[3] B. Wicher and S. Brock, "Active Disturbance Rejection Control Based Load Side Speed Controller for Two Mass System with Backlash," *2018 IEEE 18th International Power Electronics and Motion Control Conference (PEMC)*, Budapest, Hungary, 2018, pp. 645-650, doi: 10.1109/EPEPEMC.2018.8522001.

PRECISE DETERMINATION OF THE ANGULAR DISTRIBUTION OF THE WINDING INDUCTANCE OF A SWITCHED RELUCTANCE MOTOR

DOI
https://doi.org/10.18690/um.feri.4.2025.8

ISBN
978-961-286-986-1

BOGDAN FABIAŃSKI,[1] TOMASZ PAJCHROWSKI,[1]
KRZYSZTOF ZAWIRSKI[2]

[1] Poznań University of Technology, Institute of Automation, Robotics and Machine Intelligence, Poznań, Poland
bogdan.fabianski@put.poznan.pl, tomasz.pajchrowski@put.poznan.pl
[2] Stanisław Staszic State University of Applied Sciences in Pila, Pila, Poland
krzysztof.zawirski@put.poznan.pl

The article describes a precise method to obtain the angular profile of the winding inductance of a switched reluctance motor. The introduction emphasises the importance of research carried out in the context of the development of fault-tolerant control of the motor drive. The basis of the analysis presented here is the study of the current waveform accompanied by a forcing voltage, thus revealing the finite dynamics of the circuit RL. The study considers the nonlinear approximation function modeling the current waveform against other simplified methods. Further data processing and the methodology used in the context of the proprietary hardware layer allow to obtain repeatable and reliable results.

Keywords:
switched reluctance motor, optimisation of parameters, non-linear approximation, winding inductance, angular distribution

University of Maribor Press

I Introduction

The publication aims to present an automatic and precise method for determining the angular inductance distribution in a switched reluctance motor (SRM) phase winding. The inductance profile is a fundamental component of the SRM model based on the fundamental circuit equation [1-3]:

$$U_p = i_p R_p + \frac{d\Psi_p}{dt}, \tag{1}$$

where: p – phase number, U_p(V) – winding voltage, R_p(Ω) – resistance, Ψ_p(Wb) magnetic flux linkage, t(s) - time.

Assuming that the linked flux Ψ_p is dependent on the angle of the shaft position (θ_p) and winding current value (i_p) taking into account the parameter describing the dynamics of the magnetic field energy storage phenomenon in the circuit equation (winding inductance):

$$\Psi_p(\theta_p, i_p) = L_p(\theta_p, i_p) i_p \tag{2}$$

it becomes clear that the difficulty of modeling an SRM comes down to the description of its inductance variability (highly nonlinear). Even if consider some simplification of equation (2) aimed at reducing computational complexity for real-time processing [4] to the form:

$$\Psi_p(\theta_p, i_p) = F_1(\theta_p) F_2(i_p), \tag{3}$$

where: F_1 – inductance angular profile (L_p), F_2 – simplified model of saturation (independent from rotor position), the fundamental motor equations, based on the expansion of the general circuit equation (1):

$$U_p = i_p R_p + \frac{F_1(\theta_p) F_2(i_p)}{\partial i_p} \frac{di_p}{dt} + \frac{F_1(\theta_p) F_2(i_p)}{\partial \theta_p} \frac{d\theta_p}{dt} \tag{4}$$

are (assuming formula F derivative of the argument x: $F_1'(x)$):

$$\varepsilon = F_1'(\theta_p) F_2(i_p) \omega_r \tag{5}$$

for back-electromagnetic force, and:

$$T_p(\theta_p, i_p) = F'_1(\theta_p) \int_{v=0}^{i_p} F_2(\tau) dv. \tag{6}$$

for electromagnetic torque generation.
Considering the above, two 1D nonlinear relations of inductance profile (F_1) and magnetic circuit saturation modeling function (F_2) are required.

The well-determined motor model is the basis for the development of complex and precise algorithms in particular sensorless and fault tolerant control (FTC).

II Laboratory test bench

For the presented study, a dedicated laboratory stand was constructed. The stand structure and its view are shown in Fig. 1 and Fig. 2, respectively.

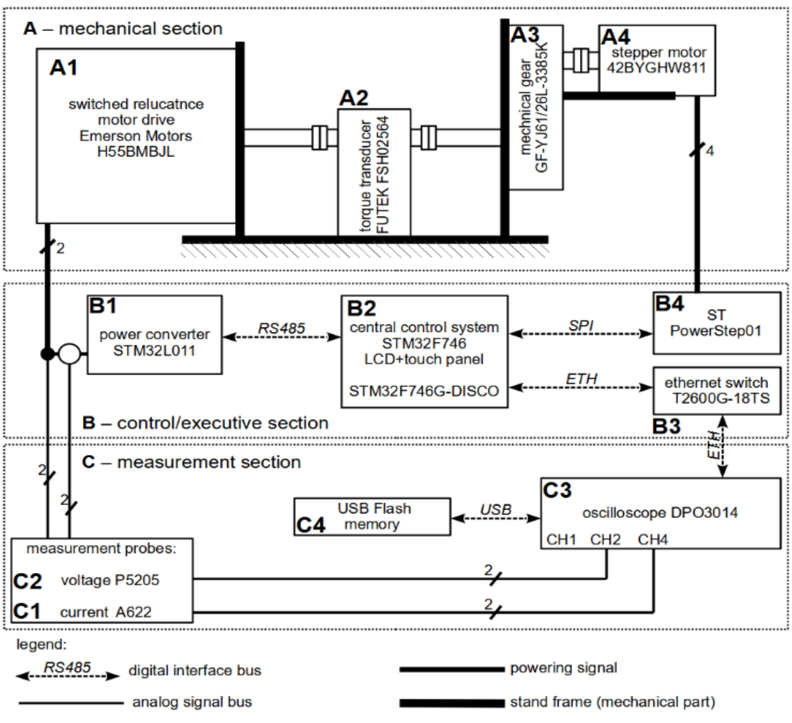

Figure1: Structure of the laboratory stand

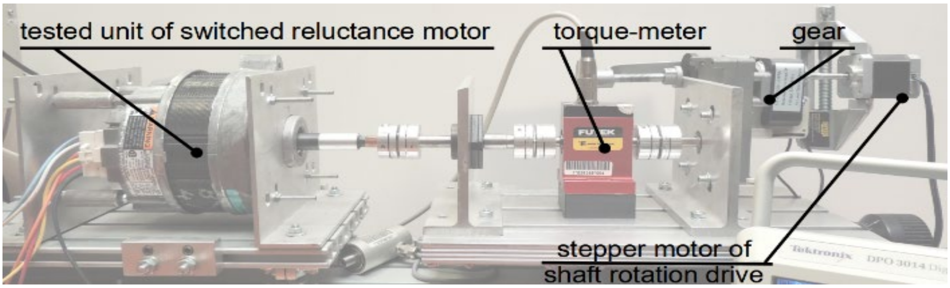

Figure 2: The mechanical part of the laboratory setup (kinematic chain)

The fully automated, proprietary laboratory test bench has many interesting solutions for data acquisition with very high precision of position angle setting, i.e. 72,5x10^{-9} *rad*.

III Raw data source

Input data for the analysis and determination of the inductance profile are series: the excitation voltage and the resulting motor phase current (Fig. 3). Data comes from remote controlled oscilloscope measurements in setup that allows to obtain best results e.g. coverage of the measurement range (in an automated process).

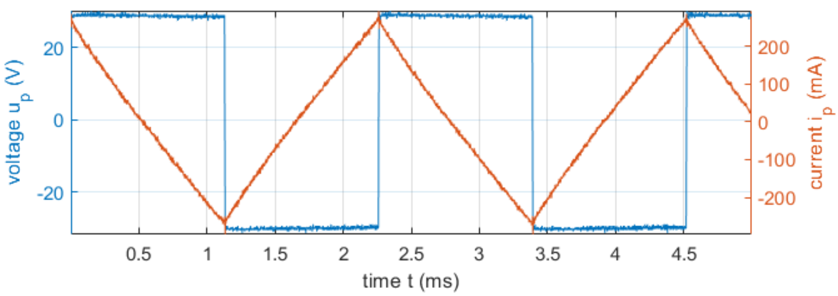

Figure 3: Waveforms of the excitation voltage and the resulting winding current

IV Approximation models

For comparison, two classes of models of the phenomenon describing the dynamics of motor current waveform were used. A simplified - linear and a more accurate nonlinear one. Three methods were used to determine the inductance L_p at a given shaft position θ_p : "*LinA*" called (with no resistance component), "*LinB*" and "*EXP*" (taking into account the time constant of the RL circuit). In linear model, the directional coefficient of regression (a_l) was calculated, what gives the final formula for (*LinA*) and (*LinB*) approach:

$$\text{(A) } L_{p-LinA} = \frac{\underline{U_p}}{a_l} \qquad \text{(B) } L_{p-LinB} = \frac{\underline{U_p} - \underline{i_p} R_p}{a_l}. \tag{7}$$

where $\underline{U_p}$, $\underline{i_p}$ – average values in registered data series.

The resulting inductance for the *EXP* method is based on the time constant value τ:

$$L_{p-EXP} = \tau R_p \ , \tag{8}$$

that results from approximation formula, where parameter β models an non-zero initial value of measured signal (Figure 3):

$$f(\tau, \beta) = \left(\frac{\underline{U_p}}{R_p} - \beta\right)\left(1 - e^{-t/\tau}\right) + \beta \tag{9}$$

V Results

Figure 4 presents a plot of inductance profiles obtained by different approximation formulas of motor winding current waveforms. When comparing, relative differences are not large, but it highly depends on measurement conditions (as on relative current peak-to-peak value). Results complies with parametric relations shown in Figure 5 and 6 obtained from accurate simulation of the experimental process. One of the most important is the peak value of current winding (i_m) as the result of PWM voltage excitation. The controlled peak current value during data acquisition for results shown in Figure 4 was 250 mA – quite small in relation to steady state value $i_A = U_p / R_p$ i.e.: 0,07 (see Figure 6 for that value).

The further studies focused only on analysis of obtained inductance profiles from best quality *EXP* approximation. The repeatability was checked for different source data series. The compensation methods of used probes measurement error (linearity, offset) and mechanical imperfections (e.g. gear clearances) were introduced. All efforts provide final, symmetric and ready to use in mathematical model reference inductance angular profile and its derivative (see equations (5) and (6)).

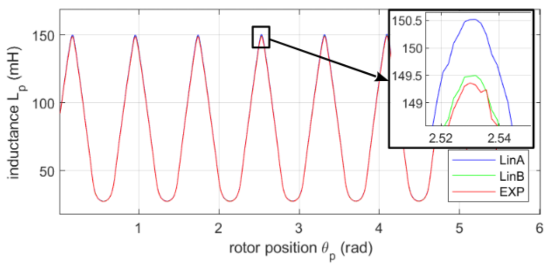

Figure 4: The plot of selected inductance profiles determined based on calculation of different forms of approximation formulas.

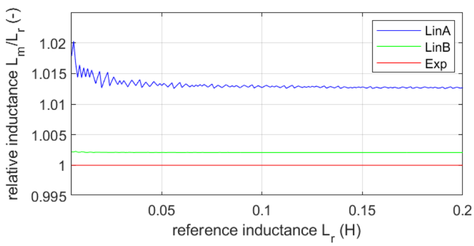

Figure 5: Computation results of relative inductance (L_m/L_r) from the reference value (L_r) for different approximation formulas used

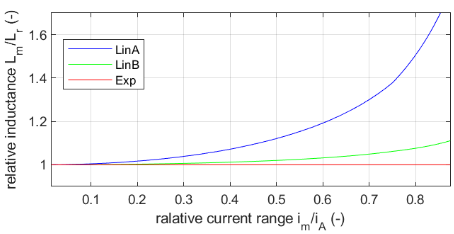

Figure 6: Calculated relative inductance value L_m/L_r in dependence of relative winding current peak value (i_m / i_A) as process parameter

VI Summary

The paper discusses a method leading to the precise determination of the angular distribution of the switched reluctance motor winding inductance based on measurements realized on a proprietary automated test bench. Finally obtained results serve as the basis for developing fault-tolerant control algorithms using nonlinear reference model calculated in real-time regime.

Notes

The article was written with the support of the Polish National Science Center (NCN, ncn.gov.pl) based on the agreement UMO-2016/23/N/ST7/03798 in a grant entitled: „Nonlinear reference model in fault tolerant control of the switched reluctance motor drive".

References

[1] R. Krishnan, "Switched Reluctance Motor Drives: Modeling, Simulation, Analysis, Design, and Applications". *CRC Press, Dec. 2017, google-Books-ID: plBgngEACAAJ*.
[2] J. Prokop, P. Bogusz, "Analysis of dynamic properties of switchable reluctance motors in MATLAB/SIMULINK system" *Przegląd Elektrotechniczny*, vol. Nr 5, pp. 119–124, 2000.
[3] B. Fabianski, K. Zawirski, "Parameter adaptation of simplified switched reluctance motor model using Newton and Gauss-Newton signal fitting methods," *COMPEL - The international journal for computation and mathematics in electrical and electronic engineering*, vol. 36, no. 3, pp. 602–618, Jan. 2017.
[4] B. Fabiański, K. Zawirski, "Simplified model of Switched Reluctance Motor for real-time calculations," *Przegląd Elektrotechniczny*, vol. R. 92, no. nr 7, pp. 19–23, 2016, doi: 10.15199/48.2016.07.03.

Quantitative Impact of Current Harmonics on Electromagnetic Lossesi n Automotive PMSMs

DOI
https://doi.org/
10.18690/um.feri.4.2025.9

ISBN
978-961-286-986-1

Krištof Rener, Martin Treven, Robert Kovačič, Uroš Kovačič, Tomaž Černe, Mohammad Mousavi, Roozbeh Naderi

TAE Power Europe, Ljubljana, Slovenia
krener@tae.com, mtreven@tae.com, rkovacic@tae.com, ukovacic@tae.com, tcerne@tae.com, mmousavi@tae.com, rnaderi@tae.com

This paper investigates the quantitative impact of current harmonics on electromagnetic losses in PMSMs used in automotive applications. We compare losses generated by sine current with those produced by conventional 2-level SVPWM inverter. A dynamic model is developed to capture the interaction between the 2-level inverter and the PMSM, accurately predicting the resulting harmonic currents. These predicted currents are then used as input for a FEA to calculate the electromagnetic losses in various motor components. Our analysis reveals that current harmonics can significantly increase the total electromagnetic losses in the motor through the whole operating range.

Keywords:
current harmonics,
PMSMs,
electromagnetic losses,
2-level SVPWM inverters,
automotive powertrain

University of Maribor Press

I Introduction

The automotive industry prioritizes compact, lightweight, and cost-effective electric motors for propulsion systems. This trend leads to the development of low-inductance Permanent Magnet Synchronous Motors (PMSMs). However, increasing battery voltages and lower motor inductances pose a challenge: higher current ripples are generated by standard 2-level Space Vector Pulse Width Modulation (SVPWM) inverters. This raises a crucial question: how do higher harmonics in the current waveform affect electromagnetic losses in these motors compared to ideal sine current supply?

This paper presents a comprehensive analysis of electromagnetic loss breakdown in automotive PMSMs with low inductance, driven by a SVPWM inverter at supply voltages in range of 800 V. We compare the losses generated by the actual harmonic-rich current to those of an ideal sine current scenario.

A non-linear PMSM model is coupled with a SVPWM inverter model in MATLAB-Simulink to accurately predict the harmonic currents. In the next step transient two-dimensional electromagnetic analysis is performed across the motor's entire torque-speed operating range for both harmonic and sine current cases. Motor losses were categorized into the losses in the stator winding, losses in the stator and rotor core and the losses in the magnets. We thoroughly analysed and compared the generated harmonic currents and the resultant electromagnetic losses in PMSM for both current scenarios.

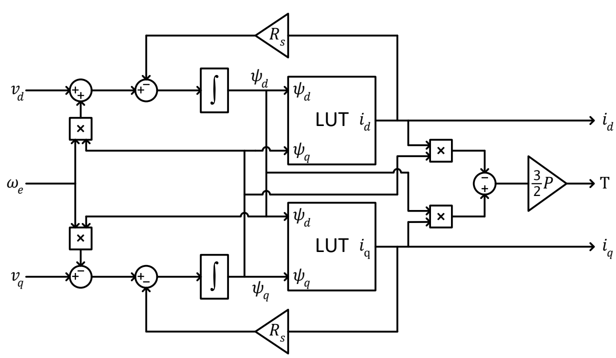

Figure 1: Non-linear motor model

II Losses calculation methods

This chapter details the modelling approaches used to accurately capture the impact of harmonic currents on electromagnetic losses in PMSMs.

To comprehensively account for harmonic current effects in the stator winding, we adopted a meticulous modelling strategy. Each wire of the motor distributed winding within the stator slots is modelled as a separate conductor. Apart from calculation of Joule losses, this is enabling the consideration of additional losses due to eddy currents, skin effect and proximity effect.

While the Bertotti loss model is commonly used for stator core losses, its sensitivity to higher harmonic magnetic fields is limited. Therefore, we implemented the Loss Surface model [4], which estimates the magnetic losses *a posteriori*, based on a model of dynamic hysteresis associated to a finite elements simulation. This model requires pre-defined material properties through a characteristic surface Magnetic field strength in dependence of Magnetic flux density and Rate of change in Magnetic flux density - H(B,dB/dt), which is normally obtained experimentally.

Like the stator winding, detailed 2D geometry is employed to model the magnets. This allows for the simulation of magnet losses under harmonic current conditions.

By adopting these tailored modelling techniques, we comprehensively investigate the impact of harmonic currents on electromagnetic losses across all crucial motor components, providing a realistic assessment of motor performance under actual operating conditions.

III PMSM loss evaluation

In PMSM stator windings, copper losses comprise DC losses arising from the magnitude of the fundamental current and the phase resistance, and AC losses dependent on the fundamental current frequency and higher harmonics. Sine current induces a 10% fluctuation in losses over one electrical period, implying a dominant DC component. Compared to sine current, harmonic current significantly amplifies copper loss fluctuations. This indicates a pronounced increase in AC losses due to higher frequency components in the current.

Stator core losses in PMSMs typically encompass hysteresis losses, classical eddy current losses induced by fundamental magnetic field changes, and excess eddy current losses caused by higher harmonic content. While the first two are primarily influenced by motor design and material properties, the presence of harmonics significantly impacts the latter category. Compared to sine current excitation, harmonic currents within the motor amplify the fluctuations of magnetic field, leading to increased eddy current losses and, consequently, elevated stator core losses.

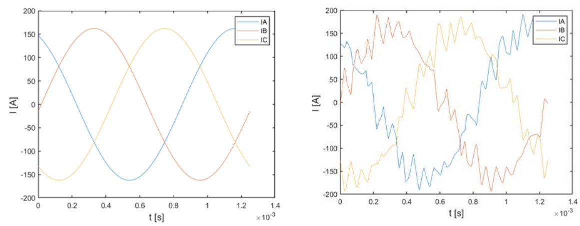

Figure 2: Sine current (left) and harmonic current (right) at 12000 rpm and 50 Nm. THD of harmonic current is 15.9 %.

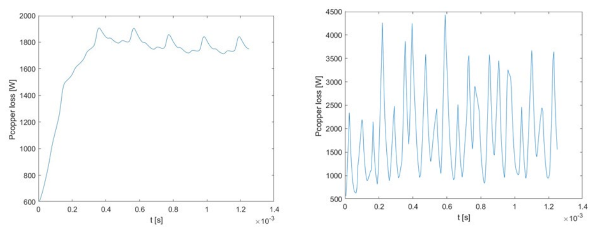

Figure 3: Winding loss at 12000 rpm and 50 Nm. Left: With sine current. Right: With harmonic current.

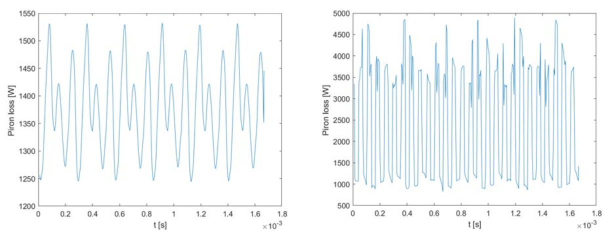

Figure 4: Stator core loss at 9000 rpm and 150 Nm. Left: With sine current. Right: With harmonic current.

Eddy currents are primarily contributor to losses in both the rotor core and permanent magnets. Similar to the previously discussed observations, harmonic currents significantly influence eddy current generation and therefore elevated losses in the rotor core and permanent magnets.

IV Results and discussion

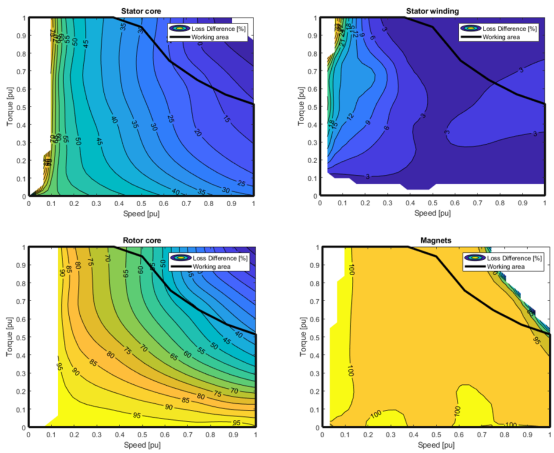

Figure 5: Percentage of loss reduction with sinusoidal current [in %].

Percentage of loss reduction was calculated as follows:

$$p_{lr} = ((P_{harmonic} - P_{sin})/P_{harmonic}) * 100 \quad (1)$$

Figure 5 unveils the relative difference in losses within key motor components when comparing sine and harmonic currents. We can observe that harmonic current has biggest relative influence on magnets, followed by rotor core. This suggests that current harmonics contribute significantly to losses in these components.

Since stator winding and core losses exceed rotor and magnet losses by approximately an order of magnitude, most motor efficiency gains come from lowering the losses in the stator. Regions of peak loss difference are at low-speed operation, where frequent inverter switching generates numerous current ripples over one electrical period, leading to magnified harmonic losses, and at low torque and high-speed operation, where relative importance of harmonic losses becomes more pronounced compared to total motor losses.

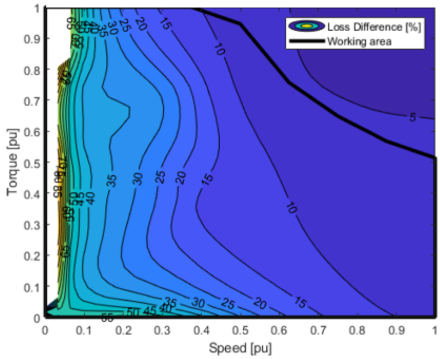

Figure 6: Combined percentage of loss reduction with sinusoidal current [in %].

V Conclusions

This study highlights the crucial role of harmonics in affecting motor performance and emphasizes the need to consider them for accurate efficiency assessments. Employing SVPWM inverters in automotive Permanent Magnet Synchronous Motors (PMSMs) injects harmonic currents, leading to elevated electromagnetic losses across the whole operational range, with most influence at low speeds. The research quantifies the specific contribution of current harmonics to various motor component losses.

Future work will validate these findings through physical testing, explore advanced control techniques for mitigating harmonic currents and consequently their losses, and analyse the subsequent impact on motor thermal behaviour and overall performance.

References

[1] J. Lee, S. Sung, H. Cho, J. Choi, K. Shin, "Investigation of Electromagnetic Losses Considering Current Harmonics in High-Speed Permanent Magnet Synchronous Motor", *Energies 2022.,* 15, 9213.

[2] M. Treven, *Dinamični simulacijski model kolesnega električnega pogona.* Ljubljana, UL FE, 2017.

[3] Altair Flux Software, *Flux user guide v2022.1.* Available online: https://altair.com/ (accessed on 31 January 2024).

[4] Thierry Gautreau, *Estimation des pertes fer dans les machines électriques. Modele d'hysteresis loss surface et application aux machines synchrones a aimants.* Grenoble, INPG, *2005.*

Comparative Analysis of Spatial-Time Harmonics of Radial Forces in the Multi-Phase Synchronous Reluctance Machines of Three- Six- and Nine- Phase Winding

Cezary Jędryczka,[1] Michał Mysiński,[1]
Łukasz Macyszyn[2]

[1] Poznan University of Technology, Faculty of Control, Robotics and Electrical Engineering, Poznań, Poland
michal.mysinski@put.poznan.pl
[2] Poznan University of Technology, Faculty of Mechanical Technology, Poznań, Poland
michal.mysinski@put.poznan.pl

The paper deals with analysis of radial forces in the multi-phase synchronous reluctance machines (SynRM). SynRM of three-, six- and nine-phase windings were studied. The field models were developed to determine normal and tangential components of magnetic flux density vector in the air-gap of the studied machines. The selected research results have been presented and discussed.

DOI
https://doi.org/
10.18690/um.feri.4.2025.10

ISBN
978-961-286-986-1

Keywords:
synchronous reluctance machines (SynRM), radial forces analysis, multi-phase windings, spatial-time harmonics, magnetic flux density

University of Maribor Press

I Introduction

Thanks to the many advantages, among others their fault tolerance as well as reduced cost of power electronic systems, a dynamic growth in interest in multiphase electric machines can be observed [2]-[4]. The paper focusses on analysis of the radial forces in the synchronous reluctance machines (SynRM) of multi-phase windings. The radial forces considered in the paper were obtained by calculating distribution of the normal component B_n and the tangential component B_t of the magnetic flux density vector. Three synchronous reluctance machines of three-, six- and nine-phase windings have been studied.

II Magnetic forces in synrm

The most important parameter derived from the forces present in an electrical machine is of course the electromagnetic torque. Considering radial and axial components of Maxwell stress tensor the radial and axial forces can be determined as well. Assuming planar symmetry of the magnetic field in the machine the axial forces are neglected, which is a common approach in analysis of electrical machines. Considering the radial forces the "local" character of this forces should be emphasized. When machines has symmetrical winding and no eccentricity the global force acting on the rotor (expressed by integral of radial component of Maxell stress tensor over air-gap circumference of is equal to 0. Figure 1 shows the components of the magnetic flux density in the machine [1].

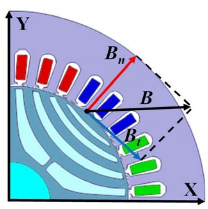

Figure 1: The components of magnetic flux density in the machine

For the analysis of the radial forces in electrical machine the distribution of tangential and radial components of the Maxwell stress tensor must be determined by means of distribution of radial B_n and tangential components of the magnetic flux density in the air-gap [1]:

$$\sigma_n = \frac{B_n^2 - B_t^2}{2\mu_0} \tag{1}$$

$$\sigma_t = \frac{B_n - B_t}{\mu_0} \tag{2}$$

where: σ_n – stress in the normal axis, σ_t – stress in the tangential axis, B_n – radial component of the magnetic flux density, B_t – tangential component of the magnetic flux density vector, μ_0 – permeability of the vacuum.

III Spatial-time harmonics

In order to comprehensively analyse the radial forces occurring in the air gap of an electric machine, it is necessary to study their spatial-time harmonics. Spatial harmonics refers to discussed above "local" character of radial forces along circumference of the air gap. In other words, with their help it is possible to observe the distribution of radial forces on the circumference of the machine within selected time instant. The time harmonics, on the other hand, show the action of the resulting stresses on a given area of the machine over the course of an assumed time. So, by analogy, it is possible to study the forces acting on a presumed area (slots, stator tooth, or rotor) in time [1]. Figure 2 shows a graphical interpretation of the spatial-time harmonic analysis.

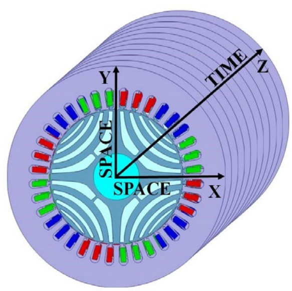

Figure 2: Graphical interpretation of the spatial-time character of radial forces

According to the graphic above, a single XY plane determines the spatial harmonics along the perimeter of the magnetic gap. In contrast, each successive layer in the Z-axis represents the next time step and thus affects the time harmonics.

IV Studied configurations

To demonstrate the effect of the number of phases on the radial forces SynRM machine, the authors proposed 3 winding configurations of three-, six- and nine-phases, respectively. In the developed field models of studied machines the planar symmetry of the magnetic field has been assumed. All models have the same geometry of the core and differ only in number of phases of the winding. The three- and nine-phase windings are single layer, while six-phase machine has double layer winding. The operating point, in term of output torque value as well torque angle are kept the same across studied variants to make feasible direct comparison of radial forces. Figure 3 shows the tested configurations of the SynRM motor models [2].

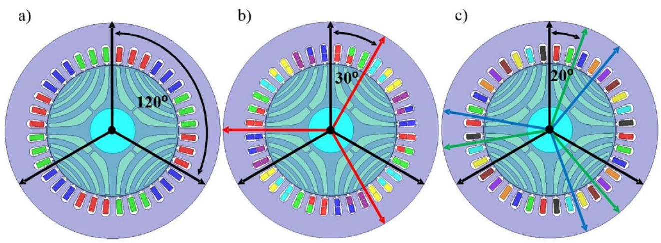

Figure 3: Model configurations: a) three-phase, b) six-phase, c) nine-phase

The phase vector diagrams of studied SynRMs are indicated in the figure above. The analysed multi-phase windings are asymmetric systems [2]. This means that the vectors cannot duplicate in the counterphase (they cannot repeat for a given vector + 180^0). Asymmetric multi-phase systems for integer value of m/3=k can be presented by k three-phase systems shifted in phase by:

$$\theta = \frac{\pi}{m} \tag{3}$$

where θ – phase angle of the three-phase systems forming multiphase system, m – number of phases.

From this, it can be deduced that a six-phase system can be formed by two three-phase systems shifted by 30^0 while a nine -phase system of three three-phase systems shifted by 20^0[3].

V Results

When studying radial forces occurring in an air gap, one can find similarities to the analysis of relativistic considerations in the context of time dilation. By analogy with a moving and stationary observer, we can relate to a stationary stator and a moving rotor. This fact makes it possible to observe the same radial forces in two ways, depending on which frame of reference we are in. Figure 4 shows the differences in the perception of radial forces depending on the reference system.

a) b)

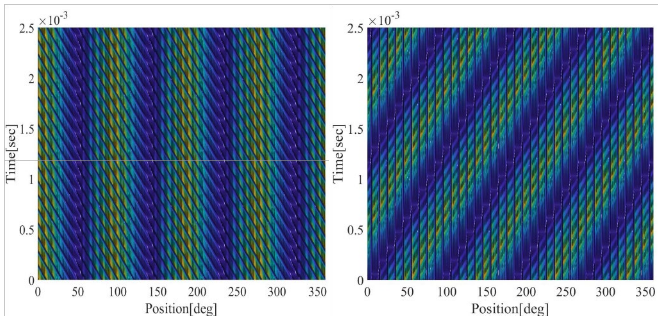

Figure 4: Differences in the perception of radial forces depending on the reference point: a) rotor reference, b) stator reference

Fig. 4(a) shows the radial forces seen from the perspective of observer on a moving rotor which maintains time invariant stresses while changing position of the slots in time. On the other hand, Fig. 4(b) shows the same radial forces seen from the perspective a stationary stator which shows the stress pulsations of the individual slots resulting from rotor rotation.

Based on Figure 2, a spatial-time study of the stresses occurring in the air gap was carried out. Analogous analyses were conducted for the 3 winding variants, taking into account the reference of the observation point (rotor and stator) and distinguishing between normal and tangential stresses. Figure 5 shows a comparison of the spatial-time distribution of the normal stresses for the 3-phase and 9-phase variants observed in a stationary reference frame linked with stator of the machine.

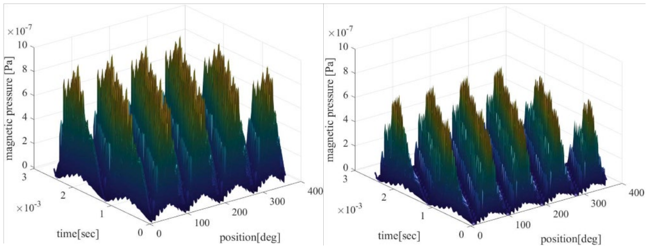

Figure 5: Spatial-time characteristics of magnetic stresses: a) three-phase winding, b) nine-phase winding

Based on the data in Figure 5, the multi-phase variants are compared. Figure 6 shows the difference between the reference 3 phase winding and the 6 and 9 phase windings.

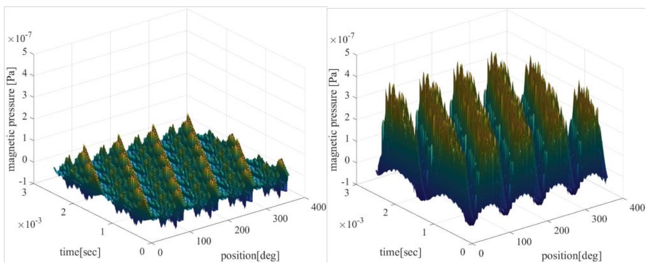

Figure 6: Magnetic stress difference with respect to three-phase winding: a) for six-phase winding, b) for nine-phase winding

As can be seen above, increasing the number of phases significantly reduces the radial forces in the air gap (see increased difference in Fig. 6(b)) by up to a third compared to the 3-phase variant.

VI Conclusions

The paper deals with analysis of radial forces in the synchronous reluctance motor (SynRM) with multiphase windings. Spatial-time analysis of magnetic stresses was carried out for tree- six- and 9-phase windings.

The detailed description of the approach including implemented analysis of spatial-time harmonics will be presented during the conference and included the scope of the extended version of the paper.

References

[1] S. Haas, K. Ellermann, Development and analysis of radial force waves in electrical rotating machines, 2017, DOI: 10.24352/UB.OVGU-2017-098

[2] C. Jędryczka, W. Szeląg, "Analysis of the multi-drive powered permanent magnet synchronous motor under drive fault conditions", SME 2017 – Nałęczów, Poland : IEEE, 2017.

[3] Scuiller F., Charpentier J., Semail E., "Multi-star multi-phase winding for a high power naval propulsion machine with low ripple torques and high fault tolerant ability", Vehicle Power and Propulsion Conference (VPPC), IEEE, 2010.

[4] Rolak M., Che H.S., Malinowski M.: Modeling and Fault-tolerant control of 5-phase induction machine. Bulletin of Polish Academy of Sciences, Technical Sciences, Vol. 63, No. 4, pp. 997–1006, 2015.

CHARACTERIZATION OF NON-HIGHLY COMPRESSED IRON POWDERS IN RING FORM FOR APPLICATION IN THE FIELD OF ELECTRICAL MACHINES

MOHAMMAD TORABI SHAHBAZ, DANIEL WÖCKINGER, EDMUND MARTH, GERD BRAMERDORFER

Johannes Kepler University Linz, Institute for Electric Drives and Power Electronics, Linz, Austria
mohammad.torabi_shahbaz@jku.at, daniel.woeckinger@jku.at, edmund.marth@jku.at, g.bramerdorfer@jku.at

In this study, non-highly compressed iron powders in a ring-shaped sample container are characterized. This approach involves the dimensioning of a non-magnetic ring-shaped container to measure the magnetic properties of ferromagnetic powders with different bulk densities. Therefore, an optimization of the container's dimensions is presented. Finally, the precise data acquisition systems for determining the material's B-H characteristics and loss curves in relevant operating points are discussed and first measuring results for several distinct material densities are presented.

DOI
https://doi.org/10.18690/um.feri.4.2025.11

ISBN
978-961-286-986-1

Keywords:
magnetic material characterization,
iron powder,
magnetization curve,
iron losses

University of Maribor Press

I Introduction

ferromagnetic materials such as laminated steel sheets made of silicon-iron (Si-Fe), nickel-iron (Ni-Fe), and cobalt-iron (Co-Fe) as well as soft magnetic composites (SMCs) and amorphous magnetic materials [1] are used.

Many studies have been conducted on analyzing the electromagnetic properties of ferromagnetics using an apparatus such as a vibrating sample magnetometer (VSM) [2,3]. However, despite its numerous advantages, utilizing a VSM entails certain limitations and concerns. One limitation is the requirement for relatively small sample sizes due to the spatial constraints of the instrument. In addition, no deformation, e.g., changing the sample's effective material density, of the sample is possible during the measurement.

Consequently, a simpler measuring system, i.e., the ring test method, according to the IEC standard [4], should be used. Setting up this method for powders involves numerous challenges related to selecting materials for the setup framework, e.g., the design of excitation systems, placing samples and sample holders, power electronics, measuring local field intensity, and controlling the system.

Several advantages are associated with characterizing magnetic materials in the form of a ring [5]. Firstly, the demagnetization field is zero, since the sample forms no magnetic poles. Secondly, the magnetic field strength and the rated change of the flux density can be indirectly estimated using simple equations. Nevertheless, a significant disadvantage is the non-homogeneous magnetic field and the very complex and time-consuming sample preparation time. Lastly, this initial study with a ring-shaped sample will allow the intrinsic properties of magnetic powders to be understood and the suitability of non-highly compressed powder materials for electromagnetic device application to be evaluated.

II Methodology

In this investigation, a method is introduced to characterize the magnetic properties of powders using a non-magnetic container in the shape of a ring to utilize the advantages of ring-shaped characterization, as schematically depicted in Figure 1. Typically, the material behavior in the desired B-field range is non-linear, and here it is non-linearly influenced by the fluctuating material density. A non-magnetic ring-shaped container is designed to hold the powders and the primary and secondary winding systems for controlling and measuring their current and induced voltage, respectively.

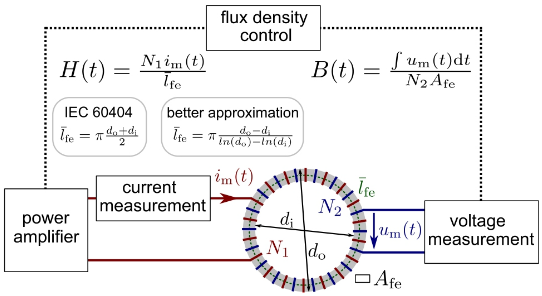

Figure 1: Experimental setup for characterizing soft magnetic materials with a ring-shaped specimen, taken from[6].

As candidate materials, pure iron powders can be mixed with insulators to create different distinct volume fractions regarding magnetic flux guidance for the samples, some of which are less than the bulk density, and some are more than the bulk density. To achieve this, varying amounts of iron powder should be compressed into the same sample holder. To achieve the goal of measuring field densities in the sample up to 1.2 T at 2 kHz and around 0.8T at approximately 10 kHz, the dimensions of the container need to be optimized. The selected values for the magnetic flux densities and frequencies correspond to the operating ranges of high-speed electric machines.

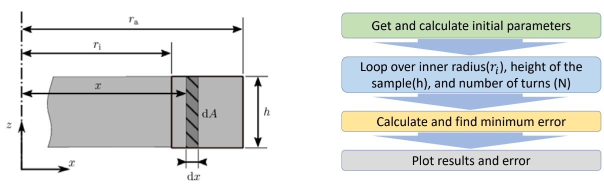

Figure 2: Ring-shaped specimen (left), optimization flowchart (right)

The key equations for calculating the magnetic flux density and inductance for the ring-shaped specimen (cross section side is shown in Figure 2 (left) are as follows:

$$B = \frac{\mu_0 \mu_r N I}{2\pi(r_a - r_i)} \ln\left(\frac{r_a}{r_i}\right) \tag{1}$$

$$L = \frac{\mu_0 \mu_r N^2 h}{2\pi} \ln\left(\frac{r_a}{r_i}\right) \quad , \tag{2}$$

where B is the magnetic flux density, μ_0 is the permeability in air, μ_r is the relative permeability, N is the number of turns for primary coil , I is the current, r_a is the outer radius, and r_i is the inner radius. The inductance and the resistance of the excitation coil determines the voltage drop of the coil which is limited by the amplifier. For optimization process, several assumptions are made. Firstly, it is assumed that the material is linear and that leakage flux and the effects of eddy currents on the resulting field are negligible. However, for the estimation of iron loss (R_{Fe}), the eddy current loss part should be considered. For loss estimation, a simple formula is used without considering the excess loss, thus it can be formulated as below:

$$R_{Fe} = K_h f B^n + K_{ec} f^2 B^2 \,, \quad 1.6 < n < 2 \tag{3}$$

where K_h is hysteresis coefficient, K_{ec} is the eddy current coefficient, and f is frequency. The ohmic resistance of the copper wire (R_{Cu}) can be calculated as follows:

$$R_{Cu} = \frac{N\left(2h + 2(r_a - r_i)\right)}{A_{cu}\sigma_{cu}} \quad , \tag{4}$$

where A_{cu} is the cross section of the wire, and σ_{cu} is the conductivity of the wire. The equivalent ohmic resistance (R_{eq}) of the coil includes both (3) , (4) , leading to a total power loss, where the according maximum total resistance R_{eq} is limited by the utilized amplifier:

$$R_{eq} = R_{Fe} + R_{Cu} \quad . \tag{5}$$

The impedance can finally calculated by using:

$$Z = \sqrt{{R_{eq}}^2 + \omega^2 L^2} \quad . \tag{6}$$

Here, ω is angular electric frequency. The maximum output voltage and current for the utilized Servowatt amplifier (DCP 780/60B) are 50 V and 15 A, respectively[7]. Based on these constraints and unknown parameters, an analysis can be conducted to identify potentially suitable configurations. A code is developed to find the optimal configuration, which is depicted as a flow chart in Figure 2 (right). The error is defined as the difference between the targeted values for flux densities and impedance with the calculated ones from the formula mentioned above (1,6) being as small as possible. The number of turns of the measuring (secondary) winding is dictated by the induced measuring voltage, which must fall within certain limits set by an amplifier and data acquisition box. With the existing data acquisition box (NI USB 6216), a voltage up to 10.4 Volts can be measured [8]. The measurement data, including the primary current and induced secondary voltage, are acquired through the mentioned data acquisition box, while applying anti-imaging and anti-aliasing filters. Real-time information is captured by the data acquisition system during the experimental process, ensuring accuracy and reliability in the characterization of magnetic properties. The anti-imaging filters smooth the signals generated by the output channel of the data acquisition box, and high-frequency content is removed by the anti-aliasing filter. Additionally, the experimental setup incorporates iterative learning control (ILC) to enhance the accuracy and efficiency of the characterization process [9]. The ILC algorithm is utilized to refine the control inputs applied to the experimental setup iteratively and to achieve the desired flux density waveform with a very low control error. The methodology allows to understand the magnetic properties of non-highly compressed iron powder in ring shapes. The results presented in the final paper will cover *B-H* characteristics at different frequencies, loss curves at various operating points relevant for electromagnetic device application, and the impact of iron powder density on all those properties.

III Conclusion and outlook

The expected results of this investigation revolve around obtaining comprehensive insights into the magnetic properties of non-highly compressed iron powders measured by samples of ring form, specifically targeting parameters essential for their application in electromagnetic devices. The results encompass *B-H* characteristics across various frequencies and loss curves corresponding to different operating point, preferably for sinusoidal flux density waveforms. The results will highlight the observed changes in hysteresis due to varying densities of iron powder, indicating a discernible shearing of the hysteresis curve, leading to a reduced non-linearity.

Acknowledgement

This project has received funding from the European Research Council (ERC) under the European Union's Horizon 2020 research and innovation programme (grant agreement No ERC-10107304).

References

[1] Krings, Andreas, et al. "Magnetic materials used in electrical machines: A comparison and selection guide for early machine design." *IEEE Industry Applications Magazine* 23.6 (2017): 21-28.
[2] Chomchoey, Nucharee, Darunee Bhongsuwan, and Tripob Bhongsuwan. "Magnetic properties of magnetite nanoparticles synthesized by oxidative alkaline hydrolysis of iron powder." *Agriculture and Natural Resources* 44.5 (2010): 963-971.
[3] Zhu, Jian Guo, et al. "Measurement of magnetic properties under 3-D magnetic excitations." *IEEE Transactions on Magnetics* 39.5 (2003): 3429-3431.
[4] Hilton, Geoffrey. "IEC Magnetic Materials 60404-Part 6: Methods of measurement of the magnetic properties of magnetically soft metallic and powder materials at frequencies in the range 20 Hz to kHz by the use of ring specimens." (2003).
[5] Tumanski, Slawomir. *Handbook of magnetic measurements*. CRC press, 2016.
[6] Bramerdorfer, Gerd, et al. "State-of-the-art and future trends in soft magnetic materials characterization with focus on electric machine design–part 1." *tm-Technisches Messen* 86.10 (2019): 540-552.
[7] DCP 780/60B Datenblatt, https://servowatt.de/download/dcp_780_datenblatt.pdf
[8] USB-6216 Specifications, https://www.ni.com/docs/de-DE/bundle/usb-6216-specs/page/specs.html.
[9] Andessner, D., et al. "Measurement of the magnetic characteristics of soft magnetic materials with the use of an iterative learning control algorithm." 2011 IEEE Vehicle Power and Propulsion Conference. IEEE, 2011.

REVIEW OF POWER SYSTEMS OF NON-THERMAL PLASMA REACTORS AND THEIR APPLICATIONS

DOI
https://doi.org/10.18690/um.feri.4.2025.12

ISBN
978-961-286-986-1

HENRYKA DANUTA STRYCZEWSKA,
GRZEGORZ KAROL KOMARZYNIEC, OLEKSANDR BOIKO
Lublin University of Technology, Department of Electrical Engineering and Superconductivity Technologies, Lublin, Poland
h.stryczewska@pollub.pl, g.komarzyniec@pollub.pl, o.boiko@pollub.pl

Atmospheric pressure cold plasma has recently attracted considerable scientific interest and found a range of practical applications. Common sources of such plasma include dielectric barrier discharge (DBD), atmospheric pressure plasma jets (APPJ), and gas arc discharge (GAD). Various nonlinear phenomena occurring within the power supply–plasma reactor system – such as harmonic generation, resonance and ferroresonance, switching overvoltages, and pulse formation – can, when properly managed, enhance reactor performance. These effects contribute to more reliable plasma ignition, increased process efficiency, and improved integration of the plasma system with the electrical grid. The examples of power supplies used in plasma processes in power generation, environmental engineering, agriculture and medicine presented in this review confirm the above statement.

Keywords:
non-thermal plasma (NTP),
DB,
GA and APPJ rectors,
power systems of NTP reactors,
non-linear phenomena in plasma generation systems

University of Maribor Press

I Introduction

Non-thermal plasma (NTP), produced through electrical discharge, is being increasingly applied across a range of interdisciplinary fields, including energy, environmental protection, agriculture, and medicine. Plasma reactors (PRs) designed to generate atmospheric pressure cold plasma (APCP) are nonlinear energy consumers that utilize various types of electrical discharges. Depending on the specific application, their power requirements can range from several hundred watts – as seen in medical and agricultural contexts – to several tens of kilowatts in energy and environmental engineering. The power of the discharge, which reflects the reactor's performance, is regulated by adjusting voltage, current, and/or frequency, depending on the discharge type.

An overview of power supply systems (PSS) for APCPs includes dielectric barrier (DB) reactors, which can be found in both classic DBD reactors and APPJ reactors, as well as two-electrode and multi-electrode GAD reactors, the latter of which can also be used as a two-electrode APPJ reactor. This selection is motivated by several factors: these types of electrical discharge are effective in generating NTP and the range of their potential applications is growing [1,2].

II Plasma reactors as electrical energy receivers

A. Plasma reactor with DBD

The DBD PR represents the capacitive-resistive receiver for the PSS. Structure of the discharge element of the DBD reactor is presented in Fig. 1(a) together with equivalent diagram (Fig. 1b), in which the non-linear conductivity G of the gas gap models the discharge after its ignition. When the applied voltage reaches the breakdown threshold, gas ionization takes place, and the discharge gap ceases to act as an insulator. Instantaneous values of supply voltage u(t), gap discharge voltage $u_g(t)$ and discharge current $i_G(t)$, presented in Figs.1(c) and 1(d), respectively.

The efficiency of a DBD reactor can be enhanced by raising the supply voltage frequency. However, this must be balanced against the associated rise in gas temperature within the discharge gap, which typically hinders the formation of particles and reactive species in plasma processes and necessitates the implementation of dedicated electrode cooling systems.

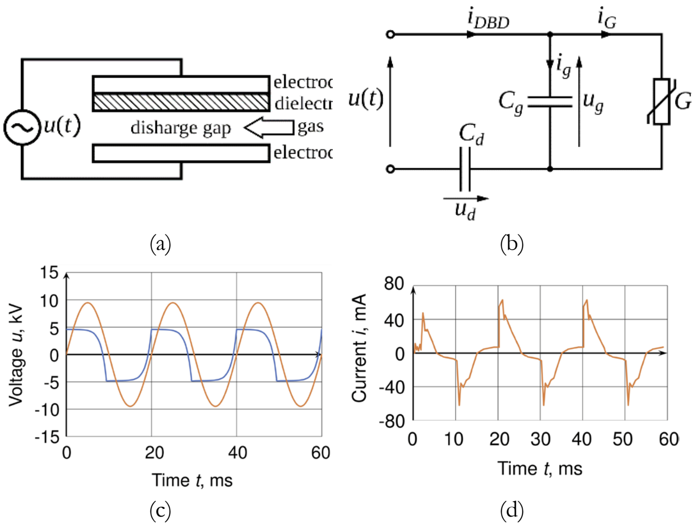

Figure 1: [2]: Structure of the DBD reactor (a); equivalent electrical diagram (b); numerical PSpice modelling results: supply voltage and gap voltage, (c), and discharge gap current (d), where: C_d – dielectric capacitance, C_g – discharge gap capacitance, G – non-linear conductance of the DBD, $u(t)$ – power source voltage, i_{DBD}, i_g and i_G – currents of the DBD PR, gap and non-linear conductance, respectively.

The discharge power and energy efficiency of plasma generation in a DBD system are influenced by several factors, including the geometry of the discharge components, the physical and chemical properties of the input gas, and key electrical parameters of the PSS – such as voltage amplitude, waveform, frequency, internal impedance of the power source.

The PSS of DBD PR has the character of a real voltage source, often at high frequency, so that the voltage between the reactor electrodes can be reduced while maintaining the same efficiency of the plasma process. This means smaller dimensions of the power transformer's, as well as greater homogeneity of discharge without sparks or arcing.

B. GAD plasma reactor

A key advantage of GAD is its capability to generate NTP directly within polluted gases at atmospheric pressure and under conditions matching those of exhaust gas emission, eliminating the need for prior gas treatment. Figure 2 illustrates a schematic of the GAD plasma reactor electrodes, along with its equivalent electrical circuit and the theoretical voltage and current waveforms for a two-electrode GAD system.

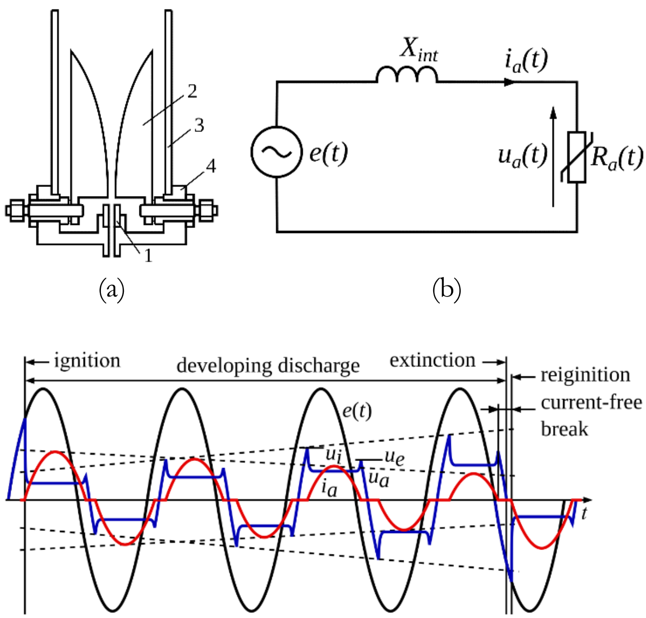

(c)

Figure 2: GAD PR electrode sketch (a) and equivalent circuit (b), theoretical voltage and current waveforms of the two-electrode GAD reactor (c) [2], where: 1 - nozzle for introducing process gas, 2 - high-voltage electrode, 3 - glass tube, 4 – body; $e(t)$ – PS voltage, X_{int} - internal reactance of the PS, R_a -non-linear resistance of the GAD PR, u_a – GAD voltage, i_a – GAD current, u_i - GAD ignition voltage, u_e - GAD extinction voltage.

The GAD PR in a PSS operates as a nonlinear resistive load, which often requires an auxiliary ignition system depending on the type and composition of the working gas. Once ignition occurs, it is crucial to rapidly and efficiently limit the reactor current to preserve non-thermal discharge conditions. The PSS for a GAD-based reactor should function as a true current source. The discharge current ia(t) is approximately sinusoidal, while the post-ignition voltage ua(t) remains nearly constant, between 1.5 – 1.6 kV when air is used as the working gas [3,4].

C. APPJ reactors

APPJ-type reactors are designed to produce stable, low-temperature plasma capable of exerting targeted effects on objects of various shapes and sizes. These reactors are commonly used in applications such as biological decontamination, medical treatments, and surface modification [5,6,7]. Plasma is typically generated within a nozzle, and a forced gas flow carries it out of the reactor toward the object being processed, forming a uniform glow discharge for effective plasma-chemical interaction. The design of APPJ plasma reactors uses solutions in which one of the electrodes is covered with DB, as in DBD PR, or with metal electrodes, as in GAD reactors. Various strategies are currently employed in APPJ technology to maintain non-thermal plasma conditions at atmospheric pressure.

These include optimizing gas flow parameters, configuring the geometry of the electric field, and selecting an appropriate power supply system [8–11].

III Power supply systems of plasma reactors with DBDs and GADs

Systems for generating non-thermal, non-equilibrium plasma can be powered using DC, pulsed, or sinusoidal voltages, with operating frequencies ranging from a few hertz, through radio frequencies (RF), up to several kilohertz or even hundreds of megahertz in the case of microwave plasma reactors. The power supply systems (PSS) for such plasma reactors typically include voltage conversion components – such as high-voltage transformers and magnetic switches (chokes) – as well as frequency converters, including thyristor and transistor inverters, pulse generators, and magnetic frequency converters. Power supply systems for APCP-generating plasma reactors must fulfill a range of specific requirements, including: (1) the type of electrical discharge used for plasma generation; (2) the chemical composition and physical properties of the working gas; (3) the pressure conditions within the discharge chamber; (4) the geometry of the discharge components; (5) the necessity to reliably initiate and sustain cyclic reactor operation post-ignition; (6) key electrical parameters such as power, voltage, frequency, number of phases, and output impedance; and (7) additional components that enhance compatibility with the electrical grid, including frequency filters and reactive power compensation systems. The article reviews the design of NTP generator power systems and their selected applications.

References

[1] Henryka D. Stryczewska and Kenji Ebihara (eds), *Advanced Technologies for Energy and Environment*, ISBN: 978-83-7947556-8, Publisher: Lublin University of Technology, Lublin 2023.

[2] Stryczewska H. D., Supply Systems of Non-Thermal Plasma Reactors. Construction Review with Examples of Applications, *Appl. Sci.* 2020, 10, 3242; doi:10.3390/app100932.

[3] Salazar-Torres A. et al, 2015, Impulse Three Phase Power Supply Used for a Gliding Plasma Discharge, *J. Phys.*: Conf. Ser. 591 012062 591

[4] Krupski, P. and Stryczewska, H.D. A Gliding Arc Microreactor Power Supply System Based on Push–Pull Converter Topology. *Appl. Sci.* 2020, 10, 3989.

[5] Fanellia, F.; Fracassi, F., Atmospheric pressure non-equilibrium plasma jet technology: general features, specificities and applications in surface processing of materials. *Surf. Coat. Technol.* 2017, 322, 174-201.

[6] Malik, M. A.; Schoenbach K. H.; Abdel-Fattah T. M. and others, Low Cost Compact Nanosecond Pulsed Plasma System for Environmental and Biomedical Applications, *Plasma Chem Plasma Process*, vol. 37, No 1, pp. 59-76, Jan. 2017.

[7] Yong-Nong C. and Chih-Ming K., Design of Plasma Generator Driven by High-frequency High-voltage Power Supply, *J. Appl. Res. Technol. 2013, 11(2), 225-234*.

[8] Młotek M., Reda, Reszke E, Ulejczyk B, Krawczyk K., A gliding discharge reactor supplied by a ferro-resonance system for liquid toluene decomposition, *Chem. Eng. Res. Des. 2016, 111, 277-283*.

[9] Kalisiak, S.; Holub, M.; Jakubowski, T. Resonant inverter with output voltage pulse-phase-shift control for DBD plasma reactor supply. In Proceedings of the 13th European Conference on Power Electronics and Applications, Barcelona, Spain, 8–10 September 2009; pp. 1–9.

[10] Komarzyniec, G.; Aftyka, M. Cooperation of the Plasma Reactor with a Converter Power Supply Equipped with a Transformer with Special Design, *Energies* 2023, 16, 6825.

[11] Koliadimas, A.; Apostolopoulos, D.; Svarnas, P.; et al. Micro-Processor Based Modular Pulsed High Voltage Power Supply For Driving Atmospheric-Pressure DBD Plasmas. *IEEE Trans. Plasma Sci.* 2019, 47(3), 1621-1628.

Nanofluids Containing Electromagnetic Nanoparticles: The Review of Electrical Properties and Applications

Oleksandr Boiko, Henryka Danuta Stryczewska, Grzegorz Karol Komarzyniec

Lublin University of Technology, Department of Electrical Engineering and Superconductivity Technologies, Lublin, Poland
o.boiko@pollub.pl, h.stryczewska@pollub.pl, g.komarzyniec@pollub.pl

This paper presents a brief review of the electrical properties of nanofluids containing metallic, metallic oxide, graphene nanoparticles, as well as carbon nanotubes. The key factors, such as the alignment of magnetic nanoparticles (NPs), NPs size and shape, surfactants, temperature, base fluid, and NPs types, that demonstrate a significant impact on the electrical properties of nanofluids are analyzed. The applications of nanofluids in transformers (oil, cores, paper impregnation), PVT systems, and hydrogen production are described.

DOI
https://doi.org/10.18690/um.feri.4.2025.13

ISBN
978-961-286-986-1

Keywords:
nanofluids,
electromagnetic nanoparticles,
PTV systems,
hydrogen production,
electrical properties

University of Maribor Press

I General information

One of the most important factors determining the development of society, science, and technology is the efficiency of transmitting and storing energy in any form. Modern methods of energy transport and accumulation have reached such an advanced level that any improvement in their effectiveness is only possible by returning to fundamental research. Nanofluids (NFs), also known as suspensions of nanoparticles in a base fluid (BF), have the potential to become a breakthrough solution due to their significantly better properties, e.g., thermal, optical and magneto-electric, than the conventional macroscopic equivalents of their individual components. In addition, the configuration of nanofluids containing metallic NPs in the volume of a dielectric liquid are almost ideal structures for studying electrical transport, dielectric polarization, and relaxation processes because they allow the study of electric charge transfer both between individual metal NPs and between NPs and large conducting agglomerations.

The paper presents a brief discussion of the electrical properties of nanofluids containing metallic nanoparticles randomly dispersed in different types of BFs, while the greatest attention will be given to the electrical properties and application of NFs in the electrical engineering.

II Nanofluids manufacturing

All NF preparation methods can be divided into two groups: one-step and two-step. In the one-step method, the NPs are produced and dispersed into the BF during the single preparation process. For this purpose in the most cases the physical vapor deposition techniques such as evaporative deposition, laser ablation, magnetron sputtering, etc., that allow to produce uniform NPs are used. The direct evaporation and condensation of NPs are carried out in the BF.

The two-step method relies on first producing the NPs in the form of nanopowder and then directly mixing them with the BF. One of the main drawbacks of this method is NPs aggregation. That's why the common practice to solve the issue is using surfactants during mixing and ultrasonication after the NPs have been initially dispersed. The two-step method is considered to be the most economical and commercial type for large-scale NFs manufacturing. The majority of the different size nanopowders are commercially available and relatively inexpensive in comparison to single-step production.

III Electrical properties of nanofluids

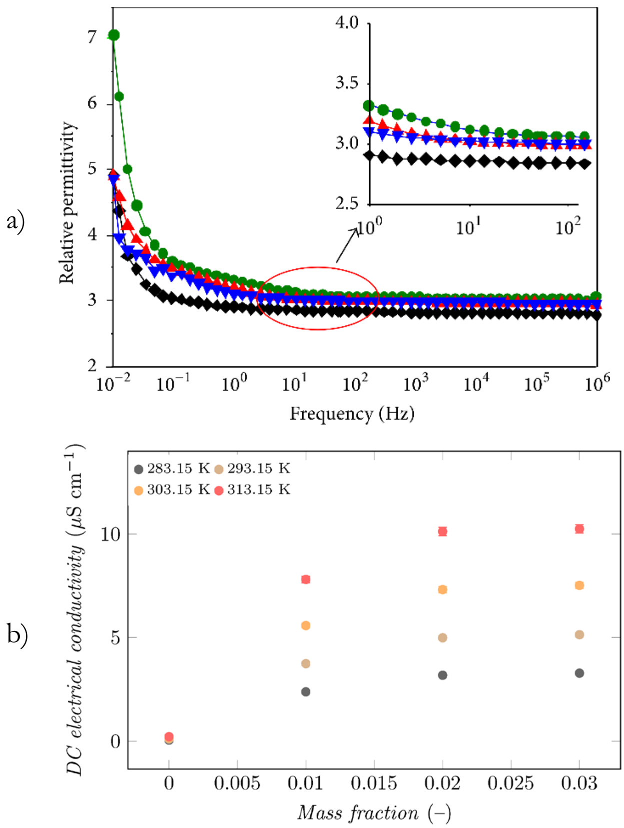

Figure 1: Impact of conductive filler concentration on: a) relative permittivity of vegetable oil-Fe_3O_4 NFs [2]**, and b) DC electrical conductivity of the $CaCO_3$-EG NFs** [3]

Taking into account that the most commonly used nanofillers are pure or/and (hybrid type) oxidized metals, graphene and CNTs, that are conductive ones, including them into the BFs, which normally are dielectric, significantly increases the electrical conductivity of the NF. The literature reports a lot of examples proving this fact. For example, mineral oil-based NFs contained Fe_3O_4 NPs; the resistivity of NF is about 10 times lower than in pure BF, and its dissipation factor rises while the concentration of Fe_3O_4 increases [1].

Another study of Fe_3O_4 NPs in vegetable oil showed that there is an impact of the nanofiller's particle size on the dielectric properties of the NFs [2].

Fig. 1.a demonstrates that an increase in NP size causes an increase in relative permittivity, especially for low frequencies.

Fig. 1.b presents the dependence of the DC conductivity of the $CaCO_3$-EG NFs on the nanofiller's mass fraction, which ranges from 0.01 to 0.03. It can be clearly seen that the conductivity increases with the increase in $CaCO_3$ concentration. The AC conductivity of NFs filled with $CaCO_3$ NPs and measured at different temperatures is more than 10 times higher in comparison to EG, as reported in [3].

The electrical properties of hybrid NFs are strictly dependent on the nanofiller's electric profiles. For example, in case of TiB_2/B_4C NFs based on propylene glycol, the electric conductivity of B_4C NF is at least about 70 times higher than the BF and about 63 times higher than mixed TiB_2 and B_4C NF. Such a situation can be associated with the differences in the conductivities and NP sizes of TiB_2 and B_4C, as it was also founded in EG-based SiO_2/Al_2O_3 hybrid NFs.

Factors that influence the electric conductivity of NFs are not only the types of nanofiller and BF, NPs mass fraction and size variations, but also sonication time (ST) during the production and surfactant/nanofiller mass ratio. ST increases significantly the conductivity when surfactant is added.

IV Selected applications of NFs in electrical engineering

The vast majority of articles describing the use of nanofluids in electrical or power systems concern transformer technologies. A lot of them relate to the improvement of transformer oil with the use of various metal oxides and graphene NPs. For example, a paper [4] reports the influence of the addition of TiO_2 (TO) and exfoliated hexagonal boron nitride (Eh-BN) NPs to the mineral oil (MO) as a base fluid on the AC breakdown voltage (ACBV), dielectric constant, and dielectric dissipation factor (DDF). It was found that nanofiller-contained oil demonstrates a way better ACBV (TO NF, approx. 46 kV, Eh-BN NF, approx. 75 kV) than pure MO (approx. 35 kV). The highest dielectric constant at 90°C was observed in Eh-BN NF, while the least was observed in pure MO. In the case of DDC, an inverse tendency was noted.

The exploitation life of a transformer depends largely on the oil-impregnated paper's insulating characteristics. Research [5] showed that the maximum AC breakdown voltage of Fe_3O_4 NF-impregnated paper is 9.1% higher than that of pure oil-impregnated ones. The situation is similar in the case of DC breakdown voltage; its value increases by about 10.0% in comparison to just oil impregnation. However, paper impregnation by NF with conductive NPs leads to an increase in electrical conductivity and dielectric loss afterwards, which should be taken into account when power equipment is designed.

NFs can also find applications in cooling systems for photovoltaic thermal (PVT) systems [6]. Egyptian scientists conducted research on traditional polycrystalline solar panels simultaneously under the same weather conditions for three experimental arrangements: the first module was a reference; the second was water-cooled; and the third module was cooled by a mixture of water and Al_2O_3 NPs (only 0.05% volume concentration). They examined the electrical conversion efficiency in relation to the coolant used. It was discovered that the use of active Al_2O_3 NF cooling causes the biggest drop in PVT operating temperature (about 22.83%), which is crucial for the PV panel performance. This fact corresponds to the obtaining of the highest value of electrical efficiency of about 12.94% by the third module, while the efficiencies of the second and first modules are 12.53% and 11.99%, respectively.

NFs are beginning to be increasingly investigated for hydrogen production in the PVT panels through the electrolysis process. During the electrolysis, the water splits into hydrogen and oxygen, while the first is separated and stored. Adding graphene or CNTs (i.e., carbon black with concentrations of 0.01 wt%~0.3 wt%) to water can significantly enhance hydrogen production, even up to 23.62% in comparison to pure water, as reported in [7].

V Conclussions

Nanofluids containing metallic, metal oxide, graphene, and carbon nanotube nanomaterials demonstrate great application potential in not only heat transfer technologies but also in systems, the main issues of which are the insulating properties of electric or power devices, cooling systems for PV panel efficiency enhancement, PV energy conversion, energy and hydrogen storage systems, etc. If the key factors of the thermal properties of NFs, such as the alignment of magnetic NPs, NP size and shape, pH of the base fluid, surfactants, solvents, and hydrogen bonding, temperature, base fluid, and NP types, are studied at an advanced level, the influence of these parameters on their electric properties and dielectric performance needs more in-depth investigation. This will allow for the creation of more energy-efficient technologies for sustainable energy development as well as technologies that are friendly to the natural environment and ecology.

References

[1] B.X. Du, X.L. Li, J. Li, "Thermal Conductivity and Dielectric Characteristics of Transformer Oil Filled with BN and Fe_3O_4 Nanoparticles", *IEEE Trans. Dielectr. Electr. Insul.*, vol. 22, No. 5, pp. 2530-2536, 2015.

[2] B.X. Du, J. Li, F. Wang, W. Yao, S. Yao, "Influence of Monodisperse Fe_3O_4 Nanoparticle Size on Electrical Properties of Vegetable Oil-Based Nanofluids", *J. Nanomater.*, vol. 2015, 560352, 2015.

[3] J. Traciak, D. Cabaleiro, J.P. Vallejo, J. Fal, "Thermophysical and Electrical Properties of Ethylene Glycol-Based Nanofluids Containing $CaCO_3$", *Processes*, vol. 12, No. 1, 172, 2024.

[4] M. Maharana, M.M. Bordeori, S.K. Nayak, N. Sahoo, "Nanofluid-based transformer oil: effect of ageing on thermal, electrical and physicochemical properties", *IET Sci. Meas. Technol.*, vol. 12, No. 7, pp. 878-885, 2018.

[5] B. Du, Q. Liu, Y. Shi, Y. Zhao, "The Effect of Fe_3O_4 Nanoparticle Size on Electrical Properties of Nanofluid Impregnated Paper and Trapping Analysis", *Molecules*, vol. 25, 3566, 2020.

[6] A. Ibrahim, M.R. Ramadan, A. Khallaf, M. Abdulhamid, "A comprehensive study for Al_2O_3 nanofluid cooling effect on the electrical and thermal properties of polycrystalline solar panels in outdoor conditions", *Environ. Sci. Pollut. Res.*, vol. 30, No. 49, pp. 106838-106859, 2023.

[7] S.H. Wei, B.V. Balakin, P. Kosinski, "Investigation of nanofluids in alkaline electrolytes: Stability, electrical properties, and hydrogen production", *J. Clean. Prod.*, vol. 414, pp. 137723, 2023.

SATURATION MODEL FOR PLASTIC-IRON COMPOSITES WITH LOW IRON CONCENTRATION

FLORIAN DREISHING, CHRISTIAN KREISCHER
Helmut Schmidt University / University of the Federal Armed Forces Hamburg, Chair for Electrical Machines and Drive Systems, Hamburg, Germany
florian.dreishing@hsu-hh.de, christian.kreischer@hsu-hh.de

This paper deals with the experimental magnetic characterization of composites made of a plastic base material and iron-powder. The iron concentration is kept very low to obtain a low permeable but mechanically soft material for the construction of a bendable linear motor. From the experimental characterization a saturation model is derived that can be used for a Finite Element Analysis to study, if the force-to-weight-ratio of the bendable linear motor can be increased using the plastic-iron composite.

DOI
https://doi.org/
10.18690/um.feri.4.2025.14

ISBN
978-961-286-986-1

Keywords:
plastic-iron-composite,
saturation model,
magnetic material model,
bendable linear motor,
magnetic characterization,
low iron concentration

University of Maribor Press

I Motivation

Bendable linear motors have advantages over conventional stiff linear motors in Soft-Robotic applications [1] or as drives for soft exoskeletons, also called exosuits [2, 3]. For these application fields a bendable linear motor is developed. The first prototype of the motor was designed as an ironless permanent magnet tubular linear synchronous motor (PMTLSM) [4]. The primary of the motor consists of ring coils connected to a three-phase winding that are casted into a tubular shell using a soft rubber. The secondary is constructed from NdFeB ring magnets mounted on a flexible rope. For the benefit of bendability ferromagnetic components were preliminarily excluded from the motor design. To increase the force-to-weight-ratio, a coating of the motor with a material that is mechanically soft on the one hand, but on the other hand magnetically conductive, is investigated. The new material should replace the part of the primary cast outside of the stator coils, so that the magnetic flux of the motor is concentrated there. Thus, the stray flux is reduced and the motor force increased.

In order to evaluate, if such a composite of a soft elastomer and iron powder is able to increase the motors force-to-weight ratio, an experimental characterization is conducted. Based on that, a saturation model is proposed and parametrized regarding the experimentally obtained data.

II Experimental Material Characterization

There are several possibilities to measure the BH-curve of magnetic materials, whereas the Epstein-method [5] or the Single-Sheet-tester (SST) [6] are the most widely used ones. Both are defined by international standards and well suited for the characterization of material samples in the shape of iron sheets. For the characterization of plastic-iron-composites however, it is very difficult to manufacture sheet-shaped specimen, so that another measurement method is applied. The method is defined by standard IEC 60404-6 [7], which is explicitly defined for sintered, pressed or casted materials. As defined in the standard, ring specimen of the plastic-iron composite are casted and two coils are wound on it – one for excitation and one for measuring the magnetic response.

The excitation coil is fed by a sinusoidal current $i(t)$ which is generated by a signal generator whose output is amplified by a linear amplifier. Due to the current an alternating magnetic field inside of the ring specimen is generated, thus the voltage $u(t)$ is induced in the measurement coil. From the measured current and voltage waveforms $i(t)$ and $u(t)$ the magnetic field intensity $H(t)$ and the magnetic flux density $B(t)$ are calculated based on the number of turns N_1 (measurement coil) and N_2 (excitation coil), the mean path length of the magnetic field l_m and the cross-section area of the ring specimen A with (1) and (2). The integration constant B_0 becomes zero in stationary state.

$$H(t) = \frac{N_2}{l_m} \cdot i(t) \tag{1}$$

$$B(t) = -\frac{1}{N_1 A} \int_0^t u(\tau)\, d\tau + B_0 \tag{2}$$

The measurement is done for frequencies between 50 Hz and 1000 Hz showing no significant frequency dependency of the magnetic properties. The followingly presented results were obtained for the measurement at 1000 Hz. The temperature is monitored during the experiment using a thermoelement and kept below 40 °C to eliminate thermal influences.

For the experiment four specimens are prepared with a hard epoxide resin as a base plastic material and iron powder with a purity of 99 % and an average particle size of 90 µm. The volumetric iron power concentration amounts to 4,75 % for specimen 1, 5.91 % for specimen 2, 6.86 % for specimen 3 and 7.94 % for specimen 4. The iron concentration is limited to these low values because the cast material becomes too viscous in the liquid state aggravating the cast process. Also, with increasing iron concentration it has to be assumed that the material becomes more brittle, so the bendability of the linear motor would be limited. The soft rubber, that is used in the linear motors cast, cannot be used for the experimental characterization since it is not able to withstand the mechanical stress during the coil winding process. After casting, the specimens are hardened and the coils are wound on them. In Fig. 1 the low-pass-filtered (100 kHz cut-off frequency) measured BH curve of specimen 1 is presented exemplarily.

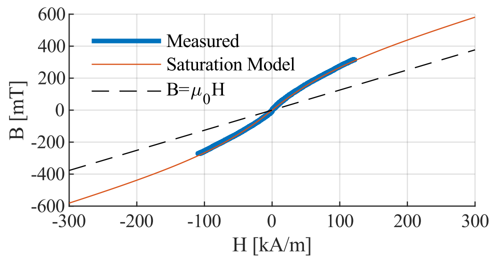

Figure 1: Measured BH curve of specimen 1

II Nonlinear Saturation Model

The measured curves show an increased slope for field intensities close to zero. With increasing field intensity, the slope of the curve decreases due to saturation and becomes parallel to the air field curve, which is a linear curve with the slope of μ_0. Hysteresis is present but does not have a significant impact on the curves.

To describe this behavior mathematically, the measured data are used to fit a nonlinear saturation model that can be used in a Finite Element Analysis of the bendable linear motor. In the literature approaches to represent BH-curves by analytic functions can be found [8–10]. However, they are mainly used to describe high permeable material with saturation flux densities typically above 1 T and accordingly high permeabilities. Because of that, these functions are not intended to be used to describe low permeable material as investigated in this study. To overcome this problem, a custom function defined by (1) to (3) is elaborated.

$$B(H) = B_1(H) + B_2(H) \tag{3}$$

$$B_1(H) = \mu_0 H \left[1 + k_b \left(\frac{\pi}{2} - \text{atan}(\alpha H) \cdot \text{sgn}(H)\right)\right] \tag{4}$$

$$B_2(H) = \frac{2b_0}{\pi} \text{atan}(\alpha H) \tag{5}$$

In this function, $B_1(H)$ is dominant for low values of H, where the slope of the curve is above the slope of the air curve μ_0. For increasing H the slope decreases, which is represented by the atan function with k_b controlling the maximum slope. The multiplication with the signum function guarantees that all BH data points are in the first or third quadrant. The function $B_2(H)$ is dominating for high values of H, where the slope decreases and the BH curves continue parallel to the air field curve. The difference between the air curve and the analyzed BH-curve for infinite H is controlled by the parameter b_0. The transition between the influence of the functions B_1 and B_2 is determined by the atan terms with the transition factor α. To demonstrate the fitting quality, the fitted function for the measurement of specimen 1 is presented in Fig. 1 together with the original measurement data.

The fitted curves for all four specimens are presented in Fig. 2 and the corresponding regression parameters are listed in Table I including the regressions root mean square error (RMSE) values.

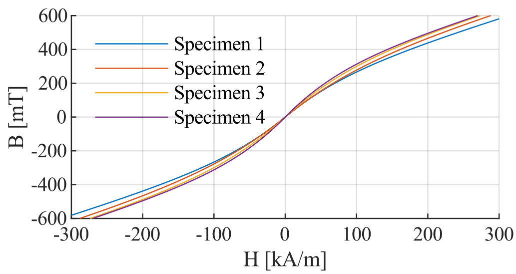

Figure 2: Fitted BH curves of the four specimens

The curves show that with increasing iron concentration the maximum slope of the curve increases slightly, thus the relative magnetic permeability μ_r of the material rises. However, the iron concentration in the range between 4,75 % to 7,94 % does not have a significant impact indicating a saturation of the small iron particles for low magnetic fields. The maximum μ_r can be obtained from the gradient of the BH curve [7] and amounts to about 3.5 for specimen 4.

III Conclusion

An experimental characterization based on international standard IEC 60404-6 of a plastic-iron composite with low iron concentration is performed. The analysis shows that relative permeabilities up to 3.5 are reached for a volumetric iron concentration of 7.94 %. The iron concentration of the analyzed specimens varying between 4.75 % and 7.94 % turns out to have a minor impact on the permeability indicating material saturation for low field intensities. The BH-curves are successfully used to parametrize a nonlinear saturation model for low permeable materials. In the next step, the found material models are used to re-optimize the bendable linear motor regarding the force-to-weight ratio using the obtained saturation models in a Finite Element Analysis.

Acknowledgment

Funded by dtec.bw – Digitalization and Technology Research Center of the Bundeswehr, Project: KIKU. dtec.bw is funded by the European Union NextGenerationEU.

References

[1] J. Kim, J. W. Kim, H. C. Kim, L. Zhai, H.-U. Ko, and R. M. Muthoka, "Review of Soft Actuator Materials," *Int. J. Precis. Eng. Manuf.*, vol. 20, no. 12, pp. 2221–2241, 2019, doi: 10.1007/s12541-019-00255-1.

[2] A. L. Kulasekera, R. B. Arumathanthri, D. S. Chathuranga, T. D. Lalitharatne, and R. C. Gopura, "A Low-Profile Vacuum Actuator: Towards a Sit-to-Stand Assist Exosuit," *2020 3rd IEEE International Conference on Soft Robotics (RoboSoft)*, pp. 110–115, 2020, doi: 10.1109/RoboSoft48309.2020.9115999.

[3] Z. Yao, C. Linnenberg, A. Argubi-Wollesen, R. Weidner, and J. P. Wulfsberg, "Biomimetic design of an ultra-compact and light-weight soft muscle glove," *Prod. Eng. Res. Devel.*, vol. 11, no. 6, pp. 731–743, 2017, doi: 10.1007/s11740-017-0767-y.

[4] F. Dreishing and C. Kreischer, "Optimization of Force-to-Weight Ratio of Ironless Tubular Linear Motors Using an Analytical Field Calculation Approach," *IEEE Trans. Magn.*, vol. 58, no. 9, pp. 1–4, 2022, doi: 10.1109/TMAG.2022.3166771.

[5] IEC, "IEC 60404-2 Magnetic materials - Part 2: Methods of measurement of the magnetic properties of electrical steel strip and sheet by means of an Epstein frame (IEC 60404-2:1996 + A1:2008)," 2009, doi: 10.31030/1495294.

[6] IEC, "IEC 60404-3 Magnetic materials - Part 3: Methods of measurement of the magnetic properties of electrical steel strip and sheet by means of a single sheet tester," 2021, doi: 10.31030/3268081.

[7] IEC, "IEC 60404-6: Magnetic materials - Part 6: Methods of measurement of the magnetic properties of magnetically soft metallic and powder materials at frequencies in the range 20 Hz to 100 kHz by the use of ring specimens," 2003.

[8] M. Mirzaei and P. Ripka, "Analytical Functions of Magnetization Curves for High Magnetic Permeability Materials," *IEEE Trans. Magn.*, vol. 54, no. 11, pp. 1–5, 2018, doi: 10.1109/TMAG.2018.2827932.

[9] V. Pricop, E. Helerea, and G. Scutaru, "Fitting magnetic hysteresis curves by using polynomials," in *2014 International Symposium on Fundamentals of Electrical Engineering (ISFEE)*, 2014, pp. 1–6.

[10] M. Jesenik, M. Beković, A. Hamler, and M. Trlep, "Analytical modelling of a magnetization curve obtained by the measurements of magnetic materials' properties using evolutionary algorithms," *Applied Soft Computing*, vol. 52, pp. 387–408, 2017, doi: 10.1016/j.asoc.2016.10.027.

DOI
https://doi.org/
10.18690/um.feri.4.2025.15

ISBN
978-961-286-986-1

WIRELESS POWER TRANSFER FOR UAV APPLICATIONS: A PARAMETRIC APPROACH FOR COUPLER DESIGN

MOHAMMED TERRAH,[1, 2, 3] MOSTAFA KAMEL SMAIL,[1, 2, 3] LIONEL PICHON,[1, 2] MOHAMED BENSETTI[1, 2]

[1] Université Paris-Saclay, Group of Electrical Engineering Paris GeePs, CentraleSupélec, Gif-sur-Yvette, France
mohammed.terrah@geeps.centralesupelec.fr,
mustafa-kamel.smail@geeps.centralesupelec.fr, lionel.pichon@geeps.centralesupelec.fr,
mohamed.bensetti@geeps.centralesupelec.fr
[2] Sorbonne Université, Group of Electrical Engineering Paris GeePs, Paris, France
mohammed.terrah@geeps.centralesupelec.fr,
mustafa-kamel.smail@geeps.centralesupelec.fr, lionel.pichon@geeps.centralesupelec.fr,
mohamed.bensetti@geeps.centralesupelec.fr
[3] Institut Polytechnique des Sciences Avancées IPSA, Ivry-sur-Seine, France
mohammed.terrah@geeps.centralesupelec.fr,
mustafa-kamel.smail@geeps.centralesupelec.fr

This paper explores Wireless Power Transfer (WPT) for Unmanned Aerial Vehicles (UAVs) battery recharging. To enhance the performance of WPT various parameters such as frequency, compensation topology, and the number of coils turns are examined. The objective is to identify the most suitable combination in terms of efficiency, weight, and feasibility. The aim of this procedure is to ensure a maximum WPT efficiency while having a minimum additional weight, thereby providing autonomous recharging processes, and extending the duration of the UAV mission. The analysis is carried out through simulations and measurements, taking into account the variations of the coupling factor due to potential lateral misalignment of the parallel coils.

Keywords:
wireless power transfer,
unmanned aerial vehicle,
compensation topology,
frequency,
efficiency,
FEM modelling,
misalignment

University of Maribor Press

I Introduction

UAVs have quickly become essential and versatile tools in today's world, driving innovation across numerous sectors. Among their most impactful applications is inspection [1]. Whether in infrastructure, energy, agriculture, or environmental monitoring, UAVs provide an efficient means of surveying areas that are difficult to access or pose safety risks. Outfitted with advanced technology, they can perform detailed inspections and deliver real-time data, enabling swift detection of potential issues, reducing operational costs, and enhancing safety for personnel. However, their limited battery life and the need for physical recharging often at the initial takeoff point pose constraints. These limitations significantly reduce the overall duration and effective range of their missions.

To extend the UAV's mission time and make the charging process more autonomous, this paper proposes equipping an inductive WPT system into the UAV. A number of research work have been carried out to solve this problem. In [1], researchers developed a WPT system for UAVs designed for transmission line inspection, achieving 100 W of power with an efficiency of 83%. In [2], a buck converter was added before the battery to boost charging current and reduce power losses, resulting in a 9% improvement in overall efficiency. Another approach in [3] introduced a 70 W WPT system, using landing gear made from aluminum tubing as the receiver. In [4], the authors investigated Series-Series (SS) and Series-Parallel (SP) compensation topologies to improve efficiency while reducing mass. Also, in [5], various coupler designs were tested to determine which offered the best performance for dynamic WPT.

New perspectives can be explored to enhance the current approaches. Studying the WPT efficiency as a function of various parameters is necessary to minimize the UAV downtime during recharging. Analyzing the size of the additional components may provide relevant insights, considering the potential significant increase in weight to the UAV and its potential impact on aerodynamic performances.

The goal of this paper is to design a lightweight WPT system that that targets maximum efficiency despite misalignment (d_x), which can occur during the landing of the UAV. To achieve this, a new parametric approach is proposed, considering key factors such as resonance frequency, compensation topology, and the number of coil turns. The study is divided into two main parts: modeling and simulation, followed by experimental validation. For the modeling phase, COMSOL Multiphysics is used to determine the electrical parameters of the magnetic coupler, while MATLAB Simulink is used to simulate the entire electrical circuit to evaluate the WPT system efficiency. The experimental validation focuses on the validation of the coupler's electrical parameters using a mechanical test bench, allowing for an in-depth analysis of the effects of misalignment.

II WPT system setup

The WPT system is conceived to be integrated into the DJI F450 drone model, which operates without landing skids (Fig. 1). Adding landing skids could increase the overall weight of the UAV and likely cause aerodynamic issues if not properly integrated [6].

The WPT system configuration, shown in Fig. 1, is composed of two main sections: the transmitting and receiving units. The transmitting (primary) side includes an AC power source, a transmitting coil T_x, and a compensation capacitor C_1. On the receiving (secondary) side, the system features a receiving coil R_x, a compensation capacitor C_2, a rectifier to convert AC to DC, and a battery. To enhance magnetic coupling and shield the onboard electronics, a ferrite plate is positioned above the receiving coil.

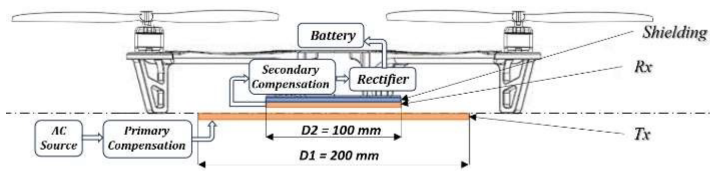

Figure 1: Representation of a WPT system for UAV

III WPT system analysis

For the electrical circuit, SP compensation topology is accounted (Fig. 2) due to its ability to provide high coupling efficiency while requiring fewer turns on the receiving coil [4]. The number of turns for the coils was determined through electromagnetic modeling, resulting in $N_1 = 8$ for the transmitting coil and $N_2 = 2$ for the receiving coil. This configuration achieves an efficiency of over 90% while keeping the receiving coil R_x lightweight.

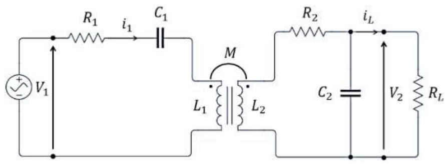

Figure 2:Electrical circuit of the WPT system

The electromagnetic modeling is carried out by Finite Element Method (FEM) as shown in Fig. 3 to obtain the self-inductances L_1, L_2 and the mutual inductance M as a function of misalignment. These values are then used in the electrical circuit to evaluate the system's power efficiency both at resonance and off-resonance, as the efficiency is directly affected by the coils misalignment.

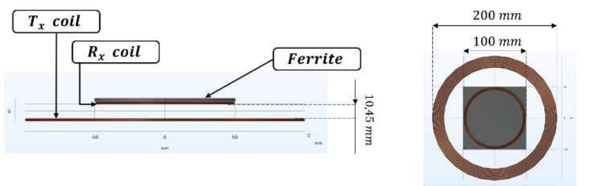

Figure 3: Coil geometries modeled by finite element method

To validate the model experimentally, the inductances $L1$, $L2$, and M are measured across different cases of misalignment d_x using an RLC meter at different frequencies (Fig. 4). The measured inductances are then compared to the results of the FEM model to assess accuracy.

a) Transmitter coil (8 turns coil)

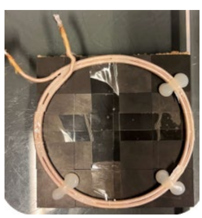

b) Receiving coil (2 turns coil) + ferrite

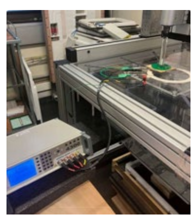

c) RLC meter measurements

Figure 4: Magnetic coupler prototype and validation

Following the validation of the FEM model, the maximum efficiency of the coupler (Fig. 5.b) and the values of capacitors C_1 and C_2 (Fig. 5.a) are assessed at perfect alignment for different operating frequencies.

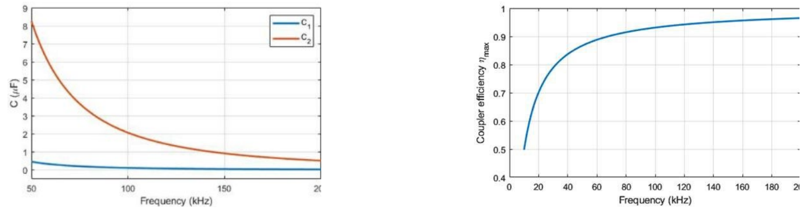

a) Compensation capacitors values versus frequency b) Coupler efficiency versus frequency

Figure 5: Results of the frequency study

Fig. 5a demonstrates that the value of the secondary compensation capacitor decreases significantly as the operating frequency increases. Meanwhile, Fig. 5b shows that maximum coupling efficiency improves with higher frequencies. To achieve at least 90 % efficiency, the system must operate at a minimum of 65 kHz. Selecting 150 kHz strikes a good balance, offering both high efficiency and a reduced capacitor size, an important consideration for onboard UAV applications.

SP compensation topology, and M varies with misalignment. Three different cases are identified :

1. $V_1 = 12$ V and C_1 adapted for each "d_x"
2. $V_1 = 12$ V, $i_1 \leq 10$A and C_1 adapted for each "d_x"
3. $P_1 \leq 120$ W ($V_1 = 12$ V, $i_1 \leq 10$A) & fixed capacitor C_1

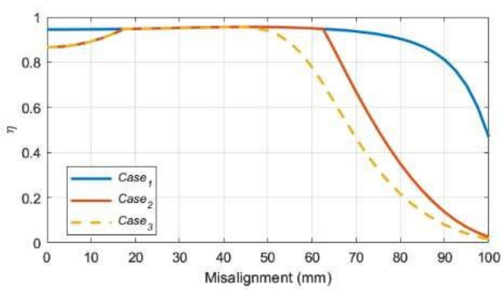

Figure 6: System efficiency versus misalignment

Fig. 6 shows the impact of constraints on the coupler efficiency. In Case 1, the efficiency remains above 80% up to $90\ mm$ misalignment. However, in Case 2, where the power source is limited to $120\ W$, the efficiency drops under 80% at $68\ mm$ of misalignment, which affect the receiving current. With a fixed primary capacitor C_1 (Case 3), the efficiency falls under 80% at approximately $60\ mm$ misalignment, leading to insufficient source power for wireless transfer. This prompts a further study of various compensation topologies to optimize the WPT system for the DJI F450.

IV Conclusion

This paper explores the impact of key parameters, specifically the frequency and compensation topology, on the performance of a WPT system. The results reveal a potential reduction in value (size) of the secondary capacitor's by increasing the frequency, leading to an optimal selection of the capacitor and frequency. However, constraints on the source power and the primary compensation capacitor may reduce the system's tolerance misalignment. These results require more studies on compensation topologies and coil turns.

Experimental validation supports the finite element model for optimizing the coupler dimensions, which will be described in the extended version. Additional factors, such as the weight of the receiving parts, will also be taken into account. The comprehensive analysis aims to determine optimal coupler dimensions, enhancing misalignment tolerance while maintaining high WPT efficiency.

References

[1] S. Duan, X. Lu, H. Wu, H. Zhang, Z. Zhang and G. Wang, "Unmanned Aerial Vehicle Wireless Power Transfer System for Long-Distance Transmission Line Patrol", in *2022 IEEE International Power Electronics and Application Conference and Exposition (PEAC)*, 2022.

[2] X. Gao, C. Liu, Y. Huang and Z. Song "Design of An UAV-Oriented Wireless Power Transfer System with Energy-Efficient Receiver" in *IECON 2020 The 46th Annual Conference of the IEEE Industrial Electronics Society*, 2020.

[3] T. Campi, S. Cruciani, F. Maradei and M. Feliziani "Innovative Design of Drone Landing Gear Used as a Receiving Coil in Wireless Charging Application" *Energies*, vol. 12, n° 18, 2019.

[4] T. Campi, F. Dionisi, S. Cruciani, V. De Santis, M. Feliziani and F. Maradei "Magnetic field levels in drones equipped with Wireless Power Transfer technology" in *Asia-Pacific International Symposium on Electromagnetic Compatibility (APEMC)*, 2016.

[5] K. Kadem, M. Bensetti, Y. Le Bihan, E. Labouré and M. Debbou, "Optimal Coupler Topology for Dynamic Wireless Power Transfer for Electric Vehicle" *Energies*, vol. 14, n° 13, janv. 2021.
[6] S. Pang, J. Xu, Z. Xie, J. Lu, H. Li, and X. Li and Lightweight UAV's Wireless Power Transfer System for Constant Current Charging Without Secondary Feedback Control" *IEEE Trans. Veh. Technol.*, vol. 72, n° 12, p. 15611-15621, 2023.

Performance Analysis of an IPMSM When Applying Heavy Rare-Earth-Free NdFeB PMs

Pavel Ogrizek, Mitja Garmut, Martin Petrun
University of Maribor, Faculty of Electrical Engineering and Computer Science, Institute of Electrical Power Engineering, Maribor, Slovenia
pavel.ogrizek@um.si, mitja.garmut@um.si, martin.petrun@um.si

The pursuit of greener technologies has prompted research into alternatives to heavy rare-earth (HRE) permanent magnet (PM) materials in electric machines, notably Interior Permanent Magnet Synchronous Machines (IPMSMs). This study examines how an IPMSM performs with HRE-free PMs, aiming to reduce environmental impact and costs linked to HRE material use. Using a two-dimensional transient Finite Element Method (2D-FEM) IPMSM model in Ansys Maxwell 2D, torque and power characteristics across different speed ranges for IPMSM models with two HRE-free PM materials and traditional HRE PMs were compared. Scaling law was implemented on HRE-free PM models to maintain the maximum torque.

DOI
https://doi.org/10.18690/um.feri.4.2025.16

ISBN
978-961-286-986-1

Keywords:
interior permanent magnet synchronous machine (ipmsm), permanent magnet (pm), heavy rare earth free (HRE-free), dy-free NdFeB, torque-speed envelope

University of Maribor Press

I Introduction

The contemporary household electrical devices, cordless power tools, and electric or hybrid vehicles are equipped with Interior Permanent Magnet Synchronous Machines (IPMSM) incorporating rare-earth permanent magnets (PMs). High efficiency and high torque density IPMSM typically use rare-earth NdFeB magnets. Such rare-earth PMs include elements like dysprosium (Dy) and terbium (Tb) to reduce the risk of permanent demagnetization at elevated temperatures. Nd is a light rare-earth element, while Dy and Tb are heavy rare-earth (HRE) elements [1]. HRE PMs deposits are unevenly distributed, and recent production has been concentrated in specific countries. Additionally, there is a growing need to minimize the usage of HRE elements due to the associated risks and costs of working with such scarce resources [2].

The main goal of this study was to replace HRE with HRE-free PMs in an IPMSM, analyze the machine's electromagnetic performance, and compare it with the baseline configuration. Another important aspect was scaling (downscaling or upscaling) the HRE-free design to maintain maximum torque and operation range compared to the baseline design.

II Theoretical background

A. IPMSM d-q model

Voltage equations of an IPMSM in the *d-q* rotating reference frame where the *d*-axis of the rotating reference frame is aligned to PM flux-linkage Ψ_{PM} are defined by (1) and (2):

$$u_{\mathrm{d}} = Ri_{\mathrm{d}} - \omega_{\mathrm{e}}\Psi_{\mathrm{q}} = Ri_{\mathrm{d}} - \omega_{\mathrm{e}}L_{\mathrm{q}}i_{\mathrm{q}} \tag{1}$$

$$u_{\mathrm{q}} = Ri_{\mathrm{q}} + \omega_{\mathrm{e}}\Psi_{\mathrm{d}} = Ri_{\mathrm{q}} + \omega_{\mathrm{e}}(\Psi_{\mathrm{PM}} + L_{\mathrm{d}}i_{\mathrm{d}}) \tag{2}$$

where i_{d}, i_{q} and $u_{\mathrm{d}}, u_{\mathrm{q}}$ are the *d-q* reference frame voltages and currents, R is the phase resistance and ω_{e} is the electrical angular velocity. Flux linkage in the *q*-axis due to the current excitation is defined as $\Psi_{\mathrm{q}} = L_{\mathrm{q}}i_{\mathrm{q}}$, where L_{q} is incremental inductance in the *q*-axis. The total flux linkage in the *d*-axis is defined as $\Psi_{\mathrm{d}} = \Psi_{\mathrm{PM}} +$

$L_d i_d$, where Ψ_{PM} is the flux-linkage due to the PM, and product of current and incremental inductance L_d in d-axis is flux-linkage in the *d*-axis due to current excitation.

The model's parameter estimation was performed based on a finite element method (FEM) model of the IPMSM implemented in Ansys Maxwell 2D software. The analysed IPMSM has 4 poles, tangential interior PMs and 3-phase, 6-slot stator with double-layer fractional-slot concentrated windings. We evaluated 5 different operation points (OPs), i.e., 5 different i_d and i_q combinations with a 2D transient FEM analysis. To evaluate the steady state performance, currents i_d, i_q and the electrical angular velocity ω_e were defined as the inputs within the numerical analysis. From the results, non-linear dependences $\Psi_d(i_d, i_q)$, $\Psi_q(i_d, i_q)$ and $T_{em}(i_d, i_q)$ were obtained for all OPs. Obtained variables depended on current combinations and were average values with respect to rotor position. Ψ_{PM} was calculated from no-load. Detailed workflow for parameter estimation was presented in [3]. Based on the obtained variables torque- and power vs speed characteristics were calculated with equations for maximum torque per ampere (MTPA) and field-weakening (FW) control, as presented in [4].

B. Evaluated PM materials

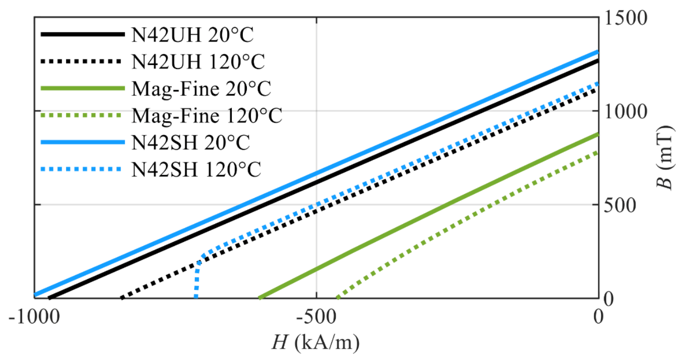

Figure 1: Demagnetization curves for evaluated PM materials at 20°C and 120°C.

Magnetic properties of three commercially available PM grades are presented in Figure *1* at 20°C and 120°C, respectively. The baseline design used HRE NdFeB (Arnold Magnetics N42UH). The applied HRE-free PMs for comparison were two compression-bonded NdFeB PMs: specifically, N42SH from JL MAG Rare-Earth Co. [5], and Mag-Fine MF18C from Aichi Corporation. Mag-Fine PMs use copper and aluminum for diffusion instead of Dy and Tb [6].

III Results

A comparison of obtained Torque- and power-versus-speed characteristic's for IPMSMs with the discussed PM materials are presented in Figure *2*. All characteristics were calculated with demagnetization curves for 120℃, which was assumed the steady state temperature of PMs. The analysis results showed that by replacing the N42UH PMs in the IPMSM model with HRE-free N42SH, the maximum torque in MTPA region is increased by 2%, meanwhile the use of Mag-Fine PMs decreases it by 28%. This is related to the remanent magnetic flux density and coercivity.

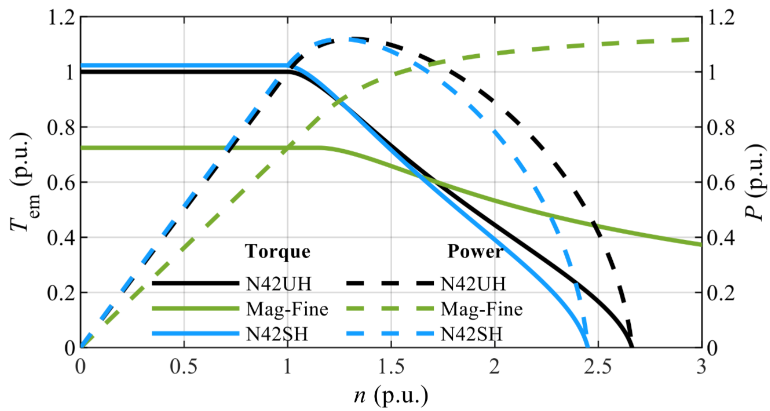

Figure 2: Comparison of torque- and power-vs-speed characteristic's for N42UH, Mag-Fine, and N42SH PMs in the IPMSM design at maximum current and temperature of PMs of 120℃.

It was observed that in FW region with Mag-Fine PMs in the model, significantly higher speeds and wide constant power range were achieved due to significantly lower remanent magnetic flux density. On the other hand, with N42SH and N42UH PMs, considerably lower speeds were reachable and the constant power ranges were significantly shorter. The obtained values of respective maximum speeds are collected in Table 1.

To maintain the baseline maximum torque with presented HRE-free PM materials, axial scaling was applied. Specifically, the IPMSM model featuring Mag-Fine PMs underwent upscaling through a 28% increment in stack length, while the variant employing N42SH PMs underwent downscaling via a 2% reduction in stack length. After scaling the targeted maximum torque was reached, as visible on Figure 3. In FW region the upscaled model with Mag-Fine PMs again reached significantly higher speeds compared to other two designs. Despite scaling, there has been a notable shift in the base speed of scaled model. In the case of Mag-Fine, the base speed point was shifted to the left and with a significant decrease in comparison to the baseline design. Conversely, for N42SH, the base speed was shifted slightly to the right with an increase relative to the baseline model. Base speed values for the all the designs are presented in Table 1.

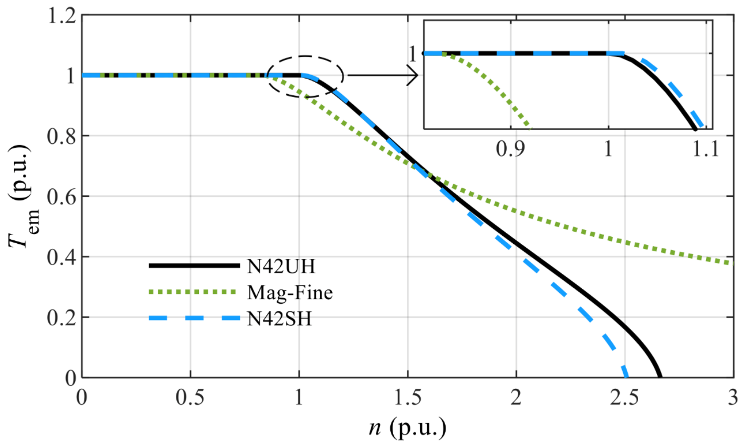

Figure 3: Comparison of torque-vs-speed characteristics for N42UH (baseline), upscaled Mag-Fine and downscaled N42SH based IPMSM designs at maximum current and temperature of PMs of 120℃.

Table 1: Comparison of base speed, maximum speed, and maximum torque.

IPMSM model	PM type	Base speed (p.u.)	Maximum speed (p.u.)	Maximum torque (p.u.)
Baseline	N42UH	1	2.66	1
	Mag-Fine	1.15	≫3	0.72
	N42SH	0.99	2.45	1.02
Axial scaled	Mag-Fine	0.83	≫3	1
	N42SH	1.02	2.51	1

IV Conclusion

Utilizing two HRE-free NdFeB, N42SH and Mag-Fine (MF18C) PMs as alternatives to the standard HRE NdFeB (N42UH) demonstrates the potential for enhancing or compromising IPMSM performance, contingent on the chosen PM material. A straightforward substitution with N42SH PMs led to increase in maximum torque within the MTPA region, with reduction of maximal operating speed. Conversely, the adoption of Mag-Fine PMs resulted in a torque reduction, albeit enabling significantly higher operational speeds suitable for high-speed applications. The results of axial scaling of the HRE-free NdFeB PM IPMSM models were:

- maintaining the same maximum torque as the baseline design,
- shifting the base speed, i.e. upscaling shifts the base speed point to the left side (a decrease), meanwhile downscaling shifts to the right (an increase) compared to the baseline base speed.

Moreover, there is a room for further optimization of IPMSM geometry with HRE-free PMs to maximize the maximum torque or speed. In the full paper a detailed analysis of back electromotive force, torque components versus load angle, and demagnetization risks will be presented.

References

[1] A. Al-Qarni and A. E.-. Refaie, "On Eliminating Heavy Rare-Earth PM Elements for High Power Density Traction Application Motors," in *2021 IEEE International Electric Machines & Drives Conference (IEMDC)*, 17-20 May 2021 2021, pp. 1-8, doi: 10.1109/IEMDC47953.2021.9449542.

[2] S. Soma, H. shimizu, E. Shirado, and S. Fujishiro, "Magnetic Form of Heavy Rare-Earth Free Motor for Hybrid Electric Vehicle," *SAE International Journal of Alternative Powertrains,* vol. 6, no. 2, pp. 290-297, 2017, doi: 10.4271/2017-01-1221.

[3] M. Garmut, S. Steentjes, and M. Petrun, "Parameter identification for MTPA control based on a nonlinear d-q dynamic IPMSM model," *COMPEL - The international journal for computation and mathematics in electrical and electronic engineering,* 2022-12-12 2022, doi: 10.1108/compel-09-2022-0331.

[4] S. Morimoto, M. Sanada, and Y. Takeda, "Wide-speed operation of interior permanent magnet synchronous motors with high-performance current regulator," *IEEE Transactions on Industry Applications,* vol. 30, no. 4, pp. 920-926, 1994-01-01 1994, doi: 10.1109/28.297908.

[5] L. JL MAG Rare-Earth Co. *Demagnetization curves, Heavy rare earth free technology*. [Online]. Available: https://www.jlmag.com.cn/en/about.php?cid=70

[6] A. S. Corporation. *Magfine technical datasheet*. [Online]. Available: https://www.aichi-steel.co.jp/_assets/dl/products_development/products/magFine_catalog.pdf

MODELLING OF NONLINEAR MAGNETIC PROPERTIES OF CURRENT TRANSFORMERS WITH PIECEWISE BÉZIER CURVES

DOI
https://doi.org/10.18690/um.feri.4.2025.17

ISBN
978-961-286-986-1

ERMIN RAHMANOVIĆ, MATEJ KERNDL,
BOŠTJAN POLAJŽER, JERNEJ ČERNELIČ, MARTIN PETRUN

University of Maribor, Faculty of Electrical Engineering and Computer Science,
Institute of Electrical Power Engineering, Maribor, Slovenia
ermin.rahmanovic@um.si, matej.kerndl@um.si, bostjan.polajzer@um.si,
jernej.cernelic@um.si, martin.petrun@um.si

The magnetic properties of iron cores of contemporary electrical devices, such as current transformers, are highly nonlinear. This work proposes a simple modelling method for the nonlinear magnetic properties using piecewise Bézier curves. An anhysteretic curve is modelled with three measured points. Two second order Bézier curves are joined to form a composite curve based on those measured points. The modelled curve was then compared with a measured anhysteretic curve of a commercial electrical steel sheet. The presented results confirm that this approach with piecewise Bézier curves shows high potential to model magnetization curves.

Keywords:
anhysteretic curve,
Bézier curve,
current transformer,
differential evolution,
magnetic properties

University of Maribor Press

I Introduction

Current transformers (CT) represent an important element of contemporary electrical power systems. Their distorted secondary quantities have a high influence on the performance of protection relays. Therefore, the precise modelling of the highly nonlinear magnetic properties of CT's iron cores represents a very important topic that needs to be addressed. A universal approach for description of the nonlinear magnetic properties is yet to be found [1]. For that reason, many different methods have been proposed. Those methods are mostly based on simple analytic functions [2]. Recently, an approach based on curves instead of functions was presented [3].

The approaches based on curves offer more flexibility to describe the nonlinear magnetic properties. Classical Bézier curves were already used to approximate magnetization curves with high accuracy [3]. The classical Bézier curves are used for simple smooth approximations. For the description of complex shapes, classical Bézier curves can be joined into a composite curve. This approach is called piecewise (PW) Bézier curves. An approach with PW Bézier curves was, e.g., successfully used to approximate the characteristics of a PV cell [4].

In most cases, the magnetic properties of CTs are represented using limited measured data. This work proposes a simple method to model the nonlinear magnetic curves using PW Bézier curves when limited data is available. The ability to model magnetization curves was in this preliminary study presented on a measured anhysteretic curve of a non-oriented (NO) electrical steel sheet. This method is based on three measured points, i.e., the origin of the coordinate system, the saturation point, and an intermediate point on the curve. To model the anhysteretic curve two Bézier curves of second order were connected to create the modelled curve.

This work is divided into four sections. Section II presents the proposed modelling method for nonlinear magnetization curves based on PW Bézier curves. Section III contains the preliminary results of the research. A measured anhysteretic curve of a NO steel sheet was compared with the modelled curve. Finally, the concluding remarks are given in Section IV.

II Modelling of magnetic properties with PieceWise Bézier Curves

A. Bézier curves

Classical Bézier curves are parametric curves defined by their order n, a set of $n+1$ control points $\mathrm{P_i}(x_\mathrm{i}, y_\mathrm{i})$ $(i = 0, \ldots, n)$ and parameter t ranging between 0 and 1 which are the start- and end-point of the curve respectively. Bézier curves are expressed by (1) [3]

$$B_*(t) = \sum_{i=0}^{n} b_{i,\mathrm{n}}(t) *_i\,,\ \ 0 \le t \le 1, \tag{1}$$

where $b_{i,\mathrm{n}}(t)$ are the Bernstein basis polynomials. Two polynomials must be calculated to define a Bézier curve, i.e., $B(t) = \left(B_\mathrm{x}(t), B_\mathrm{y}(t)\right)$. Therefore, $*$ is a placeholder for x and y depending on the control points' coordinates that are used. Bézier curves have two important properties that are exploited in engineering applications:

- Property 1: The first and last control points of a Bézier curve are interpolated by the curve.
- Property 2: The tangents formed by the first two and the last two control points define the initial and ending directions respectively [3].

B. Definition of variables

The anhysteretic curve was modelled using a PW Bézier curve in this paper. Two second order $(n = 2)$ Bézier curves were joined to create one final curve. Fig. 1 presents an arbitrary curve formed by connecting two second order Bézier curves, i.e., curve $B_1(t) = \left(B_{\mathrm{x},1}(t), B_{\mathrm{y},1}(t)\right)$ and curve $B_2(t) = \left(B_{\mathrm{x},2}(t), B_{\mathrm{y},2}(t)\right)$. The first curve $B_1(t)$ was defined by control points $\mathrm{P_0}, \mathrm{P_1}$, and $\mathrm{P_2}$ and the second curve $B_2(t)$ by control points $\mathrm{P_2}, \mathrm{P_3}$, and $\mathrm{P_4}$ as shown in Fig. 1.

We assumed that three measured points of the anhysteretic curve are known, i.e., the origin $(0,0)$, the saturation point, and an intermediate point on the curve. The values of control points $\mathrm{P_0}$, $\mathrm{P_4}$ and $\mathrm{P_2}$ were set to be equal to those three measured points respectively.

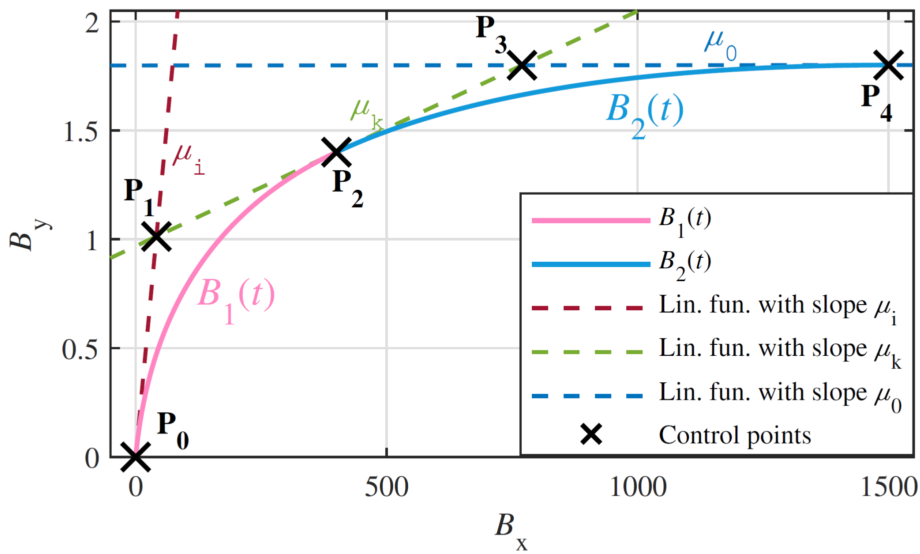

Figure 1: Definition of variables for the modelling approach with a PW Bézier curve.

The positions of the remaining control points P_1 and P_3 were uniquely defined by three permeabilities, i.e., μ_i, μ_k, and μ_0. The slope of the magnetization curve in the saturation region is known and equal to the relative permeability in vacuum, i.e., $\mu_0 = 4\pi \cdot 10^{-7}$ Vs/Am. The anhysteretic curve is the steepest in the low-field region. Consequently, the slope of the curve is here the largest and is defined with the initial permeability μ_i. Permeability μ_k defines the slope of the tangent line in control point P_2. Linear functions with arbitrary chosen μ_i and μ_k are presented in Fig. 1.

C. Parametric continuity rules

To ensure a curve with physical properties, the so-called parametric continuity rules were incorporated in the modelling process. They are defined as:

- C^0 continuity: curves intersect at one end point,
- C^1 continuity: equality of first derivatives at the intersecting point, and
- C^2 continuity: equality of second derivatives at the intersecting point.

Continuity C^0 was included by exploiting Property 1 where control point P_2 represented the last point of $B_1(t)$ and the first point of $B_2(t)$ (2)

$$B_1(t=1)=B_2(t=0)=\mathrm{P}_2\,. \tag{2}$$

Furthermore, continuity C^1 was considered by forcing control points $\mathrm{P}_1, \mathrm{P}_2$ and P_3 to lie on the same linear function with slope μ_k (3) as presented in Fig. 1.

$$\frac{\mathrm{d}B_{\mathrm{y},1}}{\mathrm{d}B_{\mathrm{x},1}}(t=1)=\frac{\mathrm{d}B_{\mathrm{y},2}}{\mathrm{d}B_{\mathrm{x},2}}(t=0)=\mu_\mathrm{k} \tag{3}$$

Continuity C^2 was used to express the objective function for the optimization process.

D. Methodology

Property 2 was exploited to prescribe the slope at the origin P_0 to μ_i and the slope at which the saturation point P_4 is reached to μ_0. This was achieved by placing P_1 to form a linear function with P_0 with slope μ_i. Similarly, P_3 was placed in such a way to form a linear function with P_4 with slope μ_0. Additionally, control points P_1, P_2 and P_3 must lie on the same linear function (here defined with μ_k) to obey the C^1 continuity rule. Finally, the intersection of linear functions with slopes μ_i and μ_k defined the position of P_1, and the intersection of linear functions with slopes μ_k and μ_0 defined the position of P_3. The determination of the positions of P_1 and P_3 is graphically depicted in Fig. 1.

However, permeabilities μ_i and μ_k are in most cases not known a priori. For this reason, we used the differential evolution (DE) algorithm to vary the values of slopes μ_i and μ_k and minimize the objective function (4).

$$F=\left(\frac{\mathrm{d}^2B_{\mathrm{y},1}}{\mathrm{d}B_{\mathrm{x},1}^2}(t=1,\mu_\mathrm{i},\mu_\mathrm{k})-\frac{\mathrm{d}^2B_{\mathrm{y},2}}{\mathrm{d}B_{\mathrm{x},2}^2}(t=0,\mu_\mathrm{i},\mu_\mathrm{k})\right)^2 \tag{4}$$

The objective function (4) is equal to the square of the difference between the second derivatives of the second order Bézier curves in the joint point P_2. The constraints during the calculation were:

- $\mu_\mathrm{i}>0$ and $\mu_\mathrm{k}>0$;

- $x_0 < x_1 < x_2$ and $x_2 < x_3 < x_4$;
- $y_0 < y_1 < y_2$ and $y_2 < y_3 < y_4$.

III Results

To validate the proposed modelling approach, we measured the major loop of a NO27 steel sheet. The anhysteretic curve was then calculated as the mean value between the ascending and descending branches of the major loop [3]. Fig. 2 presents the measured and modelled anhysteretic curve of the NO27 steel sheet.

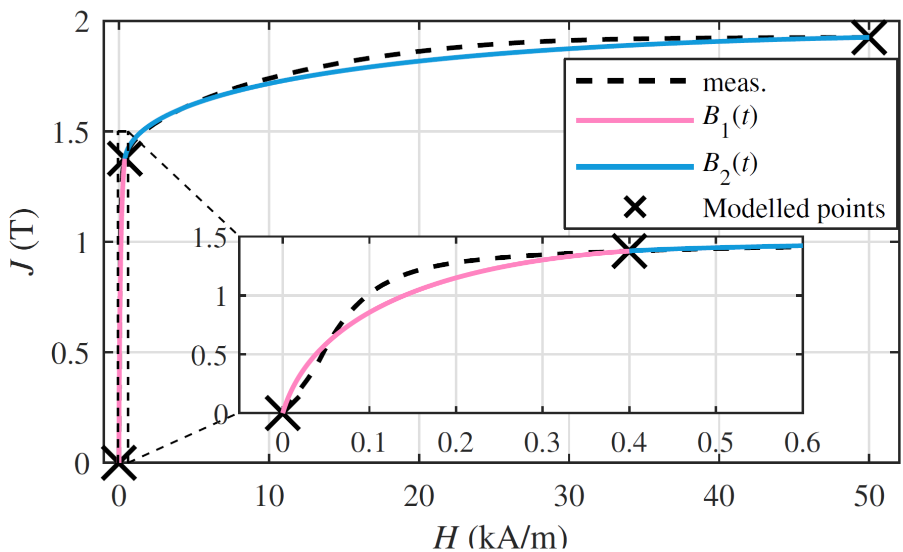

Figure 2: Modelled anhysteretic curve of a NO27 steel sheet with two joint second order Bézier curves.

The choice of the origin and saturation point is straightforward whereas the intermediate point was determined by varying its position along the measured curve. For each of those sets the PW Bézier curve was constructed and the NRMS error ε (Eq. (16) in [3]) was calculated. The set where the NRMS error was the lowest is plotted in Fig. 2, i.e., $\mathrm{P}_0(0,0)$, $\mathrm{P}_2(400,1.3765)$, $\mathrm{P}_4(50000,1.9252)$, $\mu_\mathrm{i} = 19753$, and $\mu_\mathrm{k} = 387.8757$.

The calculated NRMS deviation ε for the specific case in Fig. 2 was $\varepsilon = 0.015768$. Overall, the NRMS error ranged from 0.015768 to 0.0171494. This result is better than the results achieved by approximating measured data with most analytic functions presented in [3]. Compared with approximations with classical Bézier curves, the PW approach had slightly worse results than the sixth order Bézier curve [3]. This implies that the PW approach has high potential in the field of modelling magnetization curves when limited data is available.

IV Conclusions

Based on the presented results for a measured anhysteretic curve we concluded that the PW Bézier curves offer a simple way to model magnetization curves. This method needs less computational power than classical Bézier curves with comparable accuracy. However, the main challenge with Bézier curves remains to find a connection between the underlying physics and the parameter t.

The full paper will be extended with the application of the PW Bézier curves within a dynamic model of a CT with different iron cores. The PW Bézier curves will be validated on measurements performed on a CT.

References

[1] G. Mörée and M. Leijon, "Review of Hysteresis Models for Magnetic Materials," *Energies,* vol. 16, no. 9, p. 3908, 2023-05-05 2023, doi: 10.3390/en16093908.

[2] M. Jesenik, M. Mernik, and M. Trlep, "Determination of a Hysteresis Model Parameters with the Use of Different Evolutionary Methods for an Innovative Hysteresis Model," *Mathematics,* vol. 8, no. 2, p. 201, 2020-02-06 2020, doi: 10.3390/math8020201.

[3] E. Rahmanović and M. Petrun, "Analysis of Higher-Order Bézier Curves for Approximation of the Static Magnetic Properties of NO Electrical Steels," *Mathematics,* vol. 12, no. 3, p. 445, 2024-01-30 2024, doi: 10.3390/math12030445.

[4] R. Szabo and A. Gontean, "Photovoltaic Cell and Module I-V Characteristic Approximation Using Bézier Curves," *Applied Sciences,* vol. 8, no. 5, p. 655, 2018-04-24 2018, doi: 10.3390/app8050655.

Analysis of a High Power Density Axial Flux Permanent Magnet Synchronous Machine with Active Cooling

DOI
https://doi.org/10.18690/um.feri.4.2025.18

ISBN
978-961-286-986-1

Cezary Jędryczka,[1] Michał Mysiński,[1]
Wojciech Pietrowski,[1] Bartosz Ziegler,[2]
Tomasz Krakowski[2]

Poznan University of Technology, Institute of Electrical Engineering and Electronics, Poznan, Poland
cezary.jedryczka@put.poznan.pl, michal.mysinski@put.poznan.pl,
wojciech.pietrowski@put.poznan.pl
Poznan University of Technology, Institute of Thermal Energy, Poznan, Poland
bartosz.ziegler@put.poznan.pl, tomasz.krakowski@put.poznan.pl

The article discusses the synthesis and analysis of a high-power-density axial flux permanent magnet synchronous motor (AFPMSM) with active cooling. The research included electromagnetic and thermal analysis. In the electromagnetic part, numerical analysis employing 3D finite element method were carried out to analyze the influence of machine geometry and current density on the overall machine performance and the achieved power density. In the thermal approach, an active cooling concept with a cooling channel located in the winding was analyzed. Numerical thermodynamic models of the winding were developed, based on which the various approaches of the investigated solution were considered and their impact on improving the power density of the machine assessed.

Keywords:
high power density axial flux machine,
active cooling,
conjugate heat transfer,
aircraft propulsion,
finite element method

University of Maribor Press

I Introduction

Given the growing interest in electrically powered aircrafts and development of generally called electromobility, scientists and engineers from many centers around the world are seeking for electric motor structures of high power density [1]-[3]. In the research field on high power density electrical machines, the axial flux machines are getting more and more attention due to ability to achieve by optimization higher power density levels than in classical machines of radial direction of the main flux [4]. Core saturation and current density in the winding should be pointed out first as key limiting factors of increasing power density in electric machines.

The paper focuses on the synthesis and analysis of a high power density axial flux permanent magnet synchronous motor with active direct cooling of the winding designed to allow for high values of the current density. The machine has no ferromagnetic core in the stator. As is has been demonstrated among others in [4], axial flux motors (AFM) are characterized by increased torque values compared to radial flux motors. This is because the *AFM* structure provides a larger working area of the flux interacting between rotor and stator. In addition, the reduction of the machine's dimensions in the z-axis allows it to increase its dimensions in the radial direction, which also translates into increased torque.

In the design of electrical machines, one of the main factors determining power is the thermal efficiency of the system. The winding is selected to flow a certain amount of current through it. In addition, magnets are also sensitive to thermal loads that cause demagnetization. The best solution to overcome these problems is the use of active cooling systems. Active cooling systems allows for dissipating excessive heat; however, they are simultaneously source of design problems due to the increased weight and complexity of the powertrain system. In addition, application of active cooling systems in aircrafts needs of proper selection of coolants due to high variation of temperatures and pressures during on ground and in flight operation of the powertrain system.

II High power density axial flux machine structure

The structure of the proposed machine has been shown in Fig. 1. The electromagnetic circuit of the machine consists of stator coils forming a three phase concentrated winding, and two mechanically fixed rotors formed by axially magnetized arc segmented permanent magnets and back iron.

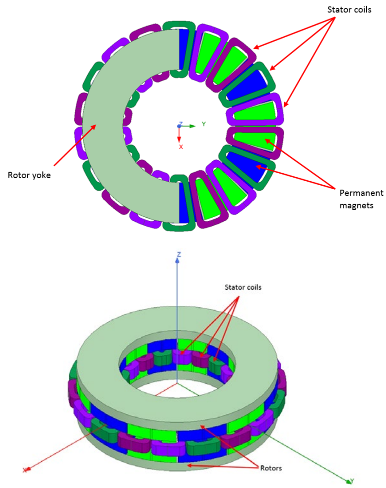

Figure 1: Structure of studied AFPMSM

The machine has been designed assuming typical power level required from the propulsion system of C-23b aircraft type, i.e. 200 kW, it has been assumed that machine will cooperate with reduction gear of the gear ratio about 10:1. Therefore machine rated speed has been assumed to be equal to about 20 000 rpm.

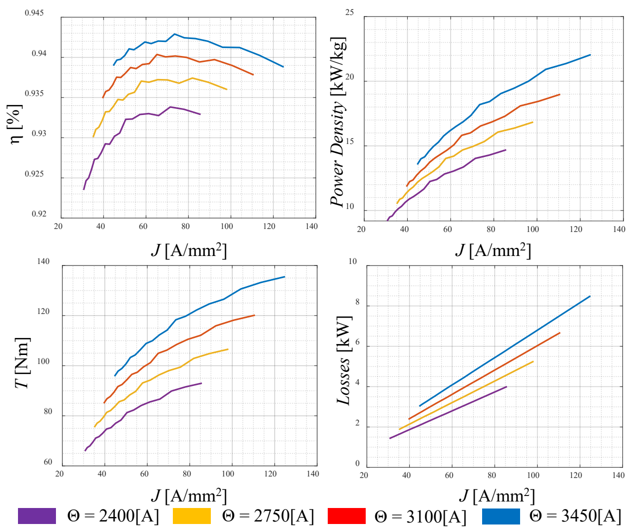

Figure 2: Determined torque and efficiency characteristics of the machine

The machine performance, in terms of achieve power density, has been determined by means of 3D finite element method. The derived characteristics of the output torque T, power density, losses and the determined efficiency η taking into account changes in current flow Θ are shown in Figure 2.

III Winding thermal management (thermal approach)

Traditionally, heat is dissipated from the windings through wire-to-wire conduction and air circulation across the winding surface. However, wire insulation and air gaps significantly limit the bulk winding conductivity, reducing it by two orders of magnitude compared to solid copper without insulation and air gaps. This form of cooling, known as passive cooling, operates without forced air flow (E.g. fans). The development of additive manufacturing (AM) technology, especially the use of metal 3D printers, offers significant potential to enhance cooling capacity by introducing cooling channels [5]. This is particularly effective with coolants possessing higher volumetric heat capacity than air. Certain dielectric liquids, such as some alcohols or hydrocarbons, demonstrate high heat dissipation potential when in direct contact with the conductor.

To demonstrate cooling capability, a conjugate heat transfer (CHT) analysis of ethanol flow through two channels parallel to the current flow was conducted. The channel cross-section equals 10% of the winding cross-section, which is formed by 7x7 mm. Various coolants, coolant flow rates, and current densities were analysed, with results presented in Figure 3. Heat from current flow was modelled as a constant volumetric heat source ranging from 10.8 to 172 MW/m^3, corresponding to 25 to 100 A/mm^2 at copper room temperature resistivity. After computations, the current density for a given volumetric heat source is corrected for the resistivity at the given temperature.

The CHT analysis offers the opportunity to evaluate the influence of mass flux and thermal properties of coolant on the average heat transfer coefficient for a given winding geometry. These results are depicted in Figure 4. Notably, water and ethanol exhibit significant potential in dissipating heat, as demonstrated by the outlier when compared to typical air cooling. The validity of using computational fluid dynamics (CFD) to assess heat transfer coefficients is clear when a high- quality computational mesh with fully resolved boundary layers is employed. This requires the centroid distance of the first layer of computational grid cells to have a y+ value of approximately 1 (non-dimensional wall distance). The accuracy of using y+ as a mesh metric is supported by comparing CFD results with experimental data in literature[6].

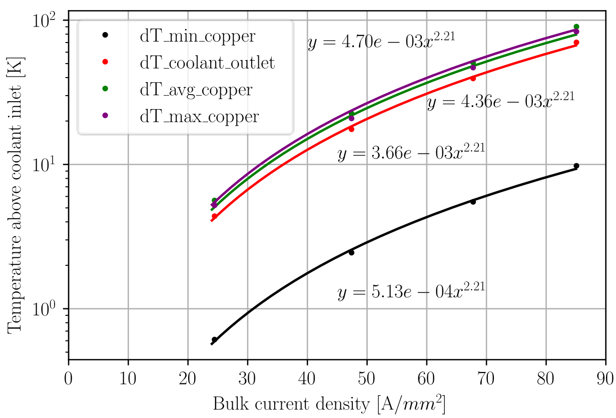

Figure 3: Temperature profile of winding and coolant for different current density

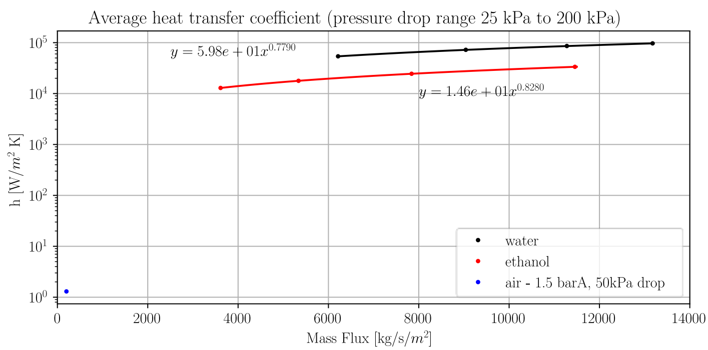

Figure 4: Average heat transfer coefficient in pressure drop range from 25 kPa to 200kPa

IV Conclusions

In summary, winding cooling analysis showcases the potential for improving cooling capacity through new technologies opportunities and coolant selection. The axial flux motor, coupled with additive manufacturing capabilities, presents a significant opportunity to enhance power density by improving cooling efficiency. The more detail about modeling techniques as well as detailed description of research will be presented and discussed during the conference and included in the full version of the paper.

References

[1] Rendón, M.A., Sánchez, R.C.D., Gallo, M.J., and Anzai, A.H., Aircraft hybrid-electric propulsion: development trends, challenges and opportunities, J. Control, Autom. Electr. Syst., 2021, vol. 32, no. 5, pp. 1244–1268. https://doi.org/10.1007/s40313-021-00740-x,

[2] Yoon, Xuan Yi, Martin J., Yuanshan Chen and Haran K., "A high-speed, high-frequency, air-core PM machine for aircraft application," 2016 IEEE Power and Energy Conference at Illinois (PECI), Urbana, IL, USA, 2016, pp. 1-4, doi: 10.1109/PECI.2016.7459221,

[3] J. Z. Bird, "A Review of Electric Aircraft Drivetrain Motor Technology," in IEEE Transactions on Magnetics, vol. 58, no. 2, pp. 1-8, Feb. 2022, Art no. 8201108, doi: 10.1109/TMAG.2021.3081719,

[4] Surong Huang, Jian Luo, Leonardi F. and Lipo T. A., "A comparison of power density for axial flux machines based on general purpose sizing equations," in IEEE Transactions on Energy Conversion, vol. 14, no. 2, pp. 185-192, June 1999, doi: 10.1109/60.766982.

[5] Thabuis, X. Ren and Y. Perriard, "Enhanced Electric Motors Using Multi-Functional 3D Printed Winding With Integrated Heat Sinks" *IEEE Transactions on Energy Conversion*, vol. 38, No. 2, pp. 849-858, 2023,

[6] Hettegger M., Streibel B., Biro O. and Neudorfer H., "Measurements and Simulations of the Convective Heat Transfer Coefficients on the End Windings of an Electrical Machine" *IEEE Transactions on Industrial Electronics,* vol. 59, No.5, pp. 2299-2307, 2012,

Comparison of Simple Modeling Approaches of the Nonlinear Magnetic Properties of a Single-Phase Transformer

Jelena Stupar, Ermin Rahmanović,
Gorazd Štumberger

University of Maribor, Faculty of Electrical Engineering and Computer Science,
Institute of Electrical Power Engineering, Maribor, Slovenia
jelena.stupar@um.si, ermin.rahmanovic@um.si, gorazd.stumberger@um.si

This paper analyses the potential of several analytic functions to describe the nonlinear magnetic properties of a single phase transformer's iron core. A dynamic model of a single phase transformer with analytic functions describing magnetic properties was prepared in Simulink and used to calculate the inrush currents. The parameters of the chosen analytic functions were determined using differential evolution by minimizing the deviation between measured and calculated inrush currents in the time and frequency domains simultaneously. The ranking of the applied analytic functions based on the lowest deviation between measured and calculated currents is presented.

DOI
https://doi.org/
10.18690/um.feri.4.2025.19

ISBN
978-961-286-986-1

Keywords:
single-phase transformer,
nonlinear magnetic
properties,
analytic functions,
differential evolution,
inrush currents

University of Maribor Press

I Introduction

Transformers are commonly used devices in power systems and electronics applications. Because of their widespread use, it is essential to reliably model the transformer's behavior. The most complex task in the modeling approach is the description of the nonlinear magnetic properties of the iron core.

There are many different methods to represent the nonlinear magnetic properties of the iron core. A detailed description of the nonlinear magnetic properties requires the implementation of a hysteresis model, e.g., the well-known Preisach, Jiles-Atherton (JA) or Zirka-Moroz hysteresis models [1]. The implementation of such models is usually not straightforward, and non-standardized measurements are necessary for the parameter identification process in some cases. For this reason, researchers often use simplified descriptions of the iron cores of electrical machines. The simplest approach to model the nonlinear magnetic properties is using the single-valued history-independent anhysteretic curve. The anhysteretic curve is the mean value between the descending and ascending branches of the hysteresis major loop and represents the input for several finite-element tools.

In this research, we focused on a simple representation of the nonlinear magnetic properties of a transformer's iron core with analytic functions, e.g., the sigmoid functions. This approach is equal to the representation of the nonlinear magnetic properties with an anhysteretic curve. Recently, sigmoid functions were successfully used to model and approximate various magnetization curves [2], [3]. Their main feature is that they describe a curve in the shape of the letter »S«. In addition to sigmoid functions, we included a sum of exponential functions proposed in [4] in the analysis.

This paper contains five sections. In Section II a dynamic model of a single-phase transformer is described. Section III contains information about the methodology used in this research, i.e., the description of chosen analytic functions, determination of their parameters and a method for the evaluation of the obtained results. Results and concluding remarks are presented in Section IV and Section V, respectively.

II Single-phase transformer

Voltage balances in the primary and secondary windings are given by Eqs. (1) and (2), which represents the dynamic model of a single-phase transformer [5].

$$u_1 = i_1 R_1 + L_{\sigma 1}\frac{\mathrm{d}i_1}{\mathrm{d}t} + N_1 A\frac{\mathrm{d}B}{\mathrm{d}H}\left(\frac{N_1}{l}\frac{\mathrm{d}i_1}{\mathrm{d}t} + \frac{N_2}{l}\frac{\mathrm{d}i_2}{\mathrm{d}t}\right) \quad (1)$$

$$u_2 = i_2 R_2 + L_{\sigma 2}\frac{\mathrm{d}i_2}{\mathrm{d}t} + N_2 A\frac{\mathrm{d}B}{\mathrm{d}H}\left(\frac{N_1}{l}\frac{\mathrm{d}i_1}{\mathrm{d}t} + \frac{N_2}{l}\frac{\mathrm{d}i_2}{\mathrm{d}t}\right) \quad (2)$$

In Eqs. (1) and (2) u_1 and u_2 are the primary and secondary voltages, i_1 and i_2 are the primary and secondary currents. The magnetic nonlinear properties of the transformer's iron core are described by the term $\mathrm{d}B/\mathrm{d}H$, where B is the magnetic field density and H is the magnetic field strength. The definitions of the remaining parameters and their values for the transformer used in the analysis are given in Table 1.

Table 1: Single-phase transformer

Parameter	Value
Resistance of the primary winding R_1 (Ω)	11
Resistance of the secondary winding R_2 (Ω)	141.8
Leakage inductance of the primary winding $L_{\sigma 1}$ (mH)	32.97
Leakage inductance of the secondary winding $L_{\sigma 2}$ (mH)	32.97
Number of turns of the primary winding N_1	452
Number of turns of the secondary winding N_2	1722
Cross section area of the iron core A (m^2)	0.0012
Mean path length of the magnetic flux l (m)	0.308

III Methodology

A. Analytic functions

The magnetic properties $\mathrm{d}B/\mathrm{d}H$ are modeled using analytic functions. The analytic functions describe the nonlinear magnetic properties as a $B(H)$ relation. Such a choice is not coincidental, since these functions enable a straightforward calculation of their derivative, i.e., the derivative $\mathrm{d}B/\mathrm{d}H$. We decided to analyze the Langevin, Gompertz, Hyperbolic tangent, Algebraic, Logistic, Sigmoid, Elliot functions [2] and a sum of exponential functions (labeled exponential function) [4]. The derivatives of chosen analytic functions $\mathrm{d}B/\mathrm{d}H$ can be implemented directly in the dynamic model of a single-phase transformer.

B. Determination of function parameters

We used the Differential Evolution (DE) algorithm for the calculation of the parameters P_1–P_5 of the derivatives of sigmoid functions [2] and the parameters $\mathrm{C}_1, \mathrm{D}_1, \mathrm{C}_2, \mathrm{D}_2$ of the derivative of the exponential function [4]. The number of population members in the DE algorithm was set to 20, the mutation factor was 0.7, the crossover factor 0.5 and number of iterations 200. In each iteration, we solved Eqs. (1) and (2) using Matlab/Simulink and obtained the primary and secondary voltages and currents of the transformer.

The goal of the analysis was to achieve the smallest difference between the measured and the calculated current by the transformer model. We minimized the deviations from measurements and calculations in both, the time and frequency domain. Therefore, the objective function q (3) is the sum of two distinct parts, i.e., the mean square difference between calculated i_1 and measured $i_{1,\mathrm{m}}$ currents q_t and the mean square differences between the individual harmonic components q_f [4].

$$q = q_\mathrm{t} + q_\mathrm{f} \tag{3}$$

Equations for q_t and q_f are omitted due to the lack of space. They are thoroughly described in [4].

C. Evaluation of results

To evaluate the goodness of fit of the calculated currents, we applied the measure ε [5], defined by Eq. (4).

$$\varepsilon = \sqrt{\sum_{k=1}^{N} \frac{\left(i_{1,\mathrm{k}} - i_{1,\mathrm{m,k}}\right)^2}{N}} \tag{4}$$

In Eq. (4), $i_{1,\mathrm{k}}$ is the calculated primary current, $i_{1,\mathrm{m,k}}$ is the measured primary current of the transformer, N is the number of measured samples of $i_{1,\mathrm{m}}$ and $k = 1,2, \ldots, N$.

IV Results

Measurements were conducted on a single-phase transformer with parameters given in Table 1. The inrush current $i_{1,m}$ obtained in the no-load test was crucial for the analysis of the potential of analytic functions. The frequency of the primary and secondary quantities was 50 Hz. The measured primary voltage $u_{1,m}$ and measured primary current $i_{1,m}$ are shown in Fig. 1a) and b), respectively. The measured primary voltage $u_{1,m}$ in Fig. 1a) was used as the input for the transformer's dynamic model. We calculated the parameters of the derivatives of the analytic functions and evaluated their ability to describe the inrush current of a single-phase transformer based on the deviation from $i_{1,m}$.

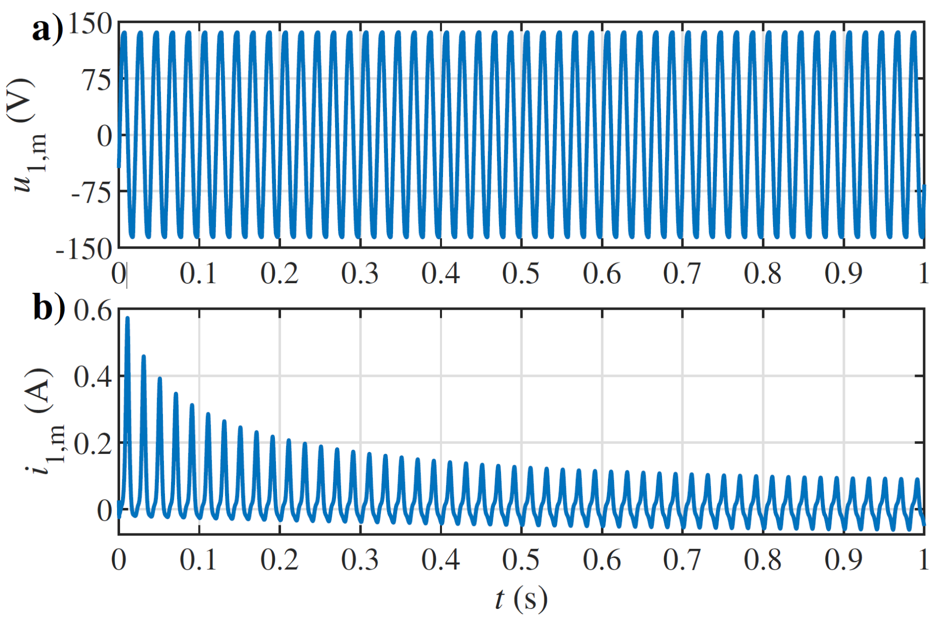

Figure 1: a) Measured primary voltage $u_{1,m}$ and b) measured primary current $i_{1,m}$.

The current calculated by applying the Logistic function has the lowest deviation from the measured current $i_{1,m}$, as it is shown in Fig. 2b) and c). Therefore, we plotted the whole calculated current by applying the Logistic function separately in Fig. 2a). Further, this result was supported by calculating the measure ε given in Table 1. The current calculated by using the Logistic function achieved the lowest value of ε. Second best fit of the current was achieved w ith the Hyperbolic tangent function. Other analyzed functions have their shortcomings in the description of the inrush current of the transformer. Currents calculated with the Langevin and Gompertz functions have the highest deviation from the measured current. The Algebraic and Sigmoid functions are suitable for the description of the steady state of the current. The Elliot and exponential function have the appropriate shape of the current, but the amplitude is not accurate.

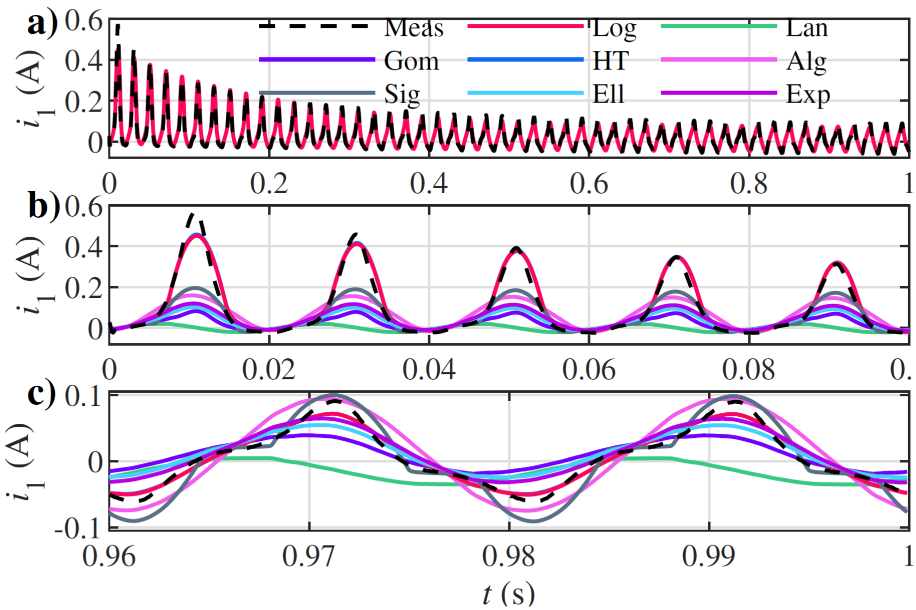

Figure 2: a) Measured current $i_{1,\mathrm{m}}$ and current i_1 calculated with the Logistic function, b) $i_{1,\mathrm{m}}$ and i_1 of all analytic functions in the first five periods and c) $i_{1,\mathrm{m}}$ and i_1 of all analytic functions in the steady state.

Table 2: Values of ε

Analytic function	Measure ε
Logistic	0.0134
Hyperbolic tangent	0.0135
Sigmoid	0.0324
Algebraic	0.0418
Exponential	0.0458
Elliot	0.0503
Gompertz	0.0589
Langevin	0.0810

V Conclusions

Based on the performed analysis, we concluded that simple analytic functions can adequately describe the nonlinear magnetic properties in the case of an inrush current of a single-phase transformer. We identified the Logistic and Hyperbolic tangent functions as the most suitable analytic functions. The final presentation will be extended with the implementation of the JA hysteresis model in the transformer's dynamic model. The results of the JA model will then be compared with results obtained with the analytic functions.

References

[1] G. Mörée and M. Leijon, "Review of Hysteresis Models for Magnetic Materials," *Energies*, vol. 16, no. 9. MDPI, May 01, 2023. doi: 10.3390/en16093908.

[2] M. Jesenik, M. Mernik, and M. Trlep, "Determination of a hysteresis model parameters with the use of different evolutionary methods for an innovative hysteresis model," *Mathematics*, vol. 8, no. 2, Feb. 2020, doi: 10.3390/math8020201.

[3] E. Rahmanović and M. Petrun, "Analysis of Higher-Order Bézier Curves for Approximation of the Static Magnetic Properties of NO Electrical Steels," *Mathematics*, vol. 12, no. 3, Feb. 2024, doi: 10.3390/math12030445.

[4] G. Štumberger, S. Seme, B. Štumberger, B. Polajžer, and D. Dolinar, "Determining magnetically nonlinear characteristics of transformers and iron core inductors by differential evolution," *IEEE Trans Magn*, vol. 44, no. 6, pp. 1570–1573, Jun. 2008, doi: 10.1109/TMAG.2007.915878.

[5] M. Toman, G. Štumberger, and D. Dolinar, "Parameter identification of the Jiles-Atherton hysteresis model using differential evolution," *IEEE Trans Magn*, vol. 44, no. 6, pp. 1098–1101, Jun. 2008, doi: 10.1109/TMAG.2007.915947.

DOI
https://doi.org/
10.18690/um.feri.4.2025.20

ISBN
978-961-286-986-1

OVERVIEW OF DFIG-BASED WIND TURBINE SYSTEMS IN EUROPE

SEYED ALI SEYED-BOUZARI,[1] ANNETTE MUETZE,[1]
JOHANN PETER BACHER,[1] BOŠTJAN POLAJŽER[2]

[1] Graz University of Technology, Institute of Electric Drives and Power Electronic Systems, Graz, Austria,
saeidbouzari@yahoo.com, muetze@tugraz.at, johann.bacher@tugraz.at
[2] University of Maribor, Faculty of Electrical Engineering and Computer Science, Institute of Electrical Power Engineering, Maribor, Slovenia
bostjan.polajzer@um.si

Doubly-Fed Induction Generators (DFIGs) when used in Wind Turbine Systems (WTS), are typically sized within the 1.5 to 6 MW power range. Currently, DFIG-based systems hold a significant position in the global market, and they are expected to experience substantial growth by 2030.

Keywords:
wind turbine systems (WTSs),
WTS developments, doubly-fed induction,
generators (DFIGs),
DFIG-based WTSs,
DFIG characteristics

University of Maribor Press

I Introduction

According to Eurostat's 2023 electricity production, consumption, and market overview [1], the shares of net electrical energy generation for the EU in 2021 were: Combustible fuels 41.9 %, nuclear 25 %, wind 13.7 %, hydro 13.3 %, solar 5.8 %, and others 0.3 %. Comparing these statistics with those of 2011 reveals that Renewable Energy Sources (RESs) have experienced significant growth from 2011 to 2021, rising from 19.5 % to 33 %. Furthermore, the Ten-Year Network Development Plan (TYNDP) 2020 [2], a joint scenario report by ENTSO-E and ENTSOG, predicts that wind will cover 29 % of the electricity generation by 2030, and this number is expected to increase to 41 % by 2040. However, RESs generally have variable and uncertain natures. They also pose challenges to the stability and reliability of the grids [3]. Therefore, wind and pumped-hydro power plants mostly use variable speed generators (VSGs) that are connected to the grid mainly through Power Converters (PCs) to allow for voltage and frequency control. This abstract focuses on the most commonly used and commercially available features of DFIG-based systems when used as VSGs in WTSs.

II Wind Turbine system developments

European Wind Industry: Europe has always been a pioneer in moving towards clean energy. According to a report, the Wind Energy in Europe, published in 2023 [4], a total of 255 GW of wind power capacity was installed in Europe by 2022, 88 % of this is onshore and 12 % is offshore. Germany maintains Europe's largest installed wind power fleet, with over 66 GW of installed capacity. Alongside Germany, Spain (30 GW), the UK (29 GW), France (21 GW), Sweden (15 GW), and Turkey (12 GW) collectively contribute to two-thirds of the total installed capacity in Europe. Exact statistics on the contribution of different generator types may not be available, but clearly, DFIGs hold a market share of approximately 50 % for electricity production within WTSs. The most important European manufacturers that supply DFIG products are ABB, VEM Motors, and Vestas. Additionally, some non-European companies support the European market, such as CRRC, GE, Shandong Huali Motor, and TD Power Systems [5].

Manufacturing Evolution: Until around 1998, most manufacturers constructed Constant-Speed Systems (CSSs) with a power range below 1.5 MW. They utilized a three-stage gearbox and a standard squirrel-cage induction generator directly connected to the grid. After 1998, many manufacturers began producing Variable-Speed Systems (VSSs) with DFIGs to meet the new grid requirements. Around 2005, several alternative VSSs were proposed. In these systems, BrushLess (BL) generators come with a gearbox and a fully rated PC [6]. In the meantime, due to the decreasing costs of power electronics components and permanent magnet materials, Direct-Drive (DD) systems have been developed [7]. In these systems, permanent magnet or electrically-excited synchronous generators are combined with a fully rated PC on the stator side, and the gearbox is eliminated to reduce the likelihood of failures and maintenance problems.

Comparison of Different Wind Turbine Systems: Table I, as presented in [6] and further amended here, provides an overview of the strengths and weaknesses of the DFIG-based systems compared to other WTSs. VSSs enable operation across a wider range of wind speeds to capture greater kinetic energy from the wind. Generally, the high-speed generators are slightly more efficient than the low-speed DD generators, although gearbox losses cannot be ignored. Additionally, the partially rated PC used in DFIG-based systems has lower losses than the fully rated PC used in DD and BL systems.

Table 1: Comparison of different wind turbine systems Strengths (+), Neutral (0), Weaknesses (-)

		Wind Turbine Systems			
		CS	DFIG	BL	DD
Energy Yield	Generator Type	+	+	+/-	-
	Mechanical Components	-	-	-	+
	Power Converter	+	0	-	-
Reliability and Maintenance	Complexity	+	-	-	-
	Mechanical Loads	-	+	+	+
	Brushes	+	-	+	+/-
	Gearbox	-	-	-	+
Voltage & Frequency Control		-	0	+	+
Operation at Different Frequencies		-	-	+	+
Grid Faults	Fault Detection	+	-	-	-
	Fault Ride-Through	+	0	+	+
	Post-Fault Recovery	-	0	+	+
Cost, Size and Weight		+	0	-	-

The reliability and maintenance of a WTS are affected by different factors such as complexity, mechanical loads, brushes, and gearbox. VSSs with more components are generally less reliable than simpler CSSs. On the other hand, VSSs primarily use pitch control [8], which involves adjusting the blades' angle to regulate the mechanical load on their components during high-speed winds. Brushes in DFIG-based systems require regular replacement, and gearbox failures may occur. These drawbacks have limited their offshore applications, where maintenance costs are considerably high.

Considerations regarding grid faults include fault detection, fault ride-through, and post-fault recovery. Traditionally, a WTS could be disconnected during a fault and reconnected after the fault has been cleared. However, as per new grid requirements, it must remain connected during faults [9]. Grid faults are typically identified by large fault currents. PCs used in VSSs do not permit currents larger than 10 to 20 % of their rating, which affects fault detection. A standard DFIG-based system with a partially rated PC may not fulfil the grid fault ride-through requirements. Additional equipment is required to ensure compliance. Potential solutions include advanced control strategies, implementing a crowbar short-circuiting the rotor windings, and sometimes utilizing additional resistances [6]. The contribution of the DFIG-based system to supply active and reactive power for frequency and voltage recovery after the fault depends on the solution chosen.

Generally, DFIG-based systems have simple and robust constructions and smaller sizes, weights, and costs compared to other categories with fully rated PCs.

III DFIG-based system characteristics

In a DFIG, the stator winding is directly connected to the grid and operates at nearly constant voltage and frequency. The rotor winding is supplied by a partially rated PC, which provides the machine with variable voltage and frequency. Control over the torque, active power, and reactive power through the rotor and stator is achieved by adjusting the amplitude, frequency, and phase of the voltage applied to the rotor. Most manufacturers adjust the synchronous speed to be in the middle of the variable speed range. This allows the DFIG to operate at sub-synchronous speeds, where the generator receives power through the rotor, as well as super-synchronous speeds, where the generator delivers power through the rotor.

Power Range: For WTS applications, DFIGs have been developed for a wide power range, spanning from several kW to over 10 MW. However, below 1.5 MW, the use of DFIGs is often not justifiable in terms of cost versus performance compared to other categories [10]. Additionally, manufacturers typically do not employ DFIGs in power greater than 6 MW [11]. Some of the most commonly installed DFIGs include Acciona AW-100/3000 (3 MW), Gamesa G83-2.0 (2 MW), and Vestas V80-2.0 (2 MW). In 2023, DFIG systems with power capacities of 2.2, 3.2, and 3.6 MW dominated the market share [5]. In the concept of DFIG-based systems, the rated power corresponds to the total power that can be generated by both the stator and the rotor. This occurs at the maximum allowable slip s at super-synchronism, typically equal to -0.25 or -0.3. When neglecting losses, the rotor power equals the stator power multiplied by this maximum slip ($P_r = -s_{max} P_s$).

Power Converter: DFIG-based systems commonly employ standard back-to-back PCs consisting of a Grid-Side Converter (GSC) and a Rotor-Side Converter (RSC) that share the DC bus. Most manufacturers use two-level converters with standard IGBTs to reduce costs for the 1.5 to 3 MW power range. However, for higher power ranges, three-level converters are expected to be the preferred option [11]. The sizing of both converters differs depending on the strategy chosen for magnetizing the machine. If the machine is magnetized from the rotor (over-excitation), the RSC must be sized to deliver the quadrature torque component and the direct magnetizing current, which is typically around 30 % of the nominal current of the machine. The GSC only needs to deliver the active current component. This strategy is primarily selected when the stator needs to operate at the unity power factor. If the machine is magnetized from the stator (under-excitation), the RSC must be sized to deliver the quadrature torque component. The GSC only needs to deliver the active current and the reactive current components [8].

Voltage level: For DFIGs with typical power capacities, low voltage (such as 400, 690, or 900 V) stator windings can be used. The typical ratio between the rotor and the stator-rated voltages, denoted as k, is within the range of 2.6 to 3.3. Therefore, the rotor winding should be designed for a medium voltage. The rotor-rated voltage is reached at a standstill ($s = 1$). However, DFIGs typically operate near synchronous speed; hence, the maximum rotor voltage at s_{max} is typically less than a third of its rated voltage ($U_{r\text{-}max} = s_{max}\ U_{r\text{-}rated}$). Thus, the rotor-side PC can be scaled down. For instance, with the most common stator-rated voltage, 690 V, and $k = 2.6$, the rotor-rated voltage would be 1794 V. With s_{max} = -0.3, the maximum rotor voltage would be 598 V, which is the maximum available voltage for the RSC. Furthermore, the GSC would require a transformer to be connected to the 690 V grid. It is worth mentioning that for the power range from 1.5 to 4 MW, the same voltage as the stator-rated voltage may be chosen for the maximum rotor voltage at s_{max}. Then, no transformer is needed to match the GSC to the power grid voltage. For this purpose, k can be chosen as $1/s_{max.}$ However, for higher powers, it may be more practical to use a transformer on the grid side [10].

Acknowledgements

This work has been supported by the Austrian Science Fund (FWF) under Grant-DOI 10.55776/I6250 and by the Slovenian Research and Innovation Agency (ARIS) under project no. J2-4475.

[12] has been used to enhance the grammar and editing of the text. However, it has not been used to generate content.

References

[1] "Electricity production, consumption and market overview," Aug. 2024. [Online]. Available: https://ec.europa.eu/eurostat/statistics-explained/index.php?title=Category:Energy
[2] "The Ten-Year Network Development Plan (TYNDP) - ENTSOG & ENTSO-E," 2020. [Online]. Available: https://2020.entsos-tyndp-scenarios.eu/
[3] S. Saha and M. I. Saleem, "Inertia Sensitivity Analysis of Power Grids with High Penetration of Renewable Energy Sources," in *IEEE Industry Applications Society Annual Meeting (IAS)*, 2022, pp. 1–18.
[4] "Wind energy in Europe: 2023 Statistics and the outlook for 2024-2030," 2024. [Online]. Available: https://windeurope.org/intelligence-platform/product/wind-energy-in-europe-2023-statistics-and-the-outlook-for-2024-2030/
[5] "Global Doubly Fed Induction Generator (DFIG) System Market – Industry Reports," 2023. [Online]. Available: https://www.precisionreports.co/global-doubly-fed-induction-generator-dfig-system-market-23317683
[6] H. Polinder, "Overview of and Trends in Wind Turbine Generator Systems," in *IEEE Power and Energy Society General Meeting*, 2011.
[7] A. Bensalah, M. A. Benhamida, G. Barakat, and Y. Amara, "Large Wind Turbine Generators: State-of-the-Art Review," in *International Conference on Electrical Machines (ICEM)*, 2018, pp. 2205–2211.
[8] G. Abad, J. López, M. Rodríguez, L. Marroyo, and G. Iwanski, *Doubly Fed Induction Machine: Modeling and Control for Wind Energy Generation Applications*. 2011.
[9] J. Morren and S. W. H. de Haan, "Ridethrough of wind turbines with doubly-fed induction generator during a voltage dip," *IEEE Trans. Energy Convers.*, vol. 20, no. 2, pp. 435–441, Jun. 2005.
[10] I. Boldea, *Variable Speed Generators, Second Edition*. 2016.
[11] V. Yaramasu, B. Wu, P. C. Sen, S. Kouro, and M. Narimani, "High-Power Wind Energy Conversion Systems: State-of-the-Art and Emerging Technologies," *Proc. IEEE*, vol. 103, no. 5, pp. 740–788, 2015.
[12] "OpenAI. (2023). ChatGPT." Available: https://chat.openai.com/chat

Modelling of Initial Magnetic Curves of Non-Oriented Laminated Steels Using Artificial Neural Networks

Beno Klopčič, Maja Lindič, Gregor Černivec

Bosch Rexroth d.o.o., Brnik, Slovenia
beno.klopcic@boschrexroth.si, maja.lindic@fs.uni-lj.si,
gregor.cernivec@boschrexroth.si

The article discusses modelling of the initial static magnetic curve of non-oriented laminated steels using artificial neural networks (ANN) for usage in electrical machine calculations. ANN enables modelling of nonlinear characteristics, which is crucial for developing electrical machines that meet application requirements. The initial magnetic curve must satisfy certain boundary conditions to be suitable for utilization in electromagnetic calculations. It is important to consider the measurement uncertainty in calculations that can be in case of ANN achieved by introducing noise injection. In conclusion, the significance and effectiveness of ANN in improving calculations and simulations in the field of electrical engineering are emphasized. This opens new possibilities for developing and understanding the magnetic properties of materials, emphasizing the significant impact and effectiveness of ANN in improving calculations and simulations.

DOI
https://doi.org/
10.18690/um.feri.4.2025.21

ISBN
978-961-286-986-1

Keywords:
artificial neural network,
initial magnetisation curve,
curve fitting,
oise inclusion,
non-oriented laminated steel

University of Maribor Press

I Introduction

For the calculations of electrical machines, we require a model of the initial static magnetic curve of the non-oriented laminated steel, further on addressed as “iron”. Accuracy, repeatability, and stability of the initial magnetic curve model is a key in the electromagnetic calculations. Even a slight deviation of the magnetic curve model can affect harmonic analysis, which in practice means a modified impact on the higher harmonics.

There already exist various analytical models that successfully describe the initial magnetic curve: Jiles-Atherton, Preisach, Dunhem, Coleman–Hodgdon, Stoner-Wohlfarth, Tellinen etc. [1]. Disadvantages vary from model to model, and they are most often associated with:

- complexity (solving differential equations etc.),
- oversimplification (assumes idealized conditions),
- large number of parameters,
- parameter sensitivity (small variation can significantly impact the model),
- calibration challenges,
- limited applicability (only for certain types of materials),
- fitting problems,
- lack of experimental validation.

The magnetic curve is typically highly nonlinear, making the ANN very suitable and powerful tool for modelling and prediction in various domains. In general, ANN can be used to model any nonlinear characteristic, however there are some challenges and limitations that need to be considered. The challenges of modelling using ANN include large amount of data for effective network training, computational resources, tuning of parameters to find the optimal combination of the hyperparameters, focus on learning patterns and data correlations rather than understanding causal data dependencies, and the potential occurrence of the model overfitting. All these are common problems in modelling using ANN. Overfitting occurs when the model becomes too complex and fits the trained data too closely, resulting in a poor generalization. There exist various of commonly used methods to prevent overfitting e.g., early stopping, regularisation, dropout etc. [2]. On the other hand, there are methods aiming to control the model's complexity by introduction of the randomness, i.e., the inclusion of noise improves generalization by introducing random data. The type of noise may vary, depending on the specific needs, such as Gaussian noise, random rotations, translations, scaling, flipping etc. This increases model robustness, improves generalization, and controls model complexity through regularization. It should be applied with caution; to avoid negative effect on the model's performance [3-6].

II Technical Information

A. Method description

We developed a model that will accurately approximate the response of the magnetic field density – B [T] in the iron in response to excitation with magnetic field strength – H [A/m], when using a limited number of experimentally obtained data points. To fabricate the model of the initial magnetic curve, which will be useful in further calculations, this must fulfil several initial requirements. Model must be a continuous function, continuously differentiable, strictly monotonically increasing, link the coordinate origin and must have μ_r=1 for high magnetic field strengths.

There were measured 12 data of SIWATT M800-50A non-oriented laminated steel. Data were obtained from the developer of the asynchronous motor calculation software [7]. Points are ranging from 1 T to 2 T. Data are shown in Table I. We used B as the input data and H as the output data.

Table 1: Experimental data

Data No.	1	2	3	4	5	6
H [A/m]	160	200	250	400	650	1000
B [T]	1,0097	1,1872	1,2889	1,4365	1,5315	1,60

Data No.	7	8	9	10	11	12
H [A/m]	1600	2500	5000	104	2·104	3·104
B [T]	1,6620	1,7254	1,8368	1,9563	2,0688	2,1051

B. Modelling procedure

Diagram in Figure 1 shows a two-step experimental process. In the first step a basic approximation of the two models in the range of the measured data was performed. Based on the results, the more appropriate one was selected. In the second step, the extended approximation – i.e., retraining was conducted. The selected baseline model was approximated to link the coordinate origin and the saturation point.

In both steps we used feedforward ANN. The Levenberg–Marquardt algorithm (LMA) was taking into account and all of the data used for training. A model with 2 hidden layers consisting of 2 neurons in the first layer and 3 neurons in the second layer was selected in both cases. Based on the preliminary tests we found this setup to be optimal for all the models.

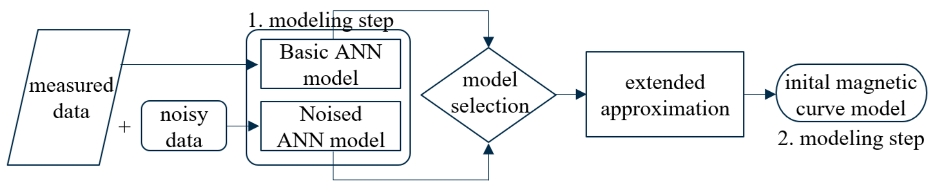

Figure1: Initial magnetic curve modelling process

In the first step, two approaches were analysed. The first approach, the *Basic ANN model*, utilized conventional ANN modeling methods without any additional techniques implemented. The second approach, the *Noisy ANN model*, incorporated a noise inclusion method: the Gaussian noise was introduced into the magnetic field strength data. The measured values were set as the mean values, with the assumed variance equal to 0,1 A^2/m^2. It was anticipated that this range effectively describes the scatter of the measurements and doesn't negatively affect the model's performance. Validation of the Gaussian noise was performed using comparative analysis between the models with/without the noise. Gaussian noise data were generated using *randn()* function in MATLAB software where 99 additional data sets were generated. A new matrix – *HM* (1) was created that included newly generated noisy data along with the measured data, where *v* represents the data variance, *N* the number of generated noisy data and *H* the magnetic field strength.

$$HM = v \cdot randn(N) + H \tag{1}$$

The suitable model was selected based on meeting the initial requirements. In the second modelling step only the selected model was analysed. To achieve a higher level of approximation accuracy, the subsequently added points were considered. These points were selected based on the initial requirements and preliminary research. The points were added to extend the initial model and cover the entire region of interest.

C. Model evaluation

Results are presented in Figure 2a. The curve of the *Noised model* appears smoother in comparison to the *Basic ANN model*, which exhibits larger transition area at higher excitation. This discrepancy is a result of the overfitting: when fitting the model, a smaller number of neurons mean that the model does not converge, while a model with one additional neuron leads to overfitting. Based on these results together with initial requirements, the *Noised ANN model* was selected as the basis for the second step of modeling.

The outcome of the second modelling step is the initial magnetic curve model, as depicted in Figure 2b. The model fully meets the requirements of being a continuous function, continuously differentiable and strictly monotonically increasing. The requirements of linking the coordinate origin and having μ_r=1 for the large excitation are met with only minor deviations. The error of the model when intersecting the coordinate origin amounts to $H(B=0\text{ T})=2{,}14\cdot10^{-2}$ A/m and the relative permeability at high excitation μ_r (B=2,3 T) =1,04. Based on the evaluation, it is determined that the magnitude of these errors should not significantly impact subsequent calculations and usfulness of the model.

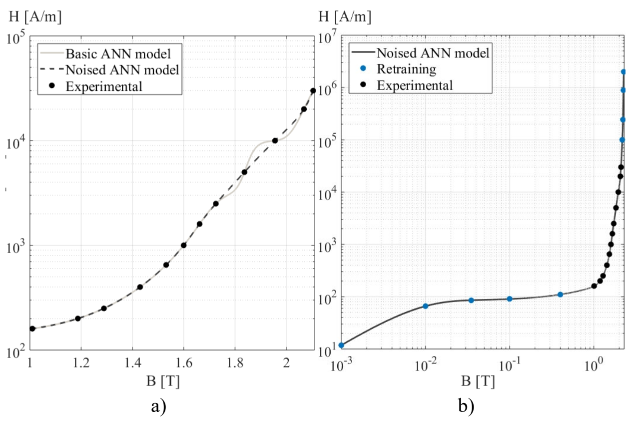

Figure 2: a) 1. modelling step - basic and Noised model, b) 2. modelling step - initial magnetic curve model

D. Conclusion

The advantages of modelling the initial magnetic curve using ANN are related to a higher model accuracy, simpler modelling process without the need to explicitly solve polynomial fitting, and possibility of exchanging with other programming languages. Such modelling method also enables the simultaneous modelling of multiple characteristics by using one ANN approximation network. However, when dealing with small data sets, insurmountable problems may arise in modelling with ANN, that cannot be solved by classical approaches. By introducing noise inclusion, it is possible to expand the data set accordingly, which increases the stability and accuracy of the model. Therefore, we conclude that the noise inclusion technique is a highly suitable tool for modeling the initial magnetic curve. Further investigations will be conducted to examine the effect of the initial magnetic curve model in the electrical machine calculations.

Acknowledgement

Authors would like to thank company Bosch Rexroth for all the professional support, resources, cooperation in the research and Aktiv inženirjev Bosch (part of trade union SKEI) for financial support.

References

[1] Mörée, Gustav, and Mats Leijon. "Review of Hysteresis Models for Magnetic Materials." Energies. 3908. pp. 0-66, 2023
[2] Rosa, João PS, et al. "Overview of artificial neural networks." Using artificial neural networks for analog integrated circuit design automation", Switzerland, Springer, pp. 21-44, 2020
[3] Zur, Richard M., et al. "Noise injection for training artificial neural networks: A comparison with weight decay and early stopping." Medical physics, pp. 4810-4818, 2009
[4] Matsuoka, Kiyotoshi. "Noise injection into inputs in back-propagation learning." IEEE Transactions on Systems, Man, and Cybernetics, pp. 436-440, 1992.
[5] Jiang, Yulei. "Uncertainty in the output of artificial neural networks." IEEE transactions on medical imaging, pp. 913-921, 2003
[6] Holmstrom, Lasse, and Petri Koistinen. "Using additive noise in back-propagation training." IEEE transactions on neural networks, 24-38, 1992
[7] Zagradisnik I. et. al. "The emLook software package for the analytical and numerical analyses of electrical machines." Przegląd Elektrotechniczny, pp. 175-178, 2010

A NOVEL RAILGUN SIMULATION MODEL BASED ON A QUASISTATIC

FERMÍN GÓMEZ DE LEÓN,[1] MAURIZIO REPETTO,[1]
ARA BISSAL[2]

[1] Politecnico di Torino, Department of Energy, Turin, Italy
fermin.gomezdeleon@studenti.polito.it, maurizio.repetto@polito.it
[2] Huawei Nuremberg Research Center, Nuremberg, Germany
ara.bissal@huawei.com

This paper presents a novel railgun simulation model based on a quasistatic study in COMSOL. Traditional analytical models are inaccurate as they use the coenergy principle to calculate the force on the armature, yielding the total force in the displacement axis. By using a numerical magnetic solution, a parametric analysis evaluates the flux linkage, armature force, and system resistance at various positions and currents. After characterizing the railgun, the transient problem is solved by coupling the parametric study results with the system's equivalent circuit. Finally, the results are compared with those from the analytical approach.

DOI
https://doi.org/
10.18690/um.feri.4.2025.22

ISBN
978-961-286-986-1

Keywords:
railgun,
quasistatic study,
analytical model,
FEM model,
coenergy principle

University of Maribor Press

I Introduction

Simulating the electromagnetic behaviour of a railgun is crucial for predicting the performance and optimizing the design. Railguns can be modelled analytically or via a Finite Element Method (FEM) software. Analytical models, like those in [1] and [2], use the coenergy principle to calculate the force acting over the armature, however, this approach actually yields the total force acting on the longitudinal axis of the rails and armature. FEM models, such as the one in [3], require the railgun's current profile as input, necessitating experimental setups and they do not allow for geometric optimization. This paper outlines a methodology for integrating both approaches and discusses the results obtained.

II Methodology

To calculate the armature position (*y(t)*), speed ($\dot{y}(t)$), and acceleration ($\ddot{y}(t)$) the following equations must be solved.

$$F(t) = m_a \cdot \ddot{y}(t) \tag{1}$$

$$\dot{y}(t) = \int_{t_0}^{t_1} \ddot{y}(t) \cdot dt + \dot{y}_0 \tag{2}$$

$$y(t) = \int_{t_0}^{t_1} \dot{y}(t) \cdot dt + y_0 \tag{3}$$

F(t) corresponds to the force exerted on the armature, and m_a is the mass of the armature. It is important to highlight that *F(t)* actually depends on the armature position and electrical current.

Figure 1 shows the drive and railgun equivalent circuit.

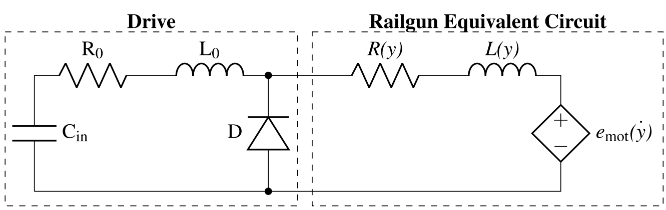

Figure 1: Railgun equivalent circuit.

C_{in} represents the capacitor bank capacitance. R_0 is the sum of the equivalent series resistance (ESR) of the capacitor bank, the connections resistance, and the PCB tracks resistance. Since the ESR is dominant in this case, R_0 is effectively set equal to the ESR. Similarly, L_0 is the total of the equivalent series inductance (ESL) of the capacitor bank and the PCB stray inductance. Again, only the ESL is considered for the L_0 calculation due to its dominance. The antiparallel diode D is placed across the capacitor bank to prevent reverse voltages. $R(y)$, $L(y)$ and $e_{\text{mot}}(\dot{y})$ denote the railgun's resistance, inductance and the back electromotive force (BEMF), respectively. The $e_{\text{mot}}(\dot{y})$ depends on the flux linkage ($\lambda(y,i)$) and armature speed:

$$e_{\text{mot}}(t) = \frac{\partial\lambda(y,i)}{\partial y}\bigg|_{i=ct} \cdot \dot{y}(t) \tag{4}$$

To solve the problem in the time domain, the kinematic equations are coupled with the equivalent circuit. Prior to this, it is necessary to determine $F(y,i)$, $\lambda(y,i)$, and $R(y,i)$. These data are obtained through a parametric sweep performed in COMSOL. The results are then integrated into the kinematic equations and in the equivalent circuit, the problem can be effectively solved in the time domain by means of numerical integration based on backward differentiation formulas.

III Results

Figures 2 – 4 show the results of the parametric sweep. Figure 2 illustrates that the force is transmitted to the armature more efficiently when it is near to the origin. In Fig. 3, it can be seen that, as there is no magnetic material, the flux linkage increases linearly with the current. In Fig. 4, it is important to highlight that no thermal effects are considered, so the railgun's resistance does not depend on the current. Additionally, the parametric sweep is based on stationary studies, so the skin effect is not considered.

Figures 5 – 7 compare the final results with those from analytical model [1], implemented in Simulink. Figure 6 shows both approaches yield similar results. Figures 7 indicates the analytical model yields a peak force 10 % higher than the COMSOL model, leading to the mismatch shown in Fig. 6.

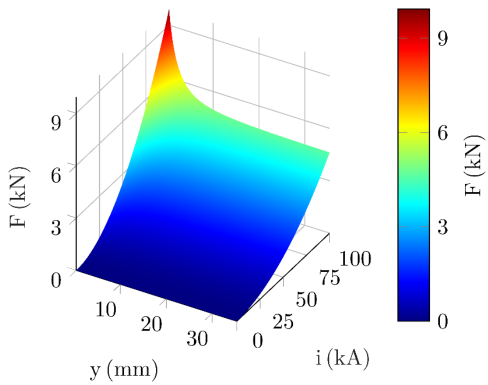

Figure 2: Force as function of the armature position and the current.

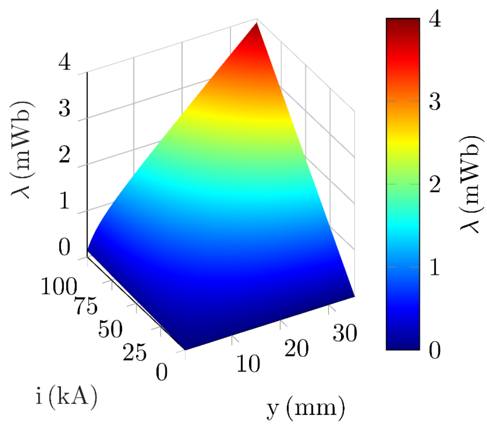

Figure 3: Flux linkage as a function of the armature position and the current.

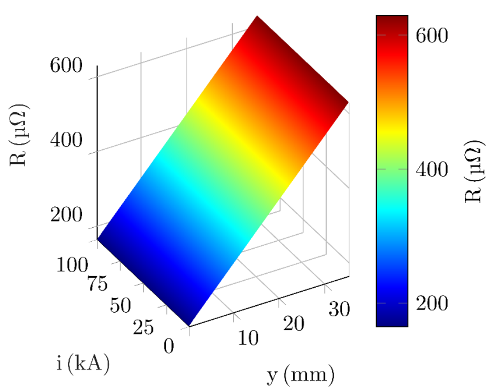

Figure 4: Resistance as a function of the armature position and the current.

IV Conclusions and future work

A novel hybrid FEM-analytical model has been proposed to address the limitations of analytical models in terms of force calculation. Future work will focus on incorporating thermal effects and the skin effect into the model to enhance its accuracy.

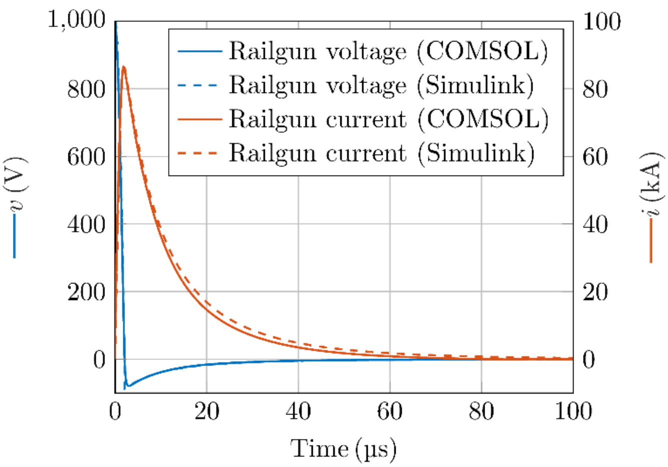

Figure 5: Force as function of the armature position and the current.

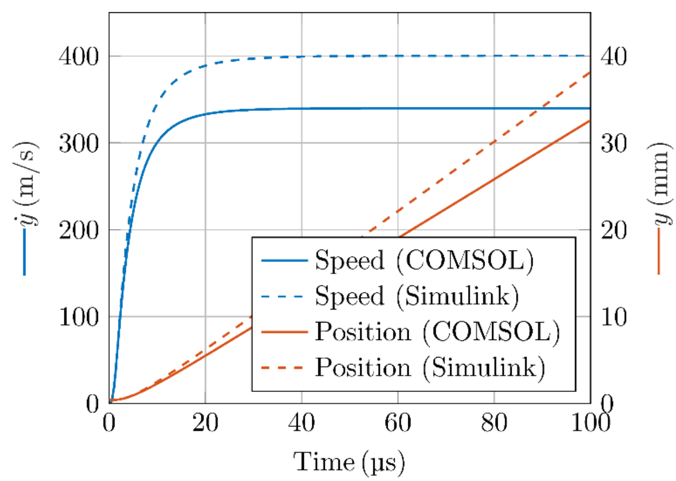

Figure 6: Flux linkage as a function of the armature position and the current.

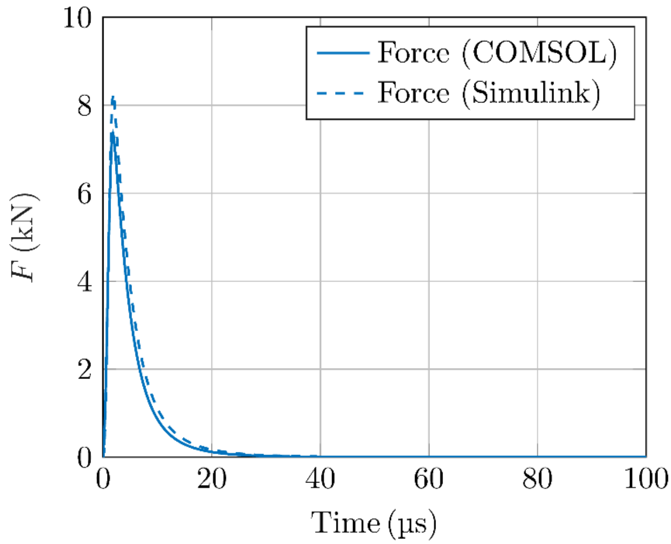

Figure 7: Resistance as a function of the armature position and the current.

References

[1] Seyed Abbas Taher, Mostafa Jafari, and Motjaba Pakdel "A New Approach for Modeling Electromagnetic Railguns" IEEE Trans. Plasma Sci, vol. 43, no. 5, pp. 1733-1741, May 2015.

[2] F. Deadrick, R. Hawke, and J. Scudder, "MAGRAC – A railgun simulation program." IEEE Trans. Magn., vol. 18, no 1, pp. 97 – 104, Jan. 1982.

[3] S. Hundertmark and M. Roch, "Transient 3-d simulation of an experimental railgun using finite element methods," 2012 16th International Symposium on Electromagnetic Launch Technology, Beijing, China, 2012

NETWORK-BASED TRANSFORMER MODELS – A TRANSIENT ANALYSIS

DOI
https://doi.org/10.18690/um.feri.4.2025.23

ISBN
978-961-286-986-1

ALEXANDER SAUSENG,[1]
ALICE REINBACHER-KOSTINGER,[1] PETER HAMBERGER,[2]
MANFRED KALTENBACHER,[1] KLAUS ROPPERT[1]

[1] Graz University of Technology, Institute of Fundamentals and Theory in Electrical Engineering, Graz, Austria
alexander.sauseng@tugraz.at, alice.koestinger@tugraz.at,
manfred.kaltenbacher@tugraz.at, klaus.roppert@tugraz.at
[2] Siemens Energy, Linz, Austria
peter.hamberger@siemens.com

This contribution is about network-based transformer models. Two models (single- and three-phase) are derived, whereas Hopkinson's analogy is used to depict the magnetic domain. Therein, an energy-based hysteresis model is incorporated to represent the magnetic core. The solution strategy is a second-order variable step size backward differentiation formula (BDF2) in time domain, yielding the transient response of the two transformers. Finally, the simulation results are compared to measurements.

Keywords:
network-based transformer models,
Hopkinson's analogy,
energy-based hysteresis model,
backward differentiation formula (BDF2),
transient response simulation

University of Maribor Press

I Introduction

Network-based transformer models are an excellent opportunity to obtain reasonable simulation results computationally cheaply. All quantities are assumed to be homogeneous, and the number of unknowns is smaller than in an approach with finite elements. One significant aspect in a transformer model is the representation of the magnetic core. This contribution derives a single- and a three-phase transformer network based on a mutual and leakage flux approach and on a topological approach, respectively. The magnetic domain in both transformer models is described using Hopkinson's analogy [1]. An energybased hysteresis model [2] depicts the transformer's core. The resulting nonlinear and hysteretic differential algebraic equation (DAE) system is solved using a second-order variable step size backward differentiation formula (BDF2). The simulated idle currents are compared to measurements, and inrush simulation results for nominal excitation are presented.

II The transformer models

The primary voltage v_p of a transformer can be described by copper and stray losses, and an induced voltage due to the mutual magnetic flux ϕ_M in the magnetic core [1], reading

$$v_\mathrm{p} = i_\mathrm{p} R_\mathrm{p} + L_{\sigma,\mathrm{p}} \frac{\mathrm{d}i_\mathrm{p}}{\mathrm{d}t} + N_\mathrm{p} \frac{\mathrm{d}\phi_\mathrm{M}}{\mathrm{d}t} \tag{1}$$

where i_p equals the primary current. Analogous to (1),

$$v_s = -i_s R_s - L_{\sigma,s} \frac{\mathrm{d}i_s}{\mathrm{d}t} + N_s \frac{\mathrm{d}\phi_M}{\mathrm{d}t} \tag{2}$$

describes the secondary voltage equation. Next, *Hopkinson*'s analogy, which equals

$$\Theta = \frac{l}{\mu(\Theta/\mathrm{l})\mathrm{A}} \phi_M = R_{mag}(\Theta)\phi_M \tag{3}$$

with Θ, l, μ, and A the magnetomotive force, the length of the magnetic flux path, the permeability, and the core's cross section, respectively, can be used to model the magnetic domain. The nonlinear and hysteretic resistance R_{mag} represents the energy-based hysteresis model, which takes Θ as an input, and outputs the magnetic flux ϕ_M.

Combining (1), (2), and (3) in one network states the singlephase transformer, as shown in Figure 1. Note that the index *i* counts only for the three-phase transformer.

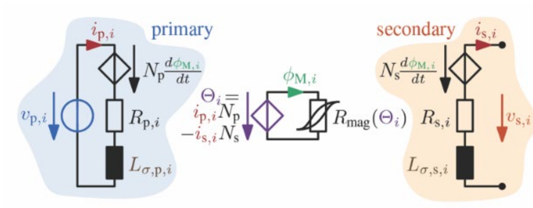

Figure 1: single-phase transformer network

A. Three-Phase Transformer

The electric domain of the three-phase transformer model is analogous to Figure 1 (three primary/secondary subnetworks with $i = \{1,2,3\}$), whereas the magnetic domain can be modeled according to the core topology, as Figure 2 depicts.

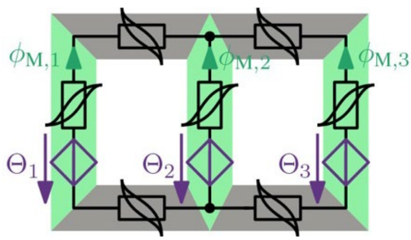

Figure 2: magnetic network of the three-phase transformer

Note that all magnetic resistances ( )are parametrized according to the length and cross section of the steel sheet regions.

III The differential algebraic equation system

The DAE system obtained from the networks can be stated with modified nodal analysis [3] as

$$\Lambda \frac{dx}{dt} + \gamma(x) = r, \tag{4}$$

where Λ, $\gamma(x)$, and r are the dynamic matrix containing derivative sources and inductances, the vector containing the linear and nonlinear and hysteretic current/voltage relations, and the exciting right hand side containing the independent sources, respectively. The vector $\boldsymbol{x}$ consists of the nodal voltages and currents over inductances and voltage sources. The system in (4) is discretized using BDF2, whereas the equation error in each time step is minimized using the *NewtonRaphson* method, enhanced with a line search algorithm.

IV Simulation results

The single- and the three-phase transformer are simulated for nominal primary voltage in the idle case, i.e. with no load connected to the secondary side(s).

A. Single-Phase Transformer

Figure 3 depicts a comparison between the simulated and measured primary current of the single-phase transformer in steady-state, which is instantaneously the case, if the sinusoidal primary voltage is switched on at ±90°.

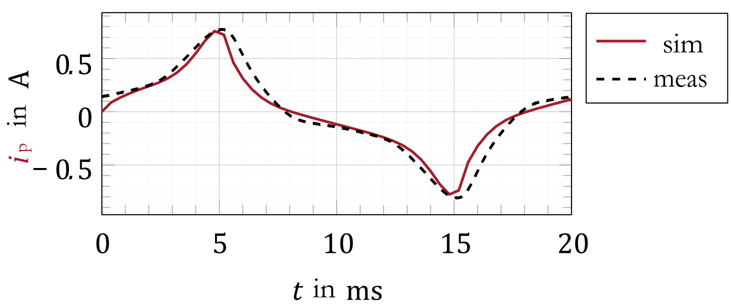

Figure 3: comparison between the simulated and measured idle current of the single-phase transformer in steady-state

Figure 4 depicts the simulation result of the inrush current of the single-phase transformer, if the sinusoidal primary voltage is switched on during the zero crossing.

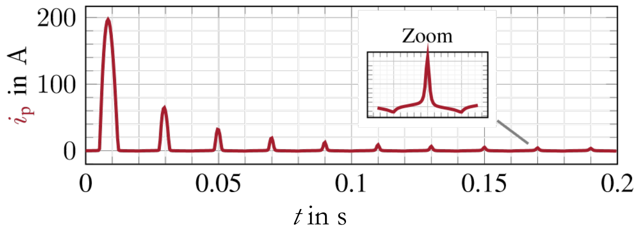

Figure 4: simulated inrush current of the single-phase transformer

Figure 5 depicts the simulated hysteresis of the single-phase transformer for a sinusoidal voltage excitation switched on at ±90°.

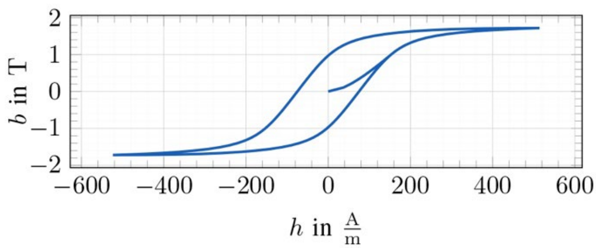

Figure 5: simulated hysteresis of the single-phase transformer

B. Three-Phase Transformer

The sinusoidal three-phase excitation for $v_{p,1,1}$, $v_{p,2}$, and $v_{p,3}$is 0°, 120°, and −120°, respectively.

Figure 6 depicts a comparison between the simulated and measured primary current of the three-phase transformer in steady-state.

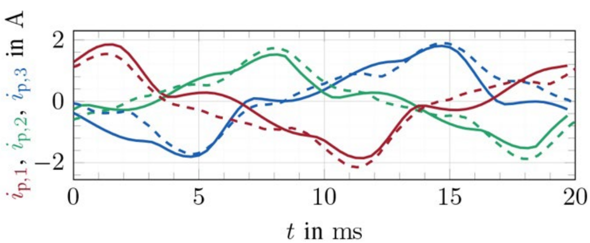

Figure 6: comparison between the simulated and measured idle current of the three-phase transformer in steady-state

Figure 7 depicts the simulation result of the inrush current of the three-phase transformer.

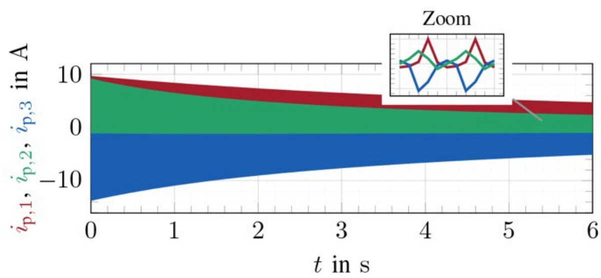

Figure 7: simulated inrush current of the three-phase transformer

V Conclusion and outlook

The algorithm is implemented in MATLAB. The *NewtonRaphson* iterations per time step are about 1 to 20, depending on the excitation level and point on the hysteresis trajectory; return points need on average more iterations. The parameters of the models are obtained from a short-circuit test; the hysteresis model is fitted to core measurements. The simulated idle currents coincide satisfactorily with the measured ones. In the full contribution, inrush measurements, the hysteresis model itself, modeling of stray paths, DC-biased excitation signals, the BDF2 algorithm, the DAE system, and different modeling topologies of the transformer's core are discussed.

References

[1] R. Yacamini and H. Bronzeado. "Transformer inrush calculations using a coupled electromagnetic model". In: *IEE Proceedings - Science, Measurement and Technology*. Vol. 141. 1994, pp. 491–498. DOI: 10.1049/ip-smt: 19941450.

[2] Anders Bergqvist. "Magnetic vector hysteresis model with dry friction-like pinning". In: *Physica B: Condensed Matter* 233 (1997), pp. 342–347. DOI: 10.1016/S09214526(97)00319-0.

[3] C. Tischendorf. "Solution of index-2 differential algebraic equations and its application in circuit simulation". PhD thesis. Fachbereich Mathematik der Humboldt-Universitat Berlin, 1996.

Analysis of Synchronous Reluctance Machine With 3D-Printed Axially Laminated Rotor Featuring Axially Alternated Layers

DOI
https://doi.org/10.18690/um.feri.4.2025.24

ISBN
978-961-286-986-1

Maksim A. Sitnikov, Floran Martin,
Anouar Belahcen

Aalto University, Department of Electrical Engineering and Automation, Aalto, Finland
maksim.sitnikov@aalto.fi, floran.martin@aalto.fi, anouar.belahcen@aalto.fi

This study delves into the strategic layer alternation along the axial direction to mitigate electromagnetic torque ripple and minimize eddy current losses within synchronous reluctance electric machine with 3D-printed axially laminated rotor. A meticulous comparative analysis is conducted, scrutinizing the printing depth in the radial direction alongside variations in the number of alternating layers to discern the optimal ratio. Emphasis is placed on implementing two distinct 3D sliced models: one incorporating current continuity between slices and the other without. The article meticulously delineates the nuances of these models and draws a comprehensive comparison with a full 3D FEM model, elucidating their respective merits and drawbacks.

Keywords:
electromagnetic torque ripple,
Eddy current losses,
synchronous reluctance machine,
3D-printed axially laminated rotor,
axially alternating layers (AAL)

University of Maribor Press

I Introduction

Advancements in 3D printing technologies have significantly expanded the possibilities in electrical engineering, particularly in electromechanics. Progress in powder management systems and post-processing techniques has increased accessibility for printing components of electric machines [1]. However, the optimal printing of high-speed electrical machines remains challenging, attributed to limited powder options and material compatibility issues during postprocessing [2].

A promising avenue is the 3D printing of an axially laminated (ALA) rotor, offering mechanical robustness against centrifugal loads. Nevertheless, industrial constraints impact component dimensions, potentially introducing imperfections in electrical machine design. Notably, increased pulsations in electromagnetic torque and rotor eddy currents arise as imperfections.

This paper examines axially alternating layers (AAL) in the rotor of synchronous reluctance machines to mitigate torque ripple and eddy current losses. Special attention is given to developing a 3D sliced model, providing computational efficiency compared to a full 3D model. The models are implemented using the commercial COMSOL software.

II Machine specification

This paper explores the synchronous reluctance machine with an ALA rotor with alternated layers depicted in Fig.1 with an expected maximum output power of 290 kW. The machine's specifications are detailed in Table 1.

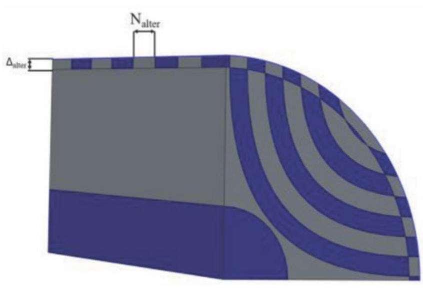

Figure 1: Quarter of ALA rotor construction with axially alternated layers

Table 1: Main machine specification

Parameter	Value
Maximum Power	290 kW
Speed	31500 rpm
Number of poles	4
Number of stator slots	36
Outer stator diameter	250 mm
Inner stator diameter	115 mm
Airgap	2 mm
Length	135 mm

III Modelling approach

A. FEM models of the machine with AAL

Two main models are considered: full 3D and sliced 3D, shown in Figure 2. The sliced model has two variations: with and without current continuity between the rotor slices.

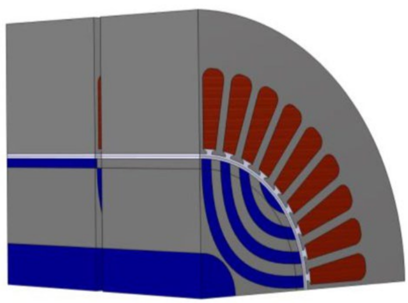

Figure 2: 3D sliced model of ALA rotor with AAL

A 3D sliced model [4] represents a packing along the z-direction of slices separated from each other. Unlike the full model, this approach does not require flux continuity between two different rotor configurations. This greatly simplifies the convergence of the FEM and increases the speed of calculations.

Importantly, in the 3D sliced model, slices must not be connected, i.e.,

$$L_{slice} = L/k_{slice}, k_{slice} > N_{slice} \tag{1}$$

where L_{slice} is the length of one slice, $N_{slice} = N_{alter}$ is the number of slices, k_{slice} is the slicing factor and N_{alter} is the number of alternating layers.

The torque T and rotor eddy current losses P are then expressed as:

$$\begin{cases} T = \sum_{i=1}^{N_{slice}} T_i \,(k_{slice} \,/\, N_{slice}) \\ T = \sum_{i=1}^{N_{slice}} P_i \,(k_{slice} \,/\, N_{slice}) \end{cases} \tag{2}$$

B. Torque ripple approximation

During the simulation, it was found that electromagnetic torque ripple, depending on the printing depth, can be approximated as follows:

$$\Delta T(\Delta_{alter}) = \left(\Delta \mathrm{T}(0) - (1.25 - 0.25(-1)^{N_{alter}})\Delta \mathrm{T}(\infty)\right) e^{-5\frac{\Delta_{alter}}{t_{rib}}} + \Delta \mathrm{T}(\infty) \tag{3}$$

where Δ_{alter} is the radial printing depth, t_{rib} the rib thickness, $\Delta \mathrm{T}(0)$ is the torque ripple without AAL, and $\Delta \mathrm{T}(\infty)$ is the torque ripple for an even number of AAL with a fully inverted layer ($\Delta_{alter} \geq 0.75 t_{rib}$, [5]).

IV Results

Figure 3 shows a comparison of 3D FEM, 3D sliced model and approximation (3) for torque ripple with an even number of AAL.

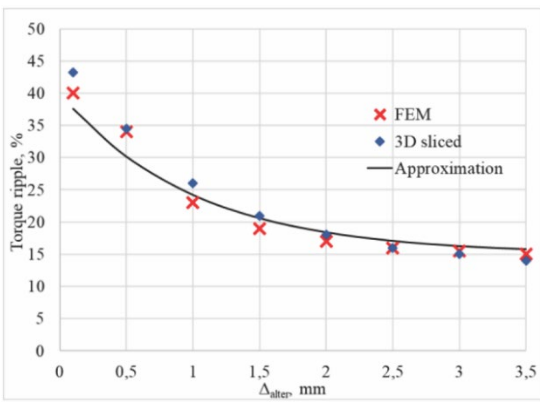

Figure 3: 3D FEM and approximation comparison for torque ripple

Figure 4 compares rotor eddy current losses as a function of radial print depth and number of layers.

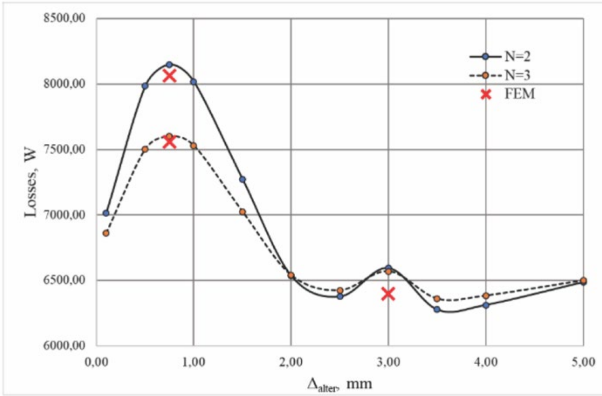

Figure 4: Losses comparison

It should be noted that the eddy current losses of the rotor and torque ripple don't depend on the increase in the number of layers and are determined only by the even or odd number of alternating layers. The dependence on the printing depth can be determined from Figure 4.

Thus, from a design point of view, Figures 3 and 4 show that it is possible to select the optimal radial depth of layer alternation such that the torque ripple can be significantly reduced and eddy current losses slightly reduced.

IV Conclusion

The effect of AAL on a synchronous reluctance machine with a 3D-printed ALA rotor was investigated. A noteworthy reduction in electromagnetic torque ripple was observed. Both eddy current losses and torque ripple were found to be influenced by the radial print depth, as well as the regularity of the AAL. Moreover, it was demonstrated that an even number of layers effectively minimizes torque ripple, albeit with a potential loss increase if the print depth is inappropriate. Conversely, an odd number of layers provides a less effective reduction in ripples but mitigates the risk of excessive losses at a shallower printing depth. Consequently, the optimal compromise for minimizing losses and attenuating torque ripples is achieved through an even number of AAL with a sufficiently substantial printing depth ($\Delta_{alter} \geq 0.75 t_{rib}$).The complete manuscript will expound a comprehensive elucidation of the simulation methodology.

References

[1] H. Tiismus, A. Kallaste, A. Belahcen, A. Rassõlkin and T. Vaimann, "Challenges of Additive Manufacturing of Electrical Machines," 2019 IEEE 12th International Symposium on Diagnostics for Electrical Machines, Power Electronics and Drives (SDEMPED), Toulouse, France, 2019, pp. 44-48, doi: 10.1109/DEMPED.2019.8864850.

[2] Aamer Nazir, Ozkan Gokcekaya, Kazi Md Masum Billah, Onur Ertugrul, Jingchao Jiang, Jiayu Sun, Sajjad Hussain, “Multi-material additive manufacturing: A systematic review of design, properties, applications, challenges, and 3D printing of materials and cellular metamaterials,” Materials & Design, vol. 226. Elsevier BV, p. 111661, Feb. 2023. doi: 10.1016/j.matdes.2023.111661.

[3] “Additive Manufacturing using Multi-Material 3D Powder Printing Technology” Grid Logic, [Accessed: February 15, 2024]. Available: https://www.grid-logic.com/ “Motor Tutorial Series” COMSOL Multiphysics, [Accessed: February 15, 2024]. Available: https://www.comsol.com/model/motor-tutorial-series110261.

[4] Ogata, K. (2010). Modern Control Engineering (5th ed.). Prentice Hall.

NEURAL NETWORK BASED OPTIMIZATION OF AN IPMSM WITHIN A BLDC DRIVE

MITJA GARMUT,[1] SIMON STEENTJES,[2] MARTIN PETRUN[1]
[1] University of Maribor, Faculty of Electrical Engineering and Computer Science, Institute of Electrical Power Engineering, Maribor, Slovenia
mitja.garmut@um.si, martin.petrun@um.si
[2] Hilti Entwicklungsgesellschaft mbH, Kaufering, Germany
simon.steentjes@hilti.com

DOI
https://doi.org/
10.18690/um.feri.4.2025.25

ISBN
978-961-286-986-1

This paper introduces a neural network based optimization framework for Interior Permanent Magnet Synchronous Machines (IPMSMs) in squarewave drive applications (i.e., Brushless Direct Current or BLDC drives) for enhanced machine performance. The focus was on reducing torque ripple while enhancing or maintaining the torque-to-current ratio. A Finite Element Method model and a Design of Experiments are employed to generate training data for neural networks. The networks enabled a multi-objective optimization, producing two designs that significantly reduce torque ripple and simultaneously increase average torque. A significant decrease in simulation time alongside an innovative approach to designing IPMSMs for squarewave drives is presented.

Keywords:
BLDC,
IPMSM,
square-wave control,
neural network,
multi-objective optimization

University of Maribor Press

I Introduction

Interior Permanent Magnet Synchronous Machines (IPMSM) are often driven by a two-level three-phase voltage source inverter by applying a squarewave (i.e., 120° commutation, block or six-step) control. Such a system is commonly referred to as a Brushless Direct Current (BLDC) drive. Operating these systems requires measuring direct current (DC) and merely six position states, provided by three Hall sensors, resulting in simplicity and cost-effectiveness. In recent years, the research on this topic has picked up [1, 2]. A common problem when operating with squarewave control is high torque ripple. To enhance the drive's performance, the primary objective was to minimize torque ripple without compromising the torque-to-current ratio. We analyzed the impact of torque ripple reduction on the torque-to-current ratio. First, a parametric Finite Element Method (FEM) model of the IPMSM was constructed, which was used to perform a simulation exited by an ideal-shaped squarewave current. A Design of Experiment (DoE) approach was used to collect simulation results to train a feedforward Neural Network (NN) [3]. A multi-objective optimization was performed to evaluate how the minimal torque ripple is connected to the torque-to-current ratio. Two designs were selected for detailed analysis.

II Theoretical background

A. abc model of an IPMSM

The voltage-balance equation of the IPMSM in the abc reference frame is given by (1)

$$\mathbf{u}_{\mathrm{abc}} = \mathbf{R}\mathbf{i}_{\mathrm{abc}} + \frac{\mathrm{d}}{\mathrm{d}t}[\mathbf{L}(\theta)\mathbf{i}_{\mathrm{abc}} + \mathbf{\Psi}_{\mathrm{m}}(\theta)], \tag{1}$$

where $\boldsymbol{i}_{abc} = [i_a\ i_b\ i_c]^T$ are the phase currents, $\boldsymbol{u}_{abc} = [u_a\ u_b\ u_c]^T$ are the phase voltages, $\boldsymbol{\Psi}_m(\theta) = [\Psi_{ma}\ \Psi_{mb}\ \Psi_{mc}]^T$ are the permanent magnet flux linkages, $\mathbf{R} = diag(R\ R\ R)$ are the phase resistances of the stator windings, $\mathbf{L}(\theta)$ is the inductance matrix and θ is the electrical angle. The electromagnetic torque is defined as (2)

$$t_{\mathrm{e}} = p_{\mathrm{p}}[\mathbf{i}_{\mathrm{abc}}^{\mathrm{T}}\frac{\partial \mathbf{\Psi}_{\mathrm{m}}(\theta)}{\partial \theta} + \frac{1}{2}\mathbf{i}_{\mathrm{abc}}^{\mathrm{T}}\frac{\partial \mathbf{L}(\theta)}{\partial \theta}\mathbf{i}_{\mathrm{abc}}], \tag{2}$$

where p_p is the number of pole pairs.

Squarewave-shaped phase currents $\mathbf{i}_{abc}$, shown in Fig. 1b) were used to excite the delta-connected 6-slot 4-pole IPMSM with Nd-Fe-B magnet and a fractional slot non-overlapping winding. In Fig. 1 the ideal squarewave-shaped current of a delta connected machine and the back Electro Motive Force (EMF) $\mathbf{e}_{abc}$ are presented, where I_p is he peak current value and e_p is the peak EMF value. The advance commutation angle a was defined as the phase shift between the fundamental harmonic component of i_b and e_b and was in this analysis set to zero.

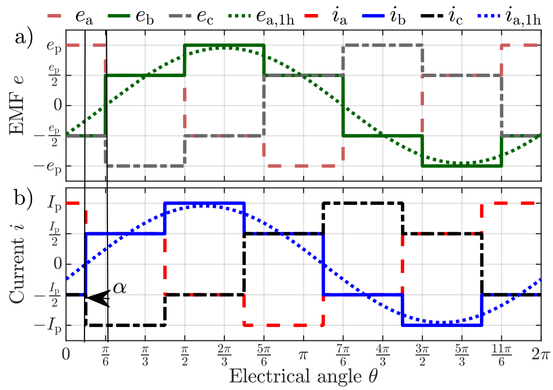

Figure 1: a) ideal shape of back EMF, b) ideal squarewave-shaped current of a delta-connected machine and advance commutation angle definition.

B. Optimisation of an IPMSM rotor

First, a parametric FEM model of the IPMSM in ANSYS Maxwell 2D was set up where 5 parameters were optimized, 1 on the stator (θ_v - slot opening angle), and 4 on the rotor (d_{rd}, d_{rq}, d_{ry} and θ_m), which are shown in Fig. 2.

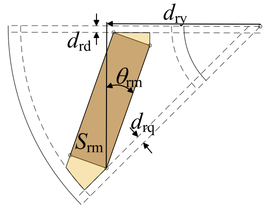

Figure 2: Parametric geometry of IPMSM

The magnet area S_{rm} was assumed constant. The input in the FEM simulation was the $\mathbf{i}_{\mathbf{abc}}$ and the output were the torque ripple $t_{\mathrm{e,ripp}}$ and the average torque $t_{\mathrm{e,avg}}$. All presented parameters were scaled to the inner radius of the stator.

An automated DoE (applying latin hypercube sampling) was performed using 6000 samples. In the next step, two feedforward NN were trained, where 5 inputs (i.e., design parameters) and 1 output (i.e., te,ripp and te,avg) were used. The Levenberg-Marquardt training function was employed and three hidden layers (20, 60, 20) were used. Fig. 3 shows the regression plot of the trained NN for both datasets.

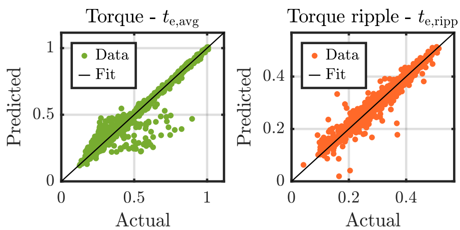

Figure 3: Regression plot of the trained NN

A two-objective optimization was performed using a multi-objective genetic algorithm in Matlab. The two objectives were minimizing $t_{\mathrm{e,ripp}}$ and maximizing $t_{\mathrm{e,avg}}$. The Pareto front with the 2 selected designs and reference design are shown in Fig. 4.

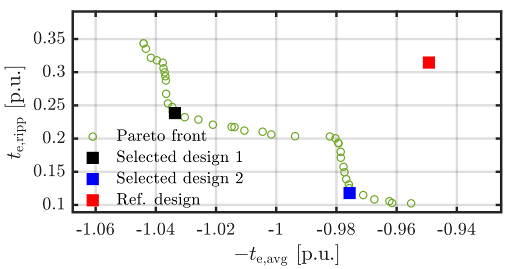

Figure 4: Pareto front with the selected designs

The selected design 1 was chosen in a way that the $t_{\mathrm{e,avg}}$ was maximized, but $t_{\mathrm{e,ripp}}$ was stil reduced. The selected design 2 was chosen in a way that $t_{\mathrm{e,avg}}$ was still improved and the $t_{\mathrm{e,ripp}}$ was reduced significantly. The design parameters are shown in Table I.

III Results

The two designs were reevaluated within FEM simulations to exclude the inherent error margin of the NN.

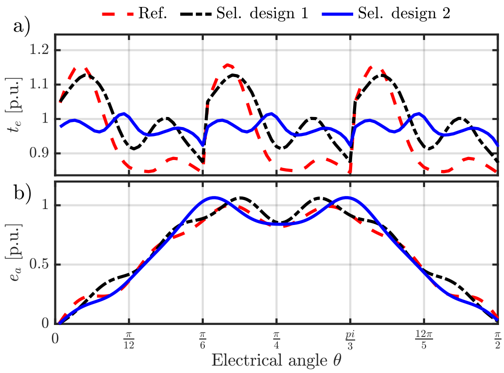

Figure 5: Torque waveform and back EMF of all three designs

Fig. 5 presents the back EMFs and the electromagnetic torque t_e of the selected designs and reference design and Table I presents the optimized values of the discussed machine designs.

Table 1: Optimization and design values

	Ref. design	Design 1	Rel. to ref.	Design 2	Rel. to ref.
$t_{e,ripp}$ [p.u.] – NN	/	0.238	/	0.1179	/
$t_{e,ripp}$ [p.u.] – FEM	0.3146	0.2531	-19.6%	0.0925	-70.6%
$t_{e,avg}$ [p.u.] – NN	/	1.033	/	0.975	/
$t_{e,avg}$ [p.u.] – FEM	0.949	1.003	5.7%	0.974	2.6%
d_{rd} [p.u.]	0.074	0.001	/	0.002	/
d_{rq} [p.u.]	0	0.13	/	0.037	/
d_{ry} [p.u.]	0.563	0.675	/	0.733	/
θ_{rm} [°]	0	-24.90	/	18.7	/
θ_v [°]	7.5	6.7	/	7.8	/

Design 1 showed 19.6% reduction of the $t_{e,ripp}$ and 5.7% increase of the $t_{e,avg}$ compared to the reference design after the FEM analysis. The waveform of the t_e did not change significantly in contrast to the reference design. The increase in $\mathbf{e}_{abc}$ led to a higher $t_{e,avg}$, further amplified by the decreased value of the $t_{e,ripp}$. The rotor in design 1 featured a V-shaped magnet configuration.

Design 2 reduced the $t_{e,ripp}$ significantly by 70.6% and increased the $t_{e,avg}$ by 2.6% compared with the reference design. The shape of $\mathbf{e}_{abc}$ aligned better with $\mathbf{i}_{abc}$, causing $t_{e,ripp}$ reduction and still increasing $t_{e,avg}$. In design 2, the rotor's configuration positioned the magnets along the outer perimeter.

IV Conclusions

A successful implementation of NN in two-objective machine optimization was showcased. By employing NN as meta-models of respective FEM models within the optimization workflow, the simulation time was reduced by a factor of 5. This workflow enabled the saving of all machine data during the DoE step, allowing for various types of optimization in post-processing using NN.

Both optimized designs show a reduction of $t_{e,ripp}$ and an increase of $t_{e,avg}$, with a minor trade-off in the secondary objective. The initial goal was achieved by reducing the $t_{e,ripp}$ and additionally improving the torque-to-current ratio with both designs. Design 1 featured a V-shape and design 2 pushed the magnets to the outer perimeter.

As the current waveform for optimization was idealized as a squarewave, the gained effect will be checked at a system-level simulation in the full paper. There the current waveform $\mathbf{i}_{abc}$ and the a change because of the commutation interval, which is a consequence of activating individual windings and their leakage inductance.

References

[1] J. Zhou, J. Lu, S. Ebrahimi, and J. Jatskevich, "A Compensation of Commutation Angle in Hall-Sensor-Controlled Brushless DC Motors for Maximum Torque per Ampere Operation," in *2022 21st International Symposium INFOTEH-JAHORINA (INFOTEH)*, 2022-03-16 2022: IEEE, doi: 10.1109/infoteh53737.2022.9751320.

[2] D. Mohanraj *et al.*, "A Review of BLDC Motor: State of Art, Advanced Control Techniques, and Applications," *Ieee Access,* vol. 10, pp. 54833-54869, 2022-01-01 2022, doi: 10.1109/access.2022.3175011.

[3] V. Parekh, D. Flore, and S. Schops, "Variational Autoencoder-Based Metamodeling for Multi-Objective Topology Optimization of Electrical Machines," *IEEE Transactions on Magnetics,* vol. 58, no. 9, pp. 1-4, 2022-09-01 2022, doi: 10.1109/tmag.2022.3163972.

MODELLING THE ANISOTROPIC PROPERTIES OF GRAIN-ORIENTED MATERIALS

FLORAN MARTIN, JULIEN TAURINES, ANOUAR BELAHCEN

Aalto University, Department of Electrical Engineering and Automation, Aalto, Finland
floran.martin@aalto.fi, julien.taurines@g2elab.grenoble-inp.fr, anouar.belahcen@aalto.fi

Grain oriented material presents highly anisotropic properties involving both the magnetocrystalline anisotropy and shape anisotropy. Whereas the former is generally well known for iron silicon alloys, the later involves a complex domain decomposition. In this paper, we propose to model the anhysteretic vector properties of grain-oriented steel sheet with a multiscale model. The complexity of the domain decomposition is simplified by a simple shape anisotropy term. The general trend of the measured anhysteretic flux density components can be reproduced by the model.

DOI
https://doi.org/10.18690/um.feri.4.2025.26

ISBN
978-961-286-986-1

Keywords:
soft magnetic material, grain oriented material, magnetocrystalline anisotropy, demagnetization anisotropy, domain configuration

University of Maribor Press

I Introduction

Grain-oriented materials presents advantageous magnetic properties in large transformer. Thanks to their large grain size, they hysteresis loss are lower than the microscopic grain in non-oriented steel sheets. Furthermore, the magnetizing current of electric application remains very low thanks to the high permeability. The Goss texture aligns the crystal easy axis, <100>, with the rolling direction and the crystal medium axis, <110>, aligns toward the transverse and the normal direction. Whereas the crystal anisotropy is strongly orienting the magnetization, the thin sheet is about ten times smaller than the grain length. This specific shape leads to a significant demagnetization effect due to stray field. The combination of both the crystal anisotropy and the shape anisotropy leads to a very specific pattern of magnetic domains [1]. In Fig. 1, the domain lancets appear near the grain boundary while magnetizing the grain-oriented toward their easy direction [2], the domain branching corresponds to the application of a magnetic field along the transverse direction [1,3,4].

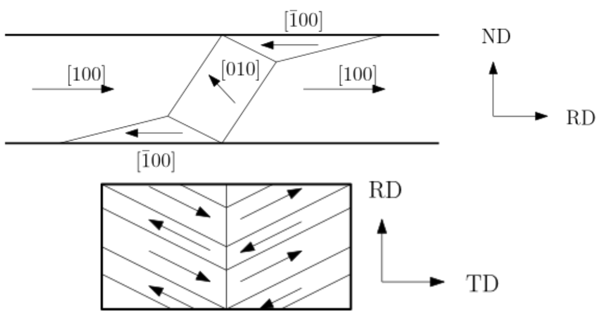

Figure1; Representation of the domain pattern in grain oriented steel sheet in the case of a magnetic field applied along the rolling direction, RD, (left) and the transverse direction, TD, (right). ND stands for the normal direction

The characterization of grain-oriented material requires a precise experimentation. Due to the specific nature of the domain decomposition, a significant magnetization component directed toward the normal direction is measured on a round rotational single sheet tester [5]. Hence, the magnetic model of grain-oriented material should account for a 3D representation of the anisotropy. Whereas the coenergy model developed in [6,7] can properly reproduced the measurements of the anhysteretic property [8], we employ the multiscale model deployed in [2] due to its inherent 3D properties and the explicit description of the grain misalignment. In our method, the demagnetization tensor presents the physical property of a unit trace with cross-coupling effect in the crystal frame.

II Multi-Scale Model for Grain-Oriented Steel Sheet

The multiscale model described in [2] is adjusted to incorporate the shape anisotropy of an oblate ellipsoid in the steel sheet frame [1]. The diagonal demagnetization tensor is rotated into the single crystal frame, leading to symmetric cross-coupling component between the normal and the transverse component when the magnetization of the domain remains along the easy axis of the crystal. Furthermore, the orientation of the magnetic domains are computed by minimizing the energy, the sum of the Zeeman energy, the magnetocrystalline anisotropy energy, and the demagnetization energy. The volume fraction of the six domains is evaluated with a Boltzmann distribution similarly as in [2]. Finally, the magnetization is reconstructed with the weighted vectorial sum of the six magnetic domains.

III Results and Discussion

The Fig.2 presents the simulation results for an ideal grain oriented steel sheet with Bunge-Euler angles (0^o, 45^o, 0^o). The magnetic field is applied in the (RD,TD) plane with three different directions with respect to the rolling direction (RD). The amplitude of the in-plane flux density and the angle of the in-plane flux density are respresented in the left and the middle. Similarly as the experiments conducted by Goričan et al. [5], the out-of plane component of the flux density is significant and can reach more than half of the saturation level (Fig.2, right).

The Fig.3 presents the measured in-plane component of the flux density for the same condition of the applied magnetic field as in the simulation. The non-monotonous behavior of the in-plane amplitude of the flux density appears for an applied field oriented by 60^o and 75^o with respect to the rolling direction. The multiscale model can reproduce this non-motonous behavior for the former field direction, only. Neverthless, the in-plane angle of the flux density can be properly approached with the multiscale model. The out-of plane component of the flux density was not measured in [8] so we can not properly compared the simulation in this case. In the future, the effect of the grain misalignment will be considered together with a proper fit of the shape anisotropy parameters. Furthermore, the shape anisotropy energy should be evaluated for the various domain configuration represented in Fig. 1.

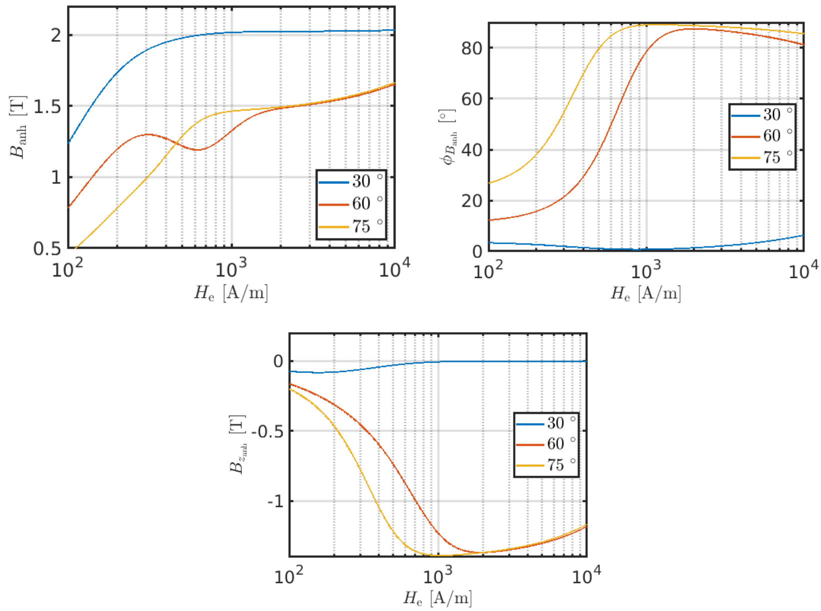

Figure 2: Multiscale simulation results for three orientations of the applied magnetic field. The amplitude of the in-plane flux density, the phase of the in-plane flux density, and the out of-plane component of the flux density are represented from left to right with respect to the amplitude of the applied field.

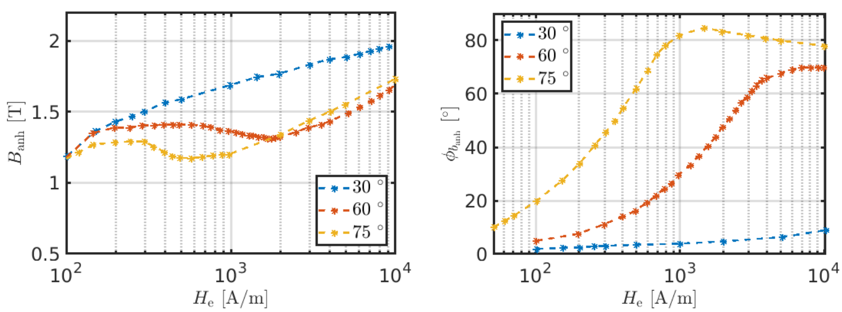

Figure 3: Anhysteretic measurement of the M6H grade of 3% FeSi grain-oriented materials [7,8]. The in-plane flux density amplitude and the in-plane phase of the flux density are represented from left to right with respect to the amplitude of the applied field for three different orientations of the magnetic field.

References

[1] A. Hubert and R. Schäfer, *Magnetic domains: The analysis of magnetic microstructure* Berlin, Springer, 2009.

[2] O. Hubert and L. Daniel, "Multiscale modeling of the magneto-mechanical behavior of grain-oriented silicon steels", *J. Magnetism and Magnetic Materials*, vol. 320, No. 7, pp. 1412-1422, 2008

[3] J. Shilling and G. Houze, "Magnetic properties and domain structure in grain-oriented 3% Si-Fe", *IEEE Transactions on Magnetics*, vol. 10, no. 2, pp. 195-223, 1974

[4] V.I. Efimov, "Domain structure of silicon iron single crystals", Soviet Physics Journal, vol. 18, pp. 685-687, 1975

[5] V. Goričan et al., "Interaction of z component of magnetic field between two samples of GO material in the round rotational single sheet tester (RRSST)", *J. Magnetism and Magnetic Materials*, vol. 304, No. 2, pp. 558-560, 2006

[6] T. Péra, F. Ossard, and T. Waeckerle, "Numerical representation for anisotropic materials based on coenergy modeling", Appl. Phys., vol. 73, No. 10, pp. 6784-6786, 1993

[7] T. Waeckerle, *Integration des aciers magnétique en électrotechnique,* HDR thesis, Laboratoire en génie électrique de Grenoble G2ELab, 2013

[8] G.M Fasching and H. Hofmann, "Meßeinrichtung für anisotrope Elektrobleche", *Archiv für technisches messen und industrielle messtechnik,* vol 396-407, pp. 57-68, 1969

THE IMPLEMENTATION OF PULSE-DENSITY MODULATED WIRELESS POWER SYSTEM USING A SLIDING MODE CONTROLLER

DOI
https://doi.org/10.18690/um.feri.4.2025.27

ISBN
978-961-286-986-1

NATAŠA PROSEN, MITJA TRUNTIČ, FRANC MIHALIČ, JURE DOMAJNKO

University of Maribor, Faculty of Electrical Engineering and Computer Science, Maribor, Slovenia
natasa.prosen@um.si, mitja.truntic@um.si, franc.mihalic@um.si, jure.domajnko2@um.si

The efficiency of the wireless power transfer (WPT) using a half-bridge inverter on the transmitter side can be increased by switching from frequency modulation (FM) to pulse density modulation (PDM). The method of generating PDM, described and implemented in this paper is based on a sliding mode controller (SMC), which also serves as a transmitter coil current controller. The current controller is in a cascade with the output voltage controller, which can be implemented either on the transmitter or on the receiver side.

Keywords:
inductive power transfer,
half-bridge inverter,
pulse density modulation,
sliding mode control,
FPGA

University of Maribor Press

I Introduction

Wireless charging is currently very popular, especially with low-powered consumer-grade mobile devices [1]. Efficiency of the transfer is usually not a concern, because of the low transferred power and slow charging speeds.

The most popular method of wireless power transfer is the inductive power transfer (IPT). The main advantages are safety, robustness, and ease of use. On the other hand, the IPT systems can transfer power only across short to medium distances with limited efficiency. The efficiency heavily depends on the coupling coefficient between the transmitter and the receiver coil. The coupling coefficient is affected by distance and misalignment between the coils. Therefore, it is important to correctly position the transmitter and the receiver coil.

Low-power systems usually replace full-bridge high-frequency inverters with half-bridge inverters. This reduces the complexity and price of the transmitter. The downside is, that the voltage and current control of the IPT system is limited to frequency modulation, which results in additional circuit losses. The solution can be pulse density modulation (PDM). The PDM is usually implemented using delta-sigma modulation, which usually results in limited modulation resolution [2].

This paper presents the different implementations of the PDM, using a sliding mode current controller, which results in better resolution and precise control of the transmitter current.

II Implementation of PDM

The IPT system is usually controlled using the fundamental or average transmitter voltage. The average transmitter voltage, generated by the half-bridge inverter using PDM can be calculated using:

$$\bar{u}_T = \left(\frac{2U_{DC}}{\pi} d \right) \sin\left(\omega_s t\right) = \bar{U}_T \sin\left(\omega_s t\right) \tag{1}$$

where d is the pulse density of the modulation, with a value between 0 and 1, with 0.1 step resolution in case the sigma-delta modulation is used [2].

However, pulse density modulation can also be implemented using sliding mode control (SMC), which is relatively easy to implement on systems with transistor switches. In IPT systems, SMC is usually implemented on the receiver side, for controlling the DC-DC converter for battery charging [3]. SMC presents non-linear control with variable structure. The change in the structure of the system is based on the location of the error signal regarding the sliding surface [4].

The bounded sliding mode surface is presented in Fig. 1. The boundary layer ε was introduced in order to reduce the chattering of the controller. The two-dimensional sliding surface $S = 0$ is dependent on the parameters x_1 and x_2. The sliding mode surface is defined by:

$$S = k_\alpha x_1 + k_\beta x_2 \tag{1}$$

where S is the sliding trajectory, which is dependent on the x_1 and x_2. Parameter k_α is the constant of the first parameter and k_β is the constant of the second parameter. Both constants should be positive.

To implement PDM on a half-bridge converter, SMC is used to control the transmitter current, instead of the output voltage of the DC-DC converter. The main objective of the SMC is to minimize the error between the reference transmitter current and the average, measured transmitter current. The error can be expressed as:

$$x_1 = I_{T,ref} - I_T \tag{2}$$

where x_1 is the first parameter of the sliding trajectory, $I_{T,ref}$ is the reference transmitter current and I_T is the measured average current.

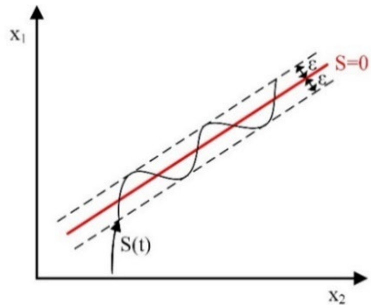

Figure 1: Sliding surface with boundary layer

The second sliding trajectory parameter is derived from the first parameter using:

$$x_2 = \int_t x_1(t)\,dt \tag{3}$$

The control output depends on the value of the sliding mode trajectory. The output of the half-bridge inverter switches from on-state to off-state with the following control law:

$$U_T = \begin{cases} \dfrac{2U_{DC}}{\pi} & S \geq \varepsilon \\ 0 & S < -\varepsilon \end{cases} \tag{4}$$

If the sliding surface is more than ε, the error is positive. The reference current is larger than the measured current. Therefore, the inverter must generate a voltage in order to increase the transmitter current. On the other hand, if the trajectory is below −ε, the error is negative. The transmitter current is greater than the reference current and the inverter should be off.

III Experimental results

The proposed implementation of the PDM was tested on a small-scale IPT system. The basic elements of the system are presented in Fig. 2. The system was powered by the constant voltage from the laboratory power supply. For the transmitter and receiver coil, two Qi-compatible coils were used. The sliding mode transmitter controller and PI voltage controller were implemented on the transmitter side using a Field Programmable Gate Array (FPGA). The wireless transfer distance was set to 6 mm. During experiments, the maximum DC-to-DC efficiency was up to 85%, at maximum output voltage and perfect coil alignment.

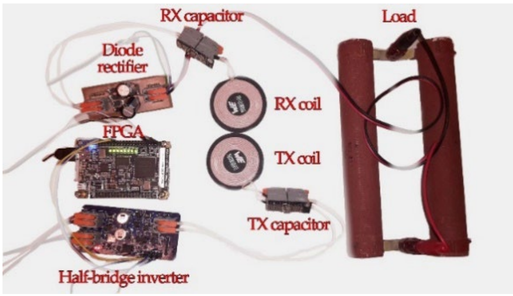

Figure 2: System with nonlinear elements

The main problem of the PDM is that the transmitter current has no constant amplitude. Therefore, it is important to control the average transmitter current and not the peak transmitter current. This can be achieved by using an averaging circuit after the current sensor.

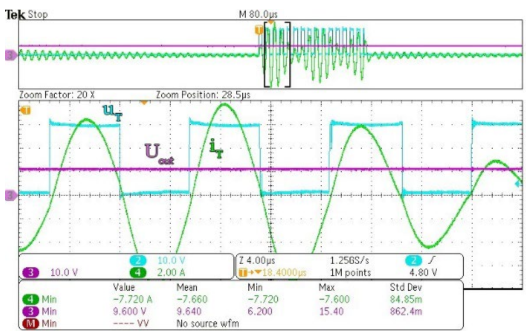

Figure 3: Detailed input signals of IPT system with perfectly aligned coils

The input signals of the operating IPT system are presented in Fig. 3, for the case, when the coils are perfectly aligned and Fig. 4., when the coils are misaligned by 10 mm in the *y* direction. In both cases, the controlled output voltage is 10 V. The blue signal represents the transmitter voltage, the green signal represents the transmitter current, and the purple signal represents the output voltage. In Fig. 4 the coupling coefficient is lower due to the coil misalignment. The current controller therefore increases the PDM, to reduce the error between reference and measured voltage.

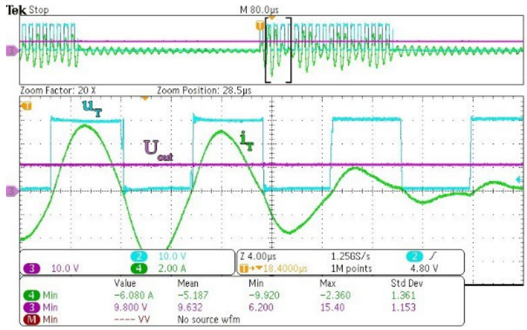

Figure 4: Detailed input signals of IPT system with misaligned coils

IV Conclusion

The efficiency of the IPT system using half-bridge inverter, can be increased by replacing frequency modulation for PDM. The PDM is usually implemented using delta-sigma modulation which result in limited modulation resolution. On the other hand, if PDM is implemented using sliding mode controller, the resolution of the modulation is increased. Additionally, the transmitter current is controlled with desired reference and can help limit the current at low coupling coefficients.

References

[1] X. Lu, D. Niyato, P. Wang, D. I. Kim, and Z. Han, "Wireless charger networking for mobile devices: Fundamentals, standards, and applications," *IEEE Wireless Communications*, vol. 22, no. 2, pp. 126–135, 2015

[2] H. Li, J. Fang, S. Chen, K. Wang, and Y. Tang, "Pulse density modulation for maximum efficiency point tracking of wireless power transfer systems," *IEEE Transactions on Power Electronics*, vol. 33, no. 6, pp. 5492–5501, 2017.

[3] V. Utkin, "Sliding mode control of dc/dc converters," *Journal of the Franklin Institute*, vol. 350, no. 8, pp. 2146–2165, 2013.

[4] Y. Shtessel, C. Edwards, L. Fridman, A. Levant et al., Sliding mode control and observation. *Springer*, 2014, vol. 10.

DOI
https://doi.org/
10.18690/um.feri.4.2025.28

ISBN
978-961-286-986-1

UNCONTROLLED GENERATION IN NINE-PHASE MACHINE DRIVE

ŽIVA STARE, RASTKO FIŠER, KLEMEN DROBNIČ
University of Ljubljana, Faculty of Electrical Engineering, Ljubljana, Slovenia
ziva.stare@fe.uni-lj.si, rastko.fiser@fe.uni-lj.si, klemen.drobnic@fe.uni-lj.si

Keywords:
permanent magnet synchronous machine,
multiphase machine,
uncontrolled generation,
field-weakening operation,
post-fault operation

Uncontrolled generation (UCG) is a phenomenon that occurs in electric drives when operating in a field-weakening and a gate signal is suddenly removed from switches. When the induced voltage is higher than the DC link voltage, a path is created for current to flow from the machine through the freewheeling diodes of the converter back into the DC link. While UCG is commonly associated with three-phase drives, the topology of some multiphase machine drives—comprising separate three-phase winding sets—enables the manifestation of UCG in only one winding set. This arrangement allows the remaining two winding sets to facilitate post-fault operation.

University of Maribor Press

I Introduction

Multiphase machines (MM) with the number of phases equal to a multiple of 3, can have their phases organised into three-phase winding sets. Each winding set (WS) consists of three phases, which have a spatial distribution of $2\pi/3$. The division into three-phase winding sets has the advantage of treating each WS as a three-phase machine and we can use the already known and accessible technology for the control.

During field weakening operation various faults can occur in the MM drive. One of the ways to control these is to deactivate the winding set in which the respective faulty phase is located. Deactivating one of the winding sets can lead to uncontrolled generation, i.e. a reverse current occurs which flows from the machine back into the DC link through free-wheeling diodes. This large diode current can damage the inverter or shorten the service life of the power devices. This phenomenon is mainly described for three-phase machine drives [1], but in this article, the focus is on a MM drive.

II Nine-phase machine DRIVE

The UCG in a MM drive is described for a nine-phase synchronous machine with surface-mounted permanent magnets (9SPM). The nine phases are organized into three winding sets. Each WS has an isolated neutral point. The sets are mutualy weakly magnetically coupled and electrically aligned. A layout of the WS alignment in a 9SPM is shown on the right-hand side of Fig. 1. This type of MM can also be found in the literature under the name modular triple three-phase machine [2].

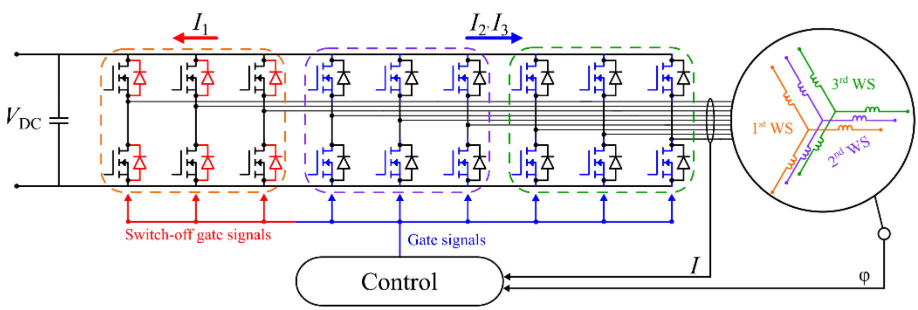

Figure 1: Schematic diagram of an uncontrolled generation in a 9SPM machine drive

III Uncontrolled generation

The UCG phenomenon in a MM drive is described with the help of Fig. 1. As shown in the figure, a nine-phase machine drive consists of a 9SPM, a nine-phase inverter, a DC link and control.

Various faults (e.g. overcurrent) in the machine drive can occur during the rotation of the machine in a high-speed range, i.e. deep in the field weakening region. Since the analysed MM consists of three winding sets that have isolated neutral points, one of the ways to protect the drive from the inevitable faults is to simply disable the faulty WS. The faulty WS is deactivated by applying switch-off gate signals to the corresponding transistors in the nine-phase inverter.

Consequently, the deactivation of certain transistors when the 9SPM rotates at high-speed causes UCG. A relatively large current (I_1 in Fig. 1) can be generated in the deactivated WS, which then flows back into the DC link via the uncontrolled rectifier (marked as red freewheeling diodes in Fig. 1) and poses a great risk to the power devices. This diode current results from the fact that the rotor speed is much higher than the base speed n_{base}, which marks the highest threshold value of the constant-torque speed range. Consequently, the amplitude of the line-to-line back electromotive force exceeds the DC link voltage V_{DC}, which means that the disabled WS operates as a generator and charges the DC circuit via the uncontrolled rectifier [1].

The rotor speed at which UCG occurs can be approximated using the following equation [1], [3],

$$n_{\text{UCG}} \approx \frac{V_{\text{DC}}/\sqrt{3}+2\cdot V_{\text{F}}}{V_{\text{DC}}/\sqrt{3}} \cdot n_{\text{base}}. \tag{1}$$

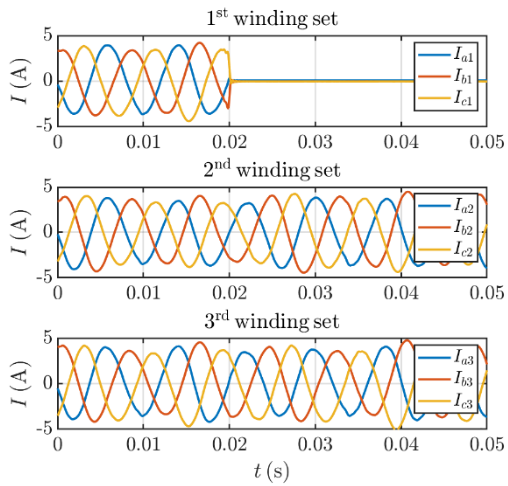

Figure 2: Phase currents of a 9SPM machine drive during a deactivation of the 1st winding set (n = 2490 rpm)

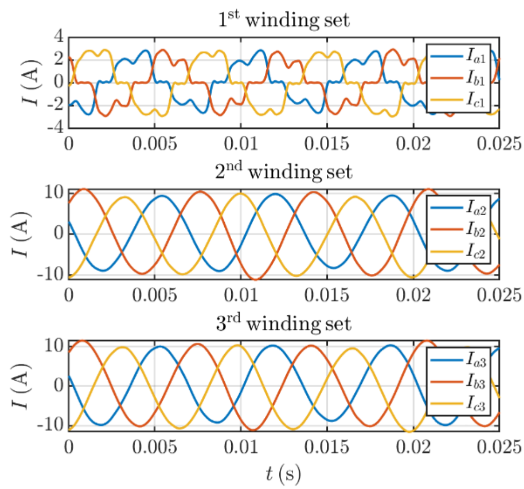

Figure 3: Phase currents of a 9SPM machine drive during uncontrolled generation (n = 3000 rpm)

The UCG can be recognised when one of the deactivated winding set's line-to-line voltages is greater than the threshold voltage $V_{DC}/\sqrt{3} + 2 \cdot V_F$, where V_F stands for the forward voltage drop of a freewheeling diode [1].

During the UCG in the deactivated WS, the other two (active) sets continue to operate as a motor, i.e. the currents I_2 and I_3 flow from the DC circuit through the controlled inverter (marked as blue transistors in Fig. 1) to the active winding sets in the machine.

IV Experimental results

For the experimental validation of the occurrence of UCG in a MM drive, a nine-phase machine drive with the parameters listed in Table 1 was used.

Table 1
Machine Drive Parameters

Parameter	Value	Unit
Base speed n_{base}	2217	rpm
DC circuit voltage V_{DC}	12	V
Maximum current I_{max}	16.6	A
Forward voltage of diodes V_F	0.7	V
Stator winding resistance R_s	80	mΩ
Self-inductance L_s	255	µH
Mutual inductance L_{m1}	17	µH
Mutual inductance L_{m2}	-31	µH
Permanent magnet flux linkage Ψ_{PM}	8.9	mWb
Number of pole pairs p_p	3	-

The measurements were carried out in the following sequence. The 9SPM drive was accelerated in a no-load operating mode to the referenced speed and then the transistors of the first winding set were intentionally switched off.

The rotor speed at which UCG occurs was calculated using (1) and the threshold value is n_{UCG} = 2665 rpm. If the reference speed of 9SPM drive is lower than the threshold value, UCG does not occur and there is no diode current in the deactivated WS. This can be seen in Fig. 2, where at time t = 0.02 s the 1st WS is deactivated and there are no phase currents in the 1st WS after the transistors are switched off. The other two sets are still active and the amplitude of the currents in them is slightly higher in order to compensate for the deactivated WS and maintain the operating point of the drive.

At rotor speeds slightly higher than n_{UCG}, UCG occurs, but the diode current is small. To demonstrate a large diode current, a measurement of the phase currents was carried out at the speed n = 3000 rpm (Fig. 3). It can be seen that the diode current in the switched-off 1st WS is large, its amplitude is about one third of the current amplitude in the active winding sets. The diode phase currents are not continuous, which is determined by the diode conduction characteristics of the uncontrolled rectifier [1]. An analysis of the d and q components of the diode current showed that the current generates braking torque (the q-component of I_1 was negative). Consequently, the two remaining winding sets must operate in a post-fault state, maintaining original operating point of the drive while compensating for the braking torque induced by the diode current.

V Conclusion

In this paper, a brief analysis of UCG in a nine-phase machine drive was carried out. It was shown analytically and with measurements that the rotor speed must be deep in the field weakening region for uncontrolled generation to occur.

In future work, we will focus on further analysing the phenomenon, also by disconnecting more than one winding set. It will also be beneficial to include simulation results.

Acknowledgement

This work was funded by the Slovenian Research and Innovation Agency (ARIS) under the Young Researchers PhD Program.

References

[1] C. Gong, Y. Hu, C. Gan, G. Chen, and M. Alkahtani, 'Modeling, Analysis, and Attenuation of Uncontrolled Generation for IPMSM-Based Electric Vehicles in Emergency', *IEEE Trans. Ind. Electron.*, vol. 67, no. 6, pp. 4453–4462, Jun. 2020, doi: 10.1109/TIE.2019.2926049.

[2] S. Rubino, O. Dordevic, E. Armando, I. R. Bojoi, and E. Levi, 'A Novel Matrix Transformation for Decoupled Control of Modular Multiphase PMSM Drives', *IEEE Trans. Power Electron.*, vol. 36, no. 7, pp. 8088–8101, Jul. 2021, doi: 10.1109/TPEL.2020.3043083.

[3] P. Pejović and J. W. Kolar, 'An Analysis of Three-Phase Rectifiers with Constant Voltage Loads', in *5th European Conference on Circuits and Systems for Communications*, Belgrade,Serbia, 2010.

Current-Transformer Saturation Reconstruction Using a Normalized Least Mean Squares Adaptive Method

Amin Saremi,[1] Younes Mohammadi,[1]
Davood Khodadad,[1] Boštjan Polajžer[2]

[1] Umeå University, Department of Applied Physics and Electronics, Umeå, Sweden
amin.saremi@umu.se, younes.mohammadi@umu.se, davood.khodadad@umu.se
[2] University of Maribor, Faculty of Electrical Engineering and Computer Science, Maribor, Slovenia
bostjan.polajzer@um.si

This paper proposes a computationally light adaptive-filtering approach, normalized least mean squares (NLMS), to model the nonlinearity caused by the current transformer (CT) iron core saturation. A simplified CT model was used to generate a dataset considering four different nonlinear iron core magnetic characteristics. The preliminary results show satisfactory results in the cases where the CT iron core nonlinearity is within certain limits.

DOI
https://doi.org/10.18690/um.feri.4.2025.29

ISBN
978-961-286-986-1

Keywords:
current transformer,
saturation,
reconstruction,
signal processing,
adaptive filter

University of Maribor Press

I Introduction

A well-known challenge in electrical power engineering is related to the saturation of the current transformer (CT) iron core. This phenomenon lowers measurement accuracy and may lead to the misoperation of protection relays. Several strategies have been suggested to mitigate the effects of CT iron core saturation, categorized into model-based, signal-processing and data-driven methods. A literature review on this topic can be found in [1–3].

This paper presents a solution based on the normalized least-mean-square (NLMS) adaptive method, commonly known as the Wiener filter. Adaptive filters, such as the NLMS method, have been utilized for decades for system identification tasks in control engineering, acoustics, and other signal-processing domains [4–5]. Despite the highly nonlinear nature of CT iron core saturation, we have explored how a computationally efficient linearized approach can still provide satisfactory predictions. In this approach, the model assumes that the system is semi-linear and adequately time-invariant within certain constraints. The objective is to identify the system by finding the finite impulse response of a linear model capable of closely approximating the input-output relationship.

II Method Description

A Dataset generation

Measured secondary currents I_S were obtained using a simplified CT model, neglecting windings resistance and leakage inductance. Thus, a first-order system with nonlinear feedback was used, with the nonlinearity capturing the magnetic characteristic of the iron core (flux versus mmf). Four different CT types were considered: CT1 with an over-sized iron core, CT2 with a standard-sized iron core, and CT3 and CT4 featuring an iron core with one or more air gaps.

Power system faults were simulated, where the magnitude of the pre-fault I_S was set as 1 A, whereas the steady-state magnitude of I_S during the fault was varied from 2 A to 15 A. Furthermore, different fault inception angles were used, including 0°, 45°, 90°. The time constant of the primary aperiodic component has also been varied in the range of 20 ms to 200 ms. In total, 798 cases were simulated, with a sampling time of 0.5 ms used to generate the measured I_S. The desired I_S were generated similarly but using a CT model with linear magnetic characteristics.

Fig. 1 shows illustrative time responses for CT3, where steady-state of I_S was 10 A, with a fault inception angle of 90° and a 100 ms primary current time constant. The aperiodic component in the current causes an increase in the magnetic flux. The saturation effect is evident in the time responses of the nonlinear model, reflecting a distortion of the measured I_S.

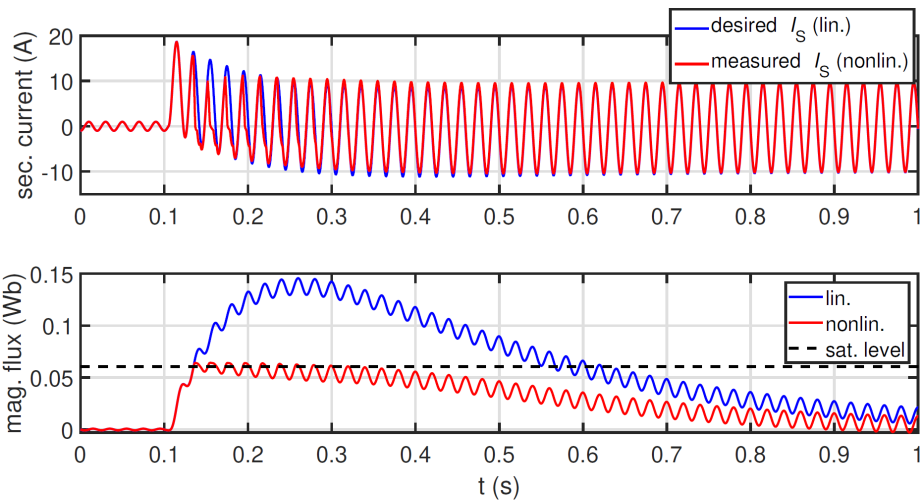

Figure 1: Time responses of linear and nonlinear models for CT3

B The NLMS adaptive algorithm

The dataset is divided into two parts. Half of the dataset (399 odd cases) is designed for training, and the remaining half (399 even cases) is reserved for the final evaluation of the method. The algorithm consists of two Wiener filters arranged in series. The first filter is 30 samples long (15 ms), whereas the second filter contains 40 samples (20 ms). For CT3 and CT4 datasets, however, both filters contain 40 samples. An initial impulse response $\hat{h}[n]$ is applied on the input signal $x[n]$, i.e., measured I_S, to generate an initial prediction $\hat{y}[n]$ according to (1), where * denotes convolution.

$$\hat{y}[n] = x[n] * \hat{h}[n] \tag{1}$$

The error signal $e[n]$ is defined as the difference between the desired response $y[n]$, and the model's prediction $\hat{y}[n]$. The adaptation process occurs by estimating a new $\hat{h}[n]$ for each sample of $y[n]$ through a small adjustment by $\Delta\hat{h}[n]$ in each iteration, as expressed in (2) where $\mu[n]$ is 'step size'.

$$\begin{aligned} \hat{h}[n+1] &= \hat{h}[n] + \Delta\hat{h}[n] \\ \Delta\hat{h}[n] &= \mu[n]\,(x[n]\,e[n]) \\ \mu[n] &= \frac{\alpha}{\beta+\sigma^2_{x[n]}}, \quad \sigma^2_{x[n]} = x^{\mathrm{T}}[n]\,x[n] \end{aligned} \tag{2}$$

Choosing an optimal step size is important for the system's accuracy and has been studied extensively [6]. In this study, we set $\beta = 0.01$, whereas α was assigned to 0.1 and 0.05 for the first and second filters, respectively.

The algorithm initially compares the input signal $x[n]$ with the entire training dataset to identify the closest case, yielding the maximum normalized correlation coefficient (NCC). Subsequently, it applies the filter coefficients obtained from the corresponding training case to the evaluation data. A representation of the described algorithm is shown in Fig. 3.

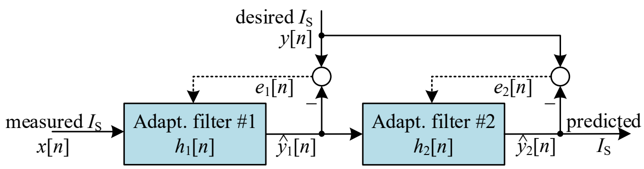

Figure 2: Blok diagram of the discussed adaptive algorithm

III Results

The predictions of the model $\hat{y}[n]$ were compared with the desired output $y[n]$. Mean Absolute Error (MAE), Root Mean Square Error (RMSE) and Total Vector Error (TVE) were calculated as follows:

- $\mathrm{MAE} = \frac{1}{N}\sum_{i=1}^{N}(\mathrm{abs}\,(\hat{y}[i] - y[i]))$, where N is the number of samples in the signal for 10 cycles after the fault inception;

– RMSE$[i]$ $= \sqrt{\frac{1}{N}\sum_{i}^{i-N}(\hat{y}[i] - y[i])^2}$ computed for a one-cycle sliding window;

– TVE$[i]$ $= \sqrt{\left(Re(\underline{\hat{Y}}[i]) - Re(\underline{Y}[i])\right)^2 + \left(Im(\underline{\hat{Y}}[i]) - Im(\underline{Y}[i])\right)^2}$ where $\underline{\hat{Y}}[i]$ and $\underline{Y}[i]$ are fundamental harmonic phasors computed for a one-cycle sliding window.

Furthermore, MAE, RMSE and TVE were calculated also for the measured I_S, i.e., by comparing the input $x[n]$ with the desired output $y[n]$. Metrics based on measured I_S are denoted as 'data', whereas metrics based on predicted I_S are denoted as 'model.' Fig. 4 shows an illustrative example for CT1, where steady-state of I_S was 9 A, the fault inception angle was 90°, and an 80 ms primary current time constant.

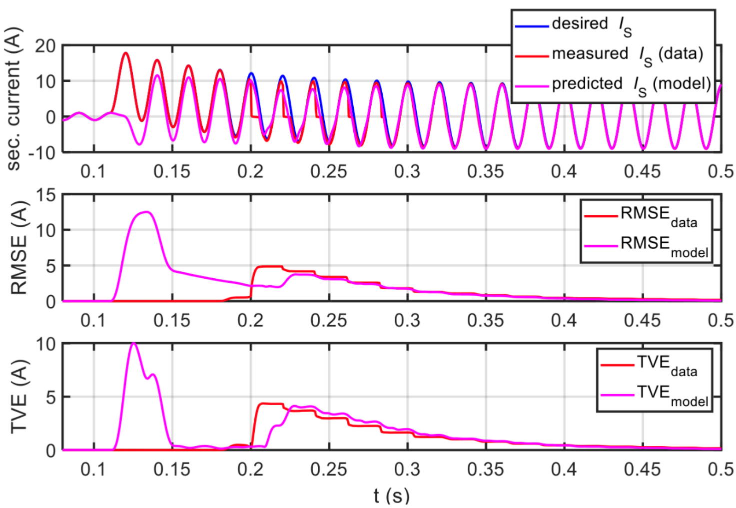

Figure 3: Results for CT1, where MAE$_{data}$ = 0.94 A, MAE$_{model}$ = 3.13 A

Fig. 5 shows MAE values for all evaluation cases related to CT1 as a function of the fault current magnitudes. The results show that the model is successful in the case of smaller fault current magnitudes (blue and red dots), generating more accurate results (smaller MAEs) than the data. However, the MAEs of the model are bigger than the MAEs of the data for higher fault current magnitudes (purple dots), which indicates the model's failure in those cases. Additionally, the time constant of the current's aperiodic component has a similar effect on MAE.

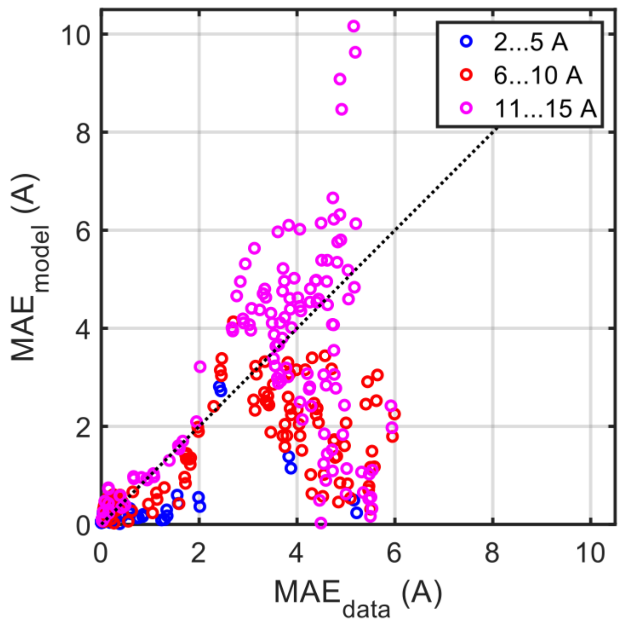

Figure 4. Comparison of MAE computed for the CT1 measurements (data) and predictions (model) for different values of the fault current magnitudes

IV Discussion and conclusions

Our objective was to explore the potential of adaptive filters, typically utilized for identifying semi-linear systems, in providing insights into iron core saturation in CTs. We deployed two Wiener filters to find the impulse response of the nearest linear system capable of producing comparable outputs. The code execution for all the 798 cases took less than 5 seconds on an Intel iCore 7 computer using MATLAB 2023b.

Preliminary results show that this approach could be effective for cases where CT nonlinearity falls within certain limits; however, it may fail for instances exceeding these limits. Although the discussed method is only partially successful, its computational simplicity and ease of implementation on real-time Digital Signal Processor (DSP) platforms warrant further investigation. Our next step involves quantifying the validity limits of our approach and applying it thoughtfully, ensuring successful prediction of the desired secondary currents.

References

[1] L. Alderete, M.C. Tavares, F. Magrin, "Hardware implementation and real time performance evaluation of current transformer saturation detection and compensation algorithms", *Electr. Power Syst. Res.*, Vol. 196, 207288, 2021.
[2] S. Key, S.-H. Kang, N.-H. Lee, S-Ry Nam, "Bayesian Deep Neural Network to Compensate for Current Transformer Saturation", *IEEE Access*, Vol. 9, pp. 154731-154739, 2021.
[3] S. Yang, Y. Zhang, Z. Hao, Z. Lin, B. Zhang, "CT Saturation Detection and Compensation: A Hybrid Physical Model- and Data-Driven Method", *IEEE Trans. Power Del.*, Vol. 37, No. 5, pp. 3928-3938, 2022.
[4] C. Paleologu, S. Ciochin, J. Benesty, S. L. Grant, "An overview on optimized NLMS algorithms for acoustic echo cancellation", *EURASIP J. Adv. Signal Process.*, 97, 2015.
[5] A. Saremi, B. Ramkumar, G. Ghaffari, Z. Gu, "An acoustic echo canceller optimized for handsfree speech telecommunication in large vehicle cabins", *EURASIP J. Audio, Speech and Music Process.*, 39, 2023.
[6] E. Hänsler, and G. Schmidt, *Acoustic echo and noise control: A practical approach.* Wiley, Hoboken, NJ, USA, 2004.

TOWARDS DESIGN RULE EXTRACTION FROM LARGE COMPUTATIONAL DATASETS BY CAUSAL CORRELATION ANALYSIS

DOI
https://doi.org/10.18690/um.feri.4.2025.30

ISBN
978-961-286-986-1

ARON SZUCS,[1,2] JUHANI MANTERE,[1] JAN WESTERLUND[1]

[1] ABB Large Motors and Generators, Technology Centre, Helsinki, Finland
aron.szucs@fi.abb.com, juhani.mantere@fi.abb.com, jan.westerlund@fi.abb.com
[2] University of Pécs, Pécs, Hungary
aron.szucs@fi.abb.com

Intuitive interpretation of the results from multi- objective numerical optimization of magnetically non-linear electrical machines is very challenging. The resulting designs are typically used "as they are" or tuned by trial and error, due to lack of deeper understanding needed for the tuning in the multi-objective Optimum Design Space (ODS). The results consisting of large sets of generic and optimum designs contain invaluable information on the emerging design rules. We recommend causal correlation analysis for design rule extraction.

Keywords:
causal correlation,
analysis,
electrical machines,
optimization,
design-rule extraction

University of Maribor Press

I Motivation for Causal Optimization and AI

Multi-objective optimization – such as genetic optimization or machine learning – for design work typically results in a black box type solution including large sets of optimum and not so optimum design data. While such results can be utilized directly by the designers, sometimes there rises the need to explain them deeper and to provide a more straightforward interpretation and wiser utilization. This can be seen as an attempt to discover the design rules inside the optimum design space (ODS), an approach commonly used in engineering.

Prior work published by the authors demonstrated the powerful capabilities of causal correlation fingerprinting which can provide insight into large datasets in a straightforward manner.[1] In this paper we introduce some approaches how design rules for electrical machines – a nonlinear magnetic problem – can be extracted by causal correlation analysis of the large sets of data coming from multi- objective optimization.

The example here is the design and optimization of magnet shapes with multi-objective goals, where part of the goals is the reduction of load torque harmonics, similarly as described in an ABB patent.[2] The methods proposed in this paper point toward an automated extraction of the relevant design rules in an optimized design space, for nonlinear magnetic problems by utilizing causal correlation analysis.

The causal correlations in the computed datasets are investigated by two approaches. One involves statistical causal analysis [2] and the other has been based on observation of the statistical correlations between variables. Our goal is to extract design rules how to reduce torque harmonics (TTHD) while remaining in the multi-objective design space. (ODS) For this analysis we separated the datasets into all computed designs and another including optimum designs in the pareto optimal front only.

The computations for the multi-objective optimization have been performed by 2D FEM analysis of the electrical machine designs considering nonlinear electromagnetics.

II Demonstration Case: Design Optimization of Permanent Magnet Generators

An industrially relevant case of electrical machine design optimization is the shaping of the permanent magnets in a rotor to reduce cogging torque and load torque harmonics. An ABB patent available publicly describes a magnet shape for such purpose and how design parameters affect these harmonics [2]. Such conclusions have been reached by the engineers going through the computed data and looking for correlations between design parameters and their effects on the performance. Fig 1 shows a picture form the patent describing the four design variables: B1 and H1 describing the total width and height of the magnet block respectively while B2 and H2 are associated with the width and height of the trapezoidal upper part of the magnet.

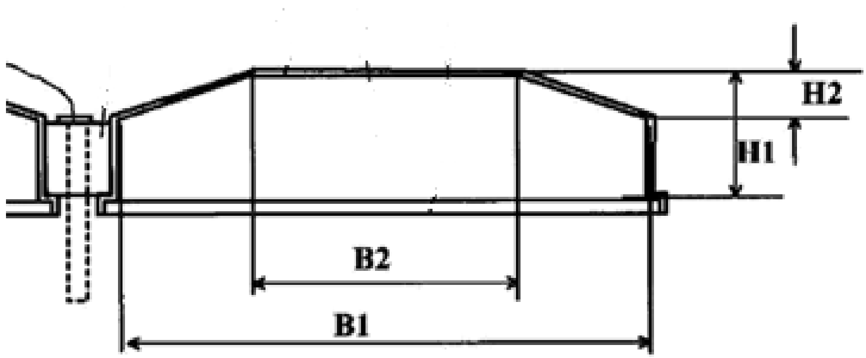

Figure 1: Shaped permanent magnet design with four design parameters.

Fig. 2 shows the dependence of cogging torque and load torque harmonics on the design parameters H2. Similar figures for the other design parameters are also described in the patent.

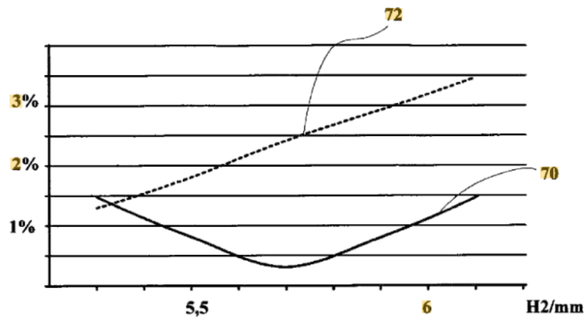

Figure 2: The effect of H2 vs cogging torque (70) and load torque harmonics (72) as described in the patent.

The challenge grows when multi-objective optimization is required. G.O. provides a set of designs for multi-objective goals but by default does not provide the clues to make new optimum designs, just offers to pick some from the pareto optimal front. Hence tuning the designs on the pareto optimal front and to find traditional design rule type correlations still requires time consuming, complex analysis of large amounts of data. The method proposed next provides support to assist and automate that creative work.

III Design Rule Extraction by Causal Correlation Analysis

Genetic optimization (GO) results not only in the pareto optimal front for recommended designs but also a large set of design variations in several generations of the optimization. These designs evolve according during genetic optimization, and we can observe how design parameters behave compared to performance parameters and in relation to each other. The relationship between design parameters can be seen as design rules and can be extracted by causal correlation analysis.

The correlation matrices between design parameters and TTHD for all designs in the optimization and for designs only existing in the ODS and their difference are shown in Fig.3.

All designs in optimization:

	B1	H1	B2	H2	TTHD
B1	1				-1
H1	-0.35131	1			
B2	-0.43703	0.071128	1		
H2	-0.37122	0.563094	0.38699	1	
TTHD	-0.4294	-0.03804	0.735515	0.27558	1

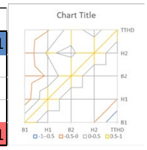

Optimized Design Space (ODS):

	B1	H1	B2	H2	TTHD
B1	1				-1
H1	0.147472	1			
B2	-0.58066	-0.54735	1		
H2	0.081175	0.342762	0.031959	1	
TTHD	-0.54935	-0.71011	0.864227	-0.27034	1

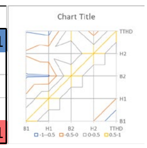

Difference:

	B1	H1	B2	H2	TTHD
B1	0	0	0	1	-1
H1	0.498778	0	0	0	0
B2	-0.14363	-0.61848	0	0	0
H2	0.452392	-0.22033	-0.35503	0	0
TTHD	-0.11995	-0.67207	0.128712	-0.54592	0

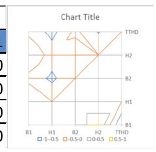

Fig. 3. The effect of the four design parameters on TTHD and on each other. Results from all designs are on the top and optimum designs on the pareto optimal front are in the middle, and their difference is in the bottom.

The causal analysis of the same datasets evolving from all designs to the ODS shown in Table I. Relevant causal correlations disappearing from all designs towards ODS are indicated in bold on the left and relevant correlations for the design rules in the ODS are indicated with bold on the right.

From these two approaches we can conclude that the highest causal correlations are between TTHD and design parameters B2 and H1 in the ODS and it is different for the “All designs”.

From the signs of the correlations one can extract a basic design rule to increase H1 and reduce B2 to reduce TTHD while remaining in the design space because H1 and B2 are also negatively causally correlated to each other in the ODS.

The correlation between H1 and B1 dropped to statistically insignificant levels in the ODS. Correlation between H1 and H2 is slightly positive so increasing H1 and slightly increasing H2 can be a design alternative as correlation between H2 and TTHD is also negative in the ODS. Another alternative could be to increase B1 also independently or with reducing B2 based on similar logic.

Table 1: Causal Correlation Analysis of All designs and the Optima

All designs:	**Designs on Pareto front:**
Causal Correlations:  Might be causal correlation: TTHD o--> B1 B2 o--> H1 H2 o--> H1 **B2 o--> B1** **H2 o--> B1** TTHD o--> H1 Seen as the Same phenomenon **B1 o--o H1** B2 o--o TTHD B2 o--o H1	Causal Correlations: 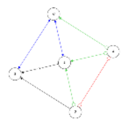 **H1 ---> H2** Might be causal correlation: TTHD o--> B1 **TTHD o--> H1** **B2 o--> H1** Seen as the Same phenomenon: **B2 o--o TTHD**

We can also study the causal correlations between actual values of the design variables and the performance parameters. In Fig. 4 we show how some of the concrete design parameter values correlate with low toque harmonic content within the ODS. This confirms the design rule on H1 above also. This approach will be explored further in the extended paper.

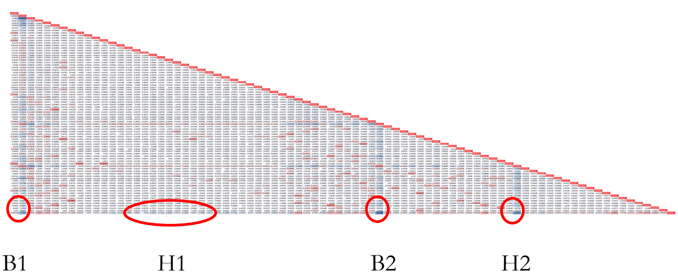

Figure 4: The correlation of the four design parameters values with TTHD and each other in the ODS. The circled areas of the optimum values show strong negative correlation with TTHD in the bottom row. B1, B2, H2 have sharp optimum ranges while H1 is more spread out.

Utilizing causal correlation analysis between design values and performance variables opens new opportunities. We can also study and identify the causal correlations between values ranges of the design variables and establish design rules easier.

IV Conclusions

The above example demonstrates the powerful potential of causal correlation analysis for design rule extraction from large electromagnetic computational datasets. The extended paper will elaborate deeper on causal correlation analysis of design parameter value ranges on performance parameters in the ODS.

References

[1] A. Szucs, "Characterizing the Performance of Field Computation and System Analysis by Causal Correlation Fingerprinting for Digital Twins," 2023 24th International Conference on the Computation of Electromagnetic Fields (COMPUMAG), Kyoto, Japan, 2023, pp. 1-4, doi:0.1109/COMPUMAG56388.2023.10411778.

[2] J Mantere, T Ryyppö, A Szucs, Permanent magnet electric machine and permanent magnet with linearly increasing air gap for an electric machine - US Patent 8,421,291, 2013

IMPROVED CONTROL OF DYNAMIC LOADS WITHIN HYDRAULIC SYSTEMS BY CONSIDERING NONLINEAR PROPERTIES OF PIPELINE FITTINGS

MYKHAYLO ZAGIRNYAK, TETYANA KORENKOVA,
VIKTORIYA KOVALCHUK, OLEKSII KRAVETS

Kremenchuk Mykhaylo Ostrohradskyi National University, Department of Systems of Automatic Control and Electric Drive, Kremenchuk, Ukraine
mzagirn@kdu.edu.ua, scenter@kdu.edu.ua, viktoriya_kovalch@ukr.net, mikhalych.83@gmail.com

It is shown that the existing methods and technical means of reducing dynamic loads in hydraulic systems do not allow to significantly reduce pressure fluctuations in the hydraulic network. It does not take into account the real hydraulic characteristics of pipeline fittings. The paper is devoted to the development of a method of reducing dynamic loads in the hydraulic systems by forming a non-uniform control law of the variable-frequency electric drive of pipeline fittings, which takes into account the nonlinear dependence of the coefficient of hydraulic resistance on the relative degree of opening of the valve's working body.

DOI
https://doi.org/10.18690/um.feri.4.2025.31

ISBN
978-961-286-986-1

Keywords:
hydrotransport system,
dynamic loads,
stopcock valve,
variable-frequency electric drive,
control law,
nonlinear hydraulic resistance coefficient

University of Maribor Press

I Introduction

During the operation of hydraulic systems (HS), processes occur in the hydraulic system, which are accompanied by increased dynamic loads in the form of surges, pressure drops and vibrations of technological equipment. They are caused by pressure fluctuations in the pipeline. The mentioned phenomena are due to a number of reasons: emergency shutdowns of power supply of pump units, rapid closing/opening of safety or shut-off and regulating fittings, etc. [1]–[4].

This situation is related to the absence of reliable and effective means of protection against surges and pressure pulsations [1]–[4]. Their main drawbacks include the impossibility of significant reduction of the amplitude of pressure fluctuations when installing air caps or liquid discharge valves, the stepwise control of pipeline fittings without taking into account its non-linear hydraulic characteristics; uncontrollability of the armature in the event of sudden interruptions in HS power supply, sensitivity to sudden changes in pressure fluctuations in the hydraulic system, triggering in the event of an accident. As a rule, an unregulated electric drive is used in HS to perform uniform or discrete closing in several stages, which does not provide ensuring the change of dynamic loads in the hydraulic system within permissible limits.

Therefore, a topical task consists in finding ways to reduce HS accident rate, one of which is to control the speed of closing/opening of pipeline fittings by using a variable-frequency electric drive (ED).

II Research method and results

The main pipeline fittings hydraulic characteristic affecting the nature of the flow of transient processes in the HS is the dependence of hydraulic resistance coefficient ξ on relative degree β of its opening (Fig. 1).

It can be described by the analytical dependence of the form:

$$\xi = A\left(\left(1/\beta\right)-1\right)^{C} + B\left(\left(1/\beta\right)-1\right)^{D} + \xi_0 \qquad (1)$$

where *A, B, C, D* – the approximation coefficients that depend on the type of pipeline fittings; ξ_0 – the coefficient of hydraulic resistance when the valve is fully opened (ξ=1).

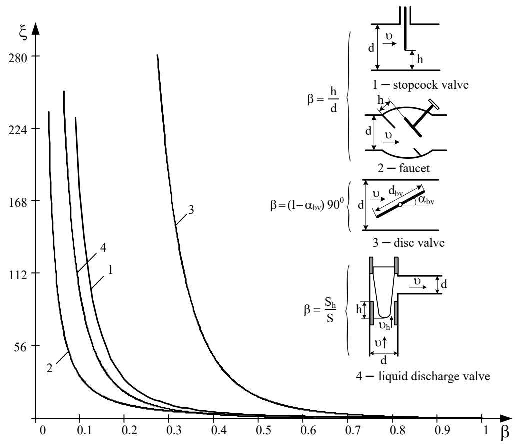

Figure 1: Dependences of hydraulic resistance coefficient ξ on relative degree β of its opening

The law of controlling the stopcock valve when it is closed is described by the expression:

$$\beta(t) = 1 - (t/t_{sh})^{1/n} \tag{2}$$

where n – the coefficient of pipeline fittings control intensity ($n \geq 1$); t, t_{sh} – the current time and the time of complete valve closure, respectively, s.

In order to reduce dynamic loads in HS pipeline network, it is proposed to form a non-uniform control law of the stopcock valve variable-frequency ED taking into account the non-linear dependence (1) on the entire interval of movement of its working body.

To study the dynamic processes in the hydraulic network with different laws of pipeline fittings control, a mathematical model of HS with a stopcock valve variable-frequency induction ED was developed, which takes into account the propagation of water hammer in the hydraulic network. Modeling parameters: rated pump pressure H_{pn} = 100 m, the flow rate of the working medium υ_n = 1 m/s, shock wave propagation speed c = 1000 m/s, pipeline length L = 5000 m, diameter d = 1.2 m, number of pipeline sections N = 20, the power of the stopcock valve drive induction motor 5.2 kW, opening/closing time 4.6 min., gear ratio r_g – 80.

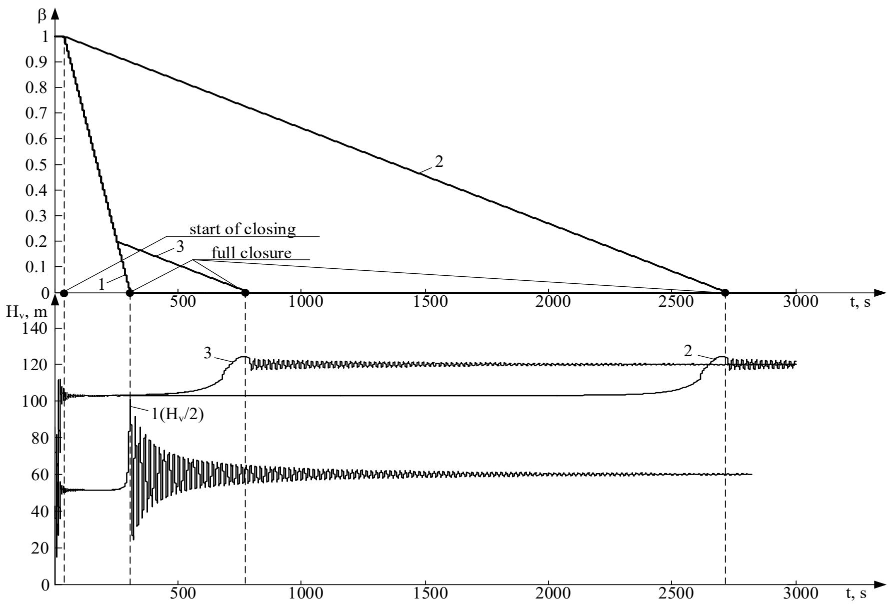

Figure 2: Graphs of transient processes in HS with the stopcock valve uniform (1, 2) and non-uniform (3) control

Fig. 2 shows the time-variable curves of changes of the head $H_v(t)$ in the pipeline network at the stopcock valve and the relative degree $\beta(t)$ of the valve opening during uniform (Fig. 2, curves 1 and 2) and non-uniform (Fig. 2, curve 3) control. Uniform control corresponds to the stopcock valve closing at a constant supply voltage frequency of 50 Hz and 5 Hz, respectively. With uneven control, the stopcock valve is closed with a supply voltage frequency of 50 Hz in the area, where β>0.2 and 5 Hz – where $\beta \leq 0.2$ respectively.

The analysis of the curves of pressure change near the stopcock valve shows that control at a constant frequency of the supply voltage equal to 50 Hz is accompanied by a rapid increase in pressure in the hydraulic network (Fig. 2, curve 1), the value of which is twice as high as the rated pressure of the pump. The largest decrease in the pipeline pressure is observed both when the value of the frequency of the supply voltage is reduced (Fig. 2, curve 2) and when the stopcock valve is unevenly controlled (Fig. 2, curve 3). However, with uneven control, the stopcock valve closing time is reduced tenfold, which is especially important in emergency modes associated with the sudden disappearance of power supply in the HS and the occurrence of liquid counterflow.

The adequacy of the obtained theoretical results is confirmed by experimental research performed on a laboratory installation of a hydraulic transport complex with a controlled stopcock valve.

III Conclusions

It has been determined that the conventional methods and technical means of reducing dynamic loads, which are used in practice, do not provide significant reduction of the amplitude of pressure fluctuations in the pipeline network and do not consider the task of controlling the electric drive of pipeline fittings in order to minimize dynamic loads in the hydraulic system. They do not take into account the real hydraulic characteristics of the valve and are based on increasing the closing time with uniform control or forming a stepped closing trajectory of the shut-off and regulating valve by using an unregulated electric drive.

It has been proven that in order to reduce dynamic loads in the pipeline network of the hydraulic system, it is necessary to form a non-uniform control law of the stopcock valve electric drive, taking into account the non-linear dependence of the hydraulic resistance coefficient on the relative degree of opening, which makes it possible to exclude dangerous pressure fluctuations in the pipeline, which can result in an emergency situations in the hydraulic system.

References

M. R. Bazargan-Lari, R. Kerachian, H. Afshar, N. Bashi-Azghadi "Developing optimal valve closure rule curve for real-time pressure control in pipes", *Journal of Mechanical Science and Technology*, iss. 27 (1), pp. 215–225, 2013.

Roy J.K., Roy P.K., Basak P. Water hammer protection in water supply system: A new approach with practical implementation // *Proceedings of ICCIA Kolkata.* – 2011. – Pp. 1–6.

G. E. Totten, V. J. De Negri, "*Handbook of hydraulic fluid technology*", second edition, Taylor & Francis Grou, 2012, 212 p. ISBN-13: 978-1-4200-8527-3 (eBook - PDF)

Choon Tan Wee, Aik Lim Kheng, Aik Lim Eng, Hin Teoh Thean. Investigation of water hammer effect through pipeline system. *International Journal on Advanced Science, Engineering and Information Technology*, 2012. Vol. 2, No. 3. PP. 246–251, DOI:10.18517/ijaseit.2.3.196

COMPUTATION OF IRON LOSSES USING FEM MODEL OF PERMANENT MAGNET SYNCHRONOUS MOTOR

DOI
https://doi.org/
10.18690/um.feri.4.2025.32

ISBN
978-961-286-986-1

LOVRENC GAŠPARIN,[1] KLEMEN DROBNIČ,[2] RASTKO FIŠER[2]

[1] MAHLE Electric Drives Slovenia d.o.o., Šempeter pri Gorici, Slovenia
lovrenc.gasparin@si.mahle.com
[2] University of Ljubljana, Faculty of Electrical Engineering, Ljubljana, Slovenia
klemen.drobnic@fe.uni-lj.si, rastko.fiser@fe.uni-lj.si

Accurate computation of iron losses in permanent magnet synchronous motors is a challenging task due to their nonlinear dependency on a motor's instantaneous loading condition. In the proposed computational procedure, a finite element method (FEM) is used for calculations of magnetic flux density in each particular mesh element. Applying a fast Fourier transform (FFT), its harmonic content is determined, followed by iron loss density calculation independently for several significant harmonics in all mesh elements over the entire stator iron core of PMSM. The proposed procedure predicts iron losses significantly better than classic approach where sinusoidal magnetic flux density is assumed.

Keywords:
permanent magnet synchronous machine,
magnetic field density,
iron losses,
finite element model,
harmonic components

University of Maribor Press

I Introduction

Modern traction drivetrain must satisfy number of specific requirements such as high dynamic performance, high torque density, high efficiency, low noise, and a wide speed range. In recent years, interior permanent magnet synchronous motors (PMSMs) have become the most popular motor traction topology for fast growing field of hybrid and electric vehicles. In order to achieve highest possible machine efficiency, the precise determination of losses is of the utmost importance and must be properly addressed already during machine design. Next to copper losses in windings, the iron losses in core lamination are the main contributor to the total losses in PMSM. Since iron losses vary strongly due to instantaneous operating condition (e.g. rated flux vs. field weakening operation) as well as on material/geometry, their accurate determination becomes a challenging task [1]. Therefore, an adequate simulation model should take into consideration lamination geometry, nonlinear material properties, different saturation levels, magnetic flux higher harmonics, etc. [2]. To take into account most of the aforementioned phenomena, FEM analysis is widely used and has become an industrial standard [3]. It ensures an accurate magnetic field computation, which is an excellent basis for further simulation of machines static and dynamic characteristics.

II Magnetic Field and Iron Loss Computation

Majority of methods for iron losses calculation are based on variation of magnetic field density *B* in a small mesh (volume) element of an iron core, whereupon total losses are decomposed into eddy current, hysteresis and excess losses, respectively. Two simplifying assumptions are commonly adopted, i.e. *B* is varying sinusoidally in time and the mesh element has an uniform distribution of *B* pointing in just one direction [4]. However, due to iron saturation and a specific lamination design, *B* also contains several prominent higher harmonics, suggesting an increase of total iron losses. Therefore, the conventional approach is not accurate enough and should be improved [5].

PMSM under consideration has 3-phase, fractional-slot winding, placed in 36 stator slots. Eight permanent magnets are buried in the rotor lamination in stamped holes. The motor is designed for mild hybrid drivetrain and features rated torque 60 Nm and maximum speed 21000 min^{-1}. For stator lamination, a soft magnetic material denoted as M270-35A is used, lamination thickness is 0.35 mm. Due to simplicity and computational efficiency, the analysis of the magnetic field density is limited to the smallest symmetrical part of a stator geometry, i.e. one stator tooth and corresponding back-iron sector. Cross-section of the stator core with designated calculation area and *x-y* coordinate system is shown in Fig. 1.

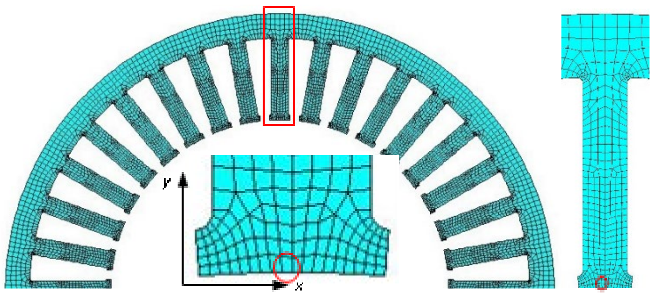

Figure 1: Selected symmetrical domain of FEM calculation, a tooth mesh of finite elements with selected single element, and defined coordinate system.

The magnetic field density B in each mesh element of the lamination segment (denoted with red square) is decomposed in tangential (B_x) and radial (B_y) component. However, the ratio between two components strongly depends on the location of the element: in elements near tooth center the B_y strongly prevails, while in back-iron elements dominates B_x. In lamination regions, where flux lines are crossing from tooth center into the back-iron and in tooth-end elements near the air-gap, both components are similarly pronounced. Additionally, saturation effect in each particular element is pronounced differently, which leads to a variety of higher harmonic components. For correct iron losses calculation, all these effects require a precise and exact examination of the magnetic field density in each mesh element by *x*- and *y*-components for several harmonic components, instead of assuming only fundamental value of B as usually adopted [6]. In a particular case of presented PMSM, the first seven harmonic components prove to be influential enough to substantially contribute to iron losses.

Magnetic field density $B_\theta = f(\theta, I_d, I_q)$ in each mesh element changes with instantaneous rotor angle θ and is also dependent on I_d and I_q current components (defined in rotor coordinates). With operating point fixed at (I_d, I_q), a number of static FEM calculations are performed, where instantaneous rotor angle θ sweeps exactly one electric period. Then, B_θ is decomposed into radial $B_{y,\theta}(I_d, I_q)$ and tangential $B_{x,\theta}(I_d, I_q)$ component. It is important to note, that $B_{x,\theta}$ and $B_{y,\theta}$ are periodic in electric angle. To determine the corresponding harmonic spectra for each component, a FFT is employed. In this way, amplitudes of $B_{x,i}(I_d, I_q)$ and $B_{y,i}(I_d, I_q)$ for i^{th} harmonic component in each particular mesh element are obtained. Consequently, it can be ascertained, how particular harmonic contributes to the final value of iron losses P_{Fe}. The described computational procedure combining FEM (Ansys) and Matlab domain is presented in Fig. 2 for a single operating point.

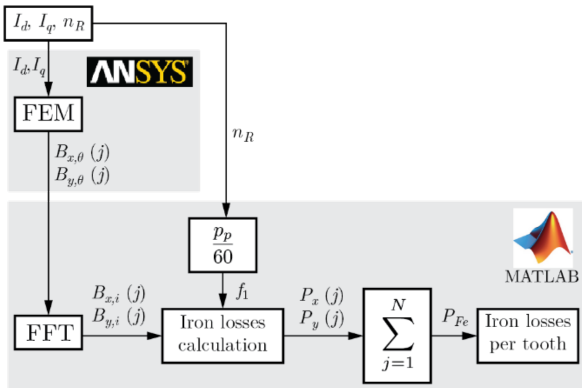

Figure 2: Flow chart of iron loss density calculation in one stator tooth for a chosen rotor speed and a single load operating point.

III Simulation and Experimental Results

Three chosen representative positions in a stator lamination segment regarding magnetic field density orientation are shown in Fig. 3: (a) a tooth end near the air-gap, where $B_{x,i}$ and $B_{y,i}$ are of a similar extent; (b) a tooth center position with dominant y direction; (c) a back-iron position with dominant x direction. A close study of Fig. 4 reveals the most influential components of iron loss density p_{Fe} in terms of direction and higher harmonics in these three positions for the specific operating point ($I_d = -463$ A, $I_q = 624$ A). Each of these three cases gives a completely different arrangement of components, however the sum of all individual components corresponds well to the expected values of loss density in the iron regions.

Measurements of iron losses were performed at no-load with no current in stator windings to exclude cooper losses, while driving the tested motor with external drive at constant speed, and subtracting previously identified friction losses afterwards. Fig. 5 presents a comparison among both calculated iron losses and measured ones, where obvious improvement of the proposed procedure can be observed. If in addition to the fundamental component also 3rd, 5th, and 7th harmonics are considered, predicted iron losses for a speed range from 0 to 12000 min^{-1} are increased up to 10 % and correspond much better to measurements. Once the improved calculation of p_{Fe} is verified by measurements at no-load, any other operating point of the loaded PMSM can be predicted in terms of P_{Fe}.

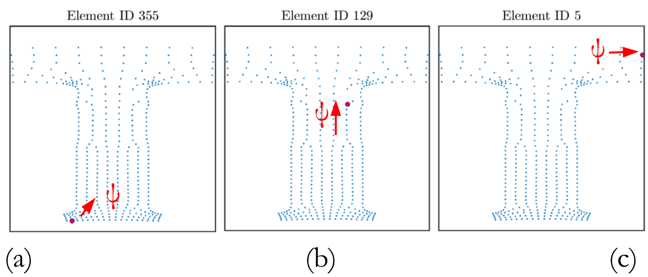

Figure 3: Selected mesh elements under investigations in three representative positions: (a) tooth end, (b) tooth center, (c) back-iron.

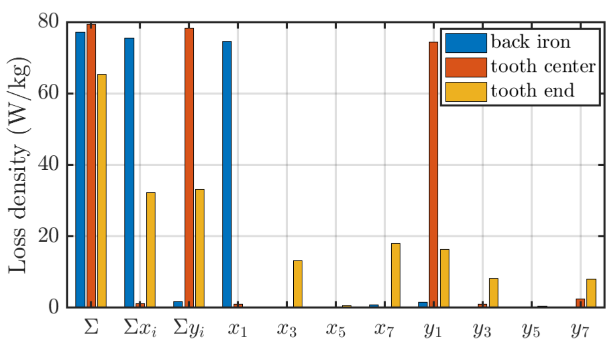

Figure 4: Components of iron loss density arranged by direction and higher harmonic components in three representative mesh elements for operating point (I_d = –463 A, I_q = 624 A).

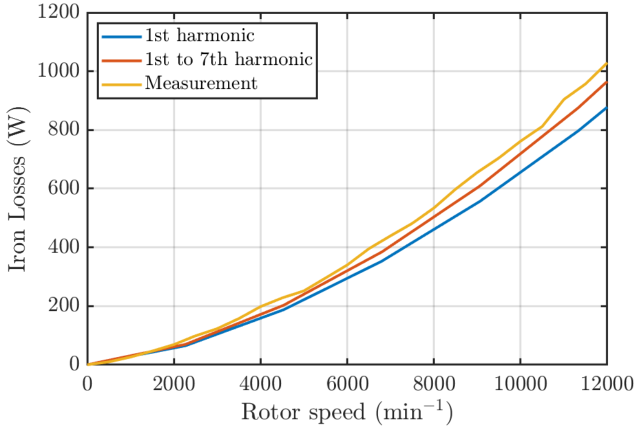

Figure 5: Improved calculation of PMSM iron losses taking into account also corresponding higher harmonics of B_x and B_y for a wide speed range.

References

[1] P. H. Mellor, R. Wrobel, D. Holliday, "A computationally efficient iron loss model for brushless AC machines that caters for rated flux and field weakened operation," *2009 IEEE IEMDC*, 3-6 May 2009, Miami, FL, USA, pp. 490-494.

[2] A. Krings, M. Cossale, A. Tenconi, J. Soulard, A. Cavagnino, and A. Boglietti, "Magnetic materials used in electrical machines," *IEEE Ind. Applicat. Mag.*, pp. 21-28, Nov./Dec. 2017.

[3] X. Chen, J. Wang, B. Sen, P. Lazari, and T. Sun, "A high-fidelity and computationally efficient model for interior permanent-magnet machines considering the magnetic saturation, spatial harmonics, and iron loss effect," *IEEE Trans. Ind. Electron.*, vol. 62, no. 7, pp. 4044-4055, Jul. 2015.

[4] N. Yogal, C. Lehrmann, M. Henke, and H. Zheng, "Measurement, simulation and calculation using Fourier transformation of iron losses for electrical steel sheets with higher frequency and temperature effects," in *22nd IEEE ICEM*, 4-7 Sept. 2016, Lousanne, Switzerland, pp. 2655-2661.

[5] V. C. do Nascimento, S. D. Sudhoff, "Continuous time formulation for magnetic relaxation using the Steinmetz equation," *IEEE Trans. Ener. Conv.*, vol. 33, no. 3, pp. 1098-1107, Sept. 2018.

[6] K. Yamazaki and Y. Seto, "Iron loss analysis of interior permanent magnet synchronous motors - variation of main loss factors due to driving condition," *IEEE Trans. Ind. Applicat.*, vol. 42, no. 4, pp. 1045-1052, July/Aug. 2006.

MAXIMISING DIESEL GENERATOR FUEL EFFICIENCY WITH LTO BATTERY INTEGRATION

MILOŠ BEKOVIĆ, PRIMOŽ SUKIČ, MATEJ PINTARIČ, LUKA PETRIČ, GORAZD ŠTUMBERGER

University of Maribor, Faculty of Electrical Engineering and Computer Science, Maribor, Slovenia
milos.bekovic@um.si, p.sukic@um.si, matej.pintaric1@um.si, luka.petric@student.um.si, gorazd.stumberger@um.si

Diesel generators are indispensable in areas lacking electricity infrastructure or requiring alternative power sources. However, while they offer significant advantages, they also suffer notable drawbacks, particularly in fuel efficiency during lower loads. Typically, generators operate in tandem with load profiles, resulting in inefficient operation during reduced loads. This article proposes a solution by integrating generator operation with a battery system. By combining the generator with batteries during periods of lower efficiency, we aim to enhance overall system efficiency.

DOI
https://doi.org/10.18690/um.feri.4.2025.33

ISBN
978-961-286-986-1

Keywords:
diesel generator,
battery storage system,
energy management system,
round trip efficiency
lithium titanate oxide

University of Maribor Press

I Introduction

A diesel generator's (DG) performance is crucial for its effective operation in providing electrical power. Several key factors contribute to its overall performance. A diesel generator's power outputIzkor is typically measured in kW or MW. It should match the electrical load requirements to ensure efficient and reliable operation. Users must ensure that the generator's capacity is adequate for the connected load to avoid overloading or underloading, which can impact efficiency and longevity.

While diesel generators have many advantages, they also come with certain disadvantages. Considering these drawbacks when evaluating whether a diesel generator is the right choice for a particular application is essential. While the full article will delve into the pros and cons comprehensively, it is worth noting that one drawback is the lower efficiency observed at smaller loads.

Despite some disadvantages, diesel generators remain widely used due to their reliability, durability, and ability to provide continuous power for extended periods. When choosing a generator, weighing the advantages and disadvantages based on the application's specific requirements is essential. Additionally, technological advancements and alternative fuels may address some of these drawbacks.

In this article, we delve into the operation of DG for a particular load scenario in the absence of a local network. Within this framework, we analyse the challenge of low efficiency at lower loads, prompting the consideration of a Battery Energy Storage System (BESS) solution. The objective is to synchronise the operation of both components to minimise primary fuel consumption, thereby optimising DG efficiency at higher loads.

II Diesel Genset and Battery Energy Storage System

A Diesel Generator

The DG's efficiency exhibits notable variations in response to load fluctuations, as seen in Fig. 1 [1]. Notably, the system attains peak efficiency in 50 to 95% of the load, while performance diminishes significantly at lower values. This underscores the economic inefficiency associated with operating the generator at lower loads; however, it highlights the generator's adaptive nature to the supplied load.

In the same graph, we observe the efficiency curve representing the return cycle of the BESS LTO alongside the converter. Notably, this curve demonstrates significantly higher efficiency, reaching approximately 85%, and remains relatively constant across a broad operating range. This consistency makes it a compelling choice for integration with DG systems, offering potential synergies and improved overall performance.

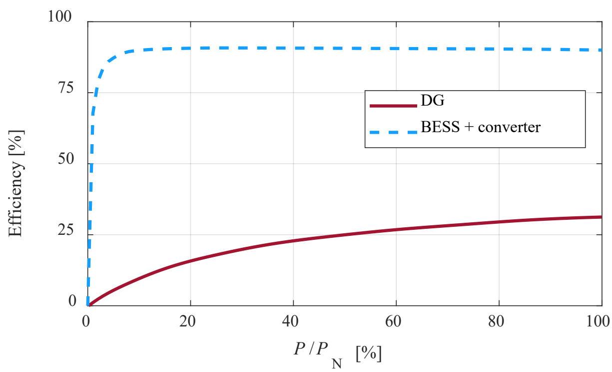

Figure 1: System with nonlinear elements.

B LTO Technology Efficiency

The graph in Figure 2 illustrates the round-trip efficiency (RTE) for BESS utilising LTO (Lithium Titanate Oxide) battery technology. Notably, the efficiency curve demonstrates variability contingent on the C ratio. A battery's "C rate" refers to the charging or discharging rate relative to its capacity. It is expressed as a multiple of the battery's capacity. In other words, the C rate measures how fast a battery is charged or discharged relative to its capacity. For example, a C rate of 1C means the battery is charged or discharged in one hour, while a 2C rate implies it would take half an hour to complete the process. Higher C rates generally result in faster charging or discharging but may also impact the battery's lifespan and efficiency.

Indeed, the relationship between the C ratio and losses in the battery is evident: larger C ratios correspond to increased losses in the battery. Simultaneously, a well-recognised observation is that efficiencies tend to degrade at lower temperatures. These characteristic curves play a pivotal role in comprehensively analysing BESS and DG performance. Understanding these dynamics is crucial for optimising system efficiency and making informed decisions about integrating BSS and DG technologies.

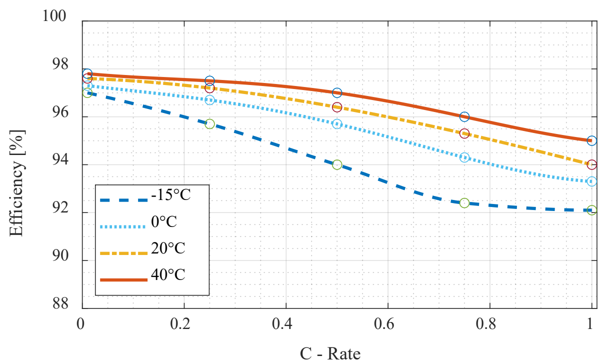

Figure 2: Measured round-trip efficiency of LTO BESS technology.

III Results

The load's characteristics heavily influence the choice of the suitable DG to power the load, whether constant or variable. In the case of variable loads, the DG's output power dynamically adjusts to match the load, ensuring seamless adaptation. However, depending on the efficiency profile, there is a risk of energy loss, emphasising the importance of selecting a DG with optimal efficiency characteristics.

The role of BESS in conjunction with DG is distinctly defined: when the load power is reduced, the DG operates at an increased power level, supplying both the load and fully charging the BESS. Once the BESS is charged, the DG ceases operation, and the load is sustained from the BESS until it discharges to a predetermined limit. In executing this process, it is imperative to assess the characteristics of the BESS, considering inherent losses.

A Constant Electric Loads

A simple generator power supply scenario is depicted in the selected example of a 450 kW DG and a 225 kW constant load. When the load remains constant, and the DG operates autonomously, the scenario is straightforward and serves as a benchmark. However, introducing a 450 kWh LTO battery alters the performance dynamics, as illustrated in Figure 3. The green curve represents the battery's starting state of charge (SoC) at 50%. In this setup, the designated DG operation was set at 90 % of its rated power, with a portion of the energy dedicated to meeting the load demand and the remainder allocated to charging the BESS.

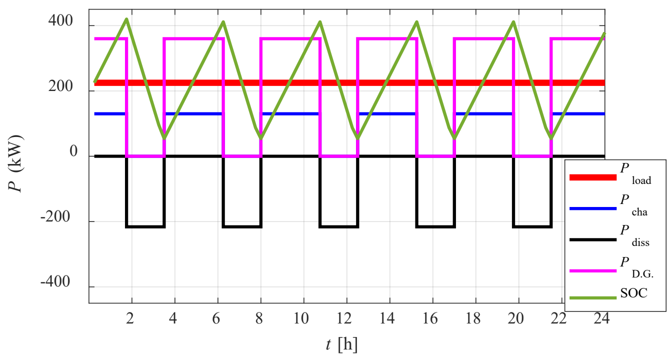

Figure 3: Power curves of charging and discharging BSS for constant load curve.

Once the BESS reaches its maximum set value (e.g., 90 % charge), the DG is stopped, and the BESS solely powers the load until it approaches the specified lower limit (in this instance, up to 10 %).

In this example, we observe five complete BESS charge and discharge cycles, prompting our interest in comparing fuel consumption. Although the DG operates at a higher power level in this scenario, the periodic interruptions due to BESS discharge diminish the clarity of potential savings.

B. Dynamic Two-Peak Electric Load

In scenarios with fewer but pronounced peaks in the load profile, the operational dynamics become notably more compelling. To illustrate this, we introduce a load profile example depicted by the red curve in Figure 4. All other simulation parameters remain consistent, allowing us to observe the charging and discharging profiles of the BESS relative to the State of Charge (SoC). The charging power P_{cha} is represented by the blue curve, while the discharging power P_{dis} is depicted in black. The green curve indicates the *SoC* and the magenta curve $P_{D.G.}$ illustrates the operation of the DG, set at 80 % of its rated power.

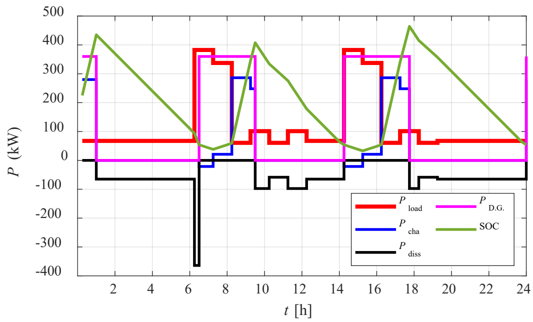

Figure 4: Power curves of charging and discharging BSS for different loads.

The energy balance depicted in Fig. 5 illustrates that a daily requirement of 2864 kWh is necessary to meet the load demand. If we rely solely on DG, this demand translates to 11246 kWh (diesel equivalent) consumed. However, when incorporating BESS with DG, the total consumption decreases to 8235 kWh, with losses accounting for an additional 74 kWh.

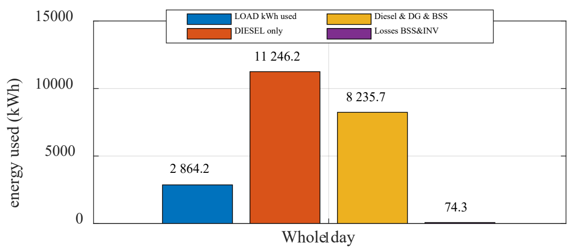

Figure 5: Energy consumption for cases of power supply with DG and combination with BESS and losses,

References

[1] V. Kiray, M. Ohran, J. N. Chijioke," Significant Increase in Fuel Efficiency of Diesel Generators with Lithium-Ion Batteries Documented by Economic Analysis", *Energies*,2021, 14, 6904. https://doi.org/10.3390/en14216904

DOI
https://doi.org/
10.18690/um.feri.4.2025.34

ISBN
978-961-286-986-1

Analysis of the Correlation Between Vibrations and the Number of Shorted Turns in the Stator Winding of a Squirrel-Cage Induction Motor

Mikołaj Marczak, Wojciech Pietrowski, Konrad Górny

Poznan University of Technology, Institute of Industrial Electrical Engineering, Poznań, Poland
mikolaj.marczak@doctorate.put.poznan.pl, wojciech.pietrowski@put.poznan.pl, konrad.gorny@put.poznan.pl

This paper presents a method for diagnosing a squirrel cage induction machine based on machine vibration analysis. The study focuses on the consideration of a winding fault in the stator winding of an induction machine. The case of a winding fault in one phase was considered. The machine vibration signal was recorded at a constant load torque. Wavelet packet decomposition was used to analyse the recorded vibration signals. The results of the wavelet analysis were correlated with the number of shorted windings. The result was a method for detecting faults in an electrical circuit using the vibration signal.

Keywords:
diagnosing,
squirrel cage induction machine,
vibration analysis,
winding fault,
wavelet packet decomposition

University of Maribor Press

I Introduction

The planet's dwindling natural resources, which are vital to industry, are one of the reasons why increasing attention is being paid to extending the life of machinery. An important aspect of this is to take advantage of technological advances that can make a significant contribution to reducing production costs and improving operational efficiency. This is closely related to the issue of equipment diagnostics.

Induction machines are one of the most widely used pieces of industrial equipment and are used in virtually every industry, including driving production belts, fans and compressors. One of the most common faults in induction machines is coil shorts in the stator winding. This article focuses on single-phase shorts because they are relatively difficult to detect. Its occurrence can rapidly accelerate the deterioration of the machine and lead to subsequent failures. One of the many diagnostic methods for induction machines is the vibration-acoustic method, which uses a vibration signal. This method is characterised by, among other things, its non-invasiveness, which is manifested in the lack of need to immobilise the machine during diagnosis and the simplicity of connecting the measurement system. In this article, wavelet packet decomposition was used to analyse the waveform of the vibration signal. The results of the wavelet analysis were correlated with the number of short circuits.

II Measurement

A measurement system was designed and built to record machine vibration waveforms. A SVANTEK SV150 triaxial accelerometer with a 958A instrument acting as a signal amplifier was used to record and archive the vibration waveforms of the induction motor. A Celma Inducta 3SIE100L4B squirrel cage induction motor was selected for testing. The machine was prepared for inter-turn short-circuit testing by routing selected coil wires outside the machine housing. The diagram of the measurement system is shown in Figure 1.

The National Instruments CompactDAQ housing, equipped with a set of measurement cards, was used to record the waveforms. The manufacturer's DAQ Express software was used to manage the measurement configuration, and Matlab was used to archive the measurements to disk and for further processing. The research used the acceleration waveform of the machine vibrations due to the vibration transducer used.

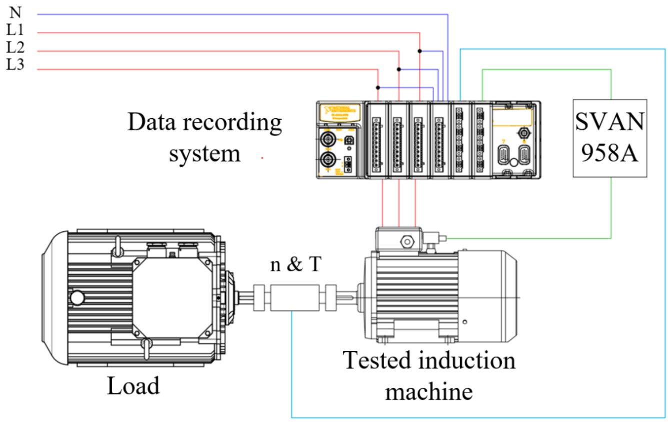

Figure 1: Diagram of the measurement system.

Selected measurement results of the machine vibration signal waveforms are shown in Figure 2. The figure shows the waveform of a healthy machine and a machine with 4 shorted turns in the stator winding. In both cases the machine was loaded with the rated torque.

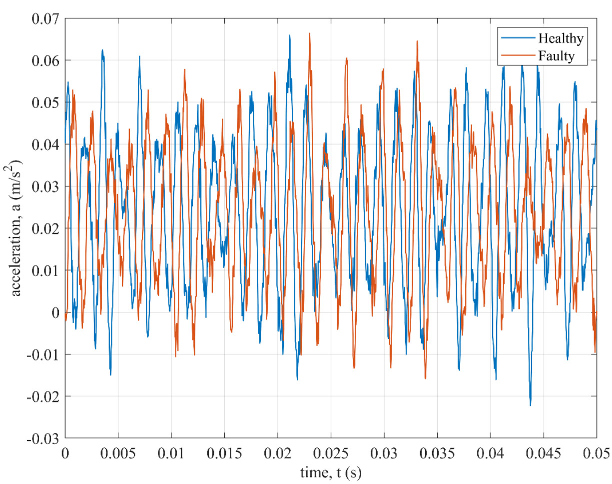

Figure 2: Waveforms of vibration acceleration for a healthy and faulty machine

III Selected results of diagnostic signal analysis

Due to the non-stationary nature of the machine's vibration waveforms, it was decided to use packet wavelet analysis. This analysis involves filtering the input signal into its approximate and detailed components. This is done using low pass and high pass filters respectively. In the next step, the approximation and detail can be filtered. As a result, the analysed signal is decomposed into a set of approximations marked with the letter A and details marked with the letter D, along with their variations depending on the level of decomposition. The whole process can be represented in the form of a decomposition tree, Fig. 3. The next step in the analysis was to calculate the energy of the approximations and details in the nodes of the decomposition tree at the lowest level.

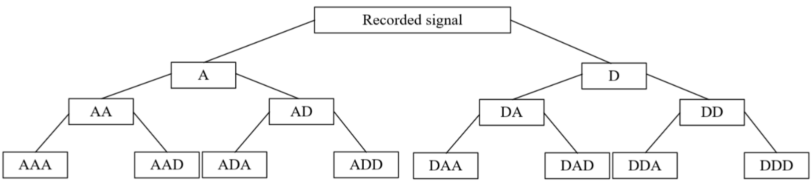

Figure 3: Structure of Wavelet Packet Decomposition

The vibration waveforms of a healthy machine and a damaged machine were selected for packet wavelet analysis for 9 load torque values, i.e. from no-load to a load of 105% of rated torque. For the damaged machine tests, the vibration waveforms were considered for the number of shorted turns from 1 to 4.

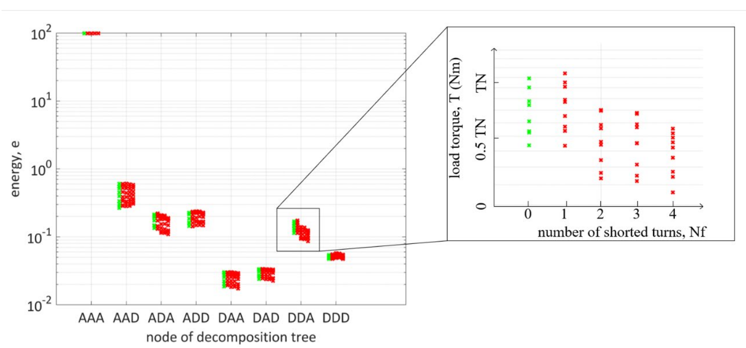

Figure 4: Energy of the machine vibration waveforms in the nodes of the decomposition tree.

The results of the packet wavelet analysis are shown in Figure 4. The healthy machine is marked in green and the damaged machine is marked in red. The figure shows the tendency that as the number of shorted turns increases, the percentage of energy transferred for the obtained ADA and DDA increases. This phenomenon would be almost impossible to observe with a smaller number of cases.

Further research was carried out to establish the relationship between machine vibration and the number of shorted turns in the stator winding. For this purpose, the correlation between these two quantities was calculated as follows.

$$\rho(A,B) = \frac{1}{N-1}\sum_{i=1}^{N}\left(\frac{A_i-\mu_A}{\sigma_A}\right)\left(\frac{B_i-\mu_B}{\sigma_B}\right) \tag{1}$$

where μA and σA are the mean and standard deviation of A; μB and σB are the mean and standard deviation of B.

The results of the correlation calculations are presented in Fig. 5.

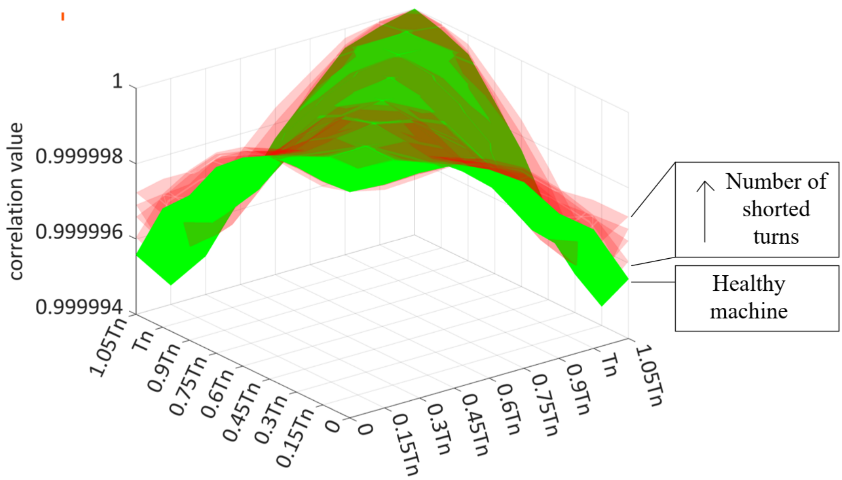

Figure 5: Correlation between vibration and the number of shorted turns.

The correlation results presented in Figure 5 clearly show the differences between the degrees of machine damage. At low load torque values, the correlation is weakest for a healthy machine. However, as the load torque increases, a stronger correlation can be observed.

IV Conclusions

The paper presents the results of vibration measurements of a damaged induction machine and the results of their analysis using packet wavelet analysis. Based on the results of the analysis, the correlation between the vibrations of the induction machine and the number of shorted turns of the stator winding is presented.

From the test results presented, it can be concluded that the method presented can be used to assess the condition of the windings of squirrel cage induction machines. The use of packet wavelet analysis is an indispensable tool for the analysis of aperiodic waveforms, such as the recorded vibration accelerations.

The conclusions and findings of this article may be particularly useful in classifying asymmetric defects. Further research suggests applications of machine learning that can assist in defect classification.

References

[1] Górny, K.; Kuwałek, P.; Pietrowski, W. "Increasing Electric Vehicles Reliability by Non-Invasive Diagnosis of Motor Winding Faults", Energies 2021, 14, 2510, doi:10.3390/en14092510.

[2] Górny, K.; Marczak, M.; Pietrowski, W. „Approximation and Extrapolation of Vibrations in Induction Machines as a Function of Numbers of Short-circuited Turns in Stator Winding", eaz-pismo.pl 2023, pp. 10-26, doi:10.17274/AEZ.2023.51.01.

[3] Dhamal, S.S.; Bhatkar, M.V. "Modelling and Simulation of Three-Phase Induction Motor to Diagnose the Performance on Inter-Turn Short Circuit Fault in Stator Winding", In Proceedings of the 2018 International Conference on Computing, Power and Communication Technologies (GUCON), Greater Noida, India, 28–29 September 2018; pp. 1166–1172.

[4] Li, Y.; Tang, B.; Jiao, S.; Zhou, Y. "Optimized multivariate multiscale slope entropy for nonlinear dynamic analysis of mechanical signals", Chaos, Solitons & Fractals, Volume 179, 2024, 114436, ISSN 0960-0779, doi:10.1016/j.chaos.2023.114436.

UNBALANCED MAGNETIC PULL IN DUAL THREE-PHASE MACHINE

KLEMEN DROBNIČ, RASTKO FIŠER

University of Ljubljana, Faculty of Electrical Engineering, Department of Mechatronics, Ljubljana, Slovenia
klemen.drobnic@fe.uni-lj.si, rastko.fiser@fe.uni-lj.si

This paper examines the emergence of unbalanced magnetic pull (UMP) in dual three-phase permanent magnet synchronous machines (DTM) during post-fault (PFO) and synthetic loading operation (SLO). Through FEM (finite element method) simulations, the paper reveals that UMP arises due to interactions between field harmonics with differing spatial orders, specifically the 4^{th} and 5^{th} harmonics during PFO and SLO. The presence of both odd and even harmonics in the machine's field spectrum is identified as a critical factor in UMP generation. The simulation results confirm that while UMP in DTM increases bearing stress and reduces lifespan, it does not compromise mechanical integrity, providing insights for machine design and control strategies under PFO and SLO.

DOI
https://doi.org/10.18690/um.feri.4.2025.35

ISBN
978-961-286-986-1

Keywords:
unbalanced magnetic pull,
dual three-phase machine,
multiphase machine,
synthetic loading,
post-fault operation

University of Maribor Press

I Introduction

Principal benefits of multiphase machines are power sharing among phases and a fault-tolerant operation that ensures continuous control over flux and torque even in the event of fault. This capability not only ensures continuous operation but also offers additional control flexibility to improve torque, minimize torque ripple, and increase redundancy and safety. Multiphase machines provide higher rated power and reduced power losses, making them suitable for diverse applications.

Among the variety of multiphase configurations, the dual three-phase machine (DTM) with two neutral points is the most popular. This design capitalizes on conventional three-phase inverter technology, enabling the use of existing, well-understood, and cost-effective power conversion strategies. The dual three-phase topology also enhances drive versatility through power sharing between winding sets. The sets can be connected to two three-phase power sources or consumers simultaneously, thereby allowing for an efficient transfer of active and reactive power across the windings. This capability can be used for synthetic loading, offering a simplified approach to determine the machine's power losses.

However, the operation of DTM introduces specific challenges, notably the issue of unbalanced magnetic pull (UMP). This phenomenon becomes particularly critical during certain modes of operation, such as post-fault operation (PFO) with only one winding set active, and during synthetic loading operation (SLO). UMP negatively influences machine's performance (noise, vibrations) and shortens bearings lifetime.

In this paper we focus on the performance of interior permanent magnet synchronous DTM during PFO and SLO. We shed light on the mechanism leading to UMP and quantitatively assess it through a series of FEM simulations.

II dual three-phase machine

DTM has 18 slots and 8 poles resulting in 20° mechanical angle between slots. Each phase winding consists of three series connected coils each spanning over two slots. Six phase windings are arranged in two three-phase winding sets *abc* and *xyz*, respectively, each having their own neutral point. The coils associated with respective winding set are placed in alternate stator slots along the circumference (Fig. 1).

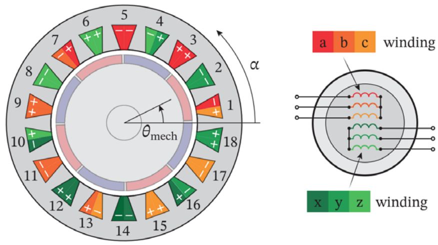

Figure 1: DTM with 18 slots and 8 rotor poles. Offset between three-phase winding sets *abc* and *xyz* is 9 slots.

Offset between winding sets *abc* and *xyz* is 9 slots or 180° mechanical. This is a standard choice among 18 offset possibilities, all of which are viable and lead to favourable properties in normal operation (NO): a) enhancement of 4th order space harmonic that interacts with rotor magnetic field and generate electromagnetic torque and b) cancelation of odd space harmonics (Fig. 2, top). During NO radial magnetic force generated by the *abc* set is counteracted by the *xyz* set resulting in cancellation of UMP [1].

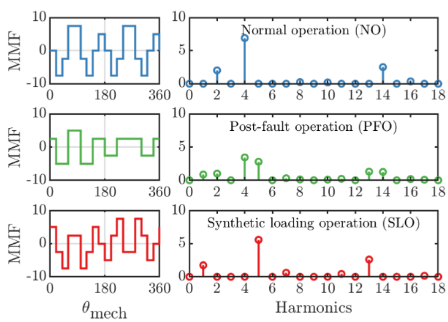

Figure 2: MMF profile (left) and harmonic spectra (right) for NO (top), PFO (middle) and SLO (bottom)

This winding layout offers enhanced fault tolerance benefits as it enable balanced PFO with derated torque output. In contrast to NO, the MMF harmonic spectrum of PFO (Fig. 2, middle) also contains odd harmonics, especially prominent is the 5th.

Similar observation can be made for SLO, a method for determining losses of electrical machines, where only odd harmonics are found in its MMF spectrum (Fig. 2, bottom). As the main rotor field harmonic is the 4th, its interaction with the armature's odd-harmonic spectrum results in undesirable effects, such as UMP.

III FE simulation

UMP refers to an asymmetrical force that acts on the rotor and occurs due to non-symmetric distribution of the magnetic field in the airgap. To estimate UMP a series of time-stepped 2D transient FEM analyses were performed using the Motor-CAD EMag module. Radial B_r and tangential B_a flux density within the airgap were calculated for a) no-load and four current levels, b) three modes of operation (NO, PFO and SLO) and c) 160 rotor positions θ_{mech} from 0° to 180° mechanical. Current displacement angle was set to 90°.

The force components F_x and F_y, exerted on a rotor with an axial length of l_{rot}, are determined by evaluating the integral along a surface with an airgap radius r_{AG} [2]

$$F_x = \frac{r_{\mathrm{AG}} l_{\mathrm{rot}}}{2\mu_0} \int_0^{2\pi} \left[B_\alpha^2 - B_r^2) \cos\alpha + 2 B_r B_\alpha \sin\alpha \right] d\alpha$$
$$F_y = \frac{r_{\mathrm{AG}} l_{\mathrm{rot}}}{2\mu_0} \int_0^{2\pi} \left[B_\alpha^2 - B_r^2) \sin\alpha + 2 B_r B_\alpha \cos\alpha \right] d\alpha \tag{1}$$

UMP is then calculated as $F_{\mathrm{UMP}} = \sqrt{F_x^2 + F_y^2}$.

A. Radial flux density and magnetic force

Fig. 3 shows radial flux density for all three operation modes. Harmonic analysis of the waveforms reveals that in NO only even harmonics exists, whereas in PFO and SLO odd harmonics appear as well as predicted by MMF profile (Fig. 2). Radial magnetic force is a consequence of interaction between these field harmonics. For NO (Fig. 4a), the force profile along the airgap exhibits half-wave symmetry, ensuring balance. Consequently, this symmetry prevents the emergence of UMP. In contrast, PFO and SLO (Fig. 4b and 4c) are not balanced which leads to UMP.

The UMP originates from the first spatial order harmonic of the force wave, which is generated by the interaction of field harmonics with spatial orders differing by one [2]. That means that UMP cannot be produced if the machine's field in the airgap comprises exclusively even or odd harmonics. In case of PFO and SLO the UMF is primarily due to interaction of 4th and 5th field harmonics (Fig. 3 bottom).

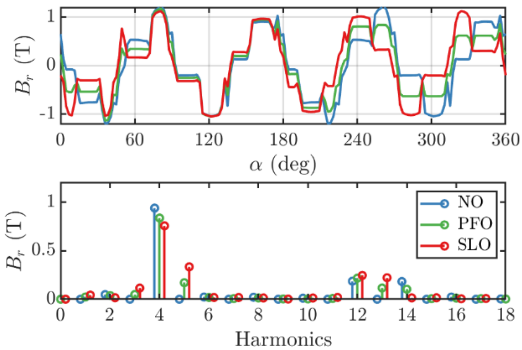

Figure 3: Radial flux density B_r at $t = 0$ s and $I_s = 100$ A for all modes

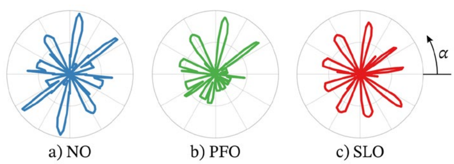

Figure 4: Radial magnetic force F_r at $t = 0$ s and $I_s = 100$ A for all modes

B. Rotor position dependence

Fig. 5 and 6 depicts UMP for 4 current levels and rotor positions in the range from 0° to 180° mechanical. The amplitude of UMP is similar for both PFO and SLO. By increasing the current the UMP ripple starts to amplify, especially for PFO. This can be attributed to the rise of higher order harmonics due to saturation.

IV Conclusion

For this DTM, PFO and SLO inevitably lead to the emergence of UMP as its field spectrum contains odd and even harmonics. The UMP adds additional strain on the bearings; however, its amplitude is still order of magnitude below bearings' load rating. It appears that at this level UMP reduces the lifespan of bearings, rather than presenting an immediate danger to mechanical integrity. Moreover, PFO and SLO are intended to be temporary, active only for a constrained period.

Table 1: Data and Parameters of Dual Three-Phase machine

Rated values	
Maximum current I_{max}	200 A
DC-link voltage U_{DC}	48 V
Motor parameters	
Number of pole pairs p_p	4
Number of stator slots	18

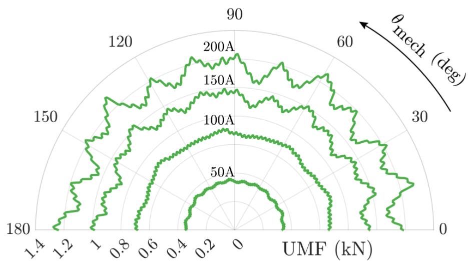

Figure 5: UMP during PFO for four currents and rotor positions from 0° to 180°

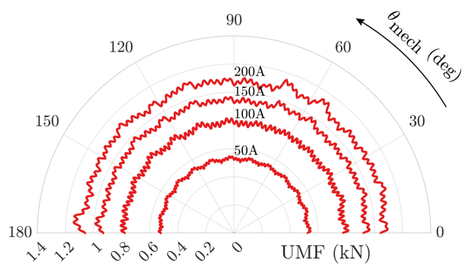

Figure 6: UMP during SLO for four currents and rotor positions from 0° to 180°

References

[1] V. I. Patel, J. Wang, W. Wang, and X. Chen, "Six-Phase fractional-slot-per-pole-per-phase permanent-magnet machines with low space harmonics for electric vehicle application," *IEEE Trans. Ind. Appl.*, vol. 50, no. 4, pp. 2554–2563, Jul. 2014, doi: 10.1109/TIA.2014.2301871.

[2] Z. Q. Zhu, D. Ishak, D. Howe, and J. Chen, "Unbalanced magnetic forces in permanent-magnet brushless machines with diametrically asymmetric phase windings," *IEEE Trans. Ind. Appl.*, vol. 43, no. 6, pp. 1544–1553, Nov. 2007, doi: 10.1109/TIA.2007.908158.

Impact of Material Property Variations and Sensor Positioning on the Coating Thickness Determination of Steel Sheets

Martin Koll,[1] Daniel Wöckinger,[1]
Christoph Dobler,[1] Gerd Bramerdorfer,[1]
Gereon Goldbeck,[1] Stefan Schuster,[2]
Stefan Scheiblhofer,[2] Norbert Gstöttenbauer,[2]
Johann Reisinger[2]

[1] Johannes Kepler University Linz, Institute of Electric Drives and Power Electronics, Linz, Austria
martin.koll@jku.at, daniel.woeckinger@jku.at, christoph.dobler@jku.at, gerd.bramerdorfer@jku.at, gereon.goldbeck@jku.at
[2] Voestalpine Stahl GmbH, Linz, Austria
stefan.schuster2@voestalpine.com, stefan.scheiblhofer@voestalpine.com, norbert.gstoettenbauer@voestalpine.com, johann.reisinger@voestalpine.com

This paper deals with investigations to determine the layer thickness of electrically conductive coatings on electrically conductive and ferromagnetic steel substrates. For this purpose, an eddy current sensor system with well-known analytical model for ideal conditions is used. Based on this, different coil setups are examined and compared with regard to sensor positioning. A robustness analysis against parameter fluctuations is carried out.

DOI
https://doi.org/10.18690/um.feri.4.2025.36

ISBN
978-961-286-986-1

Keywords:
Eddy current testing, coating thickness determination, FE simulation, analytical modeling, nonlinear effects

University of Maribor Press

I Introduction

In industry, it is often necessary to apply a coating to steel sheets to protect them against external influences that may damage the material, e.g., corrosion. In order to ensure the quality of these coatings, it is necessary to be able to accurately determine its thickness. According to the literature, an X-ray gauge is often used to determine coating thicknesses [1]. This method is typically expensive and poses problems in terms of occupational safety. For this reason, an eddy current coil system is used in this paper [2]. In the real world, however, parameter fluctuations, edge effects, noise and other undesirable influences have significant impact on the achievable measurement accuracy. The aim of this paper is to analyze these effects and to indicate their impact on the coating thickness determination.

II Methodology

In this work, a coil system consisting of a cylindrical excitation coil and two measuring coils, as shown in Fig. 1 is analyzed. For the analytical model of this arrangement, it is assumed that there is a coated steel sheet close by to the coil. The coating is non-magnetic and the substrate underneath is a ferromagnetic material, both are electrically conductive. The mutual impedance of this arrangement yields [2]

$$\zeta = \frac{j\omega\mu_0\pi N_1 N_2 \bar{r}}{(r_2-r_1)(r_4-r_3)L_2 L_6}\int_0^\infty \frac{1}{\alpha^6} J(r_2,r_1)J(r_4,r_3)e^{-2\alpha L}\left(e^{-\alpha(L_2-2L_5-L_6)}-1\right)$$
$$\times\left(e^{-\alpha L_5}-e^{-\alpha(L_6+L_5)}\right)\left(e^{-\alpha L_2}-1\right)$$
$$\times\frac{(\alpha+\beta_1)(\beta_1-\beta_2)+(\alpha-\beta_1)(\beta_1+\beta_2)e^{2\alpha_1 c}}{(\alpha-\beta_1)(\beta_1-\beta_2)+(\alpha+\beta_1)(\beta_1+\beta_2)e^{2\alpha_1 c}}\,d\alpha. \tag{1}$$

Here ω is the angular excitation frequency, N_1 and N_2 are the number of turns of the excitation coil and the measuring coil, r_i and L_i are the dimensions of the respective coil and

$$\bar{r} = \frac{r_1+r_2}{2}, \tag{2}$$

$$\beta_i = \frac{1}{\mu_i}\sqrt{\alpha + j\bar{r}^2\omega\mu_0\mu_i\sigma_i}, \ (3) \tag{3}$$

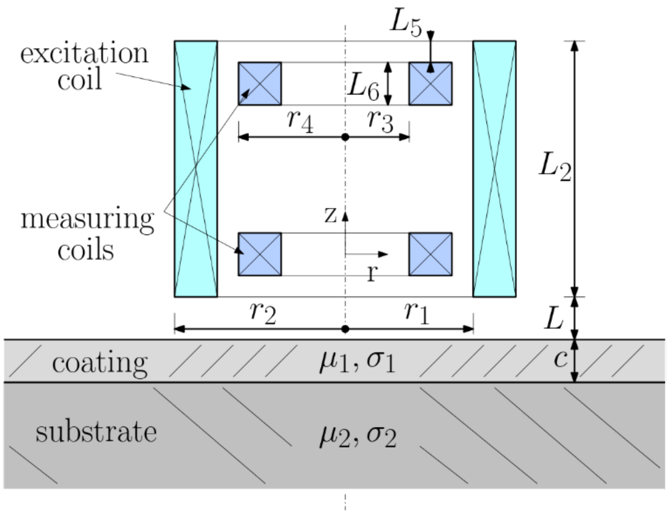

Figure 1: Drawing of Differential coil model setup with dimensioning.

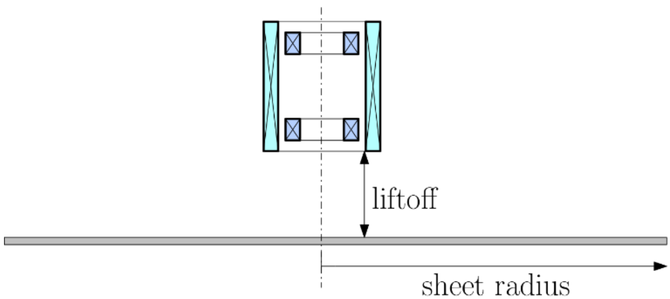

Figure 2: Sketch of the simulation setup for the analysis of the edge effect via variation of the sheet radius.

$$\alpha_i = \sqrt{\alpha + j\overline{r^2}\omega\mu_0\mu_i\sigma_i}, \tag{4}$$

$$\frac{1}{\alpha^2}\int_{x=\alpha r_1}^{\alpha r_2} x J_1(x)\,\mathrm{d}x = \frac{1}{\alpha^2} J(r_2, r_1), \tag{5}$$

with $J_1(x)$ a Bessel function of first kind and order. The relative permeability and the conductivity of the layers are μ_i and σ_i. Due to process conditions, e.g. temperature and position fluctuations of the sheet metal to be measured, it is required to position the measuring coils to be relatively far away from the specimen. In an FEA-simulation the validity of the analytical model is evaluated and the mesh rules found in [3] are extended for larger air gaps of more than 20 mm. The software FEMM [4] is used for this purpose. In an industrial plant, the assumption of an infinite extension certainly does not apply. For this reason, different coil setups, shown in Tab. 1, are examined and the edge effect as a function of the air gap is analyzed via sheet radius variations shown in Fig. 3, to determine the minimum distance of the sensor from the edge of the sheet to to exclude the influence of boundary effects.

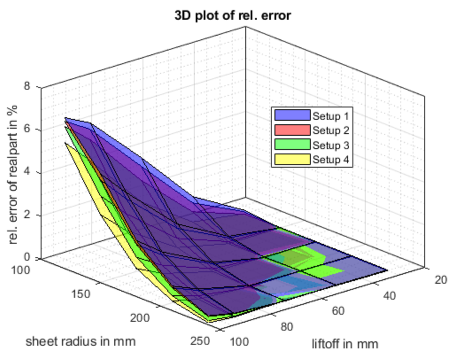

Figure 3: Relative error when comparing FEA and analytical model depending on the sheet radius and the air gap between sheet and coil.

The following applies to the investigations carried out:

$N_1 = 43$, $N_2 = 18$, $\sigma_1 = 15$ MS/m, $\sigma_2 = 5$ MS/m, $\mu_2 = 500$, $c = 10$ µm. In Fig. 3 the real part of the mutual impedance ζ of the analytical model is compared with that of the FEA simulation.

Table 1: Analyzed Coil Setups

	Setup 1	Setup 2	Setup 3	Setup 4
r1 [mm]	25	13	25	10
r2 [mm]	26	14	26	11
r3 [mm]	22	10	22	7
r4 [mm]	24	12	24	9
L2 [mm]	40	40	20	10
L5 [mm]	2.85	2.85	2.85	1.5
L6 [mm]	4.1	4.1	4.1	3

Furthermore, the analytical model is used to perform a robustness analysis with respect to parameter fluctuations. As shown in [3], the coating conductivity σ_1 must be known exactly in order to determine the thickness of the coating. The influence of a parameter change in the coating conductivity of $\pm$ 20 % on the mutual impedance curve at different operating points is shown in Fig. 4. It can be seen that with a small coating thickness and high relative permeability of the steel substrate, the influence of a coating conductivity variation on the mutual impedance is the most significant.

Measurements are carried out on a test bench shown in Fig. 5. This test bench is used to measure various sheet metal samples with different coating thicknesses between 6 µm and 24 µm and different air gaps between 1.5 mm and 20 mm.

III Outlook

The final paper will provide measurement data. The behaviour of different coating thicknesses for the same steel substrate with different air gaps is investigated. The results will be useful for the industrial use of this type of sensor to determine the thickness of coatings on steel sheets.

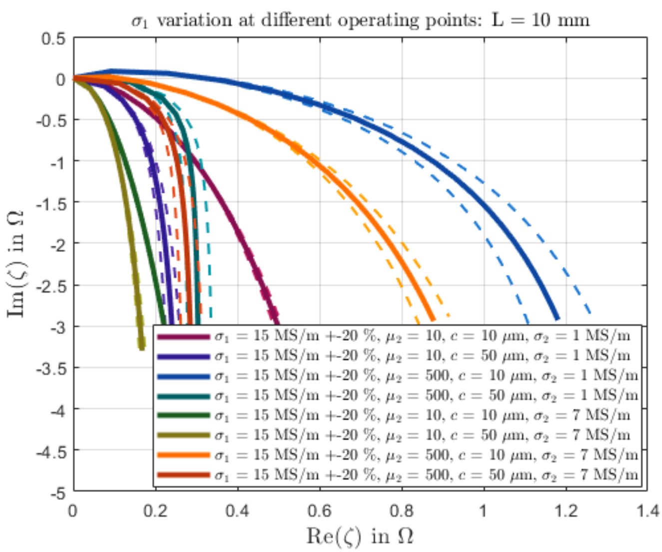

Figure 4: Effect of ±20% coating conductivity variation on the mutual impedance curve.

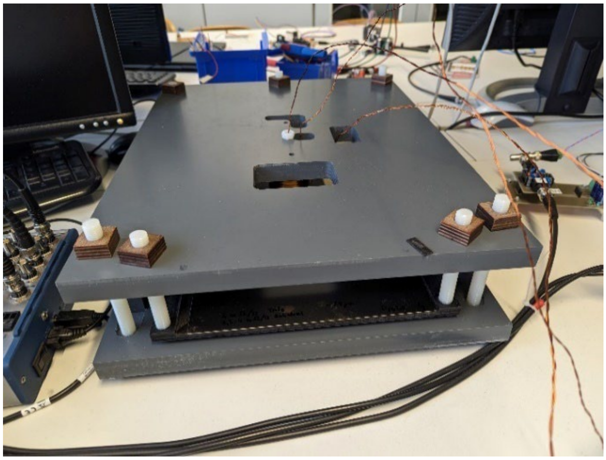

Figure 5: Test bench for measuring sheet metal samples.

Acknowledgment

This work has been supported by the COMET-K2 ”Center for Symbiotic Mechatronics” of the Linz Center of Mechatronics (LCM) funded by the Austrian federal government and the federal state of Upper Austria .

References

[1] Moriyasu, Keisuke, Daigo Kosaka, Kazuhiko Kakishita, Mitsuo Hashimoto, und Fumio Koyama. „Measurement of Plating Thickness with High Liftoff Using Eddy Current Testing“. Electromagnetic Non-Destructive Evaluation (XXI), 2018, 263–68. https://doi.org/10.3233/978-1-61499-836-5-263.

[2] Dodd, Deeds, Luquire; Spoeri. Some Eddy-Current Problems and Their Integral Solutions. Oak Ridge National Laboratory, 1969.

[3] Koll Martin, Daniel Wöckinger, Christoph Dobler, Gereon Goldbeck, Gerd Bramerdorfer, Stefan Schuster, Stefan Scheiblhofer, Norbert Gstöttenbauer, und Johann Reisinger. „Investigations on eddy current sensors regarding inline-capability of zinc coating monitoring using a model-based estimator“. Journal of Magnetism and Magnetic Materials, 2024, https://doi.org/10.1016/j.jmmm.2024.171754.

[4] Meeker, David. "Finite element method magnetics." FEMM 4.32 (2010): 162.

Model of Magnetic Precession Gear Dynamics Based on 3D Finite Element Analysis and Prototype Investigation

Łukasz Macyszyn,[1] Cezary Jędryczka,[2]
Michał Mysiński[2]

[1] Poznan University of Technology, Faculty of Mechanical Engineering, Poznan, Poland
lukasz.macyszyn@put.poznan.pl
[2] Poznan University of Technology, Faculty of Control, Robotics and Electrical Engineering, Poznan, Poland
cezary.jedryczka@put.poznan.pl, michal.mysinski@put.poznan.pl

The presented research is focussed on analysis of dynamics of a two-stage magnetic precession gear system. In the proposed mathematical model of studied gear dynamics two approaches have been considered. Firstly, the model has been defined using the torque versus angle characteristics determined by means of detailed 3D FEM model of the magnetic field. In the second approach the model is based on torque vs. angle characteristics determined by measurements of the prototype step response. The results obtained by the two methods are compared and discussed.

DOI
https://doi.org/10.18690/um.feri.4.2025.37

ISBN
978-961-286-986-1

Keywords:
magnetic gear,
Finite Element Method,
analysis of dynamics,
precession gear,
MATLAB Simulink

University of Maribor Press

I Introduction

Magnetic gears have garnered significant attention owing to the development of high-energy-density magnets utilizing rare-earth components and the refinement of precise modelling techniques for electromagnetic phenomena through Finite Element Method (FEM) analysis. In comparison to conventional mechanical gears, magnetic gears offer contactless transmission of torque, thereby mitigating wear, minimizing vibrations and noise, and providing inherent overload protection [1].

For the successful implementation of a new magnetic gear design, the development of a comprehensive model of the dynamic behaviour of the gear is necessary as the occurrence of magneto-mechanical resonances of a gear can be the cause of powertrain system failure.

The paper deals with a model of a two-stage magnetic precession gear dynamics. The construction and design of the discussed gear was introduced by the authors in [2]. Magnetic precession gear provides the possibility of obtaining a notably higher ratios compared to the currently known magnetic gears solutions.

II Design of a two-stage magnetic precession gear and model of dynamics

The two-stage magnetic precession gear (MPG) is build of four key components: the input shaft (a), the immovable ring (b), the intermediate ring (c) and the output ring with the output shaft (d). Permanent magnets are fixed to the circumferences of each ring. The kinematic scheme of discussed MPG is illustrated in Figure 1. A detailed description of the gear design and its kinematic analysis were presented in [2]

Two-stage magnetic precession gear is very complex system, because intermediate ring moves with a precession motion (which is a combination of rotations about two inclined axes). To simplify the model, only the dynamics about main axis of the gear was analysed. For better understanding the mathematical model of the gear dynamics, in Figure 2 the MPG operation was presented as a two-stage gear with 'magnetic springs' representing the analogies to torque vs. internal load angle characteristics known from synchronous machines.

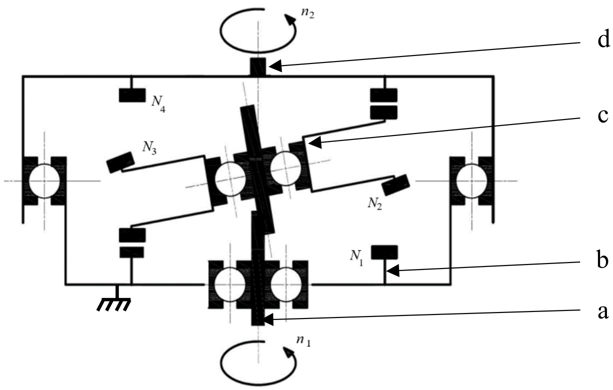

Figure 1: Kinematic scheme of the MPG [14]:
n_1 - input rotational speed, n_2 - output rotational speed
N_i - the number of neodymium magnets on the i-th ring

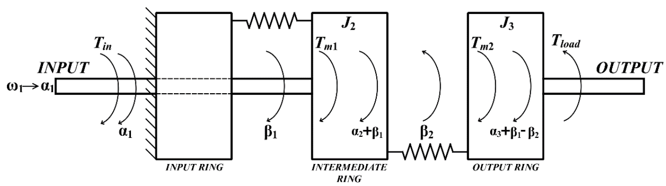

Figure 2: Graphical interpretation of a MPG dynamic model

In order to formulate the mathematical model, it is required to determine two equations of dynamics of the movable elements of the described MPG. The dynamic of the intermediate ring describes equation (1) and the dynamic of the output ring describes equation (2). Both equations contain the mechanical quantities, i.e. the load torque (T_{load}), the moments of inertia of the intermediate ring J_2 and the output ring J_3, as well as coefficients k_{f2} and k_{f3} representing mechanical friction and losses in the magnetic circuit caused by eddy currents and magnetic hysteresis phenomena. It was assumed that these 'magnetic' losses depend directly on the velocity in changes of the magnetic field.

$$J_2 \frac{d^2\alpha_2}{dt^2} = T_{m1} - T_{m2} - k_{f2}\omega_2 \tag{1}$$

$$J_3 \frac{d^2\alpha_3}{dt^2} = T_{m2} - T_{load} - k_{f3}\omega_3 \tag{2}$$

Detailed mathematical model was derived in [3].

In order to study the performance of the proposed MPG the mathematical model was implemented the MATLAB Simulink environment. Figure 3 presents model of the whole gear, while Figure 4 presents a detailed model for the second gear stage.

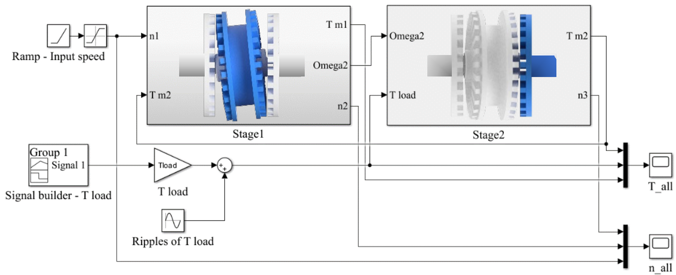

Figure 3: Model of MPG developed in MATLAB Simulink environment

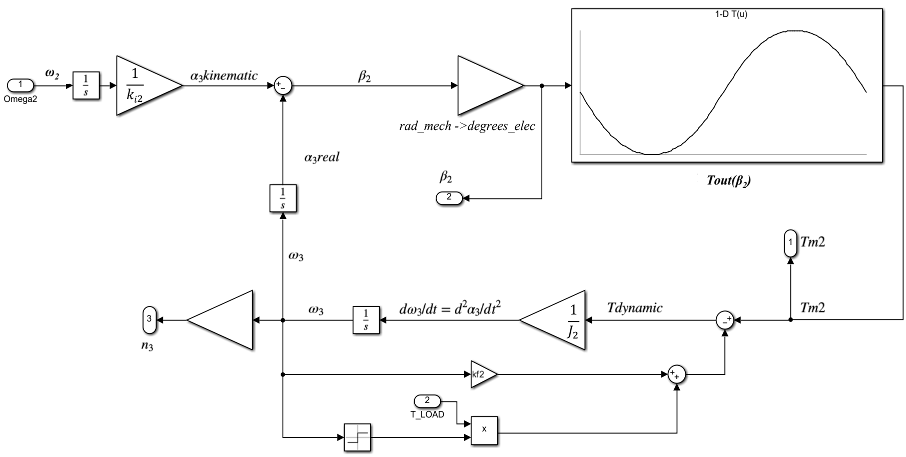

Figure 4: Model developed in MATLAB Simulink environment- second stage of MPG

In preliminary model, the magnetic torques characteristics were determined by means of the 3D FEM model of the magnetic field and implemented in Simulink as lookup table.

Then the MPG prototype was investigated on a test stand, shown in Figure 5. The dynamic response of the MPG output ring is presented in Figure 6.

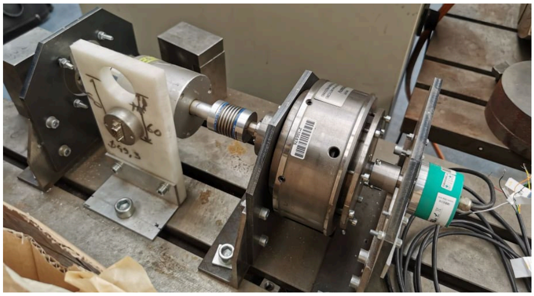

Figure 5: MPG test stand

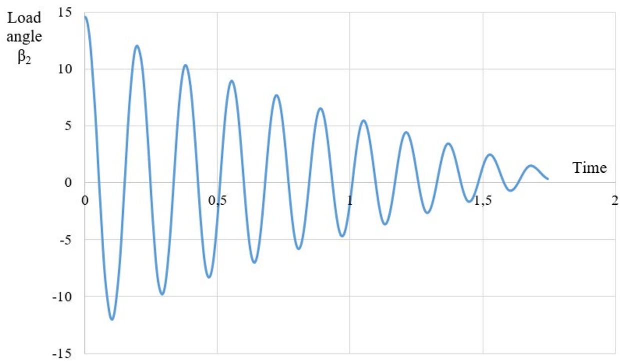

Figure 6: Dynamic response of the output ring

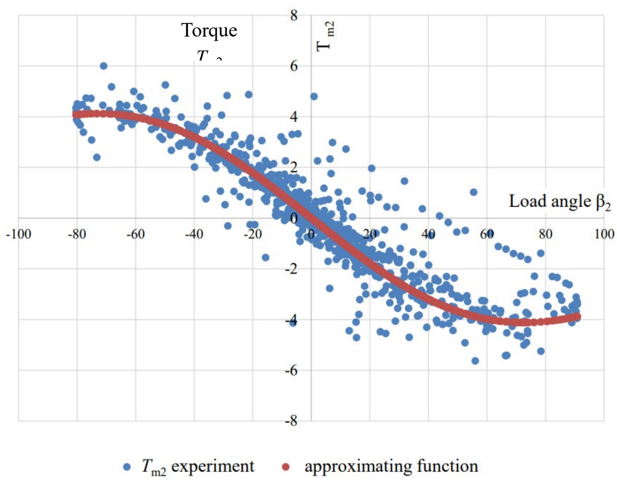

Figure 7: Approximation of magnetic torque function based on MPG prototype examnination

Based on experimental research, the magnetic torque function was approximated (Figure 7) and implemented in Simulink instead of 3D FEM characteristic.

The results of simulations carried out with both variants of model was compared and discussed.

Summary

The research described in the paper demonstrates how to carry out an analysis of the dynamics of a magnetic gear.

Detailed results of the conducted research will be presented during EPNC 2024 conference in Portorož and published in the full version of the paper.

References

[1] P. M. Tlali, R. Wang, and S. Gerber, 'Magnetic gear technologies: A review', *International Conference on Electrical Machines (ICEM)*, 2014, DOI: 10.1109/ICELMACH.2014.6960233.
[2] Ł. Macyszyn, C. Jedryczka, and R. Staniek, 'Design and Finite Element Analysis of Novel Two-Stage Magnetic Precession Gear', *Int. J. Simul. Model.*, vol. 18, 2019, DOI: 10.2507/IJSIMM18(4)487.
[3] L. Macyszyn, C. Jedryczka, and M. Mysinski, 'Analysis of a Two-Stage Magnetic Precession Gear Dynamics', *Energies*, vol. 16, no. 11, 2023, DOI: 10.3390/en16114484.

NO LOAD BEHAVIOR PREDICTION OF LARGE FIVE-LEGGED TRANSFORMERS USING TOPOLOGICAL TRANSIENT MODELS

SERGEY ZIRKA,[1] DENNIS ALBERT,[2]
ALEXANDER FRÖHLICH[3]

[1] Dnipro National University, Department of Physics and Technology, Dnipro, Ukraine
zirka@email.dp.ua
[2] OMICRON electronics GmbH, Klaus, Austria
dennis.albert@omicronenergy.com
[3] Graz University of Technology, Institute of Electrical Power Systems, Graz, Austria
a.froehlich@tugraz.at

DOI
https://doi.org/10.18690/um.feri.4.2025.38

ISBN
978-961-286-986-1

The work proposes a method of reproducing the no-load losses and currents of large five-legged transformers with the use of their transient models. This aim is achieved by employing topological transformer models based on a dynamic hysteresis model (DHM) and taking into account equivalent transformer capacitances. It is proposed to reproduce initially the measured total losses by using DHM means, and then to determine an equivalent per phase capacitance value that provides a best possible coincidence of calculated and measured current waveforms.

Keywords:
transformer model,
five-legged transformer,
capacitances,
variable core gaps,
no-load currents

University of Maribor Press

I Introduction

The choice of the core representation is an initial crucial stage in development of transient model of any transformer. As a minimum, the model should replicate, if not predict, no-load losses and currents, which is especially important for large five-legged units.

Most of the time-stepping finite element solvers are too slow and do not reproduce the so-called excess losses, which are the main loss component in high permeability grain-oriented (HGO) steels employed in large transformers. An efficient alternative is to build transformer transient models on the base of a Dynamic Hysteresis Model (DHM) included in 2019 in ATP/ATPDraw program [1] as L(i) Zirka-Moroz nonlinear branch. Its peculiarities are outlined in Section II-A.

When modeling 300 MVA and 786 MVA transformers studied in this work, significant capacitive components were observed in their no-load currents. Therefore, to replicate the measured line (terminal) currents, it is necessary to supplement transformer models with equivalent (per-phase) capacitances. Since their value C is a single fitting parameter, it is easily estimated starting with the value found in the FAT.

Before starting the modeling as a whole, it is critically important to select the proper steel from the DHM menu. It was found that only HGO steels should be used in the models of the large transformers under consideration, whereas using conventional GO steels fails in obtaining acceptable currents.

II Structure and details of the models

A. The composite DHM implemented into ATP/ATPDraw

According to the loss and field separation principle, the total magnetic field (H) formed by the DHM is the sum of the following three components [2]:

$$H = H_{\mathrm{h}}(B) + K_{\mathrm{loss}}\left[\frac{d^2}{12\rho}\frac{dB}{dt} + \delta \cdot g(B)\left|\frac{dB}{dt}\right|^{0.5}\right] \tag{1}$$

The field $H_h(B)$ is created by the history-dependent static hysteresis model. At high flux densities $B(t)$, dependence $H_h(B)$ is extended by a single-valued saturation curve. The terms in brackets represent classical eddy-current and excess fields as detailed in [2]. Multiplier K_{loss} is the loss coefficient, which allows the user to fit the DHM and thus the whole transformer model to the measured losses.

It was supposed that HGO steel 27ZDKH85 was used in both transformers considered. Specific losses W of this steel are shown in Fig. 1. The no-load losses P_0 measured for 300 MVA and 786 MVA transformers are indicated by isolated dots in the inset of Fig. 1. The lines in the inset are P_0 values evaluated with the transformer model outlined in Section II-B using K_{loss} = 0.926 and 0.85 respectively.

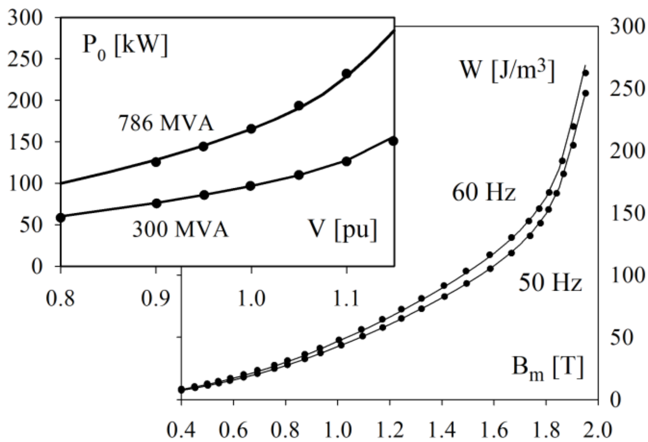

Figure 1: Specific losses W of the steel and no-load transformer losses P_0

The concave loss curves in the inset reflect the voltage and frequency dependence of the DHM (1) illustrated in Fig. 1.

B. DHM-based transformer models

A topological ATPDraw model of the step-up 786 MVA unit (YNd11) with inner (22.8 kV) delta winding and outer (525 kV) wye-connected winding is shown in Fig. 2.

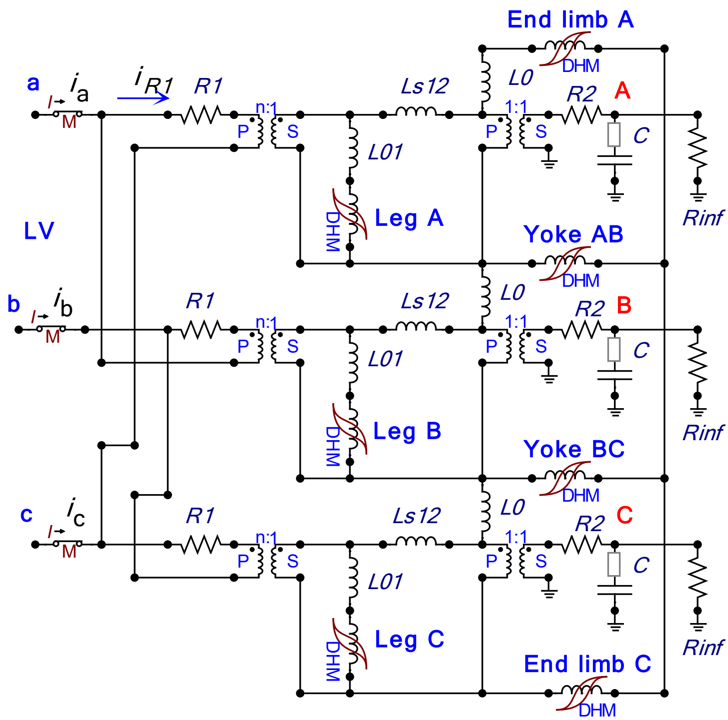

Figure 2: ATPDraw model of 786 MVA, YNd11 transformer

All major elements of the model are explained in [3]. A similar model of the three-winding 300 MVA transformer can be found in [4].

C. The effect of transformer capacitances

Additional elements of the model are equivalent per-phase capacitances *C*. They are placed at high-voltage (HV) terminals A, B, and C because of the largest capacitive contribution brought by the HV bushings [5], [6]. The introduction of capacitances is necessitated by the fact that at $C = 0$ the waveforms of the calculated line currents are quite different from the measured currents (Fig. 3 shows currents in lines A and B only because of the limited space).

However, with added capacitances ($C = 1900$ pF is easily found by trials and errors) the line currents at no-load become quite close to the measured ones (refer to Fig. 4).

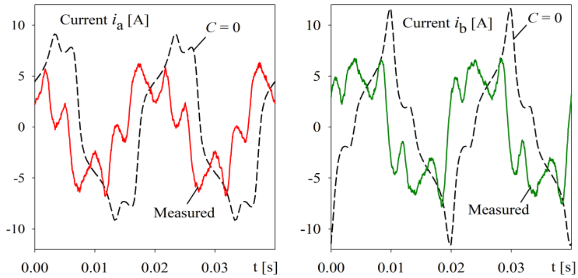

Figure 3; Measured and calculated no-load line currents at C =0

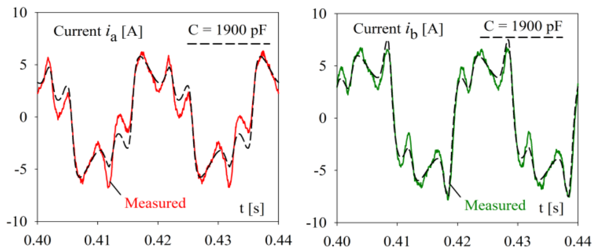

Figure 4: Measured and calculated no-load line currents at C = 1900 pF

Practically the same results are obtained if 0.27 mm thick steel H1 Carlite is used in the model with K_{loss} = 0.69. However, conventional GO steel M5 (35Z145), for which K_{loss} should be decreased to 0.35, is not suitable for the model because of the large line currents. A single period of the calculated line current $i_a(t)$ in Fig. 4 (left) is also shown by the dashed curve 1 in Fig. 5 (left). For comparison, the current in the A-phase winding resistor R1 (curve 2) and the referred magnetizing current in the DHM of leg A (curve 3) are also shown in Fig. 5 (left).

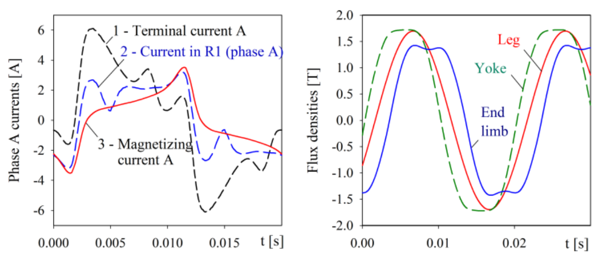

Figure 5: Phase currents (left) and flux densities (right) of the 5-legged unit

As can be seen in Fig. 5, there is nothing common between the regular magnetizing current (curve 3) and the currents shown by curves 1 and 2 (the latter waveform is typical for the five-legged transformer with inner wye-connected winding as that in the 300 MVA unit modeled). Because of the interphase interaction in the model of Fig. 2 and due to the masking effect of the excited delta-winding, it is difficult, if not impossible, to recognize the magnetizing current using the measured line currents.

In addition to the typical per-phase power pattern ($P_a<P_b<P_c$), the model with capacitances has shown a similar pattern observed for the terminal rms currents ($I_a<I_b<I_c$).

Fig. 5 (right) depicts flux densities in the leg A, yoke AB, and the left end limb. The latter two are non-sinusoidal and have different maxima, necessitating the use of the voltage-dependent DHM.

Additional transformer modeling carried out at elevated voltages has revealed experimental uncertainties caused, most probably, by imperfect core demagnetization. So, the model proposed seems to be the first to replicate the currents and losses in a wide range of experimental conditions.

References

[1] H. K. Høidalen, L. Prikler, and F. Peñaloza, *ATPDRAW Version 7.0 for Windows. Users' Manual*, NTNU, 2021, Trondheim, Norway.

[2] S. E. Zirka, Y. I. Moroz, N. Chiesa, R. G. Harrison, and H. K. Høidalen, "Implementation of inverse hysteresis model into EMTP – Part II: Dynamic model," *IEEE Trans. Power Del.,* vol. 30, no. 5, pp. 2233-2241, 2015.

[3] S. E. Zirka, D. Albert, Y. I. Moroz, and H. Renner, "Further improvements in topological transformer model covering core saturation," *IEEE Access*, vol. 10, pp. 64018-64027, 2022.

[4] S. E. Zirka, Y. I. Moroz, J. Elovaara, M. Lahtinen, R. A. Walling, H. Høidalen, D. Bonmann, C. M. Arturi, and N. Chiesa, "Simplified models of three-phase, five-limb transformer for studying GIC effects", Int. J. Electric Power and Energy Systems, vol. 103, pp. 168-175, 2018.

[5] C. Carrander, Magnetizing currents in power transformers – Measurements, simulations, and diagnostic methods, Doctoral Thesis, Stockholm, Sweden 2017.

[6] G. Rovišan, G. Plišić, F. Kelemen, "Influence of capacitive no-load current component in large power transformers," Procedia Engineering 202, pp. 176–182, 2017.

Design And Modelling of Toroidal Inductors with Different Geometries for a Single-Phase Inverter Application

RAYMOND QUINN, JOONAS VESA, PAAVO RASILO
Tampere University, Electrical Engineering Unit, Tampere, Finland
raymond.quinn@tuni.fi, joonas.vesa@tuni.fi, paavo.rasilo@tuni.fi

The prevalence of power electronic converters is increasing as part of the transition to renewable energy and electric transportation. One obstacle in improving the power density of converters is the size and mass of the electromagnetic components used in these devices. Fast and accurate design and modelling tools are required to optimise and reduce the footprint of electromagnetic components. This paper introduces a new approach based on the area-product method for rapidly designing inductors with different geometries. The behaviour of the designed inductors is simulated using a MATLAB Simulink model for laminated magnetic cores. The simulation results are presented and discussed.

DOI
https://doi.org/
10.18690/um.feri.4.2025.39

ISBN
978-961-286-986-1

Keywords:
area-product method,
inductor design,
loss models,
MATLAB Simulink,
power electronics

University of Maribor Press

I Introduction

Power electronic converters are an enabling technology of the transition to renewable energy and electric transportation. Converters utilise electromagnetic components such as inductors for purposes such as filtering. Despite the maturity of the field, electromagnetic components remain large and heavy compared to the other constituent parts of converters and remain an obstacle in improving their power density [1]. Volume and weight reduction of the electromagnetic components used in converters provides benefits such as reduced materials usage, lower cost, and better portability. To reduce the footprint of electromagnetic components, innovation in the design of ferromagnetic cores is needed which requires the development of fast and accurate design and modelling tools along with cost-effective rapid prototyping techniques for testing purposes. In this paper, a procedure for rapidly designing toroidal inductors with different core geometries is introduced. The procedure is based on the area-product method, but geometric parameters are able to be varied freely and the produced designs are not limited to standard core sizes. Once created, the behaviour of the designed inductors as L-filters in a single-phase inverter application is simulated using a MATLAB Simulink model for laminated magnetic cores based on that presented in [2]. The results can be used to determine optimal core geometries for different applications.

II Methods

A. Area-product method-based design

The area-product method is a well-established method for designing inductors which takes into account electrical, mechanical, and thermal requirements. It is described in detail in [3]. The area-product is the product of the core window area (W_a) and cross-sectional area (A_c). It is given by

$$A_\mathrm{p} = W_\mathrm{a} A_\mathrm{c} = \frac{L_\mathrm{ref} I_\mathrm{m}^2}{k_\mathrm{u} J_\mathrm{m} B_\mathrm{m}} \tag{1}$$

where L_ref is the required inductance, I_m the maximum current, J_m the maximum current density, and B_m the maximum flux density. k_u is the window utilisation factor and determines how much of the winding area is taken up by the copper winding.

Once the area-product has been calculated, the core which most closely matches the size determined by the area product calculation is selected from a catalogue. This often leads to a larger core than necessary being selected [4].

Growing accessibility to manufacturing techniques such as laser cutting and electric discharge machining allows for the rapid prototyping of cores, meaning cores which match exactly the calculated area-product can be quickly manufactured and studied. To this end, a modified area-product method was developed where hundreds of different cores, all with the same area-product, can be rapidly designed by varying the core height h and the ratio between the outer diameter d_o and inner diameter d_i of the toroidal core $k_\mathrm{d} = \frac{d_\mathrm{o}}{d_\mathrm{i}}$. Using this method, the inner diameter of the core is found from

$$d_\mathrm{i} = \left(\frac{8A_\mathrm{p}}{\pi h(k_\mathrm{d}-1)}\right)^{\frac{1}{3}}. \tag{2}$$

With this approach, 300 10.6 mH inductors were created using a MATLAB script and varying k_d between 1.4 and 2.6 for 12 different core heights between 12 mm and 80 mm. 25 designs were created for each core height. Figure 1 shows one half of the core of one of the designed inductors and the relevant geometric design parameters. Two halves are brought together, separated by an air gap, to create the whole inductor core.

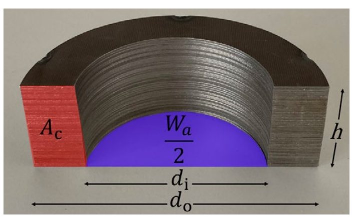

Figure 1: Example of inductor core geometric parameters

B. MATLAB Simulink inductor model

To simulate the behaviour of the designed cores, a time-domain MATLAB Simulink model for laminated cores was used [2]. The model combines eddy-current, hysteresis, and excess-loss models. Using the designed inductor geometries, equations for inductor voltage, flux linkage, magnetomotive force, and surface field strength in the core laminations are solved numerically for a given supply voltage waveform, and instantaneous power loss densities are obtained for each type of core loss. The total core losses are then found by multiplying the calculated instantaneous loss densities by the core volume and averaging over one period of the fundamental frequency. DC winding losses are also easily obtained from the model. The hysteresis curve supplied by the manufacturer for lamination material M330-35A was used to inform the model.

The inductor model was then combined with a simple single-phase inverter in Simulink with a 300 V DC input, 10.4 Ω load resistance, and switching frequency of 20 kHz. The RMS output current of the inverter was 5 A and an inductance value of 10.6 mH was selected to give a 5 % peak-to-peak current ripple at the output. Two periods of the fundamental frequency of 60 Hz were simulated and results for core losses, winding losses, current ripple, and inductance were obtained.

III Design and simulation results

Figure 2 shows the total weight of each of the designs made using the modified area-product method and their k_{d} values. Core heights increase for each set of 25 designs. Increasing the ratio between the outer and inner diameters initially reduces the weight of each design before increasing it. Similarly, weight decreases as the core height increases before beginning to increase. Many different variables can be studied in this way, including core weight, winding weight, air gap length, and volume. This can help in choosing an optimal design for a specific application.

Figure 3 shows results from the simulations which were carried out. For each set of core heights, increasing the ratio between the outer and inner diameters of the core increases the total losses. This is expected due to the increasing cross-sectional area of the cores. This trend was seen across the hysteresis, eddy-current, and excess losses which are also able to be separately studied. Winding losses showed the opposite relationship.

The inductor total losses were plotted against the price of materials for each individual inductor. It can be seen from Figure 4 that there are optimal inductors which have low losses and low costs. Attempting to reduce the losses past a certain point results in costs increasing.

IV Discussion and future work

The inductor design procedure presented in this paper allows for the rapid creation of hundreds of inductor designs for a single inductance value. Used in conjunction with the Simulink inductor model, data concerning each inductor's geometry, mass, and cost as well as power losses in power electronic applications can be easily studied, and optimal designs can be identified. The benefit of this kind of numerical inductor model is that it can model the behaviour of inductors much more quickly compared to analytical or finite element methods.

The next stage of the work is to validate the inductor model using empirical measurements taken from selected designs which will be manufactured from laminated sheets of the M330-35A material. Since the desire is to be able to produce rapid prototypes, initial tests have been carried out into which manufacturing methods are best for this purpose, with electric discharge machining showing the most promising results for cutting the core laminations. The veracity of the formulas used in calculating the effect of fringing flux as part of the area-product method are being studied using finite element analysis software. As one of the main goals of the work is to increase the power density of power electronic converters through optimisation of electromagnetic components, the inductor model will be used with the design techniques to study inductors operating in the saturation region as this offers a way of significantly reducing the sizes of the cores required.

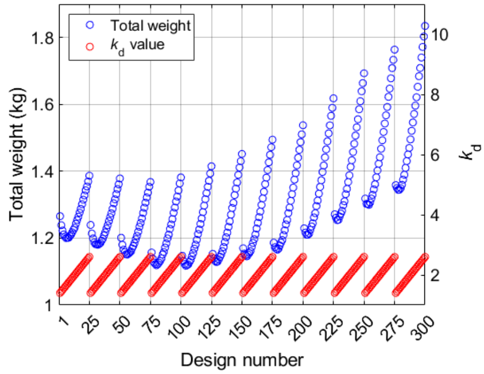

Figure 2: Total weight of each inductor design

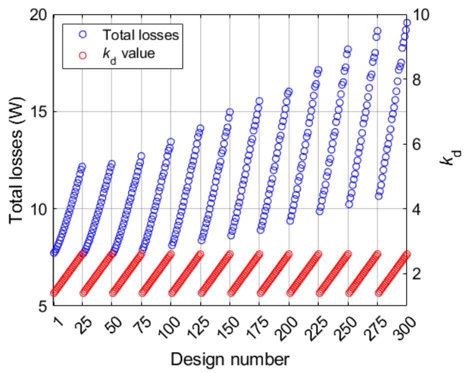

Figure 3: Total losses of each inductor design

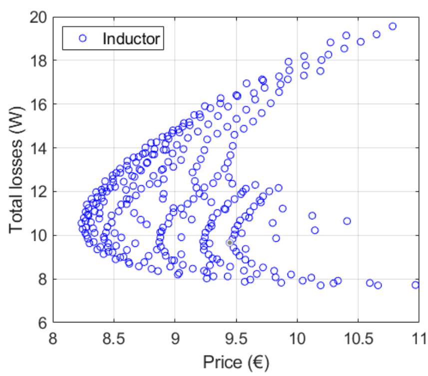

Figure 4: Losses versus price for each inductor design

References

[1] A. Oliveri, M. Lodi, and M. Storace, "Nonlinear models of power inductors: A survey", *Int. J. Circuit Theory Appl.*, vol. 50, no. 1, pp. 2–34, Jan. 2022, doi: 10.1002/cta.3147.

[2] P. Rasilo, W. Martinez, K. Fujisaki, J. Kyyra, and A. Ruderman, "Simulink Model for PWM-Supplied Laminated Magnetic Cores Including Hysteresis, Eddy-Current, and Excess Losses", *IEEE Trans. Power Electron.*, vol. 34, no. 2, pp. 1683–1695, Feb. 2019, doi: 10.1109/TPEL.2018.2835661.

[3] M. K. Kazimierczuk and H. Sekiya, "Design of AC resonant inductors using area product method", in *2009 IEEE Energy Conversion Congress and Exposition*, San Jose, CA: IEEE, Sep. 2009, pp. 994–1001. doi: 10.1109/ECCE.2009.5316501.

[4] A. Walker, G. Vakil, and C. Gerada, "Novel Core Designs to Miniaturise Passive Magnetic Components", in *2018 IEEE Transportation Electrification Conference and Expo (ITEC)*, Long Beach, CA, USA: IEEE, Jun. 2018, pp. 644–649. doi: 10.1109/ITEC.2018.8449959.

IMPACT OF NONLINEAR ANISOTROPIC MAGNETIC BEHAVIOR MODELS ON IRON LOSS MODELING IN TRANSFORMERS

DOI
https://doi.org/10.18690/um.feri.4.2025.40

ISBN
978-961-286-986-1

JOËL DRAPPIER,[1] FRÉDÉRIC GUYOMARCH,[1]
RIHEB CHERIF,[2] YVONNICK LE MENACH[1]

[1] University of Lille, Arts et Metiers Institute of Technology, Centrale Lille, Junia, Lille, France
joel.drappier@univ-lille.fr, Frederic.Guyomarch@irisa.fr,
yvonnick.le-menach@univ-lille.fr
[2] ESME, ESME Research Lab, Lille, France
rihaab.cherif@gmail.com

This paper explores the implications of nonlinear anisotropic behavior models on the simulation of magnetic losses in a transformer made of a conventional Grain-Oriented Electrical Steel (GOES) within a finite element method (FEM) simulation environment. GO laminations are commonly used to improve the efficiency of electrical machines, but their complex behavior requires accurate modeling. Nonlinear resolutions for different anisotropy models were implemented and compared with isotropic nonlinear and linear anisotropic models. Then, the iron losses were estimated using an anisotropic model developed by Appino *et al.*.

Keywords:
nonlinear anisotropic models,
iron loss modelling
grain-oriented electrical steel (GOES),
finite element method (FEM),
transformer efficiency

University of Maribor Press

I Introduction

Electrical machines are currently undergoing extensive research to enhance their efficiency by a few percentage points. One solution involves the use of grain oriented (GO) laminations. Renowned for superior magnetic performance in the rolling direction (RD) (high permeability and low magnetic losses), these steels are strategically employed to guide the magnetic flux along this preferred direction.

However, due to their inherent texture, these laminations not only exhibit nonlinear behavior but also strongly anisotropic magnetic characteristics between the RD and the transverse direction (TD). Considering the anisotropic behavior of these materials is essential when examining magnetic properties.

Implemented within the Finite Element Method (FEM) software code_Carmel, this study relies on different anisotropic behavior law models, such as the elliptical model [1] and the modified elliptical model [2]. These models rely solely on measurements in the rolling and transverse directions. A comparative analysis contrasts them with more common approaches, including nonlinear isotropic and linear anisotropic modeling.

Subsequently, an anisotropic iron loss model, proposed in [3], and recently implemented in a FEM simulation environment in [4], has been employed to estimate the iron losses in a quarter of a transformer made of GOES with Epstein frame dimensions. Nonlinear 3D magnetostatic simulations were performed. The iron losses have been computed based on FEM distributions of the **H** and **B** magnetic fields.

II Magnetic anisotropy models

A. Notations and assumptions

Defining our models involves considering the local coordinate system of laminations (RD, TD, ND), with ND representing the normal direction to the laminations. The permeability tensor μ carries the magnetic behavior of materials. It establishes the relation between magnetic induction and magnetic field according to $\mathbf{B} = \mu(\mathbf{H})\mathbf{H}$. As measured in [5], the permeability along ND is assumed to be low and linear. This assumption allows us to decouple the magnetic behavior along ND. We also assume the anhysteretic behavior.

The considered models were originally developed in 2D, and enable us to determine permeabilities in the principal plane. As mentioned in the introduction, models requiring measurements of the magnetic characteristics in the RD and TD directions were chosen. More specifically, we have chosen elliptical-type models, which will be described in detail here.

The permeability tensor μ, can be seen as a norm variation between H and B multiplied by an orientation variation. In the particular context of our models, the relationship between the angles of our fields is given by:

$$\tan\beta = \frac{\mu_{TD}(H)}{\mu_{RD}(H)}\tan\theta \tag{1}$$

μ_{RD} and μ_{TD} being the measured characteristics along the two principal directions and θ and β the respective angles of **H** and **B** with respect to the RD. For brevity, the H dependency is not indicated hereafter. Moreover, as illustrated in [6], μ is expressed as a diagonal tensor, such that:

$$\mu = \mu_{scal}\begin{pmatrix}\frac{\cos\beta}{\cos\theta} & 0\\ 0 & \frac{\sin\beta}{\sin\theta}\end{pmatrix} \tag{2}$$

with μ_{scal} the factor depending on the studied model.

B. The models

Illustrations in Fig. 1 depict the evolution of induction B according to the applied fields along RD and TD (resp. H_x and H_y). Each model, is defined such as:

- Elliptical model [1]:

$$\mu_{scal} = \left(cos^2(\beta)\,/\,\mu_{RD}^2(H) + sin^2(\beta)/\mu_{TD}^2(H)\right)^{-\frac{1}{2}}. \tag{3}$$

- Modified elliptical model [2]:

$$\mu_{scal} = \left(\cos^n(\beta) \,/\, \mu_{RD}^{n2}(H) + \sin^n(\beta)/\mu_{TD}^{n}(H)\right)^{-\frac{1}{2}}. \tag{4}$$

For our numerical examples, we choose $n = 1.4$ as proposed in [2].

- Nonlinear isotropic model: considers the magnetic characteristic along RD in the lamination, i.e. $\mu = \mu_{RD}$.
- Linear anisotropic model: linear approximations of the characteristics along the principal directions, with $\mu_{RD} = 26281.2\mu_0$ and $\mu_{TD} = 2159.5\mu_0$.

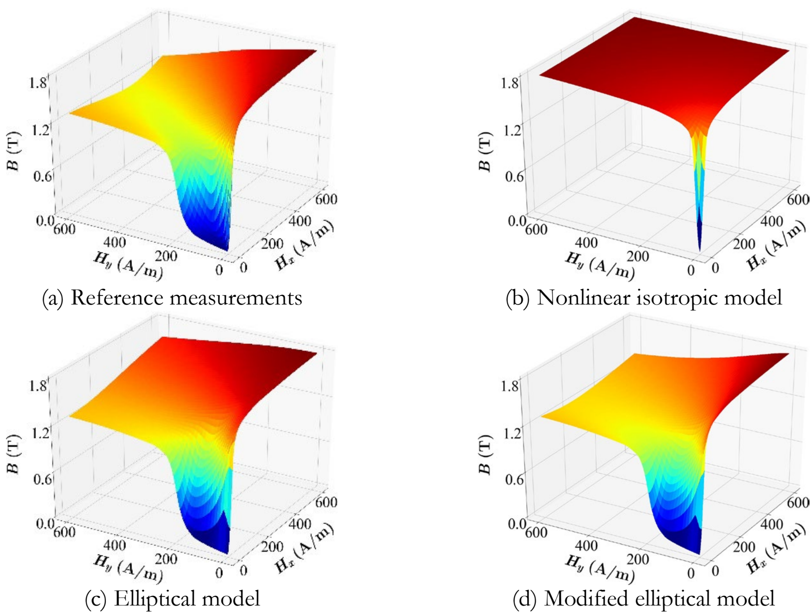

(a) Reference measurements (b) Nonlinear isotropic model

(c) Elliptical model (d) Modified elliptical model

Figure 1: Induction level as a function of the field components.

III Anisotropic loss model of appino

Concerning the iron loss model of Appino *et al.* [3], the study is based on previous work [4], performing for a linear behavior the simulation of losses in a toroidal core. This model separates total losses into three components: hysteresis losses, classical losses, and excess losses. Hysteresis losses, representing quasistatic losses per magnetization cycle, are notably calculated using the peak polarization level $\hat{\mathbf{J}}$ and the angle θ_a of the applied field $\mathbf{H}_a$. During simulation, the effects of the demagnetizing field $\mathbf{H}_d$ arising from anisotropy were carefully considered. The numerical simulation provides the distribution of the resulting field $\mathbf{H}$, such that $\mathbf{H} = \mathbf{H}_a + \mathbf{H}_d$.

IV Results

The 3D simulations of losses were carried out over a period at 50Hz, with an excitation current of 22.5mA passing through two coils of 88 turns each, positioned on a straight section of the transformer. The transformer itself consists of four laminations, similar to those in an Epstein frame, arranged in two layers, stacked so that the upper lamination in the frame corner has a horizontally oriented grain, while the lower one is vertically oriented. The maximum induction level does not exceed 1.7T, corresponding to a resulting field below 450A/m. The results in Table I and Fig. 2 show significant variations in total and local iron losses among the models. A more accurate consideration of anisotropy, as with the modified elliptical model, closer to measurements, leads to a reduction in total losses, with a loss shape markedly different from isotropic modeling. Note that linear modeling is relevant here, as we remain below the saturation point.

Table 1: Computed losses for different models.

Models	Iso. non-lin.	Aniso. lin.	Ell.	Ell. mod.
Total losses (W/kg)	0.1414	0.1183	0.1254	0.1099
Max. losses (W/kg)	3.2347	0.9602	0.3891	0.3280

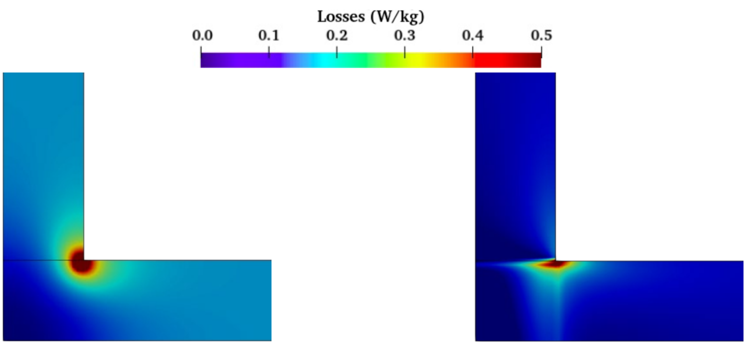

(a) Non-linear isotropic (b) Linear anisotropic

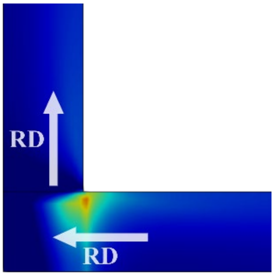

(c) Elliptical model

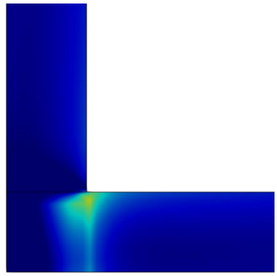

(d) Modified elliptical model

Figure 2: Specific iron losses (W/kg) of the upper laminations per model.

V Conclusion

This study emphasizes the importance of considering anisotropy in iron loss calculations, especially in the practical context of transformer modeling. Notably, it is observed that nonlinear isotropic modeling provides limited relevant information in predicting losses compared to other models that considering anisotropy, even in simpler forms. Our next step involves exploring models that are closer to material physics, requiring improvements in the robustness of the nonlinear solver.

References

[1] A. Di Napoli and R. Paggi, "A model of anisotropic grain-oriented steel," *IEEE Trans. Magn.*, vol. 19, no. 4, pp. 1557–1561, 1983.

[2] O. Bíró *et al.*, "A modified elliptic model of anisotropy in nonlinear magnetic materials," *COMPEL*, vol. 29, no. 6, pp. 1482–1492, 2010.

[3] C. Appino *et al.*, "Static and dynamic energy losses along different directions in GO steel sheets," *J. Magn. Magn. Mater.*, vol. 500, p. 166281, 2020.

[4] L. A. Millan Mirabal *et al.*, "Iron loss modeling of grain-oriented electrical steels in fem simulation environment," *IEEE Trans. Magn.*, vol. 58, no. 2, pp. 1–5, 2022.

[5] N. Hihat *et al.*, "Normal permeability of grain non-oriented, grain oriented and amorphous electrical steel sheets," *Int. J. Appl. Electromagn. Mech.*, vol. 46, no. 2, pp. 349–354, 2014.

[6] D. Huttenloher, H. Lorenzen, and R. Nuscheler, "Investigation of the importance of the anisotropy of cold-rolled electrical steel sheet," *IEEE Trans. Magn.*, vol. 20, no. 5, pp. 1968–1970, 1984.

MAGNETIC PARTICLE IMAGING OPPORTUNITIES AND CHALLENGES ON THE WAY TO THE CLINIC

DOI
https://doi.org/
10.18690/um.feri.4.2025.41

ISBN
978-961-286-986-1

MATTHIAS GRAESER
Fraunhofer Research Institution for Individualized and Cell-Based Medical Engineering, Fraunhofer IMTE, Lübeck, Germany
matthias.graeser@imte.fraunhofer.de

Magnetic Particle Imaging is a rising medical imaging technique which visualizes the distribution of magnetic particles within the human body. Besides direct visualization of blood flow dynamics, the technique can exploit the particle magnetization dependence on micro-environmental physical parameters as microsensors to measure temperature, viscosity, or binding state. Furthermore, the particles can also act as heat generators when exposed to suitable high frequency fields enabling magnetic fluid hyperthermia and triggered drug delivery. This work reviews the opportunities offered by MPI and highlights the challenges on the way to becoming an established clinical imaging modality.

Keywords:
magnetic particle imaging (MPI),
magnetic nanoparticles,
nonlinear magnetization curve,
clinical imaging,
nanoparticles,
hyperthermia,
functional imaging

University of Maribor Press

I Introduction

Magnetic Particle Imaging (MPI) was first proposed in 2005 by Gleich and Weizenecker from Philips Reasearch Laboratories in Hamburg [1]. The technology uses the nonlinear magnetization curve of magnetic nanoparticles, which act as a tracer material, to determine their spatial distribution within the patient [2]. Particles suitable for MPI are well tolerated by the human body and suitable tracer systems are available on the market for MRI imaging [3]. In contrast to MRI, MPI only images the distribution of the tracer, therefore the anatomy of the patient remains unknown. This represents a challenge and an advantage at the same time, as it increases the contrast but makes the images harder to interpret.

The goal of MPI is not to challenge or replace established imaging technologies like MRI or CT, but it can offer the possibility to improve situations, where current solutions are not optimal or fail. After the first years focussed on the instrumentation research, many medical application scenarios were demonstrated to prove that MPI can solve currently unmet needs within the clinic. The application scenarios range from stoke imaging [4], cell tracking [5] to functional imaging [6] and many more.

As MPI has proven its clinical potential in preclinical studies, the technology must now progress towards clinical scale systems and the acquisition of the first human images [7, 8].

II Opportunities and challenges for clinical usage

MPI offers a specific set of imaging properties: it comes with realtime capability with a speed of more than 46 volumes per second [9], no penetration depth dependence, high sensitivity down to pMol iron per ml [7], good image resolution down to submilimeter range [10] and a very high contrast to noise ratio due to no background image. Although not all these values were achieved until now within the same system, the unique combination offers high potential for clinical practice. MPI offers some high potential fields, some of them are shortly described in the following:

1) As the particles react to their micro-environment, they can be exploited as micro sensors within the human body with suitable functionalization. By doing so, MPI might be a nonradiation alternative for PET imaging [11].
2) The systems can be built with low footprint, low power consumption and even mobile if the resolution is not the strongest requirement. For stroke detection for example, a resolution of below 1 cm is sufficient for the diagnosis and classification. With this a small, low cost, mobile system can be built that can work within the intensive care unit or even in emergency vehicles [7].
3) As the field generators in MPI are typically able to provide a large flexibility on the field topology, the system can be used to steer and guide magnetic devices as small-scale robots for microsurgery or drug delivery systems [8].

There are many more potential benefits for a clinical scale MPI system. However, the upscaling does not come without new challenges. The larger bore diameter requires larger coils which lead to high power consumption and high voltages due to self induction. While the latter can be handled with proper coil designs, the power consumption remains a challenge. The best way to solve the power problem is to shift the attention towards the particle system. The imaging resolution of an MPI device is influenced by the gradient strength and the particle magnetization curve. If the particle magnetization is steeper, ideally a step response, the gradient can be chosen smaller to achieve the same resolution. As the gradient strength is linked quadratically to the power consumption of the gradient field generator, the particle system has a strong impact on the total power consumption. Recent research by Tay et al. has shown that tailored particle system can improve the image resolution by a factor of 10 and the signal to noise factor by 40 [12]. This resolution benefit could be omitted to reduce the gradient by a factor of ten and reduce the power consumption therefore by a factor of 100.

III Conclusion

MPI is an evolving medical imaging technology that offers a unique set of imaging parameters. On the way towards an established clinical imaging technology many challenges for particles synthesis and instrumentation are active research fields, but still need time and resources to be solved. The medical possibilities are various and can improve many clinical scenarios.

References

[1] B. Gleich and J. Weizenecker, "Tomographic imaging using the nonlinear response of magnetic particles," *Nature*, vol. 435, no. 7046, pp. 1214–1217, 2005, doi: 10.1038/nature03808.

[2] T. Knopp, N. Gdaniec, and M. Möddel, "Magnetic particle imaging: from proof of principle to preclinical applications," *Physics in medicine and biology*, vol. 62, no. 14, R124-R178, 2017, doi: 10.1088/13616560/aa6c99.

[3] F. Mohn *et al.,* "Characterization of the Clinically Approved MRI Tracer Resotran for Magnetic Particle Imaging in a Comparison Study," Feb. 2024. [Online]. Available: http://arxiv.org/pdf/2402.06350.pdf

[4] P. Ludewig *et al.,* "Magnetic Particle Imaging for Real-Time Perfusion Imaging in Acute Stroke," *ACS nano*, vol. 11, no. 10, pp. 10480–10488, 2017, doi: 10.1021/acsnano.7b05784.

[5] O. C. Sehl, J. J. Gevaert, K. P. Melo, N. N. Knier, and P. J. Foster, "A Perspective on Cell Tracking with Magnetic Particle Imaging," *Tomography (Ann Arbor, Mich.)*, vol. 6, no. 4, pp. 315–324, 2020, doi: 10.18383/j.tom.2020.00043.

[6] C. Z. Cooley, J. B. Mandeville, E. E. Mason, E. T. Mandeville, and L. L. Wald, "Rodent Cerebral Blood Volume (CBV) changes during hypercapnia observed using Magnetic Particle Imaging (MPI) detection," *NeuroImage*, vol. 178, pp. 713–720, 2018, doi: 10.1016/j.neuroimage.2018.05.004.

[7] M. Graeser *et al.,* "Human-sized magnetic particle imaging for brain applications," *Nature communications*, vol. 10, no. 1, p. 1936, 2019, doi: 10.1038/s41467-019-09704-x.

[8] J. Rahmer, C. Stehning, and B. Gleich, "Remote magnetic actuation using a clinical scale system," *PLOS ONE*, vol. 13, no. 3, e0193546, 2018, doi: 10.1371/journal.pone.0193546.

[9] J. Weizenecker, B. Gleich, J. Rahmer, H. Dahnke, and J. Borgert, "Three-dimensional real-time in vivo magnetic particle imaging," *Phys. Med. Biol.*, vol. 54, no. 5, L1-L10, 2009, doi: 10.1088/00319155/54/5/L01.

[10] P. Vogel *et al.,* "Micro-Traveling Wave Magnetic Particle Imaging— Sub-Millimeter Resolution With Optimized Tracer LS-008," *IEEE Trans. Magn.*, vol. 55, no. 10, pp. 1–7, 2019, doi: 10.1109/TMAG.2019.2924198.

[11] H. Paysen *et al.,* "Cellular uptake of magnetic nanoparticles imaged and quantified by magnetic particle imaging," *Sci Rep*, vol. 10, no. 1, p. 1922, 2020, doi: 10.1038/s41598-020-58853-3.

[12] Z. W. Tay *et al.,* "Superferromagnetic Nanoparticles Enable Order-ofMagnitude Resolution & Sensitivity Gain in Magnetic Particle Imaging," *Small Methods*, vol. 5, no. 11, e2100796, 2021, doi: 10.1002/smtd.202100796.

OPTIMIZATION OF THE FERROMAGNETIC NANOPARTICLES FABRICATION FOR MEDICAL APPLICATIONS

KATARZYNA WOJTERA, KRZYSZTOF SMOLKA, LUKASZ SZYMANSKI

Lodz University of Technology, Institute of Mechatronics and Information System, Lodz, Poland
katarzyna.wojtera@p.lodz.pl, krzysztof.smolka@p.lodz.pl, lukasz.szymanski@p.lodz.pl

DOI
https://doi.org/10.18690/um.feri.4.2025.42

ISBN
978-961-286-986-1

Carbon nanotubes possess remarkable properties, rendering them applicable across various fields, including medicine, particularly in hyperthermia treatments when filled with ferromagnetic material. This study focuses on refining the synthesis process of iron-filled multi-walled carbon nanotubes (Fe-MWCNTs) to produce high-purity nanocontainers with elevated iron content. Fe-MWCNTs were synthesized via catalytic chemical vapor deposition (CCVD), with temperature identified as a crucial determinant of synthesis efficiency. The paper also outlines the characterization of the resultant material. To gain insights into the underlying phenomena, computer simulations were conducted using COMSOL software.

Keywords:
multi-walled carbon nanotubes filled with iron (Fe-MWCNTs), catalytic chemical vapor deposition (CCVD), COMSOL Multiphysics simulations, ferromagnetic materials, hyperthermia treatments

University of Maribor Press

I Introduction

Since their discovery by Iijima in 1991 [1], carbon nanotubes have captured the attention of researchers globally due to their remarkable properties, including electrical conductivity [2], mechanical strength [3], high temperature stability, and chemical resistance [4]. These properties enable diverse industrial applications, such as electronics, textiles, supercapacitors, field emitters [1, 5], and fillers in conductive polymer composites [6]. Moreover, carbon nanotubes hold potential in biomedicine, serving as drug carriers or for hyperthermia-induced cancer cell destruction. However, realizing these applications requires efficient synthesis processes to tailor nanotube properties.

Presently, popular synthesis methods include Arc Discharge (AD) synthesis [8], Laser Ablation (LA) [9], and Chemical Vapor Deposition (CVD) [10, 11]. In the described experiments, catalytic chemical vapor deposition (CCVD) with continuous catalyst delivery via solution was employed.

The experiments aimed to optimize the evaporation temperature and dosing rate of ferrocene solution, as well as carrier gas flow rate, and determine the deposition zone temperature conducive to maximal carbon nanotube growth (referred to as the highest "forest" of nanotubes) with encapsulated iron. Encapsulation is crucial for using synthesized Fe-MWCNTs in hyperthermia, ensuring precise localization and heating within tumor tissue [12, 13]. Functionalizing Fe-MWCNT surfaces is also essential, involving iron nanoparticle removal to enhance heating efficiency [14, 15]. Maintaining low amorphous carbon impurities is imperative.

Initially, ferromagnetic-filled CNT synthesis was conducted electrothermally to establish synthesis parameters. General principles of the CCVD process were simulated, creating a heat distribution model using COMSOL Multiphysics software. This computational tool, employing the finite element method, offers high precision in analyzing various phenomena, ranging from optics to heat transfer [16].

II Materials and methods

A. Synthesis of Fe-MWCNTs

Carbon nanotubes were produced using catalytic chemical vapor deposition (CCVD) methodology [17, 18]. The synthesis setup utilized a horizontal furnace with three distinct temperature zones for precise thermal management. Zone I served as the catalyst solution evaporation area at 573K, Zone II maintained a temperature of 573K, while Zone III, the deposition zone, operated within the temperature range of 1020K to 1120K. Argon was employed as the carrier gas throughout the process. Ferrocene (Fe(C5H5)2), dissolved in xylene, functioned as the catalyst, also contributing as an additional carbon source for nanotube growth. This method was chosen due to its flexibility in adjusting parameters such as catalyst dosage, temperature in both evaporation and deposition zones, carrier gas flow rate, and synthesis duration. External injection of the mixture occurred at varying inlet velocities ranging from 10 ml/h to 18 ml/h to analyze material characteristics concerning infusion speed.

B. Modelling using Comsol Multiphysics

The next stage of the work was to simulate the general principles of the CCVD process and create a heat distribution model, which was prepared using COMSOL software. The simulation provided valuable information regarding the choice of parameters for the synthesis of Fe-MWCNTs.

The Navier-Stockes equation was used to describe the gas flow in the reactor chamber (1), (2) and (3). The flow of carrier gas (Ar2) in the quartz reactor was assumed to be laminar, so the Navier-Stockes equation for an incompressible and viscous fluid was used [19].

III Results

Fig. 1 shows the simulation of heat distribution during the CCVD carbon nanotubes synthesis process. One important part of the process optimization was the proper placement of the silicon wafer, which is the substrate for nanotube growth. The wafer should be placed so as to achieve the highest temperature stability. As mentioned earlier, the synthesis of carbon nanotubes takes place in a furnace divided into three temperature zones. In the first and second the temperature is 570 K, in the third 1070 K. The third zone in the graph below (Figure 1) starts at 60cm of the furnace. The obtained plot shows the results of simulating the temperature distribution in the furnace with the placement of silicon wafers in different places of the third temperature zone.

The results of this simulation show that the temperature on the wafer is most stable when the wafer is placed evenly in the middle of the third temperature zone or in the second half of this zone. Furthermore, when examining the process carried out in the laboratory, it was observed that less material was formed at the end of the third temperature zone than at the beginning. Hence the conclusion that the silicon substrate should be placed evenly in the middle of the third zone to ensure both better temperature stability and process efficiency.

Another aspect investigated during the computer simulations in the COMSOL environment was the determination of the heating time of the quartz reactor before the start of the synthesis process.

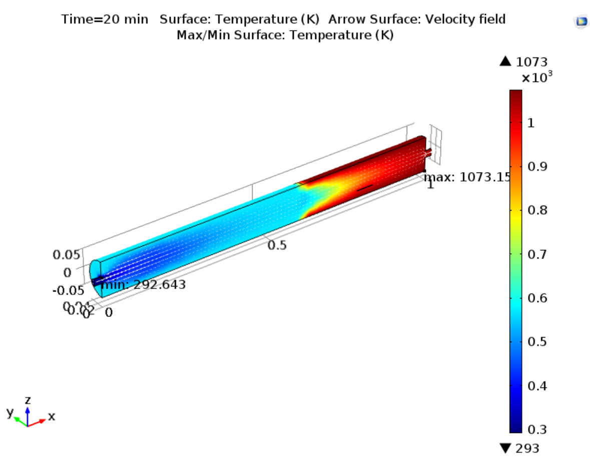

Figure 1: Heat distribution model during the synthesis process [own elaboration].

The next step of the study was to optimise the synthesis of Fe-CNTs by CCVD with respect to iron content. Since one of the objectives of the work was to obtain the highest possible iron content in the nanotubes, the results of different syntheses, in which the concentration of ferrocene-xylene mixture was changed, were compared. The iron content was examined by thermogravimetric analysis (TGA).

In the trials carried out for the synthesis of carbon nanotubes, a number of dependances have been demonstrated that define the temperature limits at which successful nanoscale processes occur. In order to present these dependency, only SEM images allowing observation of the process products have been selected and presented.

IV Conclusions

In the optimization of carbon nanotube synthesis via catalytic chemical vapor deposition (CCVD), various studies were conducted involving COMSOL simulations and experimental trials to identify optimal parameters. It was found that placing the silicon substrate in the middle of the third temperature zone yields the best results. Pre-synthesis preparation time of at least 10 minutes is necessary for the wafer temperature to reach the deposition zone temperature, aligning with existing literature. The ideal substrate thickness ranges from 0.5mm to 2.5mm, ensuring proper temperature distribution. The carrier gas flow rate should be kept below 1250 SCCM for efficient substrate transfer. Optimizing the CCVD process led to the discovery that a substrate solution concentration of 200mg/ml yields the highest quality nanotubes. Further analysis using electron microscopy and thermogravimetry revealed temperature-dependent growth rates and filling degree conditions for Fe-MWCNTs. Ongoing research involves XRD analysis to identify iron allotropic varieties and determine deposition zone temperatures for strictly ferromagnetic materials. Additionally, efforts are directed towards maximizing alpha-Fe nanotube filling in MWCNTs.

References

[1] Iijima S.: Helical microtubules of graphitic carbon, Nature 354, 1991, 56–58, [doi: 10.1038/354056a0].
[2] Filleter T., Bernal R., Li S., Espinosa H.D.: Ultrahigh Strength and Stiffness in Cross-Linked Hierarchical Carbon Nanotube Bundles, Advanced Materials 23 (25), 2011, 2855–2860 [doi: 10.1002/adma.201100547]
[3] de Heer W.A., Chatelain A., Ugarte D.: A carbon nanotube field-emission electron source, Science 270, 1995, 1179–1180.

[4] Thostenson E., Chunyu Li, Tsu-Wei Chou: Nanocomposites in context, Composites Science and Technology, 65(3–4), 2005, 491–516, [doi: 10.1016/j.compscitech.2004.11.003].

[5] Hong S., Myung S.: Nanotube Electronics: A flexible approach to mobility. Nature Nanotechnology 2 (4), 2007, 207–208 [doi: 10.1038/nnano.2007.89].

[6] Hafner J.H., Bronikowski M.J., Azamian B.R., Nikolaev P., Rinzler A.G., Colbert D.T., Smith K.A., Smalley R.E.: Catalytic growth of single-wall carbon nanotubes from metal particles, Chem. Phys. Lett. 296, 1998, 195–202

[7] Jeszka J.K., Pietrzak L.: Polylactide/Multiwalled Carbon Nanotube Composites – Synthesis and Electrical Properties. Polimery, 55(7-8), 2010, 524–528.

[8] L. Szymanski, Z. Kolacinski, G. Raniszewski, and E. Gryska, "CNTs synthesis on steel strip a in microwave plasma reactor for medical application," IEEE-NANO 2015 - 15th Int. Conf. Nanotechnol., pp. 1062–1065, 2015.

[9] J. Chrzanowska et al., "Synthesis of carbon nanotubes by the laser ablation method: Effect of laser wavelength," Phys. Status Solidi Basic Res., vol. 252, no. 8, pp. 1860–1867, 2015.

[10] K. Wojtera, M. Walczak, L. Pietrzak, J. Fraczyk, L. Szymanski, and A. Sobczyk-Guzenda, "Synthesis of functionalized carbon nanotubes for fluorescent biosensors," Nanotechnology Reviews, vol. 9, no. 1, pp. 1237–1244, Jan. 2020, doi: 10.1515/ntrev-2020-0096.

[11] G. Raniszewski, Z. Kolacinski, and L. Szymanski, "Ferromagnetic nanoparticles synthesis in local thermodynamic equilibrium conditions," IEEE-NANO 2015 - 15th Int. Conf. Nanotechnol., pp. 323–326, 2015.

[12] G. Raniszewski, A. Miaskowski, and S. Wiak, "The Application of Carbon Nanotubes in Magnetic Fluid Hyperthermia," J. Nanomater., vol. 2015, 2015.

[13] A. A. Bhirde et al., "Targeted Killing of Cancer Cells in Vivo and in Vitro with EGF-Directed Carbon Nanotube-Based Drug Delivery," ACS Nano, vol. 3, no. 2, pp. 307–316, Feb. 2009, doi: 10.1021/nn800551s.

[14] D. Chen et al., "Photoacoustic Imaging Guided Near-Infrared Photothermal Therapy Using Highly Water-Dispersible Sin-gle-Walled Carbon Nanohorns as Theranostic Agents," Advanced Functional Materials, vol. 24, no. 42, pp. 6621–6628, Nov. 2014, doi: 10.1002/adfm.201401560.

[15] A. L. Antaris et al., "Ultra-low doses of chirality sorted (6,5) carbon nanotubes for simultaneous tumor imaging and photo-thermal therapy," ACS Nano, vol. 7, no. 4, pp. 3644–3652, Apr. 2013, doi: 10.1021/nn4006472.

[16] "COMSOL Multiphysics 5.5 Reference Manual," COMSOL AB, 2019.

[17] E. Kowalska et al., "Morphology and electronic properties of carbon nanotubes grown with Fe catalyst," Journal of Materials Research, vol. 18, no. 10, pp. 2451–2458, 2003, doi: 10.1557/JMR.2003.0341.

[18] L. Szymanski, Z. Kolacinski, S. Wiak, G. Raniszewski, and L. Pietrzak, "Synthesis of Carbon Nanotubes in Thermal Plasma Reactor at Atmospheric Pressure," Nanomaterials, vol. 7, no. 2, p. 45, Feb. 2017, doi: 10.3390/nano7020045.

[19] N. S. R. et al. . Nishant Sharma. R et al., "The Simulation of Three-Dimensional Heat Transfer Through an Insulated Pipe by Variation of Solver Parameters," Int. J. Automob. Eng. Res. Dev., 2019.

TOWARDS ACCURATE SIZE PREDICTIONS OF MAGNETIC NANOPARTICLES USING SUPPORT VECTOR REGRESSION

LUKAS GLÄNZER, LENNART GÖPFERT,
THOMAS SCHMITZ-RODE, IOANA SLABU

RWTH Aachen University, Medical Faculty, Institute of Applied Medical Engineering, Helmholtz Institute, Aachen, Germany
glaenzer@ame.rwth-aachen.de, goepfert@ame.rwth-aachen.de, smiro@ame.rwth-aachen.de, slabu@ame.rwth-aachen.de

This study explores the size of magnetic nanoparticles (MNP) for applications in Magnetic Resonance Imaging (MRI) and Magnetic Particle Imaging (MPI). Emphasizing the critical role of MNP size on their response to alternating magnetic fields, the study unveils a regression model to optimize MNP synthesis towards tailored sizes of MNP. With a limited and broadly distributed data set at hand, the feasibility of building an accurate predictive model based on Support Vector Machines is shown. Integrating such a model into a continuous synthesis setup establishes a feedback loop, enabling real-time control and adaptation of synthesis parameters.

DOI
https://doi.org/10.18690/um.feri.4.2025.43

ISBN
978-961-286-986-1

Keywords:
magnetic nanoparticles synthesis,
machine learning,
Support Vector Machines,
size prediction,
process optimization

University of Maribor Press

I Introduction

Magnetic nanoparticles (MNP) have emerged as pivotal entities in the area of medical technology, offering unique advantages in diagnostic and therapeutic applications [1, 2]. This study delves into the optimization of MNP synthesis, with a particular focus on MNP size, to enhance their performance in alternating magnetic fields — an essential consideration for applications in Magnetic Resonance Imaging (MRI) and Magnetic Particle Imaging (MPI) [3]. The complex nonlinear behaviour of MNP in alternating fields [4, 5] underscores the critical role of MNP size, making it a focal point of investigation in this research.

Further, utilizing MNP holds tremendous potential in revolutionizing medical treatments, especially in the context of hyperthermia [6, 7]. Thus, the need for fine-tuned control over MNP characteristics becomes paramount. Achieving optimal magnetic response in alternating fields is crucial for unlocking the full potential of MNP in hyperthermic applications, where precise and targeted heating is essential for therapeutic efficacy.

The aim of this comparative study is to find a regression model that can accurately predict the size of MNP based on the system parameters of their continuous synthesis process. By incorporating regression models into the continuous automated synthesis setup, a sophisticated feedback loop is envisioned, creating a dynamic system that seamlessly adapts synthesis parameters based on real-time data.

II Material and methods

This study explores regression models for predicting MNP size in a comparative analysis. The data is taken form an experimental study of a continuous MNP synthesis that has been already published [8]. The dataset includes all system parameters of the synthesis setup, educt concentrations and measured MNP sizes.

The data comprises of 26 data points, each representing a single synthesis run. Each data point contains 22 features and the MNP size as the target variable.

The preparation of the data set includes the handling of missing values by either zero or mean imputation for different types of features. Data normalization and One-Hot-Encoding are applied as a last data preprocessing step to ensure an effective and unbiased modelling of the relevant features.

For the size prediction, a Support Vector Regression (SVR) [9] model was built and compared to an Elastic Net Regression [10], a regularized linear regression algorithm.

An extensive grid search was designed to find the best hyperparameters for each regression method. To account for the limited number of data points within the two data sets, an extensive cross-validation was employed. Leave-One-Out-Cross-Validation uses each single data point as a validator against the remaining data points during training, to minimize the training bias and allow a reliable performance estimation [11]. With the optimized hyperparameters for each method, the final prediction was performed with a random data split where 80 % of the data points were used as training set and the remaining 20 % constituting the validation set.

During the grid search and the final training of the models, the Root-Mean-Squared-Error (RMSE) function was used as evaluation metric. RMSE was chosen to ensure precise MNP size estimation due to its high sensitivity towards large errors.

III Results and discussion

Table 1 shows both examined regression methods and their determined hyperparameters. All hyperparameters are determined by comprehensive testing within reasonable intervals to ensure thorough exploration of the model's parameter space.

The alpha hyperparameter in Elastic Net controls the overall strength of regularization, with a value of 0.532 emphasizing a moderate regularization effect, which helps to prevent overfitting. The L1-ratio determines the balance between L1 and L2 regularization, with a value of 0.1 indicating a strong preference for L2 regularization, which is suitable to avoid feature selection.

For SVR, the optimal C value at 152.59 shows low regularization implying adaptability to specific data points. Gamma influences the shape of the regression curve. A value of 3.16 indicates sensitivity to local variations. A small epsilon of 0.1 means that the model is less tolerant to deviations in the predictions, which goes along with the desired accuracy in the MNP size prediction. The selected Radial Basis Function (RBF) kernel allows the model to capture complex relationships.

Figure 1 shows a bar chart with the RMSE values and the standard deviation of the residuals for each tested method with its identified hyperparameters.

The Elastic Net model yielded an RMSE score of 40.2, and thus has a high average magnitude of prediction errors resulting in less accurate predictions. Additionally, the standard deviation of residuals for Elastic Net is 104.57, signifying substantial variability in the prediction errors around the regression line.

Table 1: Determined hyperparameters

Method	Hyperparameter	Tested Ranges	Best Value
Elastic Net	alpha L1-ratio	[0.0, 1.0] [0.1, 1.0]	0.532 0.1
Support Vectors	C gamma epsilon kernel	[100.0, 200.0] [0.0, 5.0] [0.1, 1.0] ['linear', 'poly', 'sigmoid', 'rbf']	152.59 3.16 0.1 rbf

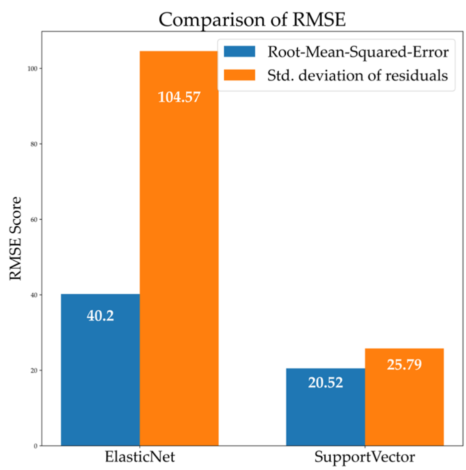

Figure 1: Validation scores for the trained regression methods with their RMSE score (blue) and the standard deviation of the residuals (orange).

In contrast, the Support Vector Regression model performed better with an RMSE score of 20.52, indicating lower prediction errors. The narrower standard deviation of residuals 25.79 in Support Vector Regression implies that it captures the underlying patterns more effectively.

Overall, the data suggests that Support Vector Regression is more suitable to accurately predict sizes of MNP. The underlying synthesis involves complex non-linear feature correlations, which can be captured via the radial basis function. For their applications, a tailored MNP size is significant. A fine tuning of the hyperparameter epsilon can prioritize accurate predictions and still allow a small error margin to enhance robustness. By definition of SVR, outliers (exhibited by experimental variability or measurement errors), are not considered.

However, given the small dataset size, high feature dimensionality, and broad distribution of MNP sizes, specific model selection and validation are crucial. Further cross-validation and exploration of domain-specific feature engineering and consideration of additional types of regression methods can enhance the robustness of the predictions.

IV Conclusion and outlook

In this study, two regression methods were assessed and compared towards their suitability regarding an accurate MNP size prediction. The two methods, Elastic Net Regression and Support Vector Regression, were investigated using a small data set of different synthesis and compared using an error function (RMSE) and the standard deviation of the prediciton residuals. The study shows, that the Support Vector Regressions yields a much smaller RMSE value of 20.52 compared to 40.2. Also its standard deviation is smaller with 25.79 compared to 104.57, which indicates a smaller variation within the prediction errors. Both values indicate an accurate precision and the suitability of the employed SVR. However, as only limited and broadly distributed data was available for comparing the two methods, an extended study incorporating a larger dataset is necessary to validate the findings. Also, the performance of other regression methods such as random forests, gradient boosting or multilayer perceptrons should be considered and compared to the ones presented in this work.

Acknowledgements

We gratefully acknowledge financial support by the German Research Foundation (grant no. 467959793), and by the Federal Ministry of Education and Research (grant no. 03VP10971). We gratefully acknowledge the financial support by the by the European Union (ERC, MAD Control, 101076174). Views and opinions expressed are however those of the author(s) only and do not necessarily reflect those of the European Union or the European Research Council Executive Agency. Neither the European Union nor the granting authority can be held responsible for them.

References

[1] G. G. Flores-Rojas, F. López-Saucedo, R. Vera-Graziano, E. Mendizabal, and E. Bucio, "Magnetic Nanoparticles for Medical Applications: Updated Review," *Macromol*, vol. 2, no. 3, pp. 374–390, 2022.

[2] Kritika and I. Roy, "Therapeutic applications of magnetic nanoparticles: recent advances," *Mater. Adv.*, vol. 3, no. 20, pp. 7425–7444, 2022.

[3] B. Mues, E. M. Buhl, T. Schmitz-Rode, and I. Slabu, "Towards optimized MRI contrast agents for implant engineering: Clustering and immobilization effects of magnetic nanoparticles," *Journal of Magnetism and Magnetic Materials*, vol. 471, pp. 432–438, 2019.

[4] D. Cabrera *et al.,* "Superparamagnetic-blocked state transition under alternating magnetic fields: towards determining the magnetic anisotropy in magnetic suspensions," *Nanoscale*, vol. 14, no. 24, pp. 8789–8796, 2022.

[5] J. Rahmer, J. Weizenecker, B. Gleich, and J. Borgert, "Signal encoding in magnetic particle imaging: properties of the system function," *BMC medical imaging*, vol. 9, p. 4, 2009.

[6] S. Lei *et al.,* "Magnetic Particle Imaging-Guided Hyperthermia for Precise Treatment of Cancer: Review, Challenges, and Prospects," *Molecular imaging and biology*, vol. 25, no. 6, pp. 1020–1033, 2023.

[7] A. Rajan and N. K. Sahu, "Review on magnetic nanoparticle-mediated hyperthermia for cancer therapy," *J Nanopart Res*, vol. 22, no. 11, 2020.

[8] L. Göpfert *et al.,* "Enabling continuous flow manufacturing of magnetic nanoparticles with a millifluidic system," *Journal of Magnetism and Magnetic Materials*, vol. 563, p. 169985, 2022.

[9] H. Drucker, C. J. C. Burges, L. Kaufman, A. Smola, and V. Vapnik, "Support Vector Regression Machines," in *Advances in Neural Information Processing Systems*, 1996.

[10] H. Zou and T. Hastie, "Regularization and Variable Selection Via the Elastic Net," *Journal of the Royal Statistical Society Series B: Statistical Methodology*, vol. 67, no. 2, pp. 301–320, 2005.

[11] G. C. Cawley, "Leave-One-Out Cross-Validation Based Model Selection Criteria for Weighted LS-SVMs," in *The 2006 IEEE International Joint Conference on Neural Network Proceedings*, Vancouver, BC, Canada, 2006, pp. 1661–1668.

CURRENT CONTROL SYSTEM FOR COUPLED COIL ARRAYS IN MPI

JAN-PHILIPP SCHEEL,[1, 2] FYNN FOERGER,[3, 4]
FLORIAN SEVECKE,[1] TOBIAS KNOPP,[1, 3, 4]
MATTHIAS GRAESER[1, 2]

[1] Fraunhofer Research Institution for Individualized and Cell-Based Medical Engineering IMTE, Lübeck, Germany
jan-philipp.scheel@imte.fraunhofer.de, florian.sevecke@imte.fraunhofer.de, tobias.knopp@tuhh.de, matthias.graeser@imte.fraunhofer.de
[2] University of Lübeck, Institute of Medical Engineering, Lübeck, Germany
jan-philipp.scheel@imte.fraunhofer.de, matthias.graeser@imte.fraunhofer.de
[3] University Medical Center Hamburg-Eppendorf, Section for Biomedical Imaging, Hamburg, Germany
fynn.foerger@tuhh.de, tobias.knopp@tuhh.de
[4] Hamburg University of Technology, Institute for Biomedical Imaging, Hamburg, Germany
fynn.foerger@tuhh.de, tobias.knopp@tuhh.de

Magnetic Particle Imaging (MPI), a novel biomedical imaging technique, maps the spatial distribution of superparamagnetic tracers. One challenge in upsizing the imaging systems from small animal to human-size is the power consumption. An energy-efficient topology for selection and focus field generators was presented using coupled multi-coil arrays. A trivial, cost-intensive solution to drive these arrays is the usage of separate 4-quadrant amplifiers for each coil. In this paper a cost-efficient and scalable alternative is presented. A current controlled design achieves currents of up to 30 A with frequencies up to 10 Hz and suppresses the inductive coupling within the arrays.

DOI
https://doi.org/10.18690/um.feri.4.2025.44

ISBN
978-961-286-986-1

Keywords:
bioelectromagnetics,
medical imaging,
magnetic particle imaging,
multi-channel current control,
coupled coil arrays

University of Maribor Press

I Introduction

MPI is a novel real time capable biomedical imaging technique that was invented at the Philips Research Laboratories in Hamburg, Germany [1]. MPI systems utilize the combination of different magnetic fields to image the spatial distribution of the SuperParamagnetic Iron Oxide Nanoparticles (SPIONs): a quasi-static magnetic gradient field with a Field Free Region (FFR), and alternating drive fields for signal generation by SPIONs. The gradient field creating the FFR is shaped by the Selection and Focus field generator (SeFo). Only in the vicinity of this FFR the SPIONs can be excited following their nonlinear magnetization curve by the drive field. Those SPIONs induce a signal in a receive coil, which can be used to reconstruct the spatial distribution. SPIONs located away from the FFR are in saturation and thus not excited by the drive field [1].

A challenge in upscaling MPI scanners to human-size is the increase in power consumption. A new SeFo topology was introduced by Foerger et al.. Simulations have shown its energy efficiency [2]. The downside of this topology is the need to control the current in each of the 18 coils individually to move the FFR on a specific trajectory within the region of interest. 4-quadrant amplifier for each coil is a trivial but cost-intensive solution.

In this paper a modular, cost-effective alternative electrical circuit design is presented to drive a coupled multi-coil setup and suppress unwanted coil coupling [3].

II Requirements of the control system

The developed SeFo consists of two coil arrays with 9 coils each, see Figure 1. Preceding simulations have shown that the SeFo coils need to be driven with sinusoidal currents of up to 30 A peak to achieve the desired gradient field strength with a frequency of up to 10 Hz. They steer the FFR in the region of interest, making the system real time imaging capable. With the flexibility of the SeFo it should also be able to apply forces and torques onto magnetic devices and nanoparticles [4,5]. Furthermore, as the coils of each array reside on the same soft-iron core the inductive coupling of the coils has to be suppressed.


Figure 1: Developed SeFo by Foerger et al. [3], coil array (left), top view of aligned setup with both arays (right)

III Technical realization

To distribute the current to the individual coils, commercially available motor drivers Dimension Engineering LLC Sabertooth Dual 60A were chosen.

These motor drivers do not have a current controlled mode, but act as a H-bridge Voltage Source Inverters (VSI), an analogue PID-controller board was developed to control the currents.

The main component of these boards is a LEM LAH-50P current transducer, which measures the current in each coil. The measured current is scaled and subtracted from the set point provided by a Red Pitaya STEMlab 125-14 stack [6]. A tuneable, discrete analogue PID-controller supplies the control variable to the motor driver and the control loop is closed.

As the coils consist of massive soft iron cores, eddy currents occur at the switching frequency of the VSI at 24 kHz. Measurements with an LCR meter were conducted at 20Hz and 25kHz showing a significant reduction of the average inductance of all 18 coils from 865 µH to 41.7 µH (-95,18%). To reduce the occurring ripple currents due to the switching frequency of the VSI, a LC-low-pass filter (Tamura NAC-20, Nichicon PHC1255100KJ) with an attenuation of ~20dB at 24Khz was introduced into the circuit.

The H-bridges are configured in the lock anti-phase mode, therefore excess energy of the coils is fed back into its power supply. A regenerative approach is introduced to further improve the energy-efficiency of the setup. A capacitor bank was designed to take up the excess energy of the coils which can be resupplied. The size of the capacitors was chosen to be able to supply the maximum possible ripple current from the VSI, as well as to be able to take up the maximum energy of the coils and keep the input voltage to the rated voltage of the motor drivers. The total capacity of the capacity bank is 92.8mF (24x2200 μF type Vishay MAL213660222E3 and 4x10000 μF type Kemet ALC70A103EH100).

An input diode (IXYS DSS2X121-0045B) prevents the return of energy to the DC sources. The total system current is supplied by two Delta Electronica SM52-AR-60 DC sources. They supply up to 120 A to the SeFo driving circuit system. A functional diagram of the setup can be seen in Figure 2.

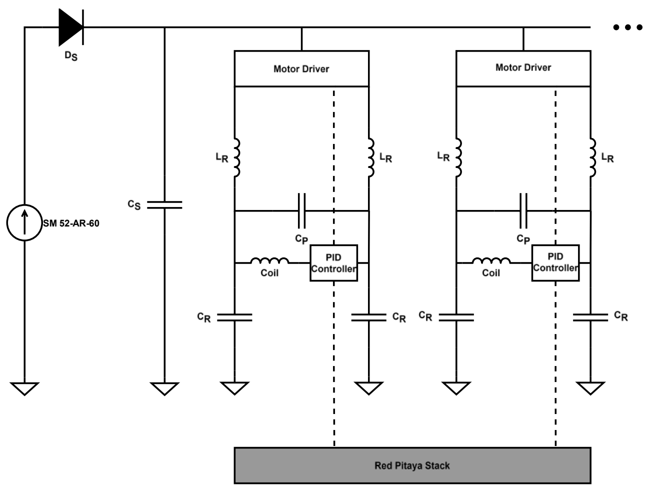

Figure 2: Functional diagram of the current control system: DC sources SM 52-AR-60 protected by the diode DS, the capacitor bank CS, VSI with the LC low pass (Lr,Cp,Cr), the coils of the SeFo, PID controller and the Red Pitaya Stemlab 125-14 stack., signal lines dashed, power lines solid

IV Test setup and results

The used hardware components can be seen in Figure 3. In a first testcase a sinusoidal current with a frequency of 10 Hz and an amplitude of 30 A was supplied as a set point, as specified in the requirements. Rectangular currents were also tested. To test the compensation of inductive coupling two coils were placed seamlessly facing each other. The first coil was excited with a current edge, while the second coil was set to 0A DC. A comparison with an uncontrolled coil was made. The results can be seen in figure 3.

The setup can drive 10 Hz sinusoidal currents with an amplitude of up to 30 A. Inductive coupling of coils on a single coil array is compensated by the PID-controller.

V Conclusion and outlook

A cost-efficient solution for driving multichannel coil arrays was proposed in this paper. The modularity of this approach allows for expansion or adaption of components. Single quadrant DC sources can be used in this configuration and the stored energy of the magnetic fields can be used regeneratively. The SeFo topology has already shown to be able to generate FFRs [7]. The total system energy efficiency is still to be measured while generating these fields.

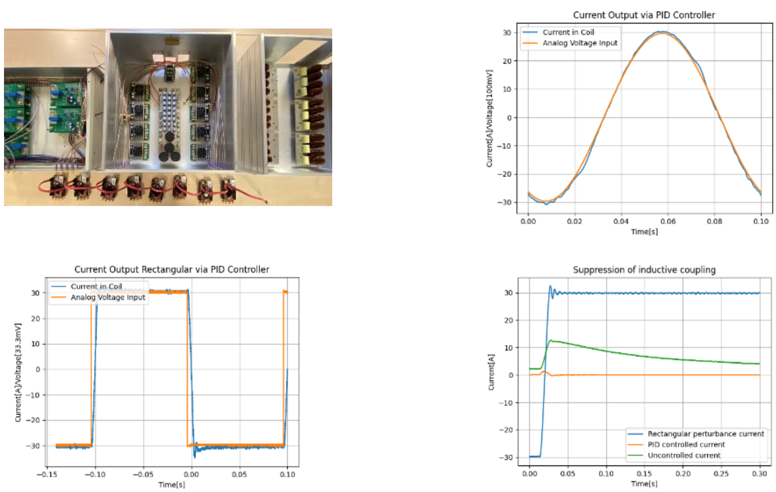

Figure 3: Top left to bottom right:
Full current control setup, left to right: PID controllers, motor drivers, capacitor bank and power diode, output filters, Red Pitaya Stack at bottom.
10Hz 30A sinusoidal current, set point orange, measured current in coil blue
5Hz 30A rectangular current, set point orange, measured current in coil blue
Suppression of inductive coupling, two coil positioned seamlessly face to face, one coil excited by a current edge blue , current in other coil is to be kept at 0A, the PID controlled current orange,the uncontrolled current green.

A for human head sized scaled up version SeFo with a similar coil array topology is being developed. The current control system based on the presented setup is updated to supply currents of up to 60A to the new SeFo. The modular design allows for easy adaptation to the new requirements. An upscaled capacitance bank is needed as larger inductances must be driven at higher currents. Due to the increased current, an input diode with a higher current rating will be needed. The output filters will be excluded in a first revision as the new coils are manufactured out of laminated electrical steel. The possibility for an external digital controller will be provided.

Acknowledgements

Research funding

This work was supported by the Fraunhofer Internal Programs under Grant No. Attract 139-600251.

Fraunhofer IMTE is supported by the EU (EFRE) and the State Schleswig-Holstein, Germany (Project: Diagnostic and therapy methods for Individualized Medical Technology (IMTE) – Grant: 124 20 002 / LPW-E1.1.1/1536).

The authors thankfully acknowledge the financial support by the German Research Foundation (DFG, grant number KN 1108/7-1 and GR 5287/2-1) and the Federal Ministry of Education and Research (BMBF, grant number 05M16GKA).

References

[1] B. Gleich and J. Weizenecker, "Tomographic imaging using the nonlinear response of magnetic particles," Nature, vol. 435, no. 7046, pp. 1214–1217, Jun. 2005, doi: 10.1038/nature03808.

[2] F. Förger, M. Graeser, and T. Knopp, "Iron core coil designs for MPI," International Journal on Magnetic Particle Imaging, p. Vol 6 No 2 Suppl. 1 (2020), Sep. 2020, doi: 10.18416/IJMPI.2020.2009042.

[3] F. Foerger, J.-P. Scheel, F. Thieben, F. Mohn, T. Knopp, and M. Graeser, "Multi-Channel Current Control System for Coupled Multi-Coil Arrays," International Journal on Magnetic Particle Imaging, p. Vol 8 No 1 Suppl 1 (2022), Mar. 2022, doi: 10.18416/IJMPI.2022.2203076.

[4] A. C. Bakenecker et al., "A microrobot for endovascular aneurysm treatment steered and visualized with MPI," International Journal on Magnetic Particle Imaging, p. Vol 8 No 1 Suppl 1 (2022), Mar. 2022, doi: 10.18416/IJMPI.2022.2203002.

[5] F. Griese, P. Ludewig, C. Gruettner, F. Thieben, K. Müller, and T. Knopp, "Quasi-simultaneous magnetic particle imaging and navigation of nanomag/synomag-D particles in bifurcation flow experiments," International Journal on Magnetic Particle Imaging, p. Vol 6 No 2 Suppl. 1 (2020), Sep. 2020, doi: 10.18416/IJMPI.2020.2009025.

[6] N. Hackelberg, J. Schumacher, M. Graeser, and T. Knopp, "A Flexible High-Performance Signal Generation and Digitization Plattform based on Low-Cost Hardware," International Journal on Magnetic Particle Imaging, p. Vol 8 No 1 Suppl 1 (2022), Mar. 2022, doi: 10.18416/IJMPI.2022.2203063.

[7] F. Foerger et al., "Flexible Selection Field Generation using Iron Core Coil Arrays," International Journal on Magnetic Particle Imaging IJMPI, p. Vol 9 No 1 Suppl 1 (2023), Mar. 2023, doi: 10.18416/IJMPI.2023.2303023.

DOI
https://doi.org/
10.18690/um.feri.4.2025.45

ISBN
978-961-286-986-1

LONG-TERM MULTIMODAL LOADING OF FIBER-BASED MAGNETIC SCAFFOLDS FOR HYPERTHERMIA APPLICATIONS

KARL SCHNEIDER, IOANA SLABU

RWTH Aachen University, Institute of Applied Medical Engineering, Aachen, Germany
schneider@ame.rwth-aachen.de, slabu@ame.rwth-aachen.de

We designed and tested an experimental setup intended for medical device quality assurance, capable of multimodal loading of fiber-based magnetic scaffolds. These magnetic scaffolds are promising for hyperthermia treatment of hollow organ cancers. To approximate the physiological conditions during magnetic hyperthermia treatment, a multimodal load consisting of a thermal load, a hydrodynamic load, and a mechanical load was considered. The effect of the multimodal load on polypropylene fibers with embedded magnetic nanoparticles was analyzed to assess changes in the mechanical properties of the fibers. We demonstrate that the nanomodified PP fibers relax according to the Poynting-Thomson model.

Keywords:
magnetic scaffolds,
multi-modal loading,
magnetic hyperthermia,
tensile test,
flow chamber

University of Maribor Press

I Introduction

Fiber-based magnetic scaffolds, polymer matrices with embedded magnetic nanoparticles (MNP), enable a myriad of clinical applications, such as magnetic hyperthermia tumor therapy. MNP generate the therapeutically necessary heat when exposed to alternating magnetic fields through non-linear magnetic relaxation processes. For hollow organ tumor treatment, nanomodified stents are implanted to reopen the occluded organ and to prevent restenosis through hyperthermal induction of cell death by application of an alternating magnetic field. The magnetic scaffold is subject to a thermal load as well as to the physiological loads during the magnetic hyperthermia treatment. To ensure patient safety and the functionality of the magnetic scaffold, i.e., the nanomodified stent, knowledge of the impact of the multimodal load on the nanomodified stent is necessary.

In this study, we investigate the impact of a long-term multimodal load on the mechanical properties of nanomodified polypropylene (PP) fibers.

II Materials and methods

The experimental setup consists of a thermal load, a hydrodynamic load, and a mechanical load. The thermal load is generated by the interaction between the MNP and the alternating magnetic field as well as through the fluid temperature. The physiological conditions in a hollow organ are approximated by the mechanical and hydrodynamic loads by placing the magnetic scaffolds under a cyclic uniaxial tensile load and exposing them to fluid flow. The main parameters of the multimodal load are given in Table 1.

Furthermore, simulations of the heating process within the magnetic scaffold were performed using COMSOL Multiphysics®. The magnetic scaffold was modeled as described in [1] with an additional fluid domain surrounding the magnetic scaffold to incorporate the cooling effect due to the hydrodynamic load. The specific loss power (SLP), i.e., the volumetric heat source of the MNP, was set to 20 W/g based on preliminary experiments.

The temperature distribution resulting from the simulations are analyzed according to the maximum, minimum and average increase in surface temperature of the nanomodified PP fiber, as well as the maximum increase in MNP temperature.

Table 1: Main parameters of the experimental setup

Parameter	Value	Unit
Magnetic field strength	5.5	kA/m
Magnetic field frequency	80	kHz
Fluid flow rate	5	ml/min
Fluid avg. pressure	1300	Pa
Fluid temperature	37	°C
Tensile load frequency	0.24	Hz
Tensile load max. strain	1	%
Tensile load min. strain	0.1	%

The mechanical properties of the nanomodified PP fibers are investigated through tensile tests using a ZwickiLine Z2.5 universal tensile testing machine and an adhesion based clamping system after EN ISO 5079:2020 [2].

III Results and discussion

The maximum surface temperature of an individual fiber strand, as shown in Figure 1, increased by 0.067 °C, with the average surface temperature increasing by 0.051°C. The maximum temperature increase of the MNP was 0.247 °C. The small temperature increase, compared to [3, 4], is due to (A) the cooling effect of the fluid flow, and more importantly, due to (B) the comparatively weak magnetic field strength at a low frequency produced by the used solenoid. Geometric constraints in the experimental setup prohibited the use of a different, stronger solenoid. As the temperature difference between the achieved fiber temperature (~37 °C) and the glass transition temperature (~-25 °C) or the melting temperature (~170 °C) of polypropylene is sufficiently large, no further nano heating effects are expected even for a therapeutically effective increase in fiber temperature [5].

In Figure 2, the stress-strain hysteresis curves from the long-term multimodal loading of the nanomodified PP fibers are shown. The maximum stress per cycle decreases from 14.77 N/mm² to 6.00 N/mm² over the course of the long-term multimodal loading. The decrease in the maximum stress is further shown in Figure 3.

The Poynting-Thomson model (equation 1), also known as the standard linear solid model, was fitted to the data showing the decrease in maximum stress per cycle [6]. The resulting parameters are given in Table 2.

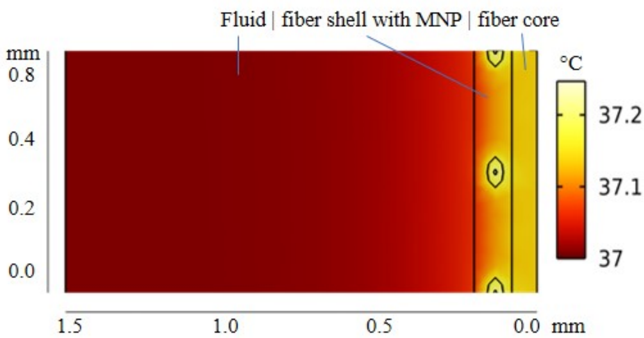

Figure 1: Simulation of the temperature distribution after application of the thermal and hydrodynamic load. The fluid domain with fluid flow is on the left, the shell of the PP fiber with the embedded MNP in the middle, and the core of the PP fiber is on the right.

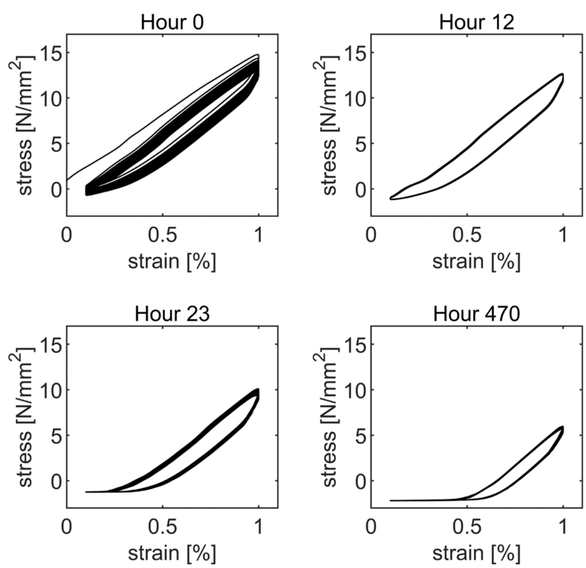

Figure 2: Stress-strain curves of the nanomodified PP fibers during multimodal loading.

$$\sigma(t) = \sigma_\infty + \bar{\sigma} \cdot e^{-\frac{t}{\tau}} \tag{1}$$

After 73.3 hours of multimodal loading 95% of the final maximum stress is achieved.

Table 2: Parameters of the poynting-thomson model

Parameter	Value	Unit
σ_∞	5.97	N/mm^2
$\overline{\sigma}$	5.82	N/mm^2
τ	93927.77	s

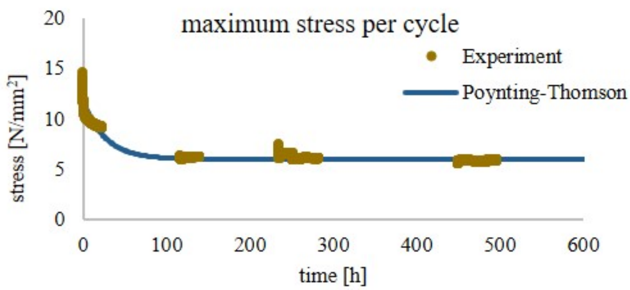

Figure 3: Decrease in maximum stress per cycle over time.

IV Conclusions

We demonstrated that nanomodified PP fibers behave according to the Poynting-Thomson model of relaxation. Figure 3 demonstrates that the maximum stress due to a 1% tensile load decreases over time and reaches saturation. Thus, preloading of the nanomodified PP fibers before implantation can prevent significant changes in the mechanical properties of the nanomodified PP fibers.

Considering the therapeutic application of magnetic hyperthermia, higher thermal loads are expected. The generation of these conditions was limited by the geometric constraints of the experimental setup. This can be solved by the utilization of a solenoid capable of producing a more powerful AMF.

Acknowledgments

We gratefully acknowledge financial support by the German Research Foundation (grant no. 467959793), and by the Federal Ministry of Education and Research (grant no. 03VP10971). We gratefully acknowledge the financial support by the by the European Union (ERC, MAD Control, 101076174). Views and opinions expressed are however those of the author(s) only and do not necessarily reflect those of the European Union or the European Research Council Executive Agency. Neither the European Union nor the granting authority can be held responsible for them.

References

[1] K. Schneider, I. Slabu, "Heating of fiber-based magnetic scaffolds for hyperthermia applications: Maintaining simulation accuracy with reduced model complexity," in *XXVII Symposium Electromagnetic Phenomena in Nonlinear Circuits*, Hamburg, pp. 40–41, 2022.

[2] DIN Deutsches Institut für Normung e. V., DIN EN ISO 5079:2021-02, Textilfasern Bestimmung der Höchstzugkraft und Höchstzugkraftdehnung an einzelnen Fasern (ISO 5079:2020); Deutsche Fassung EN ISO 5079:2020, Berlin, 2021.

[3] B. Mues et al., "Assessing hyperthermia performance of hybrid textile filaments: The impact of different heating agents," *Journal of Magnetism and Magnetic Materials*, vol. 519, 2021.

[4] B. Mues et al., "Nanomagnetic Actuation of Hybrid Stents for Hyperthermia Treatment of Hollow Organ Tumors," *Nanomaterials* Basel, vol. 11, no. 3, 2021.

[5] J. P. Greene, *Automotive plastics and composites: Materials and processing*. Oxford, William Andrew, 2021.

[6] H. T. Banks, S. Hu, Z. R. Kenz, "A Brief Review of Elasticity and Viscoelasticity for Solids," *Adv. Appl. Math. Mech.*, vol. 3, No. 1, pp. 1-51, 2011.

A Comparison of Different Modulation Techniques for Muli-Coil Inductive Power Transfer

Jure Domajnko, Miro Milanovič, Nataša Prosen
University of Maribor, The Faculty of Electrical Engineering and Computer Science, Institute of Robotics, Laboratory for Power Electronics, Maribor, Slovenia
jure.domajnko2@um.si, miro.milanovic@um.si, natasa.prosen@um.si

DOI
https://doi.org/10.18690/um.feri.4.2025.46

ISBN
978-961-286-986-1

The Inductive Power Transfer (IPT) is the most popular method of transferring power wirelessly. In order to increase the transferred power, the multi-coil structure can be used. This can also impacts the tolerance to misalignment and rotation between coils. In order to control output voltage, multiple different transmitter modulation techniques can be used. To choose the most suitable modulation method, the most popular modulation methods were implemented on the multi-coil system and experimentally tested under the same working conditions.

Keywords:
inductive power transfer,
inverter modulation,
modulation comparison,
voltage control,
efficiency comparison

University of Maribor Press

I Introduction

Wireless or more specifically inductive power transfer (IPT) gained more adoption with the development of consumer electronics and electric vehicles, due to its simplicity and robustness [1]. Currently, it is mostly used for providing power to and charging low-power devices such as smartphones, smartwatches, and wireless earphones. The main drawback of transferring power wirelessly is the overall low charging efficiency and low tolerance to misalignment.

By using different single and multi-coil structures, the misalignment tolerance of the system can be significantly improved. On the other hand, the efficiency of the transfer can be increased by transferring power at higher frequencies, using different modulation and control techniques. The modulation technique also depends on the type of high-frequency inverter on the transmitter side of the system.

The IPT system, used in experiments is based on multi-coil double DD coil topology, with better, symmetrical misalignment tolerance and higher power transfer capabilities [2]. The output is connected to a constant resistive load. The experiments with different modulation techniques were performed in order to determine the most suitable modulation technique.

II Modulation methods

The multi-coil system, which is the subject of this research consists of two directional DD coils, perpendicular to one another, forming a double DD coil structure. The double DD coil structure is used as a transmitter and as a receiver. The coil structure is presented in Fig. 1.

The transmitter and the receiver coils are compensated using widely used series-series (SS) compensation topology, which serves a constant current supply at the output of the system. Each of the transmitter coils is driven using a full-bridge inverter, capable of implementing all three most popular modulation techniques.

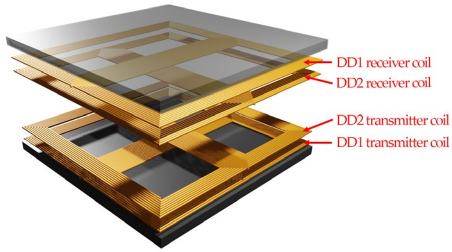

Figure 1: Basic double DD transmitter and receiver coil structure

The output voltage of the IPT system can be controlled using the amplitude of the first harmonic component of the transmitter voltage, using phase-shifted, frequency, or pulse density modulation.

A phase-shifted modulation impacts the amplitude of the first harmonic component by changing the phase angle between the modulation signal for the first and second inverter bridge legs. This can be described using:

$$u_T = \frac{4U_{DC}}{\pi}\sin\left(\frac{\phi}{2}\right)\sin(\omega t) \tag{1}$$

where u_T is the first harmonic component of the transmitter voltage, U_{DC} is the voltage of the transmitter power supply, ϕ is the phase angle of the modulation, and ω inverter frequency.

When using frequency modulation, the phase-shift angle of the inverter is 2π. Therefore, equation (1) can be simplified to:

$$u_T = \frac{4U_{DC}}{\pi}\sin(\omega t) \tag{2}$$

The first harmonic component of generated voltage is constant. SS compensated IPT system acts as a band-pass filter with resonant frequency at:

$$f_i = \frac{1}{2\pi\sqrt{L_{Ti}C_{Ti}}} = \frac{1}{2\pi\sqrt{L_{Ri}C_{Ri}}} \tag{3}$$

where f_i is the resonant frequency of the system, L_{Ti} and L_{Ri} are the inductances of the transmitter and the receiver coils and C_{Ti} and C_{Ri} are the values of compensation capacitors. The parameter i can be either 1 or 2, depending on the selected pair of coils in the double DD structure. By modulating the frequency of the transmitter, the amplitude of the induced voltage on the receiver side can be changed. However, this can impact the efficiency of the IPT system.

The first harmonic component of the transmitter voltage is also constant during the pulse density modulation (PDM) [3]. By reducing the density with the introduction of the pulse skipping, the average value of the first harmonic component can be reduced. The relationship between the transmitter voltage and PDM can be described using [4]:

$$u_T = \frac{4U_{DC}}{\pi} d \sin(\omega t) \tag{4}$$

where d is the pulse density of modulation, which can be between 0 and 1.

Phase-shifted modulation can only be implemented on the system using the full-bridge inverter. Other two techniques can also be implemented on the half-bridge inverter.

III Experimental Results

A. Experimental platform

The three most popular modulation methods were tested on the small-scale multi-coil experimental platform. The output voltage was controlled using a tuned PI output voltage controller. The main parts of the IPT system are highlighted in Fig. 2. The IPT coils are mounted on the 3D positioning mechanism, which enables the positioning of the double DD coils in the 3D space. The transmitter coil, placed on the bottom platform can be moved in the *x-y* plane and the receiver coil, placed on the top platform can be moved along the *z* axis.

The transmitter part of the system consists of a dual high-frequency inverter and two transmitter DD coils with their respective series compensation circuits. The receiver side consists of two series compensated DD coils, connected to the diode rectifiers. The communication between the transmitter and the receiver side is implemented using Bluetooth communication protocol.

The system was connected to a 25 V power supply, supplying up to 3 A of DC. The power of the system is limited by the voltage ratings of compensating capacitors and the DC voltage of the inverter. The distance between coils was between 0 and 25 mm, with angle varying between 0 and 90°. The rectifiers were connected to the constant 21.4 Ω load.

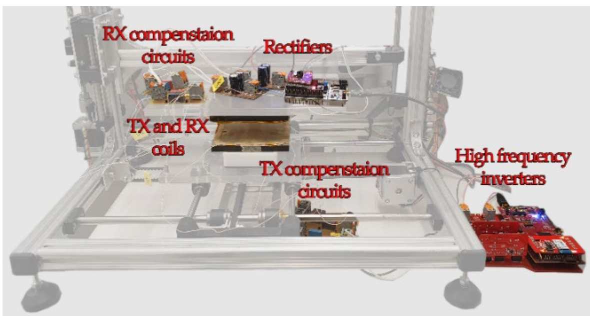

Figure 2: Multi-coil experimental platform.

B. Experimental results

The 3D positioning platform enabled the evaluation of modulation techniques under the same conditions. First, the system was tested under different output voltages, which affected the efficiency of the system. The output voltage reference was changed from 5 V to 30 V in 5 V steps. The results are presented in Table I. Among the three modulation techniques, the most efficient was phase-shifted modulation and frequency modulation was least efficient. The PDM was more efficient than frequency modulation and less efficient than phase-shifted modulation.

In all three cases, the PI controller eliminated the error due to the change of coupling coefficients between the transmitter and the receiver DD coil structures. The rotation of the coils around the *z*-axis had a greater effect on the output voltage than misalignment in the horizontal *x-y* plane. The maximum overshoot was under 10% of output voltage during the rotation and under 3% during the horizontal movement.

Table 1: Efficiency of the inductive power transfer system

Reference voltage $U_{o,ref}$	Frequency modulation	Phase-shifted modulation	Pulse density modulation (PDM)
5 V	32.92%	42.82%	35.94%
10 V	52.37%	55.03%	59.47%
15 V	56.88%	63.39%	58.12%
20 V	63.17%	68.11%	63.28%
25 V	66.22%	72.27%	69.35%
30 V	69.54%	72.36%	70.4%

IV Conclusion

The results clearly present that the phase-shifted modulation is the most efficient modulation technique, due to the use of constant frequency and ideal transistor soft-switching. Frequency and pulse density modulation should only be used in systems using half-bridge high-frequency inverters that reduce system complexity, where phase-shifted modulation is impossible to implement.

Acknowledgement

The authors acknowledge the financial support from the Slovenian Research Agency (Grant No. P2-0028).

References

[1] Z. Zhang, H. Pang, A. Georgiadis, C. Cecati, "Wireless power transfer—An overview", *IEEE Transactions on Industrial Electronics*, 66(2), 1044-1058, 2018.

[2] N. Prosen, J. Domajnko, M. Milanovič, "Wireless Power Transfer Using Double DD Coils", *Electronics*, 10(20), 2528, 2021.

[3] H. Li, J. Fang, S. Chen, K. Wang, Y. Tang, "Pulse density modulation for maximum efficiency point tracking of wireless power transfer systems", *IEEE Transactions on Power Electronics*, 33(6), 5492-5501, 2017.

[4] H. Li, K. Wang, J. Fang, Y. Tang, "Pulse density modulated ZVS full-bridge converters for wireless power transfer systems", *IEEE Transactions on Power Electronics*, 34(1), 369-377, 2018.

POLYMER COMPOSITES FOR ELECTROMAGNETIC AND ELECTROSTATIC SHIELDING

DOI
https://doi.org/10.18690/um.feri.4.2025.47

ISBN
978-961-286-986-1

ŁUKASZ PIETRZAK, ERNEST STANO, ŁUKASZ SZYMAŃSKI
Lodz University of Technology, Institute of Mechatronics and Information Systems, Łódź, Poland
lukasz.pietrzak@p.lodz.pl, ernest.stano@p.lodz.pl, lukasz.szymanski@p.lodz.pl

The article describes electromagnetic shielding capabilities of carbon nanotube polymer and multiwalled carbon nanotube nanocomposites obtained by spray – drying technique. The used method guarantees uniformly dispersed carbon nanotubes (CNTs), what resulting in forming the continuous network of CNTs inside the polymer matrix. The technique also allows working with solution that is the basis of homogeneous composite material preparation, as the agglomeration of the filler destroys the material desired electromagnetic shielding properties. In manufactured nanocomposites network of conductive filler is playing the role of the electromagnetic radiation shield and thus it is so important to develop the highly effective preparation method leads to uniform dispersion of the filler. Another important feature of the examined nanocomposites is electrostatic shielding capability based also on good uniform carbon nanotubes dispersion what makes the outcome material suitable for protecting fragile electronic devices. The filler particles used in the described process are multiwalled carbon nanotubes coming from LSCVD synthesis in our own laboratory. In this article we are introducing both the method and results for the first of filler and polymer as the basis for the future work we want to finally present.

Keywords:
electromagnetic shielding,
electrically conductive composites,
carbon nanotubes,
polymer composites,
electronic devices

University of Maribor Press

I Introduction

Electronic devices are widely used today in every field of human activity like industry, health care, or transportation. Thus it is highly probable that fragile by its nature electronics can often work in difficult conditions, also in the presence of variable magnetic fields caused for example by currents flowing in the electrical installation. That is the reason of the need of developing materials that used for housing of the electronic devices could eliminate the electromagnetic and possibly also electrostatic interference. Another important feature is the need of easy shaping and low energy cost of fabricating both the materials and housings. Also eliminating or minimizing amount of toxic waste polluting the environment is very important. Most of polymers used in industrial applications are petroleum based and thus are hardly degradable in natural environment (it can take hundreds of years) so it causes pollution or significantly rising the cost of the product concerning utilization of millions tons of wastes. The material that can meet requirements of electromagnetic shielding and static electricity protection is a polymer composite with carbon nanotubes as a filler and a biodegradable polymer matrix. The choice of carbon nanotubes (CNTs) as the filler is dictated by their great electrical and mechanical properties as well as high thermal and chemical stability [1][2]. These properties makes CNTs one of the best fillers in polymer composites [3][4]. In this publication, polylactide (PLA) has been used as the polymer matrix. It is a biocompatible polymer obtained from renewable sources[5], [6]. In addition, parts made of this polymer are fully biodegradable, and thus do not pollute the natural environment, unlike petroleum-derived polymers commonly used in electrical engineering. A major disadvantage of CNTs as a filling material is the difficulty in obtaining homogeneous dispersions in polymer matrices. Good, uniform dispersion of CNTs in the polymer matrix is a key parameter for the composite performance. In this paper we present method of preparation of nanocomposites with good dispersion of CNTs. It consist in “freezing” of a good dispersion of CNTs in the polymer solution obtained using ultrasound bath. The described method also allows other filler particles and polymer usage as long as the solution can be made.

II Methods And Results

The multiwalled carbon nanotubes, used as a filer in described composites, was synthesized using liquid source chemical vapor deposition (LSCVD) synthesis technique in own laboratory[7]. Carbon nanotubes grow in form of a carpet, perpendicularly to carpets base. Obtained material is characterized by high purity and uniform dimensions. The mentioned properties are synthesis process parameters (temperature, carrying gas and catalyst solution vapours flow) dependable. The method allows easy change of synthesis parameters in order to obtain material of desirable parameters.

Polylactide was provided by Cargill-Dow. It contains 95.9% of L-lactide and 4.1% D-lactide. Reagent grade trichloromethane (CHCl3) was used as solvent for polylactide, as the spray drying technique was used for creating the composite layers. Prior polylactide dissolving, CNT were dispersed in trichloromethane (CHCl3) using ultrasonic bath (90 min) in order to disintegrate nanotube bundles coming from the synthesis. Composite fabrication technique was described in details in authors' publication[8]. To examine of homogeneity of dispersion of the filler particles in fabricated composites scanning electron microscope Jeol JSM 5500 apparatus was used, what shows the below micrograph. Fig. 1 presents the composite obtained by spray – drying technique applied directly on Si wafer surface. What is visible on the SEM micrograph, there is no CNT agglomerates or bundles. What is also important, no charging effects can be seen, what confirms electric conductivity of the composites as the charge is effectively removed from the surface.

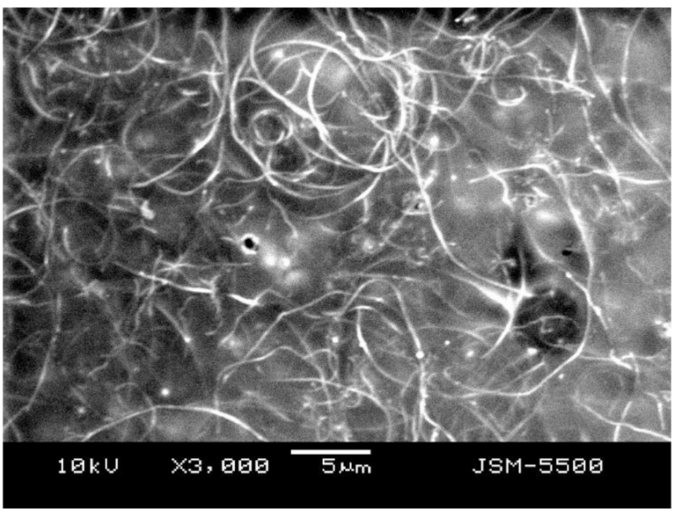

Figure 1: SEM micrograph of composite foil on Si wafer surface, applied after dispersion in CHCl3 (90 min, CNTs weight content is 2%)

All described in the article efforts' goal was creating the material comprising both electrostatic and electromagnetic shielding capabilities. Another important aspect of our research was developing method of fabrication that allows application of the protective composite layer on virtually any surface and is simple and cheap enough to be industry – friendly. The results of electric conductivity measurements in function of the CNTs content are presented on Fig. 2.

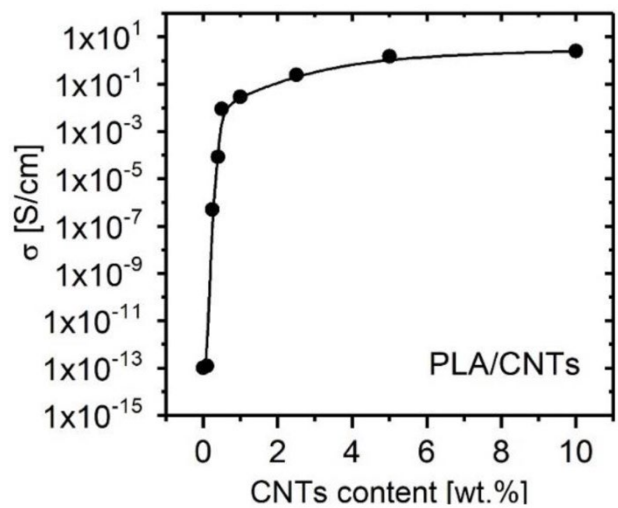

Figure 2: Electric conductivity CNTs content dependence plot; the CNTs content range is 0 to 10% by weight [8]

It is worth of mentioning, that percolation threshold is lower than 0,2% weight percent content and for effective electric charges conducting 0,25% is sufficient[7]. The next material examination analysis step was checking the electromagnetic shielding capabilities. As the experiments are still in progress, an exemplary result for a composite with a weight content of 2% is presented (Fig. 3).

One can observe damping in range from 50 to around 430 MHz and for this specimen magnitude lies in range of 10dB. What is important, dumping was achieved for layer thinner than 0.2 mm.

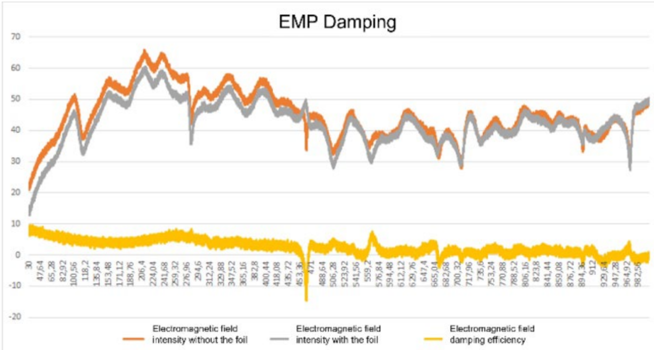

Figure 3. Shielding properties plot of 2% by weight composite foil in comparison to neat polymer

The parameters of presented polymer composites indicates that this material can be used in both electronics and electrotechnics field. Material comprises low manufacturing cost and multiple application possibilities. What is worth of mentioning, the material is also environmental friendly due to polylactide properties, as it is biodegradable. Using spray – drying applying technique making entire process industry friendly and gives possibility of use other polymers and fillers according to the needs. The authors are planning to improve material electromagnetic shielding capabilities and use different fillers and polymers to increase the range of application.

References

[1] E. Thostenson, Z. Ren, and T.-W. Chou, "Advances in the Science and Technology of Carbon Nanotubes and Their Composites: A Review," *Compos Sci Technol*, vol. 61, pp. 1899–1912, Oct. 2001, doi: 10.1016/S0266-3538(01)00094-X.

[2] L. Gao, E. T. Thostenson, Z. Zhang, and ..., "Sensing of damage mechanisms in fiber-reinforced composites under cyclic loading using carbon nanotubes," *Advanced functional* …, 2009.

[3] G. Lota, K. Fic, and E. Frackowiak, "Carbon nanotubes and their composites in electrochemical applications," *Energy Environ Sci*, 2011.

[4] M. Castellino, M. Rovere, M. I. Shahzad, and A. Tagliaferro, "Conductivity in carbon nanotube polymer composites: A comparison between model and experiment," *Compos Part A Appl Sci Manuf*, vol. 87, pp. 237–242, 2016, doi:

[5] M. A. Abdel-Rahman, Y. Tashiro, and K. Sonomoto, "Lactic acid production from lignocellulose-derived sugars using lactic acid bacteria: Overview and limits," *J Biotechnol*, vol. 156, no. 4, pp. 286–301, 2011, doi: https://doi.org/10.1016/j.jbiotec.2011.06.017.

[6] K. Hamad, M. Kaseem, Y. G. Ko, and F. Deri, "Biodegradable polymer blends and composites: An overview," *Polymer Science Series A*, vol. 56, no. 6, pp. 812–829, 2014

[7] G. Raniszewski and Ł. Pietrzak, "Optimization of Mass Flow in the Synthesis of Ferromagnetic Carbon Nanotubes in Chemical Vapor Deposition System," *Materials*, vol. 14, no. 3, p. 612, Jan. 2021, doi: 10.3390/ma14030612.

[8] L. Pietrzak, G. Raniszewski, and L. Szymanski, "Multiwalled Carbon Nanotubes Polylactide Composites for Electrical Engineering—Fabrication and Electrical Properties," *Electronics (Basel)*, vol. 11, no. 19, 2022, doi: 10.3390/electronics11193180.

Comparison of Different Offline MTPA Trajectory Estimation Methods

DOI
https://doi.org/10.18690/um.feri.4.2025.48

ISBN
978-961-286-986-1

Jernej Černelič, Martin Petrun

University of Maribor, Institute of Electrical Power Engineering, Maribor, Slovenia
jernej.cernelic@um.si, martin.petrun@um.si

The main goal of this paper was to analyse and compare different offline Maximum-Torque Per Ampere (MTPA) trajectory estimation methods for Interior Permanent Magnet Synchronous Machines (IPMSMs). The analysis was performed based on Finite Element Analysis (FEA) data of IPMSMs. The obtained results show that despite neglecting all the non-linearities, the analytical MTPA trajectory calculation with constant IPMSM parameters can model the MTPA trajectory with adequately small difference when compared to optimization-based calculation. Consequently, the MTPA trajectory calculation was further simplified with a piece-wise linear approximation of the trajectory, resulting in simpler MTPA reference calculation within the controller and adequately small deviations from optimal MTPA operating points.

Keywords:
maximum torque per ampere (MTPA),
trajectory,
fitting,
interior permanent magnet synchronous machine (IPMSM),
finite element analysis

University of Maribor Press

I Introduction

Nowadays, energy efficiency is the main driving force of development of contemporary electric machines and drives. Not only because of ever increasing energy demand and energy cost, but also due to material usage and because it improves the product usability. High efficiency electric drives can for example extend operating time of battery powered devices. The energy efficiency of electric drives can be improved not only by optimizing the drive's design but also by control techniques which minimize the power losses [1].

There are many approaches to power loss minimization which differ by the loss considered. The most significant losses of electric drives are the Joule losses, which are proportional to square of the magnitude of current. Consequently, the most used technique is Maximum Torque Per Ampere (MTPA) control, which minimizes the current consumption for the given torque, thus reducing the Joule losses and providing practical, but suboptimal solution, since total power losses might not be minimized [1]. However, there are many different methods of implementing MTPA control, and different methods for estimation of MTPA trajectories [1], [2].

II MTPA Trajectory Estimation Methods

The MTPA trajectory estimation methods are mainly being used for pole salient synchronous motors and can be according to [1] divided into offline and online methods. All offline methods require motor parameters to be determined either by measurements or Finite-Element Analysis (FEA), while some online methods can track the MTPA trajectory without knowing any motor parameter [1]. This research is limited only to comparison of most used offline MTPA calculation methods in applied engineering.

The basis of MTPA trajectory estimation is the current-dependent Interior Permanent Magnet Synchronous Machine (IPMSM) model since the cross-coupling and rotor position dependency have very little effect on dynamic performance of such machines [3]. Consequently, the simplified, well-known, IPMSM model in d-q reference frame is defined by (1) and (2),

$$u_d = R_s i_d + L_d \frac{di_d}{dt} - L_q i_q \omega p \tag{1}$$

$$u_q = R_s i_q + L_q \frac{di_q}{dt} + (\Psi_m + L_d i_d)\omega p \tag{2}$$

where the R_s is stator resistance, L_d is direct axis inductance, L_q quadrature axis inductance, Ψ_m is flux linkage due to permanent magnets, and p the number of pole pairs and ω is mechanical angular speed, while u_d, u_q are direct and quadrature axis voltages, and i_d, i_q corresponding currents. Based on (1) and (2), the torque equation (3) can be derived.

$$T = \frac{3}{2} p\left(\Psi_m i_q + \left(L_d - L_q\right) i_d i_q\right). \tag{3}$$

The nonlinear behaviour of flux-current relationship can be considered by expressing the apparent inductances and the permanent magnet flux linkage as functions of both current components, i.e., $L_d(i_d,i_q)$, $L_q(i_d,i_q)$ and $\Psi_m(0,i_q)$. Based on (3), an infinite number of (i_d, i_q) current combinations can generate the desired torque. The nonlinear MTPA optimization problem stated by (4) returns the desired torque T^* at minimum current.

$$\min_{i_{dq}} \left\| i_{dq} \right\| \text{ s.t. } T\left(i_d, i_q\right) = T^* \tag{4}$$

The first analysed MTPA trajectory estimation method was based on an analytical approach. By assuming constant motor parameters (i.e., neglecting nonlinearities), the MTPA trajectory can be calculated based on (3) and obtaining (5) [4].

$$i_d = \frac{\Psi_m - \sqrt{\Psi_m^2 + 8\left(L_d - L_q\right)^2 I_s^2}}{4\left(L_q - L_d\right)} \tag{5}$$

Another very popular method exploits Look-Up tables (LUTs) because they can contain MTPA trajectories that include nonlinear effects. Such trajectories are in general calculated from measured or FEA data by applying offline methods [5]. The measured data is usually obtained by measuring the shaft torque and stator currents at steady-state conditions. The MTPA trajectory is then determined by searching for maximum torque at different current magnitudes, as defined by (4). Meanwhile, the

FEA data-based approach is often possible only for machine developers. The main drawback of such methods is the time-consuming process of obtaining the measurement or FEA data. The advantage of these methods is that they can consider the non-linear flux-current and torque-current relationships, thus providing more accurate MTPA trajectories. However, when FEA data is used, the difference between FEA and measured data may occur which will be further investigated.

The obtained MTPA trajectories can be, however, considered by fitting an adequate mathematical function [6]. Within this work the simplest approximation function is considered, namely the piece-wise linear approximation. Moreover, the linear approximation consists of only one function which was obtained from marked points of optimization based MTPA trajectory by using minimum root-mean square error criterion for fitting. However, the number of approximation functions can also be higher.

III Results

The described analytical- and optimization-based methods for MTPA trajectory estimation were analysed based on FEA data of a V-shape IPMSM. Despite the estimation methods are very different, the results show only a small deviation between the obtained trajectories (Figure 1). In the analytically based estimation, the inductance values from no-load operation were considered. The trajectory fit could be even improved if these values would be optimized [3]. Figure 1 presents the FEA calculated constant torque lines in dependence of current components (i_d,i_q) and the maximum stator current limit I_{sMAX}.

The most significant difference in calculated MTPA trajectories can be found in the current angle β, as presented in Figure 2. The highest difference in angle β between analytical and optimization based MTPA calculation is only up to -3 ° and can be found around the maximum stator current value. The difference in current angle β between the linear and optimization-based calculation is up to -13 ° at up to half of maximum stator current.

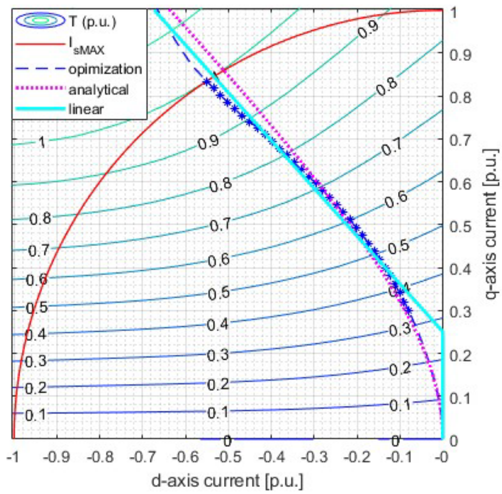

Fig.1. Constant torque lines with estimated MTPA curves

The difference in current angle β has very little effect on the generated torque. The highest difference in current needed to generate the desired torque can be found around nominal torque when comparing analytical calculation to optimization based MTPA trajectory calculation. Since the difference is less than 0,002 of maximum current, the impact on the Joule loss is negligible. Even in the case of piece-wise linear approximation of the MTPA trajectory, the difference in required current is less than 0,007 of the maximum current. Additionally, this difference occurs at low currents, where the Joule losses are also low. Because the drives are usually not operating at low torques, the proposed piece-wise linear approximation of the MTPA trajectory could be used. Consequently, the computation complexity and time within the implemented control system can be reduced which is enabling MTPA operation on simplest (and cheapest) microcontrollers.

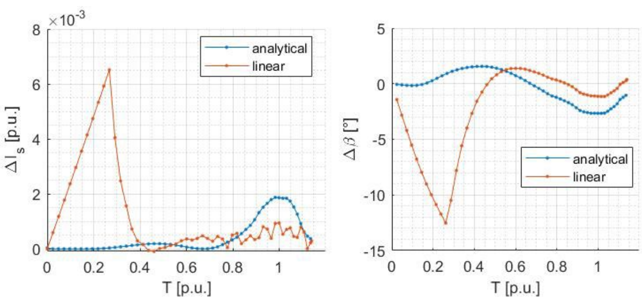

Fig.2. Comparison of analytical and optimization based MTPA trajectories

III Conclusion

This paper analysed the difference between optimization-based calculation, analytical calculation, and piece-wise linear approximation of the MTPA trajectory. The analysis was systematically performed based on FEA data. The results show a very small difference in current amplitudes and angles required to generate the desired torque despite the difference due to errors in estimated MTPA trajectories. Consequently, the simpler MTPA calculation methods could be used to simplify the control algorithms for most basic microcontrollers at a very small efficiency trade-off.

The described MTPA trajectory estimation methods will be further analysed in a future research work, where the MTPA trajectories will be estimated also based on measurements within a laboratory experimental setup.

References

[1] Dianov, F. Tinazzi, S. Calligaro, S. Bolognani, "Review and Classification of MTPA Control Algorithms for Synchronous Motors, IEEE Trans. Power Electronics, Vol. 37, No. 4, pp. 3990-4007, 2022,

[2] Yan M., Wen B., Cui Q., Peng X., "Parameter Identification for Maximum Torque per Ampere Control of Permanent Magnet Synchronous Machine under Magnetic Saturation", Control and Optimization of Power Converters and Drives, Electronics, Vol 13, No. 4, 2024

[3] Garmut M., Steentjes S., Petrun M., "Parameter identification for MTPA control based on a nonlinear d-q dynamic IPMSM model", Compel, Vol 42., No. 4, pp. 846-860, 2023,

[4] M. N. Uddin, T. S. Radwan, and M. A. Rahman, "Performance of interior permanent magnet motor drive over wide speed range," IEEE Trans. Energy Convers., vol. 17, no. 1, pp. 79–84, Mar. 2002,

[5] H. W. de Kock, A. J. Rix, M. J. Kamper, "Optimal torque control of synchronous machines based on finite-element analysis" IEEE Trans. On Industrial Electronics, Vol. 57, No. 1, 2010.

[6] Huang S., Chen Z., Huang K., Gao J., "Maximum Torque Per Ampere and Flux-weakening Control for PMSM Based on Curve Fitting", IEEE Vehicle Power and Propulsion Conference, pp. 1-5, 2010

Influence of Transformer Design in AC/DC/AC Converter Output Circuits on Plasma Reactor Characteristics

Grzegorz Komarzyniec, Oleksandr Boiko,
Henryka Danuta Stryczewska
Lublin University of Technology, Department of Electrical Engineering and Superconducting Technologies, Lublin, Poland
g.komarzyniec@pollub.pl, o.boiko@pollub.pl, h.stryczewska@pollub.pl

Three-phase arc discharge plasma reactors are challenging to maintain stable plasma parameters. Plasma performance is significantly influenced by the design of the power system and its output characteristics. This paper examines the interaction of a plasma reactor with an AC/DC/AC converter equipped with different transformer solutions to adapt the output parameters to the requirements of the plasma reactor. The design of transformers has a significant impact on the parameters of the generated plasma and the reactor's interaction with the power grid. The performance characteristics obtained for these solutions indicate that the design of the transformers has a strong influence on the performance characteristics of the reactor.

DOI
https://doi.org/10.18690/um.feri.4.2025.49

ISBN
978-961-286-986-1

Keywords:
plasma,
plasma reactor,
transformer,
power system,
operating characteristics

University of Maribor Press

I Introduction

The problem of supplying plasma reactors with electricity boils down to ensuring optimum plasma generation conditions, while ensuring good interaction with the power grid and limiting electromagnetic interference generated by the plasma reactor. Figure 1 shows a three-phase gliding arc plasma reactor. Reactors of this type are used in processes for the purification of gases from hazardous chemicals.

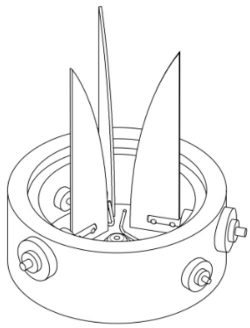

Figure 1. Costruction of the plasma reactor with gliding arc discharge

Three-phase gliding arc discharge plasma reactors are devices where stable plasma parameters are difficult to maintain electrically, physically and chemically [1]. The source of plasma, a free arc burning in a three-phase system, is the main cause of plasma instability (Fig. 2). The parameters of a long free arc plasma can change rapidly and stochastically [2][3].

Gliding arcs in three-phase systems are highly non-linear and unstable discharges that generate many voltage sinks, overvoltages and overcurrents, generate a lot of harmonics in the voltage and current feeding the plasma reactor and electromagnetic interference [4]. Due to their heterogeneous structure in cross-section and along the length of the columns of three-phase arcs in plasma reactors, they are difficult to analyse in terms of electrical, physical and chemical parameters. Furthermore, even small changes in the parameters of the electricity supply, or in the chemical or physical parameters of the plasma-generating gases, lead to changes in the conditions for the discharge to burn, which in turn involve self-regulating reactions in the plasma that change the arc structure and its characteristics.

Figure 2: Three-phase electric arc in side and top views

Control of the parameters of the plasma generated in the reactor consists of adjusting the parameters of the electrical supply, adjusting the physical parameters of the process gases and modifying their chemical composition. The regulation of plasma parameters in a gliding arc discharge reactor by means of electrical parameters is a complex, multithreaded problem and not fully understood. The shaping of the plasma parameters through the power supply system is done by selecting the voltage between DC and AC, selecting the AC voltage frequency, selecting the voltage shape, selecting the voltage and current values, controlling the harmonic content in the voltage and current. Keep in mind that the design of the power supply itself affects the discharge parameters [5]. In the case of transformer power supplies, the type of core material and, in three-phase systems, the method of connection can have an influence.

II Power Systems

An indispensable component of any power source, matching its parameters to the requirements of the receiver, is the transformer. In the case of plasma reactors, the transformer itself, in the right design, is a good and reliable power source. The transformer itself has a limited ability to influence the plasma parameters. In order to improve the control characteristics, transformer power supplies are extended with power electronic converters. Transistor converters allow the current and voltage of the plasma reactor supply to be regulated in a stepless manner, and the frequency of the voltage can also be adjusted.

Figures 3 and 4 show two solutions for this type of power supply. While both use the same AC/DC/AC converter circuit, they use matching transformers of different designs. The converter is built with a 6T+6D three-phase AC/DC transistor rectifier, a DC intermediate bus, a capacitive filter and a three-phase transistor inverter.

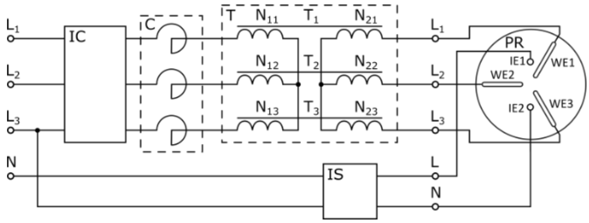

Fig. 3. Converter power supply with three single-phase transformers (PCS I)

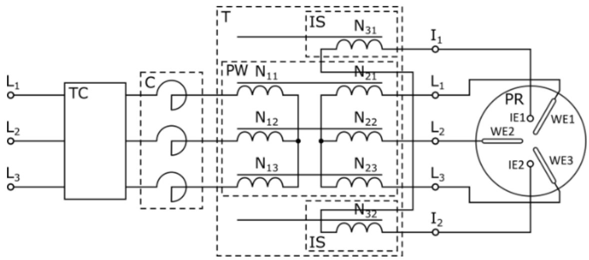

Figure 4: Converter power supply with five-column transformer (PCS II)

The PCS I power supply in Figure 3 uses single-phase transformers connected in a Yy connection group. The transformer cores were made of Metglas 2605SA1 amorphous material. Metglas cores are made as braided in the upper yoke. The PCS II power supply from Figure 4 uses a three-phase five-column transformer in a Yy connection grouping made of ET 120-27 electrical sheet. The cores are made as rolled and cut C-type. The parameters of the transformers are given in Table 1.

Table 1. Parameters of the transformers

Type	PCS I	PCS II
Power	13.8 kVA	11 kVA
Primary voltage	230 V	230 V
Secondary voltage	1.2 kV	1.2 kV
Secondary voltage of additional windings	-	1.9 kV
Primary current	20 A	15.8 A
Secondary current	3 A	2.4 A
Secondary current of additional windings	-	350 mA

Type	PCS I	PCS II
Number of turns of the primary winding	660	550
Number of turns of the secondary winding	4000	3600
Number of turns of the additional windings	-	25000

III Research on the Cooperation of Power Supplies with the Reactor

The power supplies shown in Figures 3 and 4 were tested to determine their ability to regulate plasma parameters. The results show large differences in the electrical characteristics of the plasma reactor when powered by the two power supply designs.

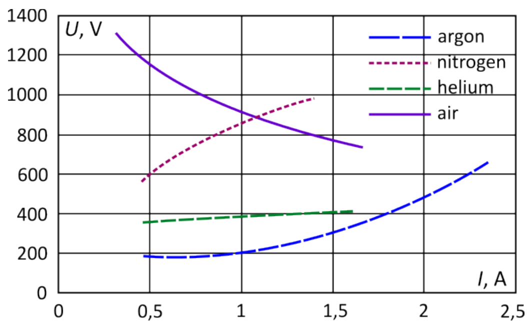

Figure 5: Current-voltage characteristics obtained for the PCS I power supply

Figure 5 shows the current-voltage characteristics for the PCS I power supply and Figure 6 for the PCS II power supply. The characteristics were plotted for four plasma-gas: argon, nitrogen, helium and air.

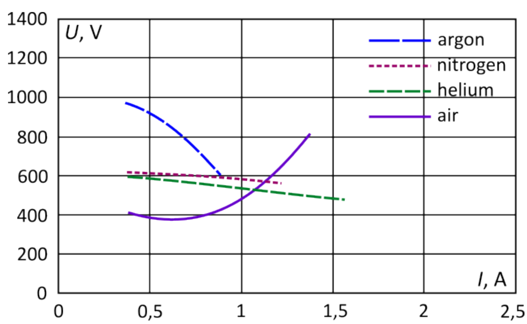

Figure 6: Current-voltage characteristics obtained for the PCS II power supply

The plotted characteristics indicate that the PCS II power supply has better control characteristics. However, taking into account other characteristics, e.g. efficiency, changes in discharge power as a function of changes in gas volume flow through the reactor, harmonic content in arc current and voltage, etc., it turns out that both power supplies have strengths and weaknesses.

IV Conclusion

The design and parameters of the matching transformer have a major impact on the interaction of the converter with the plasma reactor. The power of the transformer, the voltage and current of the secondary side, the dissipation reactance, the value of the magnetic induction in the core, the core material and the ability of the transformer to carry higher harmonics are the basic parameters to be considered. An improperly selected transformer does not allow you to take advantage of the control possibilities offered by the AC/DC/AC converter and deteriorates plasma performance. The level of electromagnetic interference, voltage collapse and overvoltage, overstress and higher harmonics generated by the plasma reactor also largely depends on the transformer design.

References

[1] N. Pourali, K. Lai, J. Gregory, Y. Gong, V. Hessel, E. V. Rebrov, "Study of plasma parameters and gas heating in the voltage range of nondischarge to full-discharge in a methane-fed dielectric barrier discharge", *Plasma processes and polymers*, Vol. 20, Issue 1, January 2023, DOI https://doi.org/10.1002/ppap.202200086.

[2] L. Potočňáková, J. Šperka, P. Zikán, J. J. W. A. van Loon, J. Beckers, V. Kudrle, "Experimental study of gliding arc plasma channel motion: buoyancy and gas flow phenomena under normal and hypergravity conditions", *Plasma Sources Science and Technology*, vol. 26, no. 4, 20 March 2017, DOI 10.1088/1361-6595/aa5ee8.

[3] J. Zhu, Y. Kusano, Z. Li, "Optical diagnostics of a gliding arc discharge at atmospheric pressure", *Atmospheric Pressure Plasmas: Processes, Technology and Applications*, pp.19-52, chapter 2, Nova science publishers, September 2016.

[4] M. P. Donsion, J. A. Guemes, AC Arc Furnaces Voltage and Current Harmonics Distortion. Influence of a SVC Installed, 2007 7th International Symposium on Electromagnetic Compatibility and Electromagnetic Ecology, 26-29 June 2007, IEEE Xplore, 29 October 2007, DOI 10.1109/EMCECO.2007.4371636.

[5] G. Komarzyniec, H. D. Stryczewska, P. Krupski, "The Influence of the Architecture of the Power System on the Operational Parameters of the Glidarc Plasma Reactor", *2019 IEEE Pulsed Power & Plasma Science (PPPS)*, Orlando, FL, USA, IEEE Xplore, 27 February 2020, DOI 10.1109/PPPS34859.2019.9009870.


KOLEKTOR
Kolektor Etra
TRANSFORMIRAMO PRIHODNOST
We are successful Slovenian company specialized in the production of power and generator transformers with a rated power up to 500 MVA and a rated voltage up to 420 kV.
For more information visit our website:
www.kolektor-etra.si

Gold Sponsor

HILTI

Silver Sponsors

imperix

KOLEKTOR

Thursday’s Coffee Break Sponsor

dem

Dravske elektrarne Maribor

Sponsors of Awards

IET Science, Measurement & Technology

emerald PUBLISHING

COMPEL

The international journal for computation and mathematics in electrical and electronic engineering

XXVIII Symposium Electromagnetic Phenomena in Nonlinear Circuits (EPNC 2024) Conference Proceedings

Martin Petrun,[1] Andrzej Demenko,[2] Wojciech Pietrowski[2] (Eds.)

University of Maribor, Faculty of Electrical Engineering and Computer Science, Institute of Electrical Power Engineering, Maribor, Slovenia
martin.petrun@um.si
Poznan University of Technology, Institute of Electrical Engineering and Electronics, Poznan, Poland
andrzej.demenko@put.poznan.pl, wojciech.pietrowski@put.poznan.pl

The Symposium on Electromagnetic Phenomena in Nonlinear Circuits (EPNC 2024) is one of the longest-running conference series, having been established in the 1970s. The aim of Symposium is to present the recent advances in the analysis, synthesis, optimisation, and inverse problems in nonlinear electromagnetics. Over the decades, it has significantly influenced research in the field of nonlinear electromagnetics. The symposium has provided a vital platform for researchers and practitioners to exchange ideas, present groundbreaking work, and discuss the latest trends and challenges in the application of nonlinear phenomena in electrical engineering. The contributions from the 2024 EPNC are featured in these proceedings. The publications primarily focus on electrical machines, magnetic materials, bioelectromagnetics, related calculation and analysis methods.

DOI
https://doi.org/
10.18690/um.feri.4.2025

ISBN
978-961-286-986-1

Keywords:
nonlinear coupled electromagnetic phenomena, nonlinear devices and systems, electromagnetics, bioelectromagnetics, nonlinear opticsm, wave propagation

University of Maribor Press

June 18th to June 21st 2024

Portorož, Slovenia

University of Maribor

Faculty of Electrical Engineering
and Computer Science

POLITECHNIKA POZNAŃSKA

POZNAN UNIVERSITY OF TECHNOLOGY

EPNC 2024